HYDRODYNAMIC MODELING OF VEGETATED ALLUVIAL CHANNEL & ITS APPLICATION IN AQUATIC ECOLOGY

A thesis submitted in partial fulfillment of the requirement for the award of the degree of

Doctor of philosophy

By

Anupal J Baruah

Department of Civil Engineering

Indian Institute of Technology Guwahati

September 2021

Dedicated to my parents and family

Certificate

It is certified that the work contained in the thesis entitled **"Hydrodynamic modeling of vegetated alluvial channel and its application in aquatic ecology"** by Anupal J Baruah, Roll Number 166104103, a student in Department Of Civil Engineering, Indian Institute of Technology, Guwahati, for the award of the degree of Doctor of Philosophy has been carried out under my supervision and this work has not been submitted elsewhere for a degree.

Arup Kumar Sarma

Professor

Department of Civil Engineering

Indian Institute of Technology, Guwahati

Guwahati-781039, Assam, India

September, 2021

Acknowledgments

I would like to express my heartfelt gratitude and sincere thanks to my thesis supervisor Dr. Arup Kumar Sarma, Professor, Department of Civil Engineering, Indian Institute of Technology, Guwahati, for his invaluable guidance and full cooperation throughout all the aspects of this research work. It was a privilege to work under his supervision and humble guidance.

I attribute this achievement to my parents Late Jitendra Nath Baruah and Aparajita Baruah, my younger brother Nilutpal Baruah and my other family members. Without their support and blessing, I couldn't have made this possible. I fondly remember my late uncle Jayanta Madhab Sarmah for his endless and continuous support and love that I have received throughout this journey.

I would also like to express my heartfelt thanks and reverence to the Chairman of the Doctoral Committee, Dr. Sudip Talukdar, Department of Civil Engineering, Indian Institute of Technology, Guwahati, for his valuable suggestions and all the help that I have received during the various stages of my research work. I am also indebted to Dr. Sreeja Pekkat, Associate Professor, Department of Civil Engineering, Indian Institute of Technology, Guwahati, and Dr. Sashindra K. Kakoty, Professor, Department of Mechanical Engineering, Indian Institute of Technology, Guwahati, for their keen interest, valuable suggestions, and guidance provided to complete my research work as members of the doctoral committee. I would like to acknowledge Dr. Hriday Mani Kalita, Assistant Professor, Department of Civil Engineering, National Institute of Technology, Meghalaya, for his support during my Ph.D. tenure.

I would like to acknowledge the Brahmaputra Board, Govt. Of India for their logistic support and the data provided during the field investigation. I am also indebted to Mr. Ranjit Deka, Director, NEHARI, for his support during the field survey.

I express my sincere thanks to the staff members of the Civil Engineering Department, Indian Institute of Technology, Guwahati, for their kind cooperation during my research work.

Last but not least, I would like to mention that it is virtually impossible to name all my friends and well-wishers who made my stay at IIT Guwahati delightful; however, I would like to specially thank Karuna Dutta, Mithun Deka, Sagarika Patowary, Gaurav Talukdar, Dipsikha Devi, Amit Kalita, Dhruba Jyoti Sarmah, Khyati Manjuri Chaudhury, Priyam Deka, Rishov Barua, Dipima Sarma, Jogen Dutta, Anurag Handique , Jyotirmoy Barman, Rahul Bhagawati, and Saurabh Kumar Sarma for their constant help and support, and for making my time at IIT Guwahati worth remembering with loads of fond memories.

Finally, I would like to thank God for giving me strength, patience, and ability to carry out my Ph.D. work with a sound mind and in good health.

Anupal J Baruah

Indian Institute Of Technology, Guwahati

ABSTRACT

The freshwater ecosystem performs numerous environmental functions, including nutrient recycling, flood attenuation, and habitat for aquatic flora and fauna. In 2015, the United Nations established the sustainable development goal 14(SDG-14), which focuses on developing a sustainable and conservative ecosystem to maintain habitat richness and diversity in the ocean and the river system. The breeding, growth, and survival of the aquatic species residing in an ecosystem are primarily governed by the hydrological changes, hydrodynamic variables, and the substrate cover in the flow domain. The required ecological flow for developing a sustainable ecosystem, flow regulations due to dams and barrages, and aquatic vegetation such as shrubs, mangroves, or even macrophytes modify the flow characteristics and affect habitat richness. The capability of the hydrodynamic models to mimic the complex river dynamics under the stochastic environments led to its application in the field of aquatic ecology. The numerical models solve the governing conservations laws and compute the flow parameters under diverse situations. For instance, at different releases from the dams and the barrages, in vegetated channels having varying roughness, and to evaluate the underwater characteristics like habitat suitability for different aquatic flora and fauna in freshwater environments.

This work mainly emphasizes developing a robust and stable two-dimensional depth-averaged shallow water model in open channel flow. A modified form of the non-conservative two-dimensional shallow water equation is solved by the second-order accurate TVD Mc-Cormack predictor-corrector finite difference scheme in MATLAB. The present shallow water formulation uses the water surface gradient in the source term and gives more flexibility to the model for application in natural terrains, especially in braided morphology. The TVD scheme used during the study removes the numerical oscillations and maintains the smoothness in the

solution domain. The main advantage of the TVD scheme is that it is free from the trial and error process while adding the right amount of dissipation in the solution. The model is calibrated and validated with the published experimental datasets, analytical results, and field-measured results. A braided stretch of the Brahmaputra River near Umananda Island and the Majuli Island, hilly terrain in Tiding River, Arunachal Pradesh, is considered for the model application to test its robustness.

The vegetation influence on the open channel flow is investigated by incorporating the vegetation drag forces within the developed shallow water model. Both rigid and flexible vegetation are used in the study. A modified expression for Manning's n parameter is used to integrate the roughness offered from the rigid emergent stems in the hydrodynamic simulation. The fully coupled flow model with the rigid stems is validated with the published experimental results. The coupled model is further applied to investigate the vegetation impact on the transcritical flow profile in a converging channel, the secondary current strength in a bend channel, and the near bank velocity profile downstream of a spur in the Brahmaputra River. Results indicate that the outer bank vegetation counteracts the centrifugally induced secondary current and reduces the velocity. It is also observed that with different vegetation arrangements, the transcritical flow profile gets modified and gradually reaches a subcritical state. The instream vegetation also affects the vertical flow structure, but the depth-averaged form of the governing equations does not propagate any information in the vertical direction. However, the estimation of vertical velocity profiles is essential near the hydraulic structures to study the scouring and erosion pattern, especially in vegetated channels with submerged vegetation. A quasi three-dimensional framework is proposed during the study by linking the developed shallow water model with the entropy theory to compute the vertical velocity profile in open channels with and without vegetation. The coupled model is applied in the Brahmaputra River near the Majuli Island, and the computed velocity profiles are compared with the current meter

reading obtained from the field. Two published experimental datasets are used to compute the vertical velocity profile in a vegetated channel having submerged flexible vegetation. The deflected height of the vegetation is calculated from the large deflection cantilever beam theory. The model results are compared with the experimental and field measured results and found satisfactory. The model performance is evaluated by using two statistical indices, MAE($\approx$0.079) and RMSE($\approx$0.1148).

With this understanding, the applicability of the shallow water model is extended in habitat modeling study in the Bhogdoi River, Assam, India. The study area is a fishing hub for the riverine community. However, the state government has proposed an irrigation scheme to improve the irrigation potential of the nearby agricultural area. The construction of the weir will be beneficial for the agricultural sector but may impact the aquatic life downstream. Thus, prior to its implementation, the adequate flow rate required for the survival of the locally available adult fish species (Bhangun fish, scientific name-Labeo Bata) is estimated from the ecohydraulic approach. The computed water level and velocity are compared with the observed results and found satisfactory. Results indicate that for the sustainability of the targeted species, the flow rate in the stream must be maintained between 30-60 m^3/sec.

TABLE OF CONTENTS

TITLE	Page number
Certificate…….....	i
Acknowledgment…….....	ii
Abstract…….....	iv
Contents…….....	vii
List of figures…….....	xiii
List of tables…….....	xix
List of notations……..	xx
List of abbreviations……...	xxiii
CHAPTER 1: INTRODUCTION	
1.1 Purpose of study…….	1
1.2 Organization of the thesis……...	4
CHAPTER 2: LITERATURE REVIEW	
2.1 Introduction…….	7
2.2 Previous works on unsteady flow simulation…….	7
2.2.1 Governing Equations…….	7
2.2.2 Solution of Governing Equation……	7
2.2.2.1 Finite difference method……..	8

2.2.2.2 Shock capturing techniques……. 13

2.2.3 Previous works on unsteady flow simulation with vegetation…….. 16

2.2.3.1 Vegetation influence on the channel hydrodynamics…… 16

2.2.3.2 Roughness models for rigid vegetation …….. 17

2.2.3.3 Previous works on unsteady flow simulation with rigid emergentvegetation…… 19

2.2.4 Previous work on the estimation of vertical velocity structure with submerged vegetation in open channel…… 22

2.2.5 Previous works on Shannon's entropy theory for velocity distribution in open channel flow…… 24

2.2.6 Previous works on the Ecohydraulic modeling…… 27

2.3 Conclusion……..... 30

CHAPTER-3 DEVELOPMENT OF MATHEMATICAL MODEL

3.1 Introduction…… 33

3.2 Assumptions made in the governing equations……. 33

3.3 Two-dimensional representation of the shallow water equations…….. 33

3.4 Transformation of the equations in boundary fitted coordinate system….. 37

3.5 Numerical solution of the shallow water model …… 43

3.5.1 Finite difference method…… 43

3.5.2 TVD McCormack predictor-corrector numerical scheme……. 44

3.5.2.1 McCormack predictor-corrector scheme……. 44

3.5.2.2 Total variation diminishing (TVD) scheme……. 46

3.5.3 Stability of the model……..... 47

3.5.4 Boundary condition……..... 48

3.6 Conclusion ……. 49

CHAPTER-4 APPLICATION OF THE SHALLOW WATER MODEL

4.1 Introduction…… 50

4.2 Application of the model with experimental test cases……. 50

4.2.1 Positive and negative surge wave propagation due to an instantaneous dam break …….. 50

4.2.2 Model behavior in a highly irregular bed elevation……..... 51

4.2.3 Steady flow over an undulating terrain……. 52

4.2.4 Transcritical flow over a hump without a shock……. 53

4.2.5 Formation of a hydraulic jump over a hump……. 56

4.2.6 Flood wave propagation at downstream of a reservoir due to a dam failure…….. 59

4.3 Development of the grid generator……. 61

4.3.1 Application of grid generator in the Brahmaputra River, near Umananda, Assam, India…….. 63

4.3.2 Application of grid generator in the Brahmaputra River near Majuli, India……. 65

4.4 Field survey for the validation of the model…… 66

4.4.1 Field survey near Umananda Island, Guwahati, Assam ……. 66

4.4.2 Field survey near Majuli Island, Assam …….. 67

4.5 Field application of the model ……..... 70

4.5.1 Application of the model near the Umananda Island, Guwahati …. 70

4.5.2 Application of the model near the Majuli Island ……. 72

4.5.2.1 Influence of boundary condition near flow-structure interaction zone 75

…….....

4.5.2.2 Exploring the dredging possibility near Nimatighat, Majuli from the 78

model application …….....

4.5.3 Application of the model in Tiding river, Arunachal Pradesh …… 83

4.6 Conclusion ……..... 89

CHAPTER-5 A FULLY COUPLED TWO DIMENSIONAL FLOW ROUTING MODEL IN VEGETATED OPEN CHANNEL

5.1 Introduction…… 92

5.2 Determination of the roughness coefficient in the vegetation area …… 92

5.3 Coupling of rigid vegetation within the hydrodynamic model …… 93

5.4 Application of the model ……..... 96

5.4.1 Flow simulation in a rectangular channel with varying vegetation 96

density…….

5.4.2 Impact of vegetation on the flow state in the Transcritical condition 100

5.4.3 Impact of vegetation on the centrifugally induced secondary current near the outer bank of a U-type channel …….. 103

5.4.4 Riparian vegetation influence on the velocity profile near recirculation zone …….. 110

5.5 Conclusion ……. 113

CHAPTER-6 A QUASI THREE DIMENSIONAL HYDRODYNAMIC MODEL FOR VERTICAL VELOCITY DISTRIBUTION IN OPEN CHANNEL FLOW WITH AND WITHOUT VEGETATION

6.1 Introduction …… 114

6.2 Vegetation model …….. 116

6.2.1 Deflection of the flexible vegetation …… 116

6.2.2 Velocity distribution in the vegetated layer ……. 117

6.2.3 Shannon's entropy theory for velocity distribution in the free water layer ……..... 120

6.3 Study area and field measurements ……..... 121

6.4 Initial and Boundary condition ……. 121

6.5 Application of the model ……. 122

6.5.1 Application of the model in the Brahmaputra River, India ……. 122

6.5.2 Estimation of vertical velocity profile with submerged flexible vegetation ……..... 125

6.5.2.1 Semi coupled approach for vertical velocity profile computation…… 126

6.5.2.2 Application of the model in vegetated channel ……. 128

6.6 Dynamics of entropy parameter in a vegetated channel …… 140

6.7 Conclusion……..... 142

CHAPTER-7 HYDROLOGICAL-HYDRODYNAMIC NEXUS FOR EVALUATION OF FISH HABITAT SUITABILITY: A CASE STUDY IN BHOGDOI RIVER, ASSAM, INDIA

7.1 Introduction ……... 144

7.2 Material and Method ……..... 146

7.2.1 Study area ……..... 146

7.2.2 Hydrological methods for ecological flow (EF) estimation…..... 147

7.2.2.1 Flow duration curve analysis (FDCA) method…… 147

7.2.2.2 Flow duration curve shifting (FDCS) method ……... 148

7.3 Hydrodynamic model ……..... 152

7.3.1 Governing equation and numerical scheme…….. 152

7.3.2 Initial and boundary condition ……..... 152

7.3.3 Stability of the model ……..... 152

7.4 Habitat suitability curves and the WUA calculation for the Bhangun fish.. 153

7.5 Result and discussion ……..... 156

7.5.1 Environmental flow rates from FDCA method …… 156

7.5.2 Environmental flow rate from (EFR) FDCS method …….. 156

7.5.3 Hydrodynamic -habitat simulation in the domain…… 157

7.6 Conclusion……..... 164

CHAPTER-8 CONCLUSION AND GENERAL DISCUSSION FOR FUTURE STUDIES

8.1 Introduction……..... 165

8.2 General discussion and conclusion ……..... 165

8.3 Major contribution of the thesis

8.4 Scope for future work ……..... 168

REFERENCE ……..... 169

PAPERS PUBLISHED/PRESENTED……... 184

LIST OF FIGURES

Figure No.	Caption	Page No.
3.1	Physical and computational domain……	37
4.1	Computed and analytical water depth from dam-break……..	51
4.2	Computed and analytical velocity from dam-break ……..	51
4.3	Preservation of still water surface over undulating terrain……..	53
4.4	Still water surface over the irregular bed…….	54
4.5	Computed unit discharge over the irregular bed…….....	54
4.(6,7)	Computed water surface elevation at 300-time step and 1000 time step……	55
4.8	Computed water surface elevation and the analytical result after reaching steady state…….	56
4.9	Computed unit discharge and analytical result…….	57
4. (10,11)	Computed water surface elevations at the time of jump formation……..	58
4.12	Computed water level and analytical result…….	58
4.13	Computed unit discharge and analytical result……	59
4.14	Dam break flow after 50 seconds of breach…….	60

4.15	Dam break flow after 100 seconds of breach…….....	60
4.16	Computed velocity vectors after the breach……	61
4.17(i-v)	Different steps of grid generation…….	63
4.18	Grid generation in the Brahmaputra River near Majuli, Assam……	65
4.19	(a)Surveyed portion near the Umananda Island ……..	67
	(b) Velocity sampling cross-section…….	67
4.20	(a) Study area and velocity measuring points …….	68
	(b) Photographs taken during the survey …….	69
	(c) Particle size distribution curve…….	69
4.21	Map of the study area……..	71
	(a) Generated grid in the computational domain …….	71
	(b) Bed level elevations(m) in the domain……	71
4.22	(a) Computed flow depth contour in the domain……	71
	(b) Comparison of computed and measured flow depth ……	71
	(c) Comparison of computed and measured velocity……..	71
4.22.1	Comparison of the present model output with MIKE21C	
	(a) Flow depth……..	72
	(b) Velocity……..	72
4.23	(a) Grids in the flow area…….	73

(a) Computed flow depth (m) ……... 74

(b) Computed velocity in the flow area……. 74

(c) Formation of recirculation zone downstream of spur……... 75

4.24 Comparison of the computed and measured

(a) Flow depth……... 75

(b) velocity……... 75

4.25 Reflection and no slip boundary condition……... 76

4.26 Study area with proposed dredging …….. 79

4.27 Bed profile before and after sandbar dredging …… 80

4.28 Near bank velocity profiles…….. 80

4.29 Flow parameter observation points near the south bank…….. 81

4.30 Location of the porcupine screen…….. 82

4.31 Computed velocity profile before and after the installation of the porcupines……... 83

4.32 Map of the study area…….. 84

4.33 (a) Modeled portion of the study area……. 85

(b) Grid generation in the study area……... 85

(c) Bed profile in the domain……... 85

4.34 (a) Computed flow depth ……. 87

(b) Computed velocity profile…….. 87

4.35	Comparison of flow depth from the present model and MIKE21C…….	88
5.1	(a) Emergent vegetation height and flow depth……..	93
	(b) Schematic representation of the discretized domain with vegetation……..	95
	(c) Flow chart of the model…….	95
5.2	Vegetation arrangement in the experimental channel……..	97
5.3	Comparison of computed and experimental velocity under different vegetation density ……. (a)Bare (b) SMD (c) SDM (d) MDS (e)DSM (f) Computed velocity profiles with all combinations (g) Manning's n Values at different vegetation arrangement	99
5.4	(a) Grids in the converging channel……...	101
	b) Distribution of vegetation in the channel ……	101
	(c) Velocity contour map …….	102
	(d) Comparison of the computed and experimental result……	102
	(e) Flow state at different vegetation density……	103

5.5	(a) Generated grids in the computational domain…….	105
	(b) Location of vegetation near the outer bank…….	105
	(c) Comparison of computed and measured water depth……..	106
	(d) Comparison of computed and measured velocity at the outlet.	106
	(e) Computed velocity vectors in the flow domain……	107
	(f) Velocity contour map with no vegetation near the outer bank..	108
	(g) Velocity contour map with vegetation density 61stems/m^2 near the outer bank ……..	108
	(h)Velocity contour maps with vegetation density 92 stems/m^2near the outer bank …….	109
	(i) Comparison of Secondary circulation strength at different scenarios……...	109
5.6	(a) Vegetation configuration at the toe of the bank…….	111
	(b) Velocity profile near the recirculation zone with and without vegetation……	112
6.1	Deflection of Flexible Vegetation……	119
6.2	Velocity profile in an open channel with submerged flexible vegetation…….	119
6.3	Vertical velocity profile at S11, S22, and S41……	123
6.4	Dip phenomenon in velocity profile near the hydraulic structures	125
6.5	Flowchart of the model……..	126

6.6	Correlation coefficient between the measured and predicted curve length of the flexible stem……..	131
6.7	Computed depth-averaged velocity profile for experiment (a) 1.2.1 (b) 4.1.1……	132
6.7	Correlation coefficient between the measured and predicted curve length of the flexible stem……..	132
6.8	Configuration of vegetation within the hydrodynamic model…..	132
6.9	Comparison of computed and measured velocity profiles at experiment number (a) 1.2.1 (b) 1.1.3 (c)2.1.1 (d) 2.2.1 (e) 3.1.1 (f) 3.2.1 (g) 4.1.1……	134
6.10	Comparison of computed and measured velocity profiles at experiment number (a) R4-1 (b) R4-2 (c)R4-3 (d) R4-4 (e) R4-5 (f) R4-6 (g) R4-7(h) R4-8 (i) R4-9……..	139
6.11	Coefficient of correlation between the measured and computed results……	139
6.12	Relation between the vegetation density and entropy parameter	141
7.1	Study Area……	147
7.2	Flow duration curve…….	148
7.3	Estimation of Environmental Flow duration curves for different EMC…….	151

7.4	Generation of Environmental flow time series from the Environmental FDC……..	152
7.5	Composite suitability index at cell -1 in a channel section……..	155
7.6	Flow rates $(m^3/s)$for different EMC, Q_{90} and Q_{95}.....	157
7.7	Flow depth contours form the hydrodynamic computations (a) Q=90 m^3/sec (b) Q=75 m^3/sec (c) Q=60 m^3/sec (d) Q=45 m^3/sec(e) Q=30 m^3/sec (f) Q=18.13 m^3/sec …….	158
7.8	(a), (b) Computed and observed water level (c) Comparison of the computed and measured velocity (d) Generated grids in the flow domain……	160
7.9	Habitat suitability curve for the adult Bhangun fish (a) Flow depth (b) Velocity (c) Channel index……..	162
7.10	Weighted usable area for the Bhangun fish in the Bhogdoi River, India……..	163

LIST OF TABLES

Table number	Caption	Page number
4.1	Statistical index for model evaluation…….	77
5.1	Discharge data at different vegetation patterns for the rectangular channel……..	97
5.2	Channel dimension and flow rate for converging channel…….	100
5.3	Channel dimension and flow rate for the U-type channel……..	104
5.4	Geometric, vegetation, and flow characteristics of the study reach……..	110
6.1	Flow and vegetation parameters for simulation(Kurbak et al. 2012)…….	130
6.2	Flow and vegetation parameters for simulation (Jarvela 2005)…..	135
6.3	Coefficient of Correlation at different $\frac{Flow\ depth}{Vegetation\ height}$…….	142
7.1	Discharges at different environmental management scenarios……	149
7.2	Habitat preference of some indigenous fish species in Assam, India	153
7.3	Statistical index for model evaluation……	161

List of notations

U	Temporal derivatives
F	Spatial derivatives in the x-direction
G	Spatial derivatives in the y-direction
S	Source terms
$\in$	Water surface elevation
hu	Discharge per unit width/unit discharge in the x-direction
hv	Discharge per unit width/unit discharge in the y-direction
Z_b	Bed surface elevation
$\frac{\partial Z_b}{\partial x}, \frac{\partial Z_b}{\partial y}$	Bed gradient in x and y-direction
g	Acceleration due to gravity
S_{fx}	Energy gradient in the x-direction
S_{fy}	Energy gradient in the y-direction
n	Manning's roughness coefficient
n_v	Modified Manning's roughness coefficient due to vegetation
h	Flow depth
H_v	Rigid vegetation height
u ,v	Depth averaged velocities in the streamwise and transverse direction
U, V	Transformed velocity in boundary fitted coordinates along the streamwise and transverse direction
$\frac{\partial \in}{\partial x}, \frac{\partial \in}{\partial y}$	Water surface gradients in x and y-direction
$\boldsymbol{\rho}$	Density of water
F_{Dx}, F_{Dy}	Drag force per unit area in x and y-direction
C_d	Drag coefficient
m	Vegetation density
A	Cross-sectional area
A_v	Frontal area of vegetation
u_v , v_v	Velocity in the stem layer along the streamwise and transverse direction.
h_v	Projected bending height of flexible vegetation
$\varepsilon, \boldsymbol{\eta}$	Body fitted coordinates
∂t	Time step for each iteration

$\partial x, \partial y$	Grid spacing in x and y direction
$\partial \varepsilon, \partial \eta$	Grid spacing in boundary fitted coordinate system
J	Jacobean matrix
P	Temporal derivatives in boundary fitted coordinates
Q	Spatial derivatives in ε direction
R	Spatial derivatives in $\boldsymbol{\eta}$ direction
O	Source terms in boundary fitted system
k	Temporal axis
L	Source terms in ε direction
M	Source terms in $\boldsymbol{\eta}$ direction
ω^p	Predicted variables
ω^c	Corrected variables
TVD	Total variation diminishing
r_i	TVD variables in the i^{th} direction
r_j	TVD variables in the j^{th} direction
C_r	Courant number
X	Grid points in the longitudinal direction
Y	Grid points in the lateral direction
V_x	Number of stems in the x-direction
V_y	Number of stems in the y-direction
R	Hydraulic radius
L	Length of the vegetated section
S_{xy}	Secondary current strength
$K_{lateral}$	Lateral flow kinetic energy
K_{main}	Main flow kinetic energy
RMSE	Root mean square error
NSE	Nash-Sutcliffe efficiency
MAE	Mean absolute error
P	Average Imposed load on the flexible stem
S	Curve length of the stem after bending
EI	Flexural rigidity of the stem

z	Any depth along the vertical
D	Stem diameter
C_f	Friction coefficient
C_p	Perimeter of the stem cross section
u_{max}	Maximum velocity in the cross section
u_{avg}	Mean c/s velocity in the vegetated region
u_v	Velocity profile at different depth from the bed to the free surface
M	Entropy parameter in the cross section
$\phi(M)$	A function of entropy parameter
h_{max}	Location of maximum velocity in the vertical
h_0	Location of zero velocity in the vertical

List of Abbreviations

1D	One dimensional
2D	Two dimensional
3D	Three dimensional
SWE	Shallow Water Equation
FDCA	Flow Duration Curve Analysis
FDCS	Flow Duration Curve Shifting
HSI	Habitat Suitability Index
HSC	Habitat Suitability Curve
CSI	Composite Suitability Index
TVD	Total Variation Diminishing
WUA	Weighted Usable Area
EF	Environmental/Ecological Flow
EMC	Environmental Management Class
EFR	Ecological Flow Rate

CHAPTER-1

INTRODUCTION

1.1 Purpose of the study

The complexity and dynamics of the river systems, the strength of the biophysical linkage between their components, and the need to respond to adverse anthropogenic impacts have led computational hydraulics as one of the key areas of hydrology. Hydrodynamic models are excellent tools to predict the uncertainties associated with the lotic environments characterized by variable discharge, hydraulic properties, sediment, and nutrient loads that may change temporally and spatially. Depending on the need and objective, one can use one-dimensional, two-dimensional, or three-dimensional models to address the complex river problems in an unsteady environment. The increasing capability of the numerical models to mimic the real field scenarios has made them advantageous over the laboratory-scale models and analytical models in many situations (Vyas et al. 2020). For instance, bed morphological variations in the braided river system, non-prismatic channel geometry, and aquatic flora –fauna are prevalent in any natural flow system. Vegetation is ubiquitous in natural flow systems. The presence of vegetation impacts the habitat richness and biodiversity in the river ecosystem (Verschoren et al. 2016). Flow-vegetation interactions mainly modify the instream roughness and flow characteristics, and thus marine habitats in the river and estuaries are influenced. The hydro-morphological changes in vegetated environments depend upon the vegetation attributes such as patch density, stem diameter, vegetation drag force, flexural rigidity, etc. Vegetation in a channel influences physical flow parameters such as secondary current strength, vertical velocity profile, vortex strength, and the flow–energy nexus. The knowledge of mean and turbulent flow structure in a vegetated environment is therefore of great importance for understanding and assessing the associated transport processes of sediments and contaminants.

However, the wide variety of vegetation types, characteristics, and diverse hydrodynamic and morphological conditions are sometimes difficult to represent in small scale experimental setups. On the other hand, the mathematical models are excellent tools for predicting the flow field and the hydraulic changes in a vegetated environment, provided vegetation can be represented appropriately in the computational flow field. Such models contribute towards an efficient and economical approach to undertake proper management strategies for the riverine community.

The computational efficiency of the hydrodynamic models to predict the flow dynamics under these complex situations expands its application in aquatic ecology and habitat sustainability in fresh, saline, and marine environments. A comprehensive understanding of various factors and components that provide a suitable environment for river health sustainability is essential for biodiversity conservation. Hydrological variations due to climate changes, dam constructions, river channelization and stabilization, river dredgings are critical factors that significantly affect the natural flow regimes and, consequently, endangering the aquatic biota. The marine species are susceptible to the existing hydraulic conditions, including depth, velocity, bed material, river bed shear stress, and water temperature in the rivers and the streams. These species mainly rely on the physical flow forces that influence dispersal, habitat use, breeding, and predation in any marine ecosystem. Through ecohydraulics, the researchers have focused on developing the relationship between the instream biota and hydraulic variables, e.g., flow depth(h) and velocity(u), through field investigation and numerical studies(Kim and Choi 2019). Thus one can confidently say that the scope of interdisciplinary issues spans the traditional boundaries of computational fluid dynamics. The potential application of computational models under the aquatic environment can predict the suitability of the flow parameters for the survival and conservation of the instream biota at the local and global scale.

The reciprocities of riparian vegetation and marine ecosystem dynamics can be effectively handled by the flexibility and robustness of the numerical models. By flexibility, one can truly understand the importance of the configuration of the riparian vegetation parameters within the shallow water models in open channel flow. For instance, vegetation covers, type of vegetation, randomness in vegetation distributions, varying density, degree of submergence, and flexural stiffness are essential parameters that need to be considered in ecohydraulics. Again, the hydrological alterations, mainly seasonal drying-wetting, highly influence ecosystem diversity in intermittent streams and are responsible for the spawning and reproduction of the aquatic habitats. The minimum flow rate required for the smooth functioning of the residing marine species is another crucial aspect that needs to be considered in ecological modeling. These are essential characteristics that need to be considered while studying the flow-sustainability nexus for the freshwater species in the marine environment. Earlier, the computational models were based on functional relationships between riparian vegetation and physical habitat and demonstrated that some characteristics of these ecosystems could be partially simulated (Glenz et al. 2008). The majority of the models were developed for specific boundary conditions and were not easily transferable to other geographical regions (MERRITT et al. 2010). However, as per the author's knowledge, no effort has been made in developing a coupled model for eco-hydrological applications in natural terrains. Thus, a holistic and efficient computational framework is necessary for proper understanding of the aquatic ecosystem and model its different components under diverse flow scenarios.

This work mainly emphasizes developing a robust and stable, linked two-dimensional flow-vegetation model for ecohydraulic application in natural terrains. A novel technique is implemented to configure the vegetation within the hydrodynamic model. Both rigid and flexible vegetation in submerged and emergent conditions are used during the study. The

ecological consequences and the impact of hydrological alterations on the local fish species in the Bhogdoi River, India, are also investigated by implementing the model.

The objectives of the present work are briefly summarized below-

1) To develop a two-dimensional free surface unsteady flow simulation model for applying it in natural flow domains with undulating bed morphology, diverse flow situations, and complex channel geometry.
2) To couple the rigid vegetation stems within the developed 2D flow model to evaluate the influence of vegetation characteristics on the flow parameters.
3) To estimate the vertical velocity structure from a quasi three-dimensional approach with and without the vegetation. The vegetation considered are mainly submerged flexible types.
4) To predict the ecological and adequate flow rate for the targeted aquatic species in the Bhogdoi River, Assam, by implementing the model.

1.2 Organization of the thesis

The complete work is divided into several stages and is presented in different chapters, as shown below

- Chapter-2 contains a brief literature review on the different forms of the governing equations, numerical methods, solution schemes, and the available hydrodynamic models for the free surface flow simulations. The literature regarding the application of the entropy theory for velocity distribution in open channel flow is incorporated. The past works on hydrodynamic modeling under vegetated environments are also included in this chapter. The reviews and methods pertaining to the vertical velocity structure in submerged flexible vegetation are briefly described. Finally, a review on the

ecohydraulic approaches applied in habitat suitability studies for aquatic species is presented.

- Chapter-3 presents the governing equations and highlights the assumptions associated with the two-dimensional shallow water equations. The detailed representation of the depth-averaged governing equations is presented here. The method adopted for grid generations and its transformation from the physical domain to the computational domain is elaborated in this chapter.
- Chapter-4 contains the application of the shallow water model in diverse flow scenarios. The calibration and validation of the model with the published experimental works are presented here. The details of the field application and validation of the model are also elaborated.
- Chapter-5 describes the methodology used to develop the fully coupled 2D flow-routing model in a vegetated channel having rigid emergent stems. The random distribution of vegetation is integrated from a novel subgrid technique. The model is calibrated and validated with the published experimental results. The coupled model is applied in a converging mixed-flow channel, U-type bent channel, and a natural channel with a series of spurs to investigate the vegetation influence on the velocity profile.
- Chapter-6 presents the development of a quasi-three-dimensional velocity distribution model in open channel flow. The model is calibrated and validated with the field-measured results. The model is further applied to compute the vertical velocity profile in a vegetated environment having submerged flexible stems. The computed velocity profiles are compared with the published experimental work.
- Chapter-7 presents a methodology to investigate the aquatic habitat sustainability in the Bhogdoi river, India. Under different streamflow events and ecological practices, the

preferable flow rate is determined from a hydrological-hydrodynamic framework. The scope of investing the impact of vegetation on aquatic habitat is also introduced.

- Chapter-8 summarizes the entire work along with some critical conclusions and identifies the future scope of the research work.

CHAPTER-2

LITERATURE REVIEW

2.1 Introduction

The ecohydraulic modeling is an effective tool to understand river and coastal hydrodynamics precisely under different flow conditions. The applications of one-dimensional (1-D) and two-dimensional (2-D) models are increasingly used to model the flow and sediment transport processes in rivers and estuaries for a long and short period(Zhang and Nepf 2011). The work conducted in this study primarily focused on predicting the flow parameters by solving the two-dimensional (2D) Saint Venant equations in the vegetated, non-vegetated environment and freshwater ecosystem. Both rigid and flexible stems of vegetation under emergent and submerged conditions are considered in the computations. The review of the past works carried out during the study has been broadly grouped into the following

(i) Previous works on unsteady flow simulation

(ii) Previous works on unsteady flow simulation with vegetation.

(iii) Previous works on Ecohydraulic modeling.

2.2 Previous works on unsteady flow simulation

2.2.1 Governing equations

The shallow water equations provide an excellent approximation to the three-dimensional Navier-Stokes equations for nearly horizontal free surface flows. These equations are mass and momentum conservation equations and are widely used in the hydrodynamic simulations of rivers, lakes, estuaries, and flood plains. Depending on the problem formulation, these equations can be expressed in one dimensional, two-dimensional, and three-dimensional forms. Generally, two-dimensional models are capable of representing

the water surface elevation, velocity profile, and flow depth under complex and diverse flow environments with more accuracy.

The depth-averaged two -dimensional conservative non-viscus shallow water equations in matrix form can be expressed as (P. et al. 2002; Alessandro and Lorenzo 2006)

$$\frac{dh}{dt}+\frac{d(hu)}{dx}+\frac{d(hv)}{dy}=0 \tag{2.1}$$

$$\frac{d(hu)}{dt}+\frac{d(hu^2)}{dx}+\frac{d(huv)}{dy}=-ghS_{ox}-ghS_{fx} \tag{2.2}$$

$$\frac{d(hv)}{dt}+\frac{d(huv)}{dx}+\frac{d(hv^2)}{dy}=-ghS_{oy}-ghS_{fy} \tag{2.3}$$

Liang and Borthwick (2009) modified the above formulation and proposed a new set of governing equations in the following manner

$$\frac{\partial}{\partial t}[\in]+\frac{\partial}{\partial x}[hu]+\frac{\partial}{\partial y}[hv]=0 \tag{2.4}$$

$$\frac{\partial}{\partial t}[hu]+\frac{\partial}{\partial x}[hu^2+.5*g*(\in^2-2\in Z_b)]+\frac{\partial}{\partial y}[huv]=-g\in S_{ox}-gS_{fx} \tag{2.5}$$

$$\frac{\partial}{\partial t}[hv]+\frac{\partial}{\partial x}[huv]+\frac{\partial}{\partial y}[hv^2+.5*g*(\in^2-2\in Z_b)]=-g\in S_{oy}-gS_{fy} \tag{2.6}$$

where $\in$ is the water surface elevation(m), h is the flow depth (m), hu and hv are the unit discharges in x and y direction (m^2/sec), g is the acceleration due to gravity (m^2/sec), S_{ox} and S_{oy} are the bed slope in x and y direction, S_{fx} and S_{fy} are friction slope in x and y-direction and Z_b is the bed surface elevation.

2.2.2 Solution of the Governing equations

2.2.2.1 Finite difference method

The governing equations used in the unsteady flow modeling are hyperbolic and non-linear. Analytical methods are quite tedious to solve these sets of equations. Hence finite difference, finite volume, and finite element numerical techniques are widely used for the solution (Tsakiris and Bellos 2014).

Finite difference methods approximate the solution by replacing the partial derivatives with the differential quotients. It solves the spatial and temporal derivatives associated with the governing equations at the discretized grid points and predicts the primitive variables at the unknown time steps.

Initialy, Houghton and Kasahara (1968) employed the Lax Wendroff finite difference method to solve Saint Venant's equation and simulated the steady flow over a ridge. By varying the ridge height and the approach velocity, they obtained three different zones in the plot of approach velocity versus ridge height. Obtained results were conforming to experimental results.

Kalkwijk and De Vriend (1980) solved the 2D depth-averaged unsteady flow equations using the finite difference method to simulate low depth steady flow in a bent channel. Governing equations were transformed into the curvilinear coordinate system. The simulated results were compared with an experimental study done in the Delft Hydraulics Laboratory of the Delft University of Technology in the Netherland. A good agreement was found between the observed datasets and simulated results.

Three second-order accurate, explicit finite difference schemes named Mac Cormack Predictor Corrector, Lambda, and Gabutti were introduced by Fennema and Chaudhry

(1986) to analyze unsteady, free-surface flows in 1D having shocks or bores. They showed the need for artificial viscosity for the removal of the numerical oscillations near the Shock.

Fennema and Chaudhry (1989) introduced the Beam and Warming implicit finite difference scheme to solve the 2D unsteady free surface flow equations. The proposed scheme is non-iterative and second-order accurate in time. Using this implicit scheme, they simulated the bore formed due to partial breaching of the dam, and the results obtained were quite satisfactory.

Fennema and Chaudhry (1989) solved the 2D unsteady free surface flow equations using Mac Cormack Predictor Corrector and Gabutti schemes. Two typical problems were considered for the model application. A strong bore was formed by a partial breach of the dam in the first case, while in the second problem, there were gradual flood waves that move through a contracted channel. The results obtained were compared with the results of another scheme, and good conformity was observed.

Bellos et al. (1991) examined the 2D dam-break flood resulting from the instantaneous collapse of the dam. The governing equations were transformed into an equivalent square grid near the boundary to overcome the discrepancies in flow characteristics determination. They adopted the Mac Cormack Predictor Corrector scheme for the integration of the governing equations. The computed results complied well with the experimental datasets.

Bhallamudi and Chaudhry (1992) solved the 2D depth-averaged unsteady free surface flow equations in boundary fitted coordinates using the Mac Cormack Predictor Corrector scheme to analyze flows in channel expansions and contractions. However, Garcia-Navarro and Saviron (1992) modified the Mac Cormack Predictor Corrector scheme to solve 1D unsteady free surface flow equations. After the corrector step, they added the Total Variation Diminishing (TVD) scheme to capture the sharp discontinuities near the steep

gradients. They applied this methodology to various test cases, and good agreements were observed between the computed and laboratory results.

Molls and Chaudhry (1995) first used the trapezoidal formulation of Beam and Warming scheme to solve 2D unsteady free surface flow equations in boundary fitted coordinates and consider effective stress. The results were compared with various experimental results, and good agreements were observed.

Molls and Zhao (2000) numerically solved the governing flow equations Beam and Warming ADI scheme and Mac Cormack Predictor Corrector scheme and simulated the supercritical flow with a wavy sidewall. Manning's equation was used to solve the Bottom friction, and a constant eddy-viscosity turbulence model was used in the effective stresses calculation. Both the models were giving results having good agreements with experimental data. However, it was observed that in Beam and Warming Scheme, the Courant number could be set up to 2.5, and in the Predictor Corrector model, it is limited to 1 only.

Wang et al. (2006) solved the 1D Saint Venant's equations using a new technique named four points finite difference form of the Muskingum Method to simulate open channel flow. In this method, a non-linear convection-diffusion equation based on Saint Venant's equations is discretized by the mixing cell method. An iterative procedure was adopted for obtaining the flow discharge. The method was tested with published analytical problems and observed events, and the computed results were compared with the Lambda scheme and the method of characteristics. Good accuracy was obtained from the new scheme.

Liang et al. (2007) proposed a different form of shallow water equation, including wetting and drying. In this approach, the governing equation is discretized by the operator splitting

technique (Strang splitting). The bed slope term is replaced by water surface slope, and the friction slope term is discretized using a semi-implicit method.

Liang et al. (2006) presented a modified TVD McCormack scheme for simulating the viscous effect on shallow water dynamics. Results from conventional and deviatoric forms of the shallow water equations (SWE) were applied in wavy topography. Results indicated that the predicted outputs from deviatoric form SWEs gave more accuracy than the conventional form.

The kinematic and diffusive formations of Saint Venant's equations in 1D were solved by Alhan and Medina. (2007) using the Mac Cormack Predictor Corrector scheme. The results obtained from this scheme were compared with the results of a modeling tool named SWMM (Storm Water Management Model), and good agreement between them was observed.

Siviglia et al. (2008) proposed a new methodology for solving the 1D Saint Venants equations and the Exner equation for sediment transport. They took a quasi-conservative formation and solved the resulting governing equations using Mac Cormack Predictor Corrector scheme. The proposed methodology is applied in the dam break flow for inviscid shallow water equations and validated with the available analytical solution, experimental, and field observed data. The computed results are found in good agreement with the observed results.

Bellos and Hrissanthou (2011) solved the 1D Saint Venant's equations using two accurate second-order schemes, Lax Wendroff and Mac Cormack Predictor Corrector scheme, and simulate flood wave propagation due to break of a reinforced concrete dam. The model was validated with results from an experimental dam break study. The performance assessment of the model in undulating terrain is carried out by providing a triangular hump downstream

of the dam. Results indicated that the model could reproduce the actual water/bed surface elevation favorably.

Yu and Huang (2014) proposed 1D and 2D coupled hydrodynamic model for free surface flow simulation. A finite-difference technique is used in the 1D model, and for the 2D model, an implicit dual time-stepping method was adopted. They found that the coupled model can accurately and efficiently simulate free-surface flows over complex terrain.

Li and Fan (2017) analyzed the 2D SWE using a novel meshless scheme based on the generalized finite difference method (GFDM). The computed model outputs are validated with published experimental results and other numerical solutions. Results indicated sufficient accuracy and the consistency of the proposed meshless scheme.

Wang et al. (2019) designed a finite difference weighted non-oscillatory (WENO) scheme for the 1D shallow water equation in varying topography. The conservative property of the proposed model is verified with some classical problems such as dam break flow, transcritical flow, steady flow over the hump, etc.

Lundgren and Mattsson (2020) derived a stable high order explicit upwind finite difference scheme and solved the shallow water equations using the SBP-SAT method. The well-balanced property of the model is maintained by adopting a modified flux splitting method for the source term. The method was tested against some classical hydraulic problems, and high order convergence was achieved.

2.2.2.2 Shock capturing techniques used in hydrodynamic modeling

Depth-averaged numerical models approximate environmental flows with free surfaces as they offer a good compromise between computational outputs and measured results. These models efficiently compute the free surface elevations and velocities in the solution domain. However, with rapid flows having discontinuities, such as hydraulic jumps, flood

fronts, bores, and breaking waves, the numerical methods cannot maintain the smoothness in the solution and lead to model failure. These disturbances propagate with time and need to be smoothened by implementing various shock-capturing and shock fitting schemes. In the early phase, the method of characteristics and alternating direction implicit (ADI) scheme was used, but these methods fail when the direction of shocks is unknown before simulation. However, the ADI method works perfectly when the Froude number is less than unity.

Two approaches, mainly shock-fitting and shock-capturing, are used to smoothing the computational domain's numerical oscillations. Artificial viscosity is a widely used shock capturing method to suppress the nonphysical oscillations and smooth the solution near steep regions (Molls and Chaudhry 1995; Rahman and Chaudhry 1998). Fiedler and Ramirez (2000) developed a 2D overland flow model coupled with a spatially variable infiltration equation. The governing flow equations were solved using McCormack finite-difference scheme and the artificial viscosity technique to smoothing the numerical oscillations. Later, different researchers have used the artificial viscosity in the shallow water model to remove the numerical oscillations from the solution domain (Seo et al. 2014; Hernandez-Duenas and Beljadid 2016; Ginting 2017; Tanaka et al. 2019).

Despite the wide application of artificial viscosity in the numerical schemes, the difficulty arises in choosing the right amount of diffusion to be added to the solution. More attention has been given to the algorithms to avoid these complexities, which are free from adjustable parameters and trial-error processes. Garcia-Navarro and Saviron (1992) proposed the TVD (Total Variation diminishing) technique that captures the sharp discontinuities and overcomes the trial and error process without generating spurious oscillations.

Louaked and Hanich (1998) first applied the TVD scheme for the shallow water equations while using the Lax-Wendroff scheme, another accurate second-order method. It does not

require solving the eigenvalues and eigenvectors of the governing equations, which significantly improves the computational economy and efficiency.

Ming and Chu (2000) presented a finite volume TVD McCormack scheme for two-dimensional open channel flow computation with sudden variations such as bores and surges, hydraulic jump, etc. The robustness and stability of the model were checked with some benchmark problems and laboratory experiments.

Based on the finite-difference flux-limited TVD scheme, Tseng (2004) proposed a simple approach to handle the source term for the 1D flow simulation with rapidly varying bed topography. The accuracy, stability, and robustness of the proposed model were checked with the analytical and experimental results.

Liang et al.(2006) used this TVD technique in the McCormack predictor-corrector scheme for simulating unsteady shallow water flow. Using this technique, they replicated a large number of hydrodynamic problems and got excellent results.

Liang et al. (2010) solved the depth-averaged shallow water-advection equation using the TVD-McCormack scheme. The model has been tested for two idealized cases, for which analytical solutions exist, and finally in the Thames estuary, considering a fictitious release. The scheme preserves monotonicity and yields robust and sufficiently accurate results.

Ouyang et al. (2013) proposed a 2D mountainous mass flow dynamics solver in MATLAB. The governing equations are solved by using the TVD-McCormack predictor-corrector finite difference scheme. For validation, they have considered the 1D and 2D benchmark dam failure problems, landslide problems in Hong Kong in 1993, and the debris flows in the Italian Alps in 2000. The computed outputs were compared with the published experimental results and found satisfactory.

Kalita (2016) used the TVD technique in the conservative form of two-dimensional governing equations and applied it in diverse flow conditions. The model behavior was found to be robust, and the predicted outputs were in good agreement with the experimental results.

Welahettige et al. (2018) proposed a modified 1D shallow-water model for venturi contraction and expansion in an open channel. The TVD scheme and explicit Runge-Kutta fourth-order method are used to solve the governing equations. The simulated results from the modified expression are validated with the experimental results and found satisfactory.

2.2.3 Previous works on unsteady flow simulation with vegetation

2.2.3.1 Vegetation influence on the channel hydrodynamics

The importance of vegetation growth in waterways cannot be underestimated for its ecological benefits in improving water quality and reducing soil erosion. The vegetation in watercourses has numerous impacts on channel hydrodynamics by altering the magnitude and direction of flow, affecting the shape of velocity profile, turbulence structures, and sediment transport. Nepf (1999) and Stoesser et al. (2003) stated that vegetation could be used as a tool to maintain the shape of rivers and prevent coastal erosion and the breaking down of wave energy. Hence, the study of flow in vegetated channels is vital for understanding and managing earthen channels, rivers, flood plains, wetlands, and similar aquatic environments by applying open channel flow principles (McNaughton 2009). Flow resistance in open channels is primarily composed of bottom friction and velocity fluctuations (Baptist et al. 2007). These fluctuations are particularly evident in vegetated channels since the flow retards within the interior of the plant stems and accelerated around the vegetation (Manners et al. 2013). The resistance is offered at the stem/leaf scale, where the momentum is directly lost through the interaction with individual vegetation characteristics (Gholami and Khaleghi 2013). This momentum loss during wave

propagation inevitably affects the vertical velocity structure in the vegetated section. For instance, the velocity profile is generally uniform over the depth when the vegetation is emergent (Stone and Shen 2002), and for submerged vegetation, the velocity profile is approximately S-shaped (Carollo et al. 2002). In both situations, the flow velocity within the vegetation zone is significantly reduced compared to that in the surface zone.

According to Mitchell (1974), emergent vegetation offers considerable resistance to flow, and reduces soil erosion. However, Gwinn and Ree (1980) also indicated the negative impact of the aquatic vegetation on the design flow rate and the channel conveyance capacity. El-Samman (1999) reported that both the density and distribution of submerged aquatic weeds significantly impact the efficiency and equitability of water distribution. Increasing the density or distribution of vegetation in a channel reduces the flow and obstructs water from reaching the downstream and, consequently, the upstream will be subjected to flooding. David (2008) identified that vegetation increases bank stability, reduces soil erosion, provides habitat for aquatic fauna, increases flood attenuation, and traps pollutants. According to Buckman (2013), the vegetation substrate can trap particulate matter, heavy metals, and oils from runoff before entering natural water bodies.

2.2.3.2 Roughness models for rigid vegetation

The expressions proposed by Petryk and Bosmajian III (1975) and Arcement and Schneider (1989) for rigid emergent vegetation were used to compute total flow resistance coefficients in the open channel. These methods are helpful for flow across floodplains having large trees which are rigid and non-submerged. Based on their work, they have proposed Manning's value in vegetation sections (n_v) as follows

$$n_v = n\sqrt{1 + \left(\frac{C_d m * A_i}{2gAL}\right)\left(\frac{1}{n_0}\right)^2 R_h^{\frac{4}{3}}} \tag{2.7}$$

where n = Manning's roughness value in the non-vegetated portion, C_d= Effective drag coefficient, A_i= Frontal area of i^{th} plant blocking the flow(m^2),D_{si} =Stem diameter(m) ,R_h=hydraulic radius(m), L= Reach length

Green (2005) stated that Manning's n could be evaluated as the fraction of flow cross-sectional area occupied by plants commonly termed as flow blockage ratio.

$$B = \frac{\sum A_{vi}}{A} \tag{2.8}$$

$$n_v = \frac{n_0}{1 - B} \tag{2.9}$$

where, A_{vi}= Area occupied by the i^{th} region of vegetation within the cross-section, B=flow blockage ratio.

Baptist et al. (2007) presented an approach for rigid vegetation based on Chezy's coefficient(C)

$$C = \sqrt{\frac{1}{\frac{1}{C_b{}^2} + \frac{C_d\, mD_s\, h}{2g}}} \quad \text{for } H_v > h \text{ (emergent vegetation)} \tag{2.10}$$

$$C = \sqrt{\frac{1}{\frac{1}{C_b{}^2} + \frac{C_d\, mD_s\, h}{2g}}} + \frac{\sqrt{g}}{\kappa} \ln\left(\frac{h}{H_v}\right) \quad \text{for } H_v < h \text{ (submerged vegetation)} \tag{2.11}$$

where, D_{si} = Stem diameter(m) , h=flow depth(m), H_v=rigid vegetation height(m), g=acceleration due to gravity (m/sec^2), C= total Chezy's roughness , C_b=roughness contribution from bed, κ=Von-Karman constant and C_d is the drag coefficient.

Luhar and Nepf (2013) presented an approach better suited for a wider array of vegetation as follows-

$$n = \left(\frac{C_d m}{2g}\right)^{\frac{1}{2}} h^{\frac{1}{6}} \quad \text{for } Hv > \text{h} \tag{2.12}$$

$$n = \frac{h^{\frac{1}{6}}}{\left(\frac{2g}{C_d}\right)^{\frac{1}{2}}\left(1-\frac{Hv}{h}\right)+\left(\frac{2g}{C_d m}\right)^{\frac{1}{2}}\left(\frac{Hv}{h}\right)} \quad \text{for } Hv < \text{h} \tag{2.13}$$

The vegetation density (m) also can be estimated from the leaf area index (LAI), which is the sum of all plant surface area per unit bed area. For emergent vegetation, the part of the vegetation below the water surface contributed to hydraulic roughness.

$$m = 0.5LAI\ \left(\frac{h}{H_v}\right) \text{ For emergent vegetation} \tag{2.14}$$

$$m = 0.5LAI \quad \text{For submerged vegetation} \tag{2.15}$$

2.2.3.3 Previous works on unsteady flow simulation with rigid emergent vegetation

Vegetation influences the channel hydrodynamics, manage the ecological balance, and maintains the environmental characteristics of water bodies. The knowledge of mean and turbulent flow structure in a vegetated environment is important to understand sediment and contaminant transport processes. However, it is challenging to represent the different vegetation types and flow conditions through experimental and analytical studies. In these situations, using a mathematical model is an excellent way to predict the vegetation-induced flow parameters in the open channel.

To simulate the flow through rigid submerged vegetation elements, Naot et al. (1996) have used a higher-order anisotropic closure, Reynold's Stress model (RSM). They have used the drag force approach and additionally accounted for the effect of shading.

Wu et al. (2001) has developed a 2D depth-integrated hydrodynamic model to study the effect of mangrove forest, considering the impact of both drag force due to the forest area and

blockage effect on mass flux through the woods. The blockage effect due to the mangrove trees was studied by considering the porosity of the mangroves. They found that blockage from the tress and the drag force plays a critical role in the flow. The velocity gets reduced in the forest area, and it gets considerably increased in the main channel.

Fischer-Antze et al. (2001) included the drag force from the cylindrical rigid stems into the sink term of the shallow water model and solved it by using the SIMPLE method and the k-Ɛ turbulence model. The rigid emergent vegetation was arranged in both simple and compound channel sections. Computed outputs were compared with the flume-measured results of Tsujimoto (1999). A good agreement was obtained between the computed and observed velocity profiles.

Stoesser et al. (2003) presented a 3D numerical model to a large-scale river domain. They have incorporated the drag force in the momentum equations and simulated a 100-year event on a reach length (3500 m) of the lower River Rhine in South-West Germany. Mean floodplain velocities and water surface elevations are measured, and good agreement was found between measured and computed results.

Wilson et al. (2005) introduced a three-dimensional finite volume approach to study the hydraulic resistance of willows in the Wienfluss test reach in Vienna. The model solves Reynold's averaged Navier-Stokes equations coupled with vegetative drag force at each cell. The turbulence terms are computed from the standard k-€ model. The proposed model has been used with both the laboratory and field environment with idealized and simulated vegetation. They found that at some vegetated sections, the model accurately predicts the velocity profiles.

The mathematical model proposed by Defina and Bixio (2005) consist of two turbulence scheme derived from Boussinesq eddy viscosity model. The computed outputs were compared with experimental findings having simple cylinders, plastic, and natural plants, arranged in a

scattered pattern. Satisfactory performance is achieved between the model and the measured results.

By double averaging the Navier–Stokes equations, Nikora et al. (2007) derived the governing free surface flow equations through the general largescale bed roughness. They have used the vegetation density in the mass conservation equation, and the drag and inertia forces of vegetation are included in the momentum equations.

Huang et al. (2011) conducted an experimental and numerical investigation on solitary wave interaction with rigid emergent stems. For numerical simulations Boussinesq equation was used, and the experimental studies were conducted in a laboratory flume with different vegetation lengths and porosities.

A 2D shallow-water model developed by Wu and Marsooli (2012) simulates the long wave propagation in a water body with rigid vegetation focusing on long-wave and dam-break waves over vegetative beaches. The computed water levels, flow velocities are in good agreement with the observed results.

Gillihan (2013) evaluated the performance of the SRH2D hydrodynamic model with rigid vegetation to simulate four discharges in the San Joaquin River. They have spatially delineated the vegetation polygons by ArcGIS shapefile and assigned the vegetation parameters to the polygons. Initially, a fixed roughness value was assumed at the non-vegetated locations and found that both approaches under-predicted the water surface elevations and over-predicted the velocities.

Yang et al. (2017) proposed a depth-limited 2D model and simulated the flow-vegetation interaction in an open channel. The drag from the vegetation was incorporated in the momentum equation and discretized using an implicit splitting scheme. The performance of the model was tested against the flume data and found satisfactory.

Zhang et al. (2017) presented an explicit one-dimensional Boussinesq model to calculate solitary wave propagation in vegetated and non-vegetated waters. This model adopts a hybrid solution combining the finite difference (FD) and the finite-volume (FV) methods. The vegetative resistance is explicitly added to a source term in the momentum equation.

Junna and Zhonglong (2019)integrated the eleven vegetation roughness computation method within the HEC-RAS 1D model and evaluated the performance and applicability in natural terrain. The coupled 1D model was then applied to the San Joaquin River and assess the performance and applicability of these different vegetation roughness methods.

2.2.4 Previous work on the estimation of vertical velocity structure with submerged vegetation in open channel

Flexible canopies are ubiquitous and occupy a more extensive section of the flow area in a vegetated terrain than the rigid stems (Ammari et al. 2017). In recent years, flexible vegetation has gained a lot of research interest because of its potential impact on the flow and velocity structure (Huai et al. 2019; van Veelen et al. 2020). Unlike rigid vegetation, the stem of the flexible vegetation bends to various degrees depending upon the velocity of flow, height, and flexural rigidity (Wilson et al. 2005). The different degrees of bending also have a distinctive impact on the flow resistance (Luhar and Nepf 2011). For instance, with the increase in velocity, the flow resistance from the flexible stems reduces, leading to further reconfiguration of the plants and the vegetation drag (Wu 2008; Shields et al. 2017). Thus, the flow characteristics with flexible vegetation are more complex to deal with than the rigid vegetation.

The presence of flexible vegetation, especially under submerged conditions, modifies the velocity profile. Under a fully submerged situation, the velocity profile estimation becomes more complex (Nepf 2011). Two-layer or three-layer methods are adopted for velocity distribution above and below the vegetation layer (Keramaris et al. 2015). These methods

divided the total water depth into a vegetated and a free water region, and the velocity profile is distributed using different approximations (Afzalimehr et al. 2019).

Klopstra et al. (2002) proposed a two-layer analytical model to distribute the velocity profile in a vegetated open channel. The vegetation layer used the momentum equation and a logarithmic profile representing the free surface layer. The model also calculates the turbulent stresses in the vegetation region from the Boussinesq hypothesis.

Baptist (2003) carried out an experimental study and 1D numerical simulation to compute the vertical velocity profile in a mobile bed channel having submerged flexible vegetation. The computed results were in good agreement with the observed results.

Velasco et al. (2008) proposed a numerical model to compute the vertical velocity profile and stem deflection. The numerical model is developed by approximating and vertically integrating the steady Reynold's equation above and below the deflected plant height. A modified mixing length model was substituted in the turbulence closure equation for the hydrodynamic computations. The model was calibrated and validated with the fourteen experimental data.

Yang and Choi (2010) proposed two layer analytical models for depth-averaged open channel flow with submerged vegetation. The model assumes a uniform distribution in the vegetation layer and a logarithmic distribution in the upper layer. A good agreement was observed between the experimental, and the model computed outputs. The developed model is capable of predicting the conveyance of a vegetated channel correctly.

Huai et al. (2013) proposed a two-layer analytical model for rigid and flexible vegetation in open channel flow. The model outputs were compared with the flume measured results, field investigations, and numerical solutions. Results from the proposed model were found convenient for practical application.

Ling and Qin (2015) proposed a coupled wave vegetation model by considering the drag and inertia force as the driving force for the vegetation motion and the gravity, buoyant force, and stem rigidity as the restoring force. An excellent agreement between the computed and measured results was observed.

Under extreme flow events, Shan et al. (2017) developed a mathematical model for rating curve estimations in a meandering compound channel with submerged flexible vegetation. The mean velocities within the canopy are linked to the depth-averaged model and found a good agreement between the predicted and measured discharge.

Pu et al. (2019)employed a two-layer velocity distribution model in their study and investigated the influence of drag (C_d) and friction coefficient (C_f) on the flow. The results indicate that vegetation drag and friction accuracy increases within a certain range of C_d and C_f. It is also observed that C_d has a more dominating influence than C_f.

2.2.5 Previous works on Shanon's entropy theory for velocity distribution in open channel flow

Vertical velocity profiles in open channels propagate the mean and maximum speed from the bed to the free surface (Xia 1997). Acoustic Doppler techniques such as Acoustic Doppler current profiler (ADCP), ADV (Acoustic Doppler velocimeter), and current meter methods are often employed to estimate the vertical profiles in the field. However, difficulties in sampling during high floods considerably reduce their application in the discharge measurements (Chen and Chiu 2004). Analytical models distribute the velocity from the river bottom to the free surface by discretizing the water column into three layers. Commonly, near the river bed, a viscous sub-layer, the linear velocity distribution, above it in the mid of the vertical, the Prandtl-von Karman logarithmic law and near the water surface a power-law profile is used to express the vertical velocity profile in a cross-section. But from the study carried out by Song and Yang (1979), the implementation of the boundary conditions between the flow layers and

the requirement of several parameters for a single water column hold the use of analytical methods in natural streams. The parametric evaluation and layer-wise boundary conditions in rivers are complex and may produce erroneous results.

Chiu (1989) initially proposed the entropy theory, a probabilistic formulation used to estimate the vertical velocity profile from the channel bed to the free surface.

This formulation was later used by Chao-Lin (1991) and expressed the mean (u_m) and maximum velocity (u_{max}) through a dimensionless entropy parameter M. The M parameter is derived from the mean and maximum velocity information at a channel section. Chao-Lin and Abidin (1995) defined the maximum and average velocity relation in terms of the entropy number. From this correlation, the discharge in natural streams was estimated.

Chiu and Tung (2002) investigated the highest velocity location in a velocity profile known as the dip phenomenon from the entropy principle. They derive the relationship between the entropy parameter, the ratio between the average to maximum velocity, and the peak velocity location.

Moramarco et al. (2004) observed a linear relationship between the average and maximum velocity at some gauged stations in Italy's upper Tiber river basin and found it reasonably accurate. They derived the vertical velocity profiles and found the derived relationship suitable under high surge events.

Moramarco and Singh (2010) studied the dependence of Shanon's entropy parameter with the hydraulic and geometric characteristics in a river cross-section. They rejected the reliance of the entropy parameter with the flood dynamics and derived a new modern definition for manning's roughness from the entropy parameter. Singh (2013) states that the empirical models used for velocity distribution are inadequate to incorporate the velocity uncertainties.

Marini et al. (2017) proposed a new two-dimensional velocity distribution approach from Shanon's entropy. A probability function was defined in a 2D symmetric rectangular domain. They have found quite a closer agreement between the experimental and the computed data. The developed model requires the maximum and average velocity data, and no parameter calibration is needed during its application.

Greco (2015) derived a discharge estimation methodology in smooth and rough irrigation ditch from the 1D entropy model. The difference between the observed and computed discharge was significantly less, indicating the reliability of the proposed approach for field application.

Ammari et al. (2017)proposed the relationship between the entropy parameter and morphological and hydraulic characteristics of the basin. The morphological characteristic includes the drainage density and path, and the hydraulic characteristics include the roughness parameter, bed slope, etc. The model findings are very satisfactory as they have observed an error of not more than 5%.

Vertical profiles also indicate the occurrence of the dip phenomenon in water. Stearns (1883) and Murphy (1904) reported the velocity dip a long time ago. Numerous investigators have conducted experimental studies and found that the channel aspect ratio (width/flow depth) and the interaction between the flow and solid wall are prominent reasons over which maximum velocity location (velocity dip) in any vertical depends.

A novel strategy is used by Yang et al. (2004) in a smooth prismatic channel to evaluate the dip in the velocity profile. The behavior of shear stress distribution and the dependency of dip correction factor numerically investigated by Absi (2011) based on RANS equations. He comes up with a differential equation to estimate the velocity profile with dip. However, a more profound investigation is required in its semi-analytical solution.

Kundu (2017) derived an analytical model to predict the velocity dip position from the entropy theory. The advantage of the approach is that it can predict the dip position at any section of the flume with any b/h ratio. The model was validated with several experimental datasets obtained from the literature.

Mirauda and Russo (2019) mathematically evaluated the velocity dip in an entire cross-section. They have considered both wide and narrow channels in their analysis. The proposed model outputs are compared with experimental data and found satisfactory.

2.2.6 Previous works on the Ecohydraulic modeling

The river and its habitat evolve naturally and manifest the diversity of life forms to maintain the river ecology. Osborne (1989) defines river ecology as a niche where a target species can reside for a fixed period. The physical flow parameters, such as water depth, shear stress, and velocity, greatly influence the river system and its habitat. The diversity and sustainability of the aquatic habitat are impacted by the interaction between multiple physical, biological, and chemical factors, which took place at different temporal and spatial scales (Dauwalter and Fisher 2008). The potential factors that affect ecosystem dynamics are hydro-meteorological changes, hydrodynamic characteristics, and biological alterations. These factors can produce various geological and habitat nexuses necessary to sustain the aquatic species in fresh, saline, and marine waters (Hannah et al. 2007; Nikora 2010).

The habitat suitability index (HSI) is one such indicator to identify the habitat availability for the freshwater and estuarine fish species in an ecosystem (Vismara et al. 2001). An increase in anthropogenic activities and rapid urbanization impacts the riparian system, undermining aquatic habitat quality, leading to a gradual loss of natural resources and creating a major environmental problem (Li et al. 2009). These activities contribute to the decline and extinction of fish species sensitive to changes in the flow regimes, channel roughness, turbulence, and

water temperature (Burkhardt-Holm et al. 2005). The decrease in habitat quality raises concern for channel restorations and habitat improvement schemes around the globe. With the increase in food and power demands, developments in the hydropower sector, channel restoration works are expected to increase significantly. These developments, however, substantially affect the aquatic ecology and biodiversity. Knowledge to improve the fish habitat suitability before implementing any river infrastructure is required for habitat conservation (Khwairakpam et al. 2020). The minimum flow needed in an aquatic ecosystem to maintain its essential functions, habitat richness, and biodiversity expediently is known as environmental flow requirement (EFR) or instream flow requirement (IFR) (Kashaigili et al. 2005; Smakhtin et al. 2004). The environmental flow rate varies with the system's nature and surroundings(Arthington et al. 2010; Yin et al. 2018). The ecological assessment models can be broadly categorized into four main types: hydrological, hydraulic, habitat simulation, and holistic. Hydrological methods use the probabilistic approach to analyze the recorded flow series data. There are several hydrological methods available for estimating environmental flow assessments (EFA). The choices between hydrological models are based on the type of river, the streamflow data availability, and the system complexity (L. et al. 2004). Streamflow variations influence the suitability of the aquatic species at different life stages. For example, the rise of river water level is favorable for the growth of some particular species, helping them swim to their spawning areas and feeding on the downstream (Pfeiffer and Ionita 2017; Peres and Cancelliere 2016). However, in some cases, low water level provides a suitable habitat condition for the aquatic organism's growth and reproduction (Poff et al. 2003). Thus, a sound understanding of the eco-hydrological reliance between the in-stream biota and the hydraulic variables is necessary to evaluate the dependency of freshwater fish species on the physical flow parameters.

Bockelmann et al. (2004) developed an Ecohydraulic model for a small stream in West Wales, UK. They have applied the 2D depth-averaged flow and solute transport model at different meanders and related the hydraulic parameters with the ecological characteristics of the benthic organisms. Based on their findings, river restoration works have been proposed.

Yi and Panayiotis (2010)applied a 3D hydrodynamic model to simulate the flow characteristics under a dam release event in Smith River, Virginia. The impact of the hydropeaking event for juvenile brown trout was addressed from the simulation. The insights from their study can assist the hydropeaking operation for the instream flow management.

Vezza et al. (2014) proposed a new methodology for habitat modeling high gradient streams in Northwest Italy. They used the MesoHABSIM model for habitat simulation, and the methodology was well adapted for the mountainous terrain.

Papadaki et al. (2016) studied the potential climate change impact on the hydrological patterns and biota for the southwestern Balkan river. Under the climate change condition, the ecological flow in the region is estimated from the IHA method. The influence of the varying hydrological regime over the Salmo Farioides fish species available in the southwestern Balkan ecosystem is evaluated from a hydraulic-habitat model.

Niayifar et al. (2018) proposed an environmental indicator that considers the habitat generated by the wakes downstream of macro roughness elements (individual stones) that serves as a shelter zone for aquatic species. The proposed methodology is extended to four river streams and in a multi-objective optimization problem.

Spurgeon et al. (2019) quantified the habitat availability variations for five fish species along the Niobrara River, NE, USA. They have used a MesoHABSIM modeling approach with three flow rates. The habitat availability for fish habitat guilds was found within the range of 5% to 49%.

2.3 Summary and research gap

From the aforementioned literature study, the following concluding points can be drawn

1) Two different formulations of the shallow water equation are reported from the literature. The water depth appears as a temporal derivative in the mass conservation equation and at the source term in one formulation. However, in the second approach, water surface elevation replaces the flow depth in the respective positions.
2) The governing shallow water equations are non-linear hyperbolic, and getting the analytical solution is a difficult task. Finite difference, finite volume, and finite element methods are commonly used numerical techniques to solve these equations.
3) Out of different numerical techniques, the implementation of the finite difference method is a simple yet effective technique for the solution of the governing equations. Various investigators have used implicit and explicit finite difference schemes in shallow water modeling and have reported satisfactory and conservative outputs. The equations can be transformed into boundary fitted coordinates to apply in curvilinear geometry.
4) The nonphysical oscillations in the computational domain can be smoothened by using the artificial viscosity and the total variation diminishing (TVD) method in the numerical scheme. However, unlike the artificial viscosity technique, the TVD scheme is free from the adjustable parameters and automatically adds the required amount of dissipation near the steep gradients.
5) The hydrodynamics of the vegetated channel is different from the non-vegetated channel. Aquatic vegetation modify the flow sediment nexus, habitat availability, and turbulence structures. Depending upon the flexural rigidity and degree of submergence, vegetation is classified into rigid and flexible. The resistance offered from the vegetation increases the roughness and alters the velocity field.

6) Literature indicates that different investigators have provided the expressions for roughness factor calculation in a vegetated open channel with rigid emergent stems. The expressions are derived by relating the hydraulic properties with the vegetation characteristics such as vegetation density, stem diameter, vegetation height, etc.

7) Integrating vegetation in the shallow water model can predict the flow parameters under adverse hydrologic and topographical conditions. The researchers have given effort in developing the coupled flow-vegetation models for applying in natural terrain. However, a robust coupling strategy can be developed to integrate the different vegetation characteristics such as stem spacing, vegetation density, and diameter within the shallow water model for hydrodynamic simulation in natural channels.

8) The governing shallow water equations are depth-averaged equations due to which the vertical velocity profiles are difficult to achieve. Analytical and full 3D models are difficult to implement in a natural flow domain for their complexity in the parametric evaluation and high computational cost. The entropy theory is a probabilistic single layer formulation, and it distributes the velocity profile from the river bottom to the water surface. Different investigators have implemented Shanon's entropy theory for velocity profile estimation in the natural domains. The ability to capture the anomalies in the vertical profiles and the requirement of fewer parameters make it more suitable over other existing velocity distribution models.

9) A single framework can be developed for a natural flow domain by linking the Shanon's entropy theory with the shallow water model to get the velocity profile along any vertical.

10) The submerged flexible vegetation are ubiquitous in the open channel. In submerged conditions, the configuration of the flexible stems and the variation of the drag force under different discharges modifies the velocity profile and redistributes the flow

pattern. Various investigators have proposed the two-layer and three-layer vertical velocity distribution models for submerged flexible vegetation. However, none of the literature has mentioned the development of any quasi three-dimensional approach for getting the vertical velocity profile in vegetated flow with submerged flexible vegetation.

11) The literature indicates that the Ecohydraulic modeling provides a physical-based practical approach and management strategy to the stakeholders to restore and conserve the aquatic biota under different flow events. By integrating the habitat suitability curve to the hydrodynamic models, the minimum flow requirement for the aquatic species can be evaluated and conveyed to the riverine community.

12) From the literature reviews, it is found that there is a need to develop a robust 2D Ecohydraulic model for application in the natural flow domain. The model must be capable of simulating the flow hydrodynamics both in vegetated and non-vegetated conditions. Therefore, this research primarily focuses on integrating rigid and flexible vegetation with a 2D shallow-water model and computing the flow parameters such as flow depth, streamwise and transverse velocities in the computational domain. Moreover, by linking Shanon's entropy theory with the depth-averaged 2D model, an attempt is made to estimate the velocity profile in the vertical direction. Further, the applicability of the model in predicting the suitable parameters for the marine species is also evaluated.

CHAPTER-3

GOVERNING EQUATIONS AND NUMERICAL SCHEME

3.1 Introduction

The equations that govern the gradually varied unsteady flow are a set of non-linear hyperbolic partial differential equations. The shallow water equations provide an excellent approximation to the three-dimensional Navier-Stokes equations for nearly horizontal flow with a free surface. These continuity and momentum equations are widely used in the hydrodynamic simulations of rivers, lakes, estuaries, and flood plains. Depending on the type of problem, these equations can be expressed in one-dimensional, two-dimensional, and three-dimensional forms. However, in complex environments, the two-dimensional models generally provide a more accurate representation of the flow and velocity distribution, water surface elevation, velocity magnitude, and flow depth. The details of the two-dimensional shallow water equations, their assumptions, method of solution, and the boundary conditions are presented in this chapter.

3.2 Assumptions made in the governing equation

Some of the basic assumptions associated with the derivation of the two-dimensional governing equations are as follows

1) The pressure distribution is hydrostatic, and vertical acceleration is neglected.
2) Flow is assumed to be gradually varying along the channel
3) Fluid is incompressible, and wind shear force is neglected.
4) The channel bed is rigid, i.e., the effect of scouring and deposition is neglected.

3.3 Two dimensional (2D) representation

The two-dimensional depth-averaged non-linear shallow water equations in matrix form can be expressed as (Liang and Borthwick 2009)

$$\frac{\partial U}{\partial t}+\frac{\partial F}{\partial x}+\frac{\partial G}{\partial y}=S \tag{3.1}$$

Where,

$$U=\begin{Bmatrix}\in\\ hu\\ hv\end{Bmatrix}$$

$$F=\begin{Bmatrix}hu\\ hu^2+.5*g*(\in^2-2\in Z_b)\\ huv\end{Bmatrix}$$

$$G=\begin{Bmatrix}hv\\ huv\\ hv^2+.5*g*(\in^2-2\in Z_b)\end{Bmatrix}$$

$$S=\begin{Bmatrix}0\\ -g\in(\frac{\partial Z_b}{\partial x}-S_{fx})\\ -g\in(\frac{\partial Z_b}{\partial y}-S_{fy})\end{Bmatrix}$$

$$S_{fx}=\frac{n^2*v*sqrt(u^2+v^2)}{h^{\frac{1}{3}}}\quad ,S_{fy}=\frac{n^2*v*sqrt(u^2+v^2)}{h^{\frac{1}{3}}} \tag{3.2}$$

In the above expression, *hu* and *hv* is the unit discharge in the x and y-direction (m^2/sec), $\frac{dZ_b}{dx}$ and $\frac{dZ_b}{dy}$ bed slope in x and y direction $\in$ is the water surface elevation, g is the acceleration due to gravity, S_{fX} and S_{fy} are friction slope in x and y direction, n is the Manning's roughness value, h is the flow depth (m), u and v are the depth-averaged streamwise and transverse velocity, and Z_b bed level elevation.

Equation 3.1 in differential form can be expressed as

$$\frac{\partial}{\partial t}[\in] + \frac{\partial}{\partial x}[hu] + \frac{\partial}{\partial y}[hv] = 0 \quad (3.3)$$

$$\frac{\partial}{\partial t}[hu] + \frac{\partial}{\partial x}[hu^2 + .5 * g * (\in^2 - 2 \in Z_b)] + \frac{\partial}{\partial y}[huv] = -g \in (\frac{\partial Z_b}{\partial x}) - gS_{fx}) \quad (3.4)$$

$$\frac{\partial}{\partial t}[hv] + \frac{\partial}{\partial x}[huv] + \frac{\partial}{\partial y}[hv^2 + .5 * g * (\in^2 - 2 \in Z_b)] = -g \in (\frac{dZ_b}{\partial x}) - gS_{fy}) \quad (3.5)$$

In undulating terrains, especially in braided streams, the high degree of variations in bed level elevations and wet-dry fronts affect the model performance. Enhancing the model capability in simulating the complex topographical domains requires avoiding the bed gradient terms from the governing shallow water equations. In this work, the non-conservative formulation of the shallow water model is used where the water surface gradient rather than the bed slope appears in the source term. The main advantage of doing so is to avoid the possible anomaly associated with the inconsistent discretization of bed slope and convective terms.

Under the initial steady-state condition, balancing the flux gradient and the source term in the X-direction momentum equations (Equation-3.4 and 3.5)

$$\frac{\partial}{dx}(.5 * g * (\in^2 - 2 \in Z_b)) = -\mathrm{g} \in (\frac{\partial Z_b}{\partial x}) \quad (3.5.1)$$

Simplifying the above equation

$$\frac{g}{2}(\frac{d}{dx}(\in^2) - \frac{d}{dx}(2 \in Z_b)) = -\mathrm{g} \in (\frac{dZ_b}{dx})$$

$$2 \in \frac{d\in}{dx} - 2(\in\frac{dZ_b}{dx} + Z_b \frac{d\in}{dx}) = -2\in (\frac{dZ_b}{dx})$$

$$\in \frac{d\in}{dx} - Z_b \frac{d\in}{dx} = 0$$

$$\in \frac{d\in}{dX} = (\in - h)\frac{d\in}{dX}$$

$h\frac{d\in}{dX}$

Similarly, for y-direction momentum equation

$$\frac{d}{dy}(.5 * g * (\in^2 - 2 \in Z_b)) = -g\eta(\frac{dZ_b}{dy}) \quad (3.5.2)$$

$$\frac{g}{2}(\frac{d}{dy}(\in^2) - \frac{d}{dy}(2 \in Z_b)) = -g \in (\frac{dZ_b}{dy})$$

$$2 \in \frac{d\in}{\partial y} - 2(\in\frac{\partial Z_b}{\partial y} + Z_b \frac{\partial \in}{\partial y}) = -2\in (\frac{\partial Z_b}{\partial y})$$

$$\in \frac{\partial \in}{\partial Y} - Z_b \frac{\partial \in}{\partial Y} = 0$$

$$\in \frac{\partial \in}{\partial y} = (\in - h)\frac{\partial \in}{\partial y}$$

$$h\frac{\partial \in}{\partial y}$$

The above simplification removes the bed gradient terms from the momentum equation. Thus, the final modified form of equations become

$$\frac{\partial}{\partial t}[\in] + \frac{\partial}{\partial x}[hu] + \frac{\partial}{\partial y}[hv] = 0 \quad (3.6)$$

$$\frac{\partial}{\partial t}[hu] + \frac{\partial}{\partial x}[hu^2] + \frac{\partial}{\partial y}[huv] = -gh\frac{d \in}{\partial x} - gS_{fx} \quad (3.7)$$

$$\frac{\partial}{\partial t}[hv] + \frac{\partial}{\partial x}[huv] + \frac{\partial}{\partial y}[hv^2] = -gh\frac{\partial \in}{dy} - gS_{fy} \quad (3.8)$$

The vegetation effect on the flow dynamics is incorporated by adding the drag force in the source term of the momentum equation

$$\frac{\partial}{\partial t}[\eta] + \frac{\partial}{\partial \xi}[\boldsymbol{hu}] + \frac{\partial}{\partial \eta}[\boldsymbol{hv}] = 0 \quad (3.81)$$

$$\frac{\partial}{\partial t}[hu] + \frac{\partial}{\partial \xi}[\{huU\}] + \frac{\partial}{\partial \eta}[\{huV\}] = -gh\frac{d \in}{\partial x} - gS_{fx} - \frac{F_{Dx}}{\rho} \quad (3.82)$$

$$\frac{\partial}{\partial t}[hv] + \frac{\partial}{\partial \xi}[\{hUv\}] + \frac{\partial}{\partial \eta}[\{hVv\}] = -gh\frac{\partial \in}{dy} - gS_{fy} - \frac{F_{Dy}}{\rho} \quad (3.83)$$

The drag force from the vegetation in the x and y direction is expressed as

$$F_{Dx} = \frac{1}{2} * C_D * \rho * \mathrm{m} * A_v * u_v * \sqrt{u_v^2 + v_v^2} \quad (3.84)$$

$$F_{Dy} = \frac{1}{2} * C_D * \rho * \mathrm{m} * A_v * v_v * \sqrt{u_v^2 + v_v^2} \quad (3.85)$$

In the above expression A_v= Projected or frontal area of vegetation, C_D= Drag coefficient , m =vegetation density, u_v and v_v are the apparent velocities in x and y-direction. The expression for u_v and $v_v$proposed by (Stone and Shen 2002) as

$$u_v = \mathrm{u}\left(\frac{h_v}{h}\right)^{\frac{1}{2}} \quad ; v_v = \mathrm{v}\left(\frac{h_v}{h}\right)^{\frac{1}{2}} \quad (3.86)$$

In the above expression $h_v$is the height of the flexible vegetation height.

3.4 Transformation of equations in boundary fitted coordinate

In real field problems, the geometrical complexities are handled by using a body-fitted coordinate system. It effectively simplifies the numerical simulations in curvilinear domains.

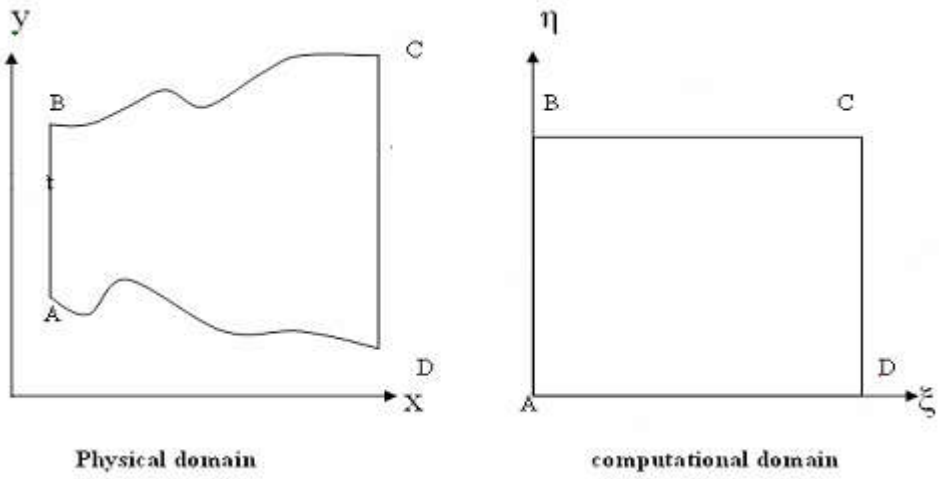

Figure 3. 1: Physical and computational domain

For instance, consider an irregular physical domain shown in figure 3.1 in Cartesian coordinates (x, y). Let (ξ, η) are the coordinates in the computational domain. The transformations procedure given by (John and Anderson 1995) is used in this work.

For two dimensional unsteady flow,(x, y, t) are the independent variables in physical space, and during the transformation, these are converted to another set of the independent variable (ξ, η, τ)

where,

$$\xi = \xi(x, y) \tag{3.9}$$

$$\eta = \eta\,(x, y) \tag{3.10}$$

$$\tau = (t) \tag{3.11}$$

The above equations in the exact differential form can be expressed as,

$$\partial\xi = \frac{\partial\xi}{\partial x}dx + \frac{\partial\xi}{\partial y}\partial y \tag{3.12}$$

$$\partial\eta = \frac{\partial\eta}{\partial x}\partial x + \frac{\partial\eta}{\partial y}\partial y \tag{3.13}$$

The equations (3.12) and (3.13) in matrix form are,

$$\begin{bmatrix}\partial\xi\\ \partial\eta\end{bmatrix} = \begin{bmatrix}\frac{\partial\xi}{\partial x} & \frac{\partial\xi}{\partial y}\\ \frac{\partial\eta}{\partial x} & \frac{\partial\eta}{\partial y}\end{bmatrix}\begin{bmatrix}\partial x\\ \partial y\end{bmatrix} \tag{3.14}$$

Now considering the inverse transformation,

$$x = x(\xi, \eta) \tag{3.15}$$

$$y = y(\xi, \eta) \tag{3.16}$$

The differential form of equations (3.14) and (3.15),

$$\partial x = \frac{\partial x}{\partial \xi}\partial \xi + \frac{\partial x}{\partial \eta} d\eta \tag{3.17}$$

$$\partial y = \frac{\partial y}{\partial \xi} d\xi + \frac{\partial y}{\partial \eta} d\eta \tag{3.18}$$

Again, the equations (3.16) and (3.17) can be written as,

$$\begin{bmatrix} \partial x \\ \partial y \end{bmatrix} = \begin{bmatrix} \frac{\partial x}{\partial \xi} & \frac{\partial x}{\partial \eta} \\ \frac{\partial y}{\partial \xi} & \frac{\partial y}{\partial \eta} \end{bmatrix} \begin{bmatrix} \partial \xi \\ \partial \eta \end{bmatrix} \tag{3.19}$$

From equations (3.14) and (3.19),

$$\begin{bmatrix} \frac{\partial \xi}{\partial x} & \frac{\partial \xi}{\partial y} \\ \frac{\partial \eta}{\partial x} & \frac{\partial \eta}{\partial y} \end{bmatrix} = \begin{bmatrix} \frac{\partial x}{\partial \xi} & \frac{\partial x}{\partial \eta} \\ \frac{\partial y}{\partial \xi} & \frac{\partial y}{\partial \eta} \end{bmatrix}^{-1}$$

$$\Rightarrow \begin{bmatrix} \frac{\partial \xi}{\partial x} & \frac{\partial \xi}{\partial y} \\ \frac{\partial \eta}{\partial x} & \frac{\partial \eta}{\partial y} \end{bmatrix} = \frac{\begin{bmatrix} \frac{\partial y}{\partial \eta} & -\frac{\partial x}{\partial \eta} \\ -\frac{\partial y}{\partial \xi} & \frac{\partial x}{\partial \xi} \end{bmatrix}}{\begin{vmatrix} \frac{\partial \xi}{\partial x} & \frac{\partial \xi}{\partial y} \\ \frac{\partial \eta}{\partial x} & \frac{\partial \eta}{\partial y} \end{vmatrix}}$$

$$\Rightarrow \begin{bmatrix} \frac{\partial \xi}{\partial x} & \frac{\partial \xi}{\partial y} \\ \frac{\partial \eta}{\partial x} & \frac{\partial \eta}{\partial y} \end{bmatrix} = \frac{\begin{bmatrix} \frac{\partial y}{\partial \eta} & -\frac{\partial x}{\partial \eta} \\ -\frac{\partial y}{\partial \xi} & \frac{\partial x}{\partial \xi} \end{bmatrix}}{\begin{vmatrix} \frac{\partial \xi}{\partial x} & \frac{\partial \xi}{\partial y} \\ \frac{\partial \eta}{\partial x} & \frac{\partial \eta}{\partial y} \end{vmatrix}}$$

$$=> \begin{bmatrix} \frac{\partial \xi}{\partial x} & \frac{\partial \xi}{\partial y} \\ \frac{\partial \eta}{\partial x} & \frac{\partial \eta}{\partial y} \end{bmatrix} = \frac{1}{J} \begin{bmatrix} \frac{\partial y}{\partial \eta} & -\frac{\partial x}{\partial \eta} \\ -\frac{\partial y}{\partial \xi} & \frac{\partial x}{\partial \xi} \end{bmatrix} \tag{3.20}$$

where,

$$\begin{vmatrix} \frac{\partial x}{\partial \xi} & \frac{\partial x}{\partial \eta} \\ \frac{\partial y}{\partial \xi} & \frac{\partial y}{\partial \eta} \end{vmatrix} = \begin{vmatrix} \frac{\partial x}{\partial \xi} & \frac{\partial y}{\partial \xi} \\ \frac{\partial x}{\partial \eta} & \frac{\partial y}{\partial \eta} \end{vmatrix} = J \tag{3.21}$$

From equation (3.19) following relations are derived,

$$\frac{\partial \xi}{\partial x} = \frac{1}{J} \frac{\partial y}{\partial \eta} \tag{3.22}$$

$$\frac{\partial \xi}{\partial y} = -\frac{1}{J} \frac{\partial x}{\partial \eta} \tag{3.23}$$

$$\frac{\partial \eta}{\partial x} = -\frac{1}{J} \frac{\partial y}{\partial \xi} \tag{3.24}$$

$$\frac{\partial \eta}{\partial y} = \frac{1}{J} \frac{\partial x}{\partial \xi} \tag{3.25}$$

In the equations (3.22) to (3.25), the Jacobian J and $\partial y/\partial \eta$, $\partial x/\partial \eta$, $\partial y/\partial \xi$, and $\partial x/\partial \xi$ ensure the grid transformation. These matrices are computed numerically from the known coordinates (x, y). Now, considering equation 3.1

$$\frac{\partial U}{\partial t}+\frac{\partial E}{\partial x}+\frac{\partial F}{\partial y}=S$$

$$\frac{\partial U}{\partial t}+\frac{\partial E}{\partial \xi}\frac{\partial \xi}{\partial x}+\frac{\partial E}{\partial \eta}\frac{\partial \eta}{\partial x}+\frac{\partial F}{\partial \xi}\frac{\partial \xi}{\partial y}+\frac{\partial F}{\partial \eta}\frac{\partial \eta}{\partial y}\ =\mathrm{S} \tag{3.26}$$

Multiplying by the Jacobean (J) on both sides of equation (3.26)

$$J\frac{\partial U}{\partial t}+J\frac{\partial E}{\partial \xi}\frac{\partial \xi}{\partial x}+J\frac{\partial E}{\partial \eta}\frac{\partial \eta}{\partial x}+J\frac{\partial F}{\partial \xi}\frac{\partial \xi}{\partial y}+J\frac{\partial F}{\partial \eta}\frac{\partial \eta}{\partial y}=JS \tag{3.27}$$

Again, using the chain rule, equation 3.27 can be written as,

$$J\frac{\partial E}{\partial \xi}\frac{\partial \xi}{\partial x}=\frac{\partial}{\partial \xi}\left[E\left(J\frac{\partial \xi}{\partial x}\right)\right]=\mathrm{J}\left(\frac{\partial \xi}{\partial x}\right)\frac{\partial E}{\partial \xi}+E\frac{\partial}{\partial \xi}\left(J\frac{\partial \xi}{\partial x}\right) \tag{3.28}$$

Rearranging the terms of equation(3.28)

$$J\left(\frac{\partial \xi}{\partial x}\right)\frac{\partial E}{\partial \xi}=\frac{\partial}{\partial \xi}\left[E\left(J\frac{\partial \xi}{\partial x}\right)\right]-E\frac{\partial}{\partial \xi}\left(J\frac{\partial \xi}{\partial x}\right) \tag{3.28a}$$

Similarly,

$$J\left(\frac{\partial \eta}{\partial x}\right)\frac{\partial E}{\partial \eta}=\frac{\partial}{\partial \eta}\left[E\left(J\frac{\partial \eta}{\partial x}\right)\right]-E\frac{\partial}{\partial \eta}\left(J\frac{\partial \eta}{\partial x}\right) \tag{3.29}$$

$$J\left(\frac{\partial \xi}{\partial y}\right)\frac{\partial F}{\partial \xi}=\frac{\partial}{\partial \xi}\left[F\left(J\frac{\partial \xi}{\partial y}\right)\right]-F\frac{\partial}{\partial \xi}\left(J\frac{\partial \xi}{\partial y}\right) \tag{3.30}$$

$$J\left(\frac{\partial \eta}{\partial y}\right)\frac{\partial F}{\partial \eta}=\frac{\partial}{\partial \eta}\left[F\left(J\frac{\partial \eta}{\partial y}\right)\right]-F\frac{\partial}{\partial \eta}\left(J\frac{\partial \eta}{\partial y}\right) \tag{3.31}$$

Now, the equation (3.27) can be rewritten using the equations (3.28) to (3.31)

$$J\frac{\partial U}{\partial t}+\frac{\partial}{\partial \xi}\left[E\left(J\frac{\partial \xi}{\partial x}\right)\right]-E\frac{\partial}{\partial \xi}\left(J\frac{\partial \xi}{\partial x}\right)+\frac{\partial}{\partial \eta}\left[E\left(J\frac{\partial \eta}{\partial x}\right)\right]-E\frac{\partial}{\partial \eta}\left(J\frac{\partial \eta}{\partial x}\right)$$
$$+\frac{\partial}{\partial \xi}\left[F\left(J\frac{\partial \xi}{\partial y}\right)\right]-F\frac{\partial}{\partial \xi}\left(J\frac{\partial \xi}{\partial y}\right)+\frac{\partial}{\partial \eta}\left[F\left(J\frac{\partial \eta}{\partial y}\right)\right]-F\frac{\partial}{\partial \eta}\left(J\frac{\partial \eta}{\partial y}\right) \quad (3.32)$$
$$=JS$$

Substituting equation 3.33-3.25 in equation 3.32 and simplifying, we get

$$J\frac{\partial U}{\partial t}+J\frac{\partial}{\partial \xi}\left[E\left(\frac{\partial \xi}{\partial x}\right)+F\left(\frac{\partial \xi}{\partial y}\right)\right]+J\frac{\partial}{\partial \eta}\left[E\left(\frac{\partial \eta}{\partial x}\right)+F\left(\frac{\partial \eta}{\partial y}\right)\right]=JS \quad (3.33)$$

$$\frac{\partial P}{\partial t}+\frac{\partial Q}{\partial \xi}+\frac{\partial R}{\partial \eta}=O \quad (3.34)$$

where,

$$P=JU$$

$$Q=J\left[E\left(\frac{\partial \xi}{\partial x}\right)+F\left(\frac{\partial \xi}{\partial y}\right)\right]$$

$$R=J\left[E\left(\frac{\partial \eta}{\partial x}\right)+F\left(\frac{\partial \eta}{\partial y}\right)\right]$$

$$O=JS$$

Now, the continuity equation can be expressed as,

$$\frac{\partial}{\partial t}[J\in]+\frac{\partial}{\partial \xi}\left[J\left\{\frac{\partial \xi}{\partial x}(hu)+\frac{\partial \xi}{\partial y}(hv)\right\}\right]+\frac{\partial}{\partial \eta}\left[J\left\{\frac{\partial \eta}{\partial x}(hu)+\frac{\partial \eta}{\partial y}(hv)\right\}\right]=0$$

$$\frac{\partial}{\partial t}[J \in] + \frac{\partial}{\partial \xi}\left[Jh\left\{\frac{\partial \xi}{\partial x}(u) + \frac{\partial \xi}{\partial y}(v)\right\}\right] + \frac{\partial}{\partial \eta}\left[Jh\left\{\frac{\partial \eta}{\partial x}(u) + \frac{\partial \eta}{\partial y}(v)\right\}\right] = 0$$

$$\frac{\partial}{\partial t}[J \in] + \frac{\partial}{\partial \xi}[JhU] + \frac{\partial}{\partial \eta}[JhV] = 0 \tag{3.35}$$

where,

$$U = \frac{\partial \xi}{\partial x}(u) + \frac{\partial \xi}{\partial y}(v)$$

$$V = \frac{\partial \eta}{\partial x}(u) + \frac{\partial \eta}{\partial y}(v)$$

U and V are the transformed velocity components in ξ and η directions, respectively.

Momentum equation in ξ direction can be written as,

$$\frac{\partial}{\partial t}[Jhu] + \frac{\partial}{\partial \xi}\left[J\left\{\frac{\partial \xi}{\partial x}(hu^2) + \frac{\partial \xi}{\partial y}(huv)\right\}\right] + \frac{\partial}{\partial \eta}\left[J\left\{\frac{\partial \eta}{\partial x}(hu^2) + \frac{\partial \eta}{\partial y}(huv)\right\}\right] = -Jgh\frac{d \in}{dx} - JghS_{fx}$$

$$\frac{\partial}{\partial t}[Jhu] + \frac{\partial}{\partial \xi}[J\{huU\}] + \frac{\partial}{\partial \eta}[J\{huV\}] = -Jgh\frac{d \in}{dx} - JghS_{fx} \tag{3.36}$$

Similarly, momentum equation in η direction can be expressed as

$$\frac{\partial}{\partial t}[Jhv] + \frac{\partial}{\partial \xi}[J\{hUv\}] + \frac{\partial}{\partial \eta}[J\{hVv\}] = -Jgh\frac{d \in}{dy} - JghS_{fy} \tag{3.37}$$

Equations (3.35) to (3.37) can together be written in matrix form as,

$$\frac{\partial P}{\partial t} + \frac{\partial Q}{\partial \xi} + \frac{\partial R}{\partial \eta} = O \tag{3.38}$$

where,

$$P = J\begin{bmatrix}\in\\ hu\\ hv\end{bmatrix}, Q = J\begin{bmatrix}hU\\ huU\\ hUv\end{bmatrix}, R = J\begin{bmatrix}hV\\ hVu\\ hVv\end{bmatrix}, O = Jgh\begin{bmatrix}0\\ -\frac{d\in}{dx} - S_{fx}\\ -\frac{d\in}{dy} - S_{fy}\end{bmatrix} \quad (3.38.1)$$

With the vegetation,

$$P = J\begin{bmatrix}\in\\ hu\\ hv\end{bmatrix}, Q = J\begin{bmatrix}hU\\ huU\\ hUv\end{bmatrix}, R = J\begin{bmatrix}hV\\ hVu\\ hVv\end{bmatrix}, O = Jgh\begin{bmatrix}0\\ -\frac{d\in}{dx} - S_{fx} - \frac{F_{Dx}}{\rho}\\ -\frac{d\in}{dy} - S_{fy} - \frac{F_{Dy}}{\rho}\end{bmatrix} \quad (3.38.2)$$

3.5 Numerical solution of the shallow water model

The governing equations of unsteady free surface flow are non-linear hyperbolic partial differential equations for which closed-form solutions are not available. These equations are generally targeted to solve by employing numerical methods viz finite difference, finite volume, and finite element method.

3.5.1 Finite difference method

The finite difference methods allow the conversion of partial derivatives to algebraic differential quotient based on Taylor series expansion. The solution of the algebraic approximations is carried out over the discretized domain. Thus, a finite-difference solution involves three steps:

a. Discretize the solution domain into the finite-difference grid points.

b. Approximate the derivative terms by finite difference equivalence at the grid points.

c. Prescribe the initial and boundary conditions to the model.

The finite-difference computations are broadly classified into explicit and implicit methods. The direct computation of the dependent variables made in terms of known quantities is said to be explicit. However, in implicit methods, the dependent variables are defined by a couple of equations and solved successively.

3.5.2 TVD McCormack predictor-corrector numerical scheme

3.5.2.1 McCormack predictor-corrector scheme

MacCormack predictor-corrector is an explicit finite difference scheme, second-order accurate both in space and time. The scheme mainly consists of two steps called the predictor step and the corrector step. In the predictor step, the algebraic equations are solved by the forward difference method. The solution is further corrected in the corrector step using the backward difference method. The implementation of this scheme is relatively simple comparatively other methods, and it efficiently handles the transcritical flow, hydraulic jump, and shock wave regions. Numerous investigators have used it for solving the unsteady flow equations in diverse situations and yield satisfactory results.

(i) Formulation and solution for 2D governing equations

A splitting algorithm is employed in the solution by dividing the two-dimensional equations into two one-dimensional equations and solved at each time step. Using the operator splitting techniques proposed by (Strang 1968) equation (3.35-3.37) can be expressed in matrix form as

$$\frac{\partial P}{\partial t} + \frac{\partial Q}{\partial \xi} = L \tag{3.42}$$

$$\frac{\partial P}{\partial t} + \frac{\partial R}{\partial \eta} = M \tag{3.43}$$

Where,

$$\text{L}= \begin{pmatrix} 0 \\ -Jgh\left(\frac{d\epsilon}{dx} - s_{fx}\right) \\ -Jgh\left(\frac{d\epsilon}{dy}\right) \end{pmatrix} \quad \text{M}= \begin{pmatrix} 0 \\ -Jgh\left(\frac{d\epsilon}{dx}\right) \\ -Jgh\left(\frac{d\epsilon}{dy} - s_{fy}\right) \end{pmatrix} \tag{3.44}$$

The equations are solved consecutively in four cycles. In the first sweep, the calculation starts with predicting the primitive variables in ξdirection equations from the known initial value. The predicted values are corrected in the corrector step. In the second sweep, the equations are solved in the η direction using the updated variables following the predictor and corrector step. The updated variables from the second sweep are used to calculate the new flow variables in η direction in the third sweep. Finally, in the fourth sweep, the updated variables from the previous cycle are used to compute the flow variables next time step. It is mandatory to mention that except for the incoming variables entire computational procedure is the same from sweep-1 to sweep-4. For instance, in ξdirection, sweep 1 uses the initial values, and in sweep -4, updated variables from the previous steps are used in the computation. The detailed procedure of the numerical scheme used in the first sweep in ξdirection is presented below.

Predictor-

$$P_i^{\,p} = P_i^{\,k} - \frac{\Delta t}{\Delta \xi}(Q_i - Q_{i-1})^k + \Delta t * L_i^{\,k} \tag{3.45}$$

Corrector-

$$P_i^{\,c} = P_{i,j}^{\,k} - \frac{\Delta t}{\Delta \xi}(Q_{i+1} - Q_{i,j})^p + \Delta t * L_i^{\,p} \tag{3.46}$$

$$P_{i,j}^{\,k+1} = \frac{1}{2}(P_{i,j}^{\,p} + P_{i,j}^{\,c}) + TVD_i \tag{3.47}$$

A similar process is adopted in theη direction for the next sweep by changing the subscript to j. In equations (3.46) and (3.47), Δt is the time interval between the computational steps, $\Delta\xi$ and $\Delta\eta$ are the spacing between the successive points in the computational domain.

3.5.2.2 Total variation diminishing (TVD) scheme

The second-order accurate characteristics of the McCormack predictor-corrector scheme often lead to dispersion errors in the solution domain. These errors are more prominent near the steep gradient regions, resulting in spurious oscillations that end up with model failure. There are several numerical techniques available to handle these oscillations. The total variation diminishing (TVD) scheme is one such shock-capturing technique to capture the sharp discontinuity in the numerical models. The beauty of this approach is that it can automatically take the required amount of dissipation in the computational domain. This method consists of the addition of an extra step after the corrector step. The TVD scheme can be expressed as

$$TVD_i=[B(r_i^{+})+G(r_{i+1}^{+})].\Delta\omega_{i+1/2}[B(r_{i-1}^{+})+B(r_i^{-})].\Delta\omega_{i-1/2+} \tag{3.48}$$

In the above expression, TVD variables for i^{th} direction,

$$\Delta\omega_{i+1/2} = \omega_{i+1}-\omega_i \tag{3.49}$$

$$\Delta\omega_{i-1/2} = \omega_i - \omega_{i-1} \tag{3.50}$$

$$r_i^{+}=\frac{\Delta\epsilon_{i-1/2}.\Delta\epsilon_{i+1/2+\Delta(hu)_{i-1/2}}.\Delta(hu)_{i+1/2+\Delta(hv)_{i-1/2}}.\Delta(hv)_{i+1/2}}{\Delta\epsilon_{i+1/2}.\Delta\epsilon_{i+1/2+\Delta(hu)_{i+1/2}}.\Delta(hu)_{i+1/2+\Delta(hv)_{i+1/2}}.\Delta(hv)_{i+1/2}} \tag{3.51}$$

$$r_i^{-}=\frac{\Delta\epsilon_{i-1/2}.\Delta\epsilon_{i+1/2+\Delta(hu)_{i-1/2}}.\Delta(hu)_{i+1/2+\Delta(hv)_{i-1/2}}.\Delta(hv)_{i+1/2}}{\Delta\epsilon_{i-1/2}.\Delta\epsilon_{i-1/2+\Delta(hu)_{i-1/2}}.\Delta(hu)_{i-1/2+\Delta(hv)_{i-1/2}}.\Delta(hv)_{i-1/2}} \tag{3.52}$$

Similarly, for j^{th} direction,

$$TVD_j= [B(r_j^{+})+B(r_{j+1}^{+})].\Delta P_{j+1/2} - [B(r_{j-1}^{+})+ B(r_j^{-})].\Delta P_{j-1/2} \tag{3.53}$$

$$\Delta\omega_{j+1/2} = \omega_{j+1}\text{-}\omega_j \tag{3.54}$$

$$\Delta\omega_{j-1/2} = \omega_j\text{-}\omega_{j-1} \tag{3.55}$$

$$r_j{}^{+} = \frac{\Delta\epsilon_{j-1/2}.\Delta\epsilon_{j+1/2+\Delta(hu)_{j-1/2}}.\Delta(hu)_{j+1/2+\Delta(hv)_{j-1/2}}.\Delta(hv)_{j+1/2}}{\Delta\epsilon_{j+1/2}.\Delta\epsilon_{j+1/2+\Delta(hu)_{j+1/2}}.\Delta(hu)_{j+1/2+\Delta(hv)_{j+1/2}}.\Delta(hv)_{j+1/2}} \tag{3.56}$$

$$r_j{}^{-} = \frac{\Delta\epsilon_{j-1/2}.\Delta\epsilon_{j+1/2+\Delta(hu)_{j-1/2}}.\Delta(hu)_{j+1/2+\Delta(hv)_{j-1/2}}.\Delta(hv)_{j+1/2}}{\Delta\epsilon_{j-1/2}.\Delta\epsilon_{j-1/2+\Delta(hu)_{j-1/2}}.\Delta(hu)_{j-1/2+\Delta(hv)_{j-1/2}}.\Delta(hv)_{j-1/2}} \tag{3.57}$$

The function B () in equation (3.49) and equation (3.54) is defined as,

B(x) =0.5*C*[1-ϕ(x)] and super bee flux limiter function is

Φ(x) =max (0, min (2x, 1))

Where C = f (C_r), C_r is the courant number

3.5.3 Stability of the model

The stability of the time marching numerical models is ensured from the Courant-Friedrichs-Lewy (CFL) condition. The value of Δt must be specified in such a way that it satisfies the CFL criteria. The CFL condition can be expressed as (Kalita 2016)

$$C_r = \frac{[\max[(u + \sqrt{g*h}),(v + \sqrt{g*h})]]*\Delta t}{\min(\Delta x,\Delta y)} \tag{3.58}$$

where Δx = grid spacings in the x-direction, Δy=grid spacing in the y-direction, Δt=computational time step, and C_r is the Courant number. For the explicit schemes, this value is limited to 1 only.

3.5.4 Boundary condition

The initial and boundary conditions are essential for the smooth functioning of the numerical model. The boundary conditions are used at upstream and downstream of the model. At the upstream, an open boundary is used through which flow enters the domain. The flow rate is assigned at the upstream boundary. Depending upon the data availability, two boundary conditions are provided downstream. If the water stage data is available from the gauged station, a constant water level value is assigned; otherwise, a second-order extrapolation technique is used at the downstream boundary.

For second order extrapolation, value of any variable (f) at 'n' node will be,

$$f(n) = 2\,f(n-1) - f(n-2) \tag{3.59}$$

Near the solid banks, free slip and no-slip boundary conditions are available to assign. In free slip conditions, the water surface ($\in$) and streamwise velocities (u) are extrapolated from interior points. No cross-flow through the boundaries is ensured by keeping the transverse velocities (v) to zero. However, in the no-slip condition, both the velocities (u,v) is made zero value. The non-submerged groins in the flow domain are simulated with the reflection boundary condition. The reflective boundary condition is applied when flow attacks a rigid wall and bounces back. The direction of the normal velocity component is altered to have zero resultant velocity at the solid wall.

3.6 Conclusion

Following concluding remarks can be drawn from this chapter

1) The non-conservative forms of two-dimensional shallow water equations have been presented here. Depending upon the domain complexity and flow behavior, two different forms of shallow water models are discussed. A modified form is derived by

balancing the flux gradients and the source term in x and y directions. The present formulation uses the water surface gradient rather than the bed slope in the source term. The main advantage of doing so is to avoid the possible anomaly associated with the inconsistent discretization of bed slope and convective terms.

2) The governing equations are expressed in a boundary-fitted coordinate system to handle the non-prismatic channel geometry. The physical domain is converted into a computational domain at which hydrodynamic computations are carried out.

3) The second-order accurate, explicit TVD Mc-Cormack predictor-corrector scheme is employed in the solution of the governing equations. The total variation diminishing (TVD) technique is used to maintain the smoothness in the solutions near the steep gradients.

4) The upstream and downstream boundary conditions used in the model are discussed. The free slip and no-slip boundary conditions are assigned to the banks. The non-submerged groins are simulated with the reflecting boundary condition. Flow rates are specified at the upstream boundary, and at the downstream boundary, the water stage value or the extrapolation method is assigned.

CHAPTER-4

APPLICATION OF THE SHALLOW WATER MODEL

4.1 Introduction

A well-balanced shallow water model is characterized by the robustness, stability, and capability to preserve quiescent water over an irregular bed. Before the field application, the model performance is investigated by applying it to some classical hydraulic problems. A total of six experimental and analytical test cases have been considered in the simulation. The computed outputs are compared with the published experimental results. Later, the developed model is applied in two different reaches of the Brahmaputra River, Assam, India, and the highly steep terrain of the Tiding River in Arunachal Pradesh, India. The model findings are calibrated and validated with the field measured data.

4.2 Application of the model in experimental test cases

4.2.1 Positive and negative wave propagation due to an instantaneous dam break

In the first case, the model is used to represent a classical dam-break flow. The instantaneous dam break results (at t=0) a positive wave movement downstream and a negative wave movement in the reservoir. This simulation is performed to check the shock-capturing capability of the numerical model at the time of the collapse. The channel is rectangular, frictionless, and horizontal, having a length of 1000m and a width is 50m. The computational domain is discretized into 100x5 grid points with grid spacing of Δx=10m and Δy=10m. The dam is located at the center of the channel. The upstream and downstream water levels are maintained at 10m and 2m, respectively. The banks are simulated as the no-slip boundary. The time step (Δt) for the computation is 0.5 seconds, giving a courant number of 0.67. The computed outputs are compared with the analytical solutions provided by (Isaacson et al. 1958).

Figures 4.1 and 4.2 show the comparison of the computed water depth and flow velocity along the centreline after 30 s of the dam break. Results indicate a satisfactory agreement between the analytical and the computed flow depth and the velocity profile.

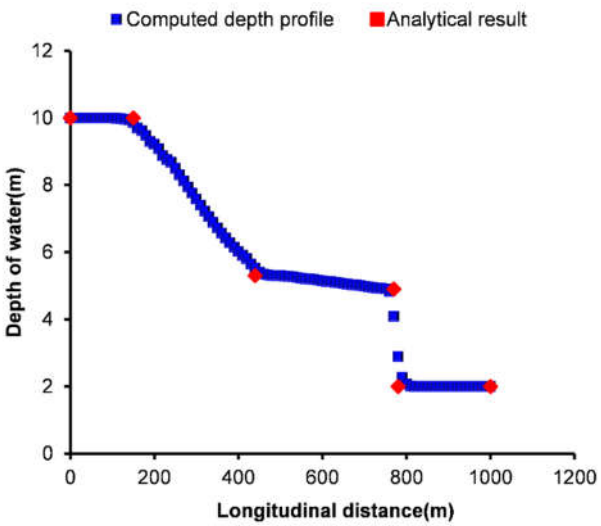

Figure-4.1 Computed and analytical water depth from dam break

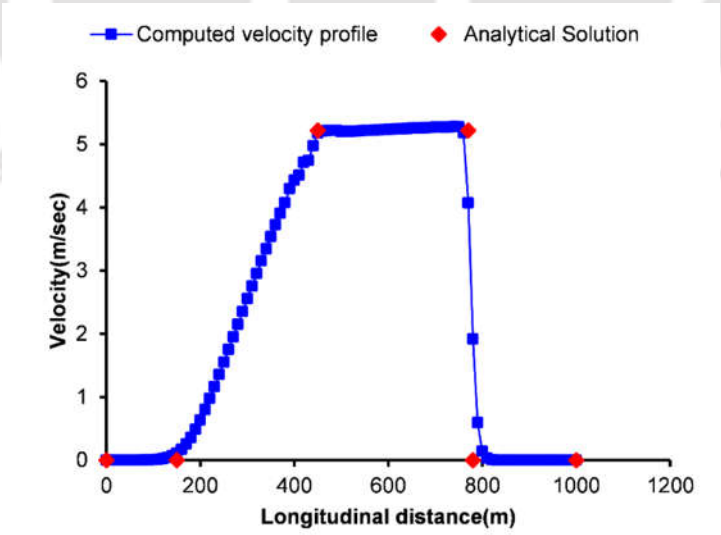

Figure 4.2: Computed and analytical velocity from dam break

4.2.2 Model behavior in a highly irregular bed profile

This simulation is performed to evaluate the model's capability to maintain a quiescent water level above an undulating bed profile. This property is commonly termed a well-balanced state of the model. It is coined by (Goutal 1997) to check the model performance in complex terrain. The channel length and width are 1500m and 25m. The expression for the bed profile is taken from (Zhou et al. 2001). The entire domain is discretized into 300x5 grid points with grid spacing in the x and the y-direction as $\Delta x=\Delta y=5$m. Manning's n value is considered as 0.1. The time step is specified as Δt =0.35 sec, leading to a maximum Cr value of 0.78. Initially, the velocity components (u, v) are assigned zero values, and a stage ($\in$) of 15m is considered over the computational domain. The $\in$ value is kept as 15 m at the upstream and downstream boundary, and the solid walls are assigned with a free slip condition. However, with these boundary conditions, the model provides a horizontal water surface throughout the domain, as shown in figure 4.3, and established the well-balanced state of the model in undulating topography.

4.2.3 Steady flow over an undulating terrain

In this case, a constant discharge is applied over the irregular bed elevation. The length and width of the channel are 1500m and 25m. The grid spacing is maintained similar to the previous case ($\Delta x=\Delta y=5$m). Manning's n value is taken as 0.1. The time step value is taken as 0.3 seconds which gives a Courant number of 0.73. A unit discharge of 0.75m^2/sec is assigned at the upstream boundary, and a water level of 15m is provided at the downstream boundary.

The simulated outputs show that the model maintains its well-balanced behavior with this flow and boundary condition. No discrepancy is noticed in the computed outputs. Figure 4.4 and figure 4.5 show the computed water surface elevation and unit discharge along the centreline of the channel. Results indicate a satisfactory model performance supporting the physical state of flow.

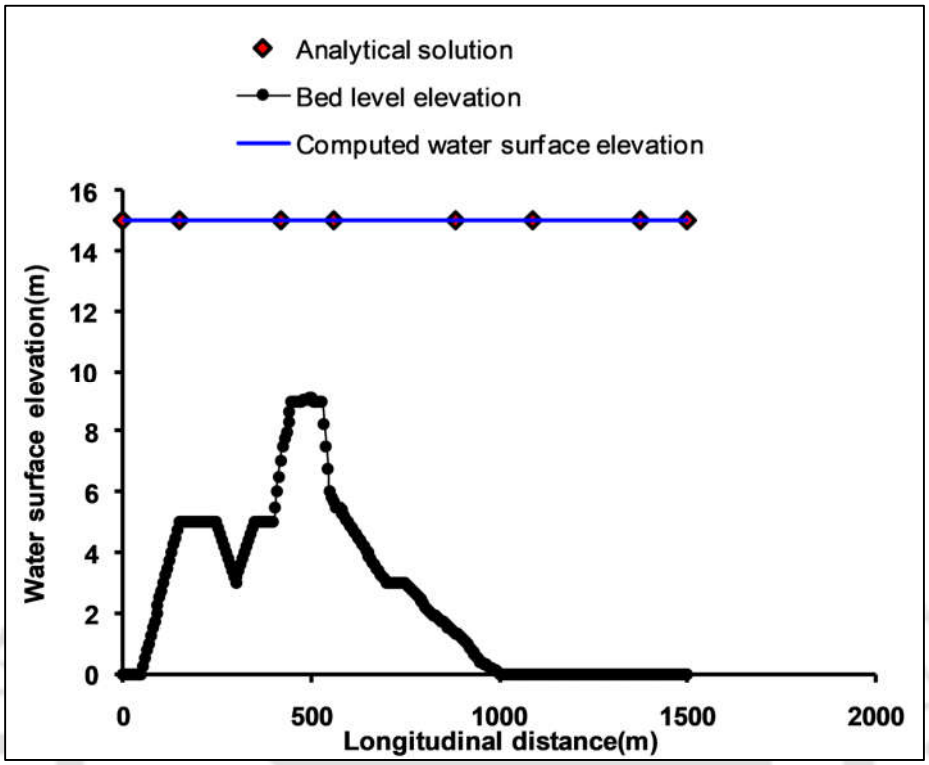

Figure 4.3: Preservation of still water surface over undulating terrain

4.2.4 Transcritical flow simulation over a hump without a shock

The occurrence of mixed-flow or transcritical flow is a common phenomenon in any physical domain. When the flow changes from subcritical to supercritical, an abrupt change or shock occur in the flow structure at the transition zone.

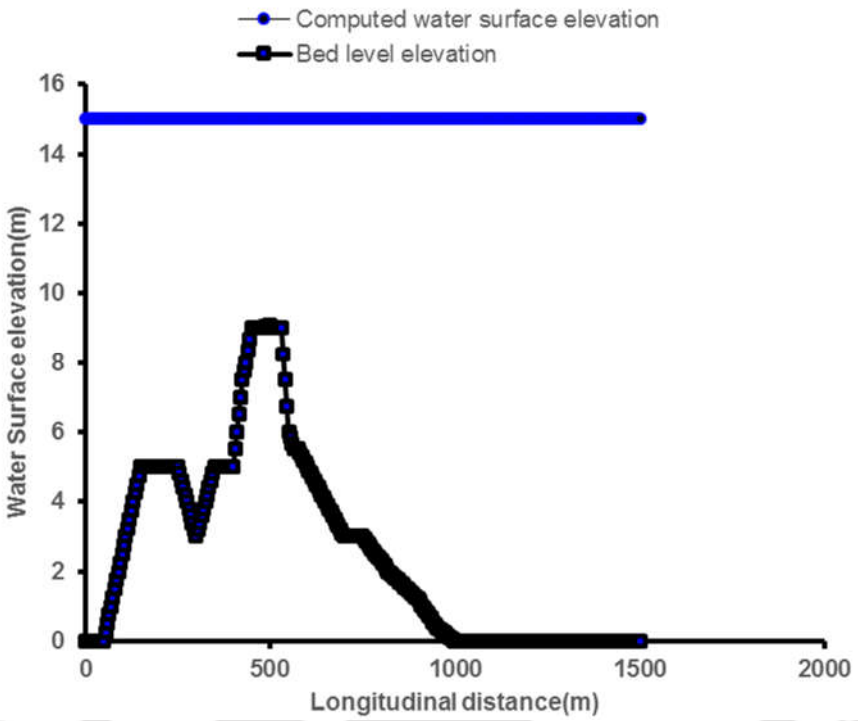

Figure 4.4: Still water surface over the irregular bed

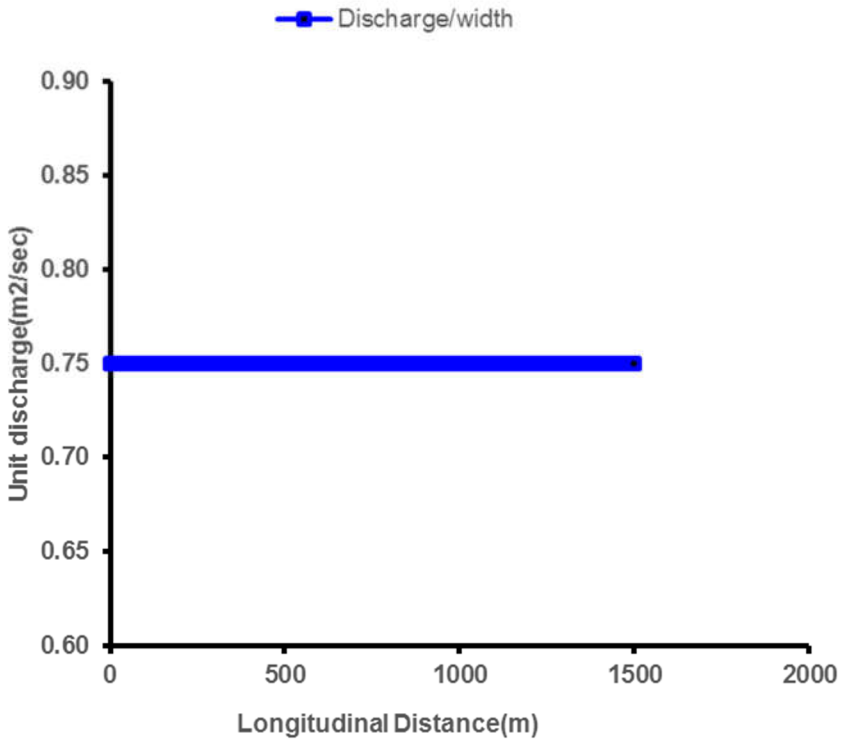

Figure 4.5: Computed unit discharge over the irregular bed

In this case, the model capability in simulating the mixed flow over a wavy terrain is investigated. The equation of the hump in the bed profile is (Zhou et al. 2001)

$$\text{Equation of the bed profile, } Z_b = 0.2 - .05(x-10)^2 \quad \text{if} \quad 8<x<12 \qquad (4.1)$$

$$0, \text{ Otherwise}$$

The channel is 25m long and 1m wide. The grid spacings in the x and y direction are Δx=.25m and Δy=0.2m. Manning's roughness value is set to 0.1. The solid side walls are simulated as free slip boundary conditions. A unit discharge of q=1.53 m^2/sec is assigned at the upstream, and the downstream water level is maintained at 0.66m. The computational time step is taken as 0.3 seconds, which gives a Courant number of 0.85. The computed water surface elevation at the 300-time step and 1000 time step are presented in Figures 4.6 and 4.7.

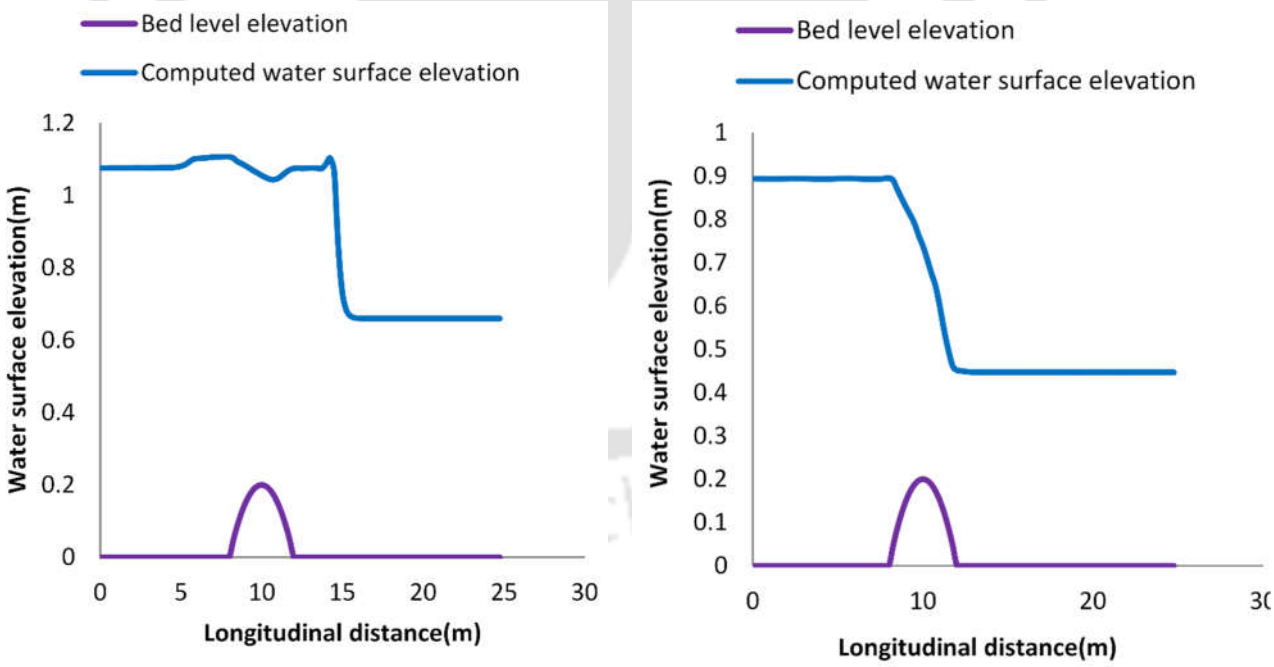

Figure 4. (6,7): Computed water surface elevation at 300 time step and 1000 time step

The computed water surface elevation after reaching the steady-state and the exact solution is presented in figure 4.8. Results are found quite satisfactory. However, near the hump, a small discrepancy is observed in the unit discharge computation(figure 4.9).

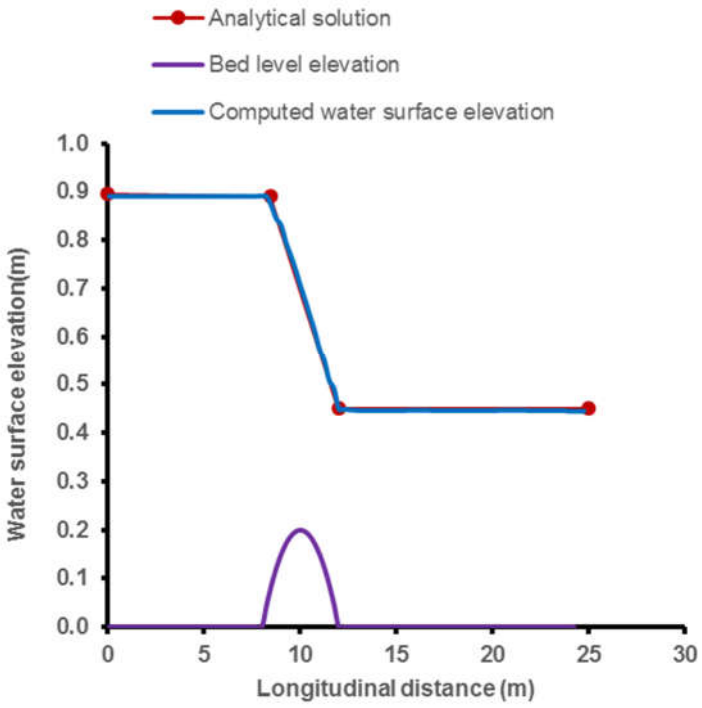

Figure 4.8: Computed water surface elevation and analytical result after reaching steady state

4.2.5 Formation of a hydraulic jump over a hump

The hydraulic jump in an open channel commonly occurs due to the flow change from a subcritical to a supercritical state. This sudden change near the transition region is highly unstable and discontinuous. The numerical models must be robust enough to capture these discontinuities and maintain the smoothness in the solution.

The flow domain is discretized into grid points with $\Delta x=0.25$m and $\Delta y=0.2$m. The equation of hump in the bed profile is similar to the previous case. At the upstream boundary, the unit discharge is $0.18 m^2/sec$ is assigned, and the downstream water level is maintained at 0.33m. The solid walls are simulated with free slip boundary conditions. The computational time step

is taken as 0.3 sec, which gives a Courant number of 0.85. Manning's n value is considered as 0.1 throughout the computation.

At the time of the jump formation, the water surface elevations along the channel centreline are presented in figures 4.10 and 4.11. Computed results show the model's efficiency in smoothing the shocks near the sharp gradient regions. The comparison of the computed steady-state water level with the analytical solution is shown in figure 4.12 and found satisfactory. Near the mid-channel, a percentage error of 11% to 17% is noticed in the computed and observed unit discharge (figure-4.13). However, prior investigators have also confirmed the error range between 10, 15, 23, and 15 %. (Zhou et al. 2001; Liang and Borthwick 2009; Kalita 2016)) in discharge estimation.

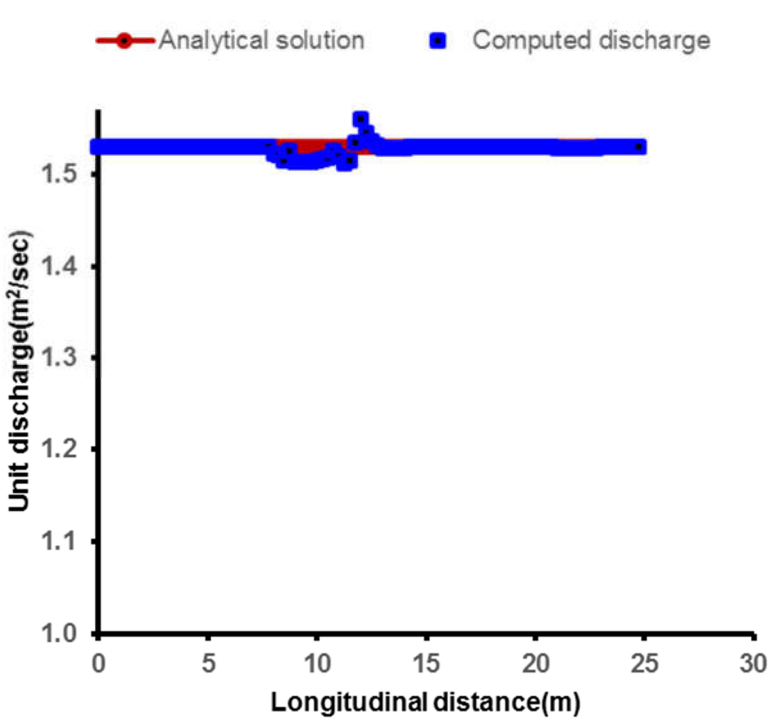

Figure 4.9: Computed unit discharge and analytical result

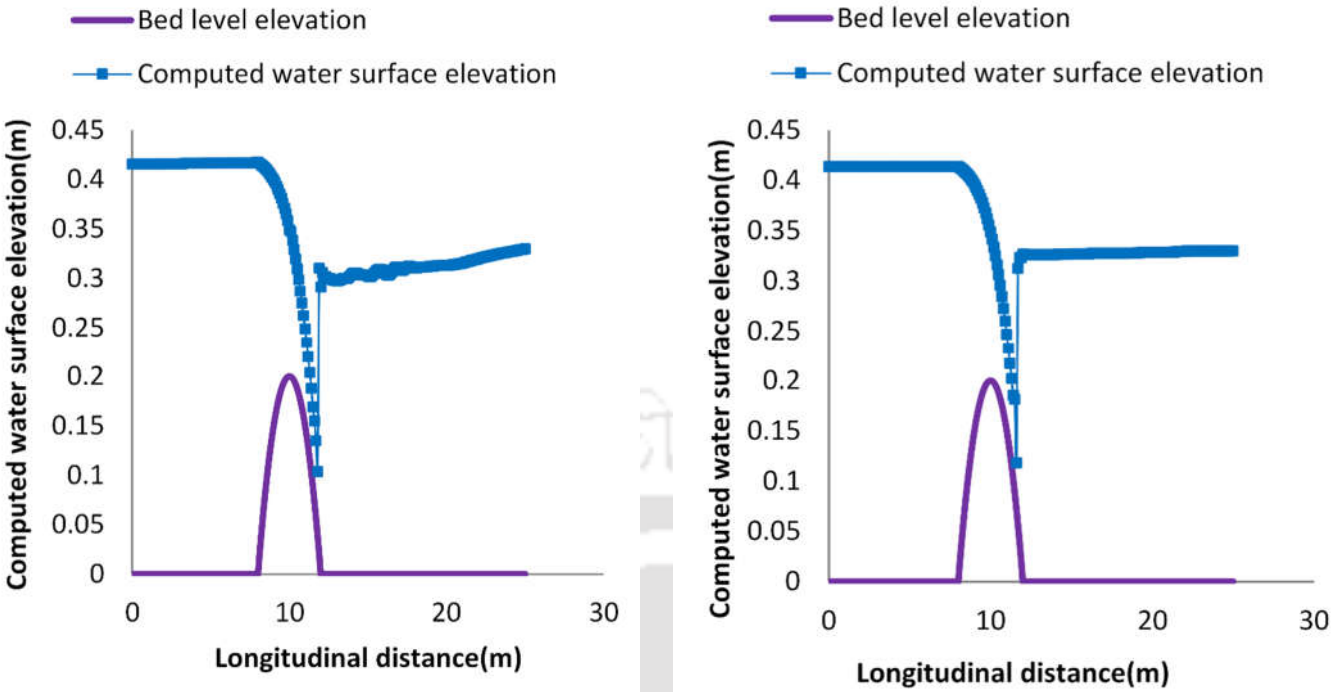

Figure 4. (10,11):Computed water surface elevations at the time of jump formation

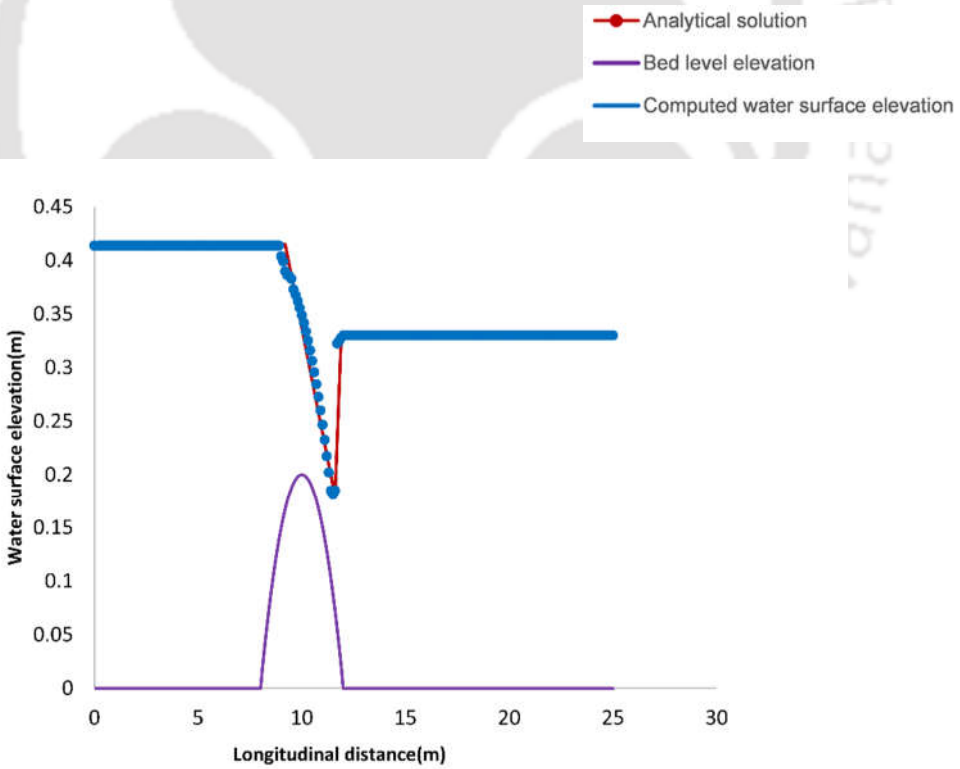

Figure 4.12: Computed water level and analytical result

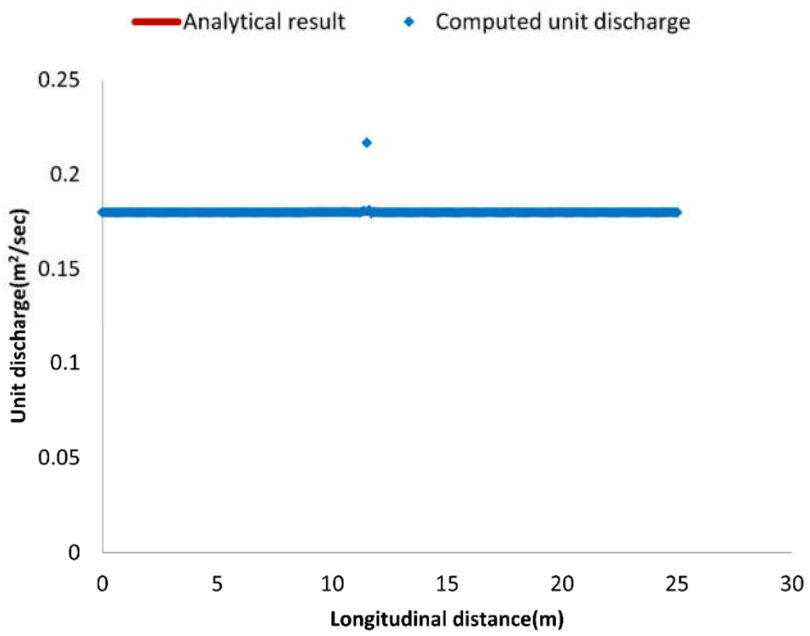

Figure 4.13: Computed unit discharge and analytical result

4.2.6 Flood wave propagation downstream of a reservoir due to a dam collapse

The propagation of flood waves over the flood plain due to the collapse of a dam causes heavy loss of life and property. This simulation is performed to investigate the model's capability to capture the two-dimensional wave propagations due to a dam breach. A dam with a barrier in a frictionless channel is considered in the simulation. The channel length is 500m, and the width is 300m. The dam is located at a distance of 250m from the upstream, having a breach width of 70m. A rectangular barrier of size 40mx50m is provided at a distance of 375 m from upstream, 110m from the left boundary, and 140m from the right boundary.

The flow domain is discretized into 100x60 grid points with a grid spacing of $\Delta x=\Delta y=5$m. The computational time step for each simulation is 0.1 s. The upstream and downstream water level is 10m and 2m. A no-slip boundary condition is specified at the right bank and the left bank. Variables at the inlet and outlet are extrapolated from the interior points. The water waves fan out through the breached portion and propagate downstream. The wave propagation after 50 seconds and 100 seconds of the breach is presented in figure-4.14 and figure-4.15. The

computed velocity vectors in the flow area are shown in figure 4.16. The maximum velocity is observed near the breached location. The computation shows that the model maintains its stability and robustness under the critical dam-break event.

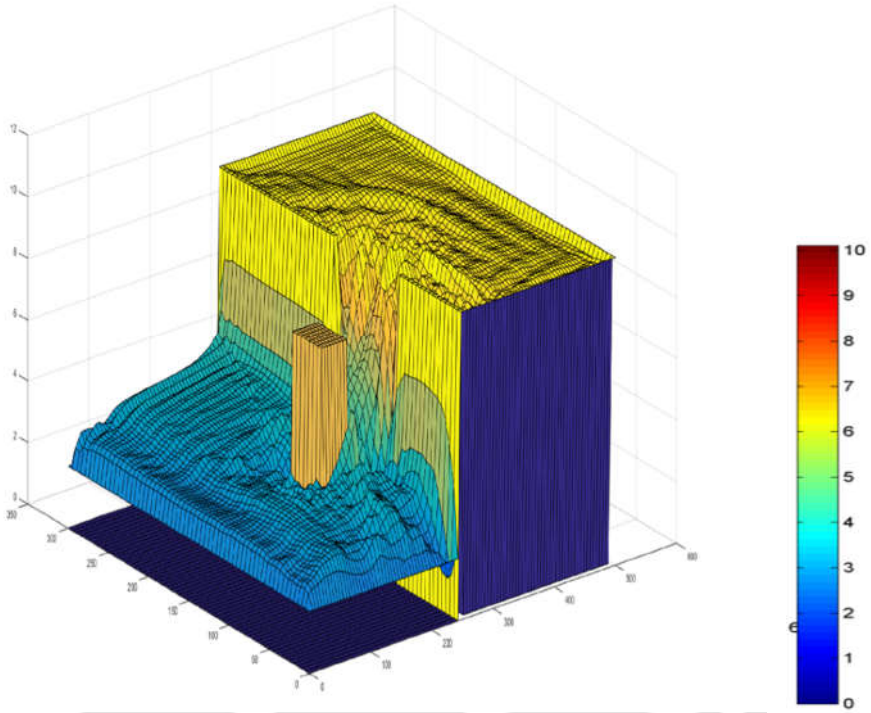

Figure 4.14: Dam break flow after 50 seconds of breach

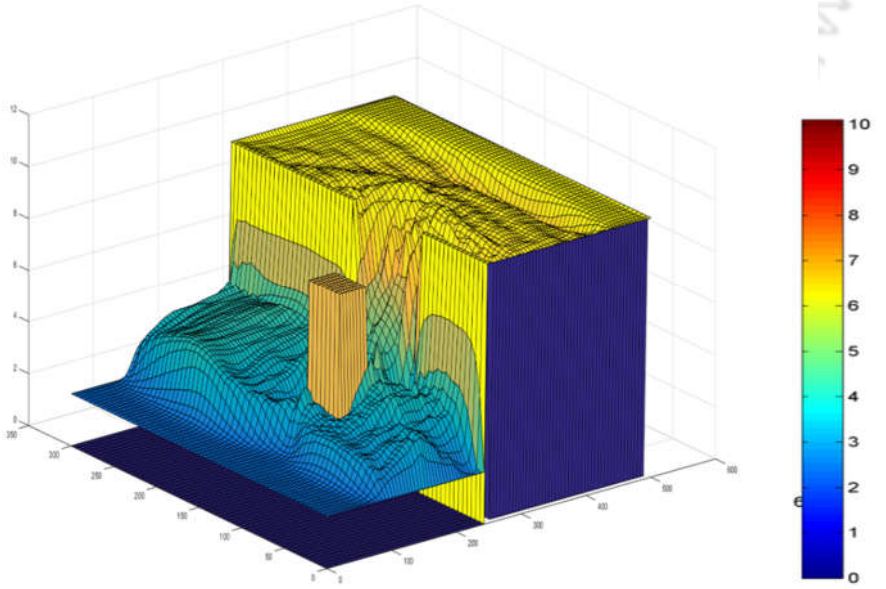

Figure 4.15: Dam break flow after 100 seconds of breach

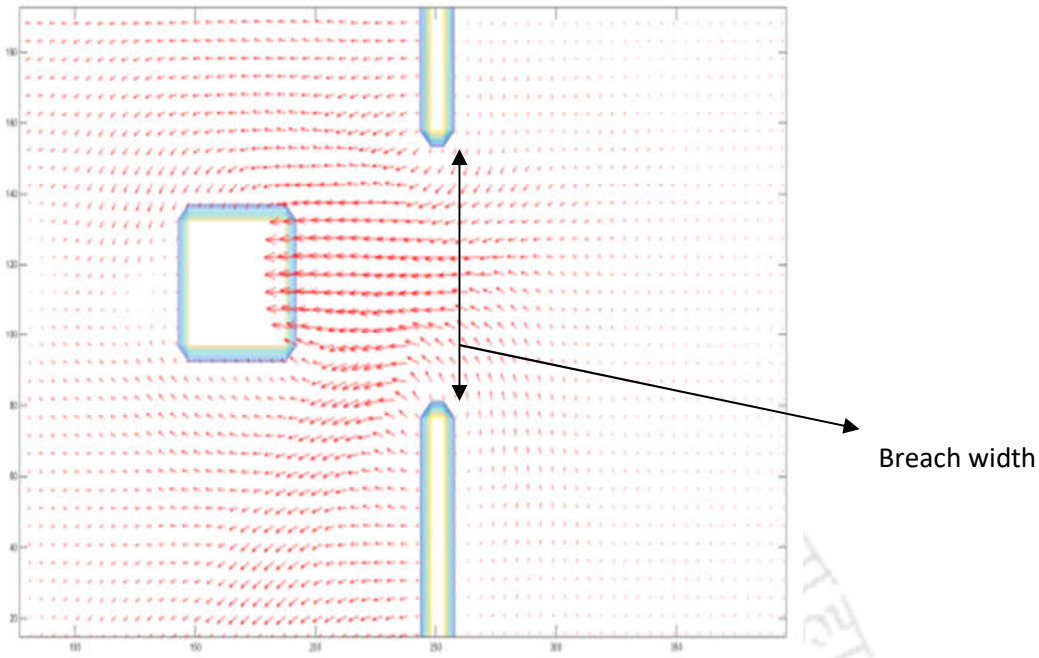

Figure 4.16: Computed velocity vectors after the breach

4.3 Development of grid generator for hydrodynamic simulation

The grid points generation over the computational domain is an essential and preliminary requirement for two-dimensional hydrodynamic modeling. Irrespective of the numerical methods opted for the solution of the governing equations, the domain discretization is a critical preprocessing aspect in streamflow simulations. The physical space must be covered with mesh points to apply and solve the governing conservation laws over the discrete elements. The application of 2D models in natural flow domains requires adequate meshing to replicate the physical complexities in the computational space. For instance, most rivers have curvilinear geometry, sand bars, groin walls, porcupine screens, intake structures, and vegetation that need to be incorporated during the computations. The inaccurate configuration of these elements in the flow domain gives erroneous computational results.

The simple grid generation tools are unable to handle these complexities. In general, as compared to unstructured grids, the curvilinear grid cells give high-resolution meshes near the sharp bends and provide more accurate outputs in computation (Bomers et al. 2019)(Bomers et al. 2019). A set of elliptic partial differential equations is solved to generate the mesh points over the flow domains. The elliptic equations have the advantage of maintaining the smoothness and orthogonality between the grid points. The simplest form of Laplace equation is expressed as (John and Anderson 1995)

$$\frac{\partial^2 \xi}{\partial x^2}+\frac{\partial^2 \xi}{\partial y^2}=0 \tag{4.2}$$

$$\frac{\partial^2 \eta}{\partial x^2}+\frac{\partial^2 \eta}{\partial y^2}=0 \tag{4.3}$$

In the above expression, (x, y) are the independent variables, and (ξ, η) are the dependent variables. The irregularity in the channel geometry is handled by transforming the equation from the physical space to the computational space. The equations 4.2-4.3 can be modified using the Jacobean functions (Equation 3.22-3.25) and can be expressed as

$$\alpha \frac{\partial^2 x}{\partial \xi^2}-2\beta \frac{\partial^2 x}{\partial \xi \partial \eta}+\gamma \frac{\partial^2 \xi}{\partial \eta^2}=0 \tag{4.4}$$

$$\alpha \frac{\partial^2 y}{\partial \xi^2}-2\beta \frac{\partial^2 y}{\partial \xi \partial \eta}+\gamma \frac{\partial^2 y}{\partial \eta^2}=0 \tag{4.5}$$

where

$$\alpha=\left(\frac{\partial x}{\partial \eta}\right)^2+\left(\frac{\partial y}{\partial \eta}\right)^2 \tag{4.6}$$

$$\beta = \left(\frac{\partial x}{\partial \xi}\right)\left(\frac{\partial x}{\partial \eta}\right) + \left(\frac{\partial y}{\partial \xi}\right)\left(\frac{\partial y}{\partial \eta}\right) \tag{4.7}$$

$$\gamma = \left(\frac{\partial x}{\partial \xi}\right)^2 + \left(\frac{\partial y}{\partial \xi}\right)^2 \tag{4.8}$$

The equations (4.4-4.8) are solved using the central finite difference method in MATLAB. A graphical user interface (GUI) is developed for grid generation. Figure -4.17 shows the layout of the GUI. Initially, a georeferenced map of the modeled area is prepared and stored. The georeferenced information is expressed in the Georeferenced Tagged Image File Format (GeoTIFF) or Tagged Image File Format (Tiff). The unit system must be assigned in Universal Transverse Mercator (UTM). After browsing the image, the load image button is clicked to display the image in the GUI. The polylines are selected by clicking the polyline button, and the computational area boundary is marked over the image. The number of grids in the x and y direction is then assigned over the bounded domain. Jacobie's iteration method is adopted for the mesh generation within the modeled area. Some application of the grid generator is presented in the following sections.

4.3.1 Grid generation in the Brahmaputra River near the Umananda, Assam, India

A georeferenced image of the Brahmaputra River near Umananda Island is loaded in the grid generator. The polylines are drawn over the study area, and the number of grid points in the x and y direction is assigned in the bounded region.

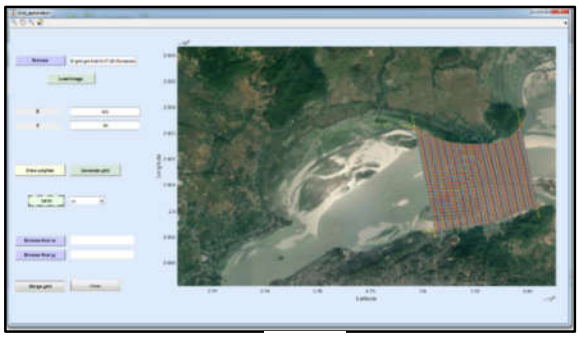

(a)

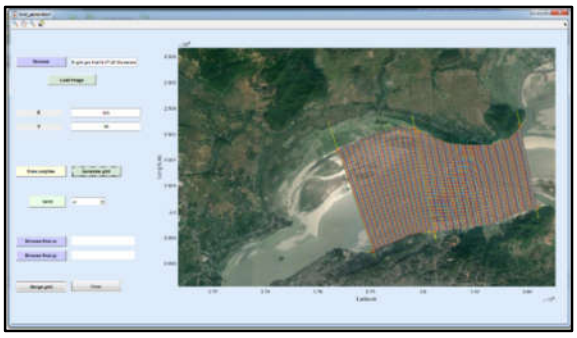

(b)

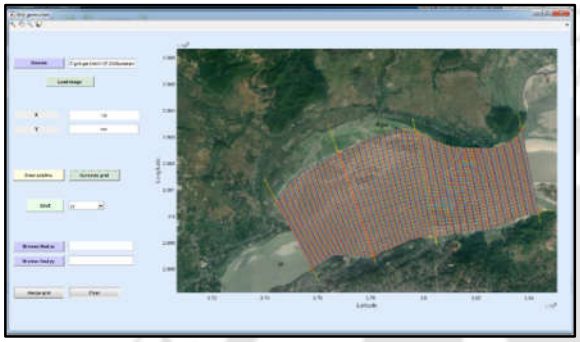

(c)

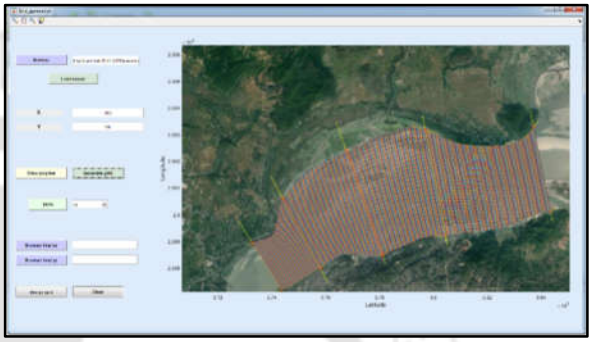

(d)

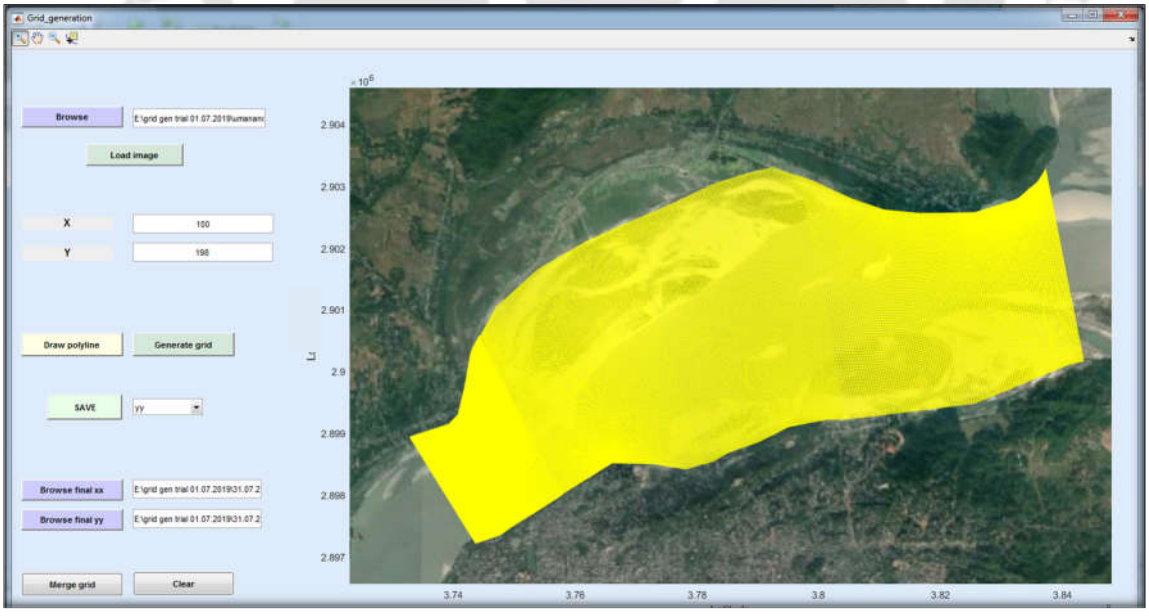

(e)

Figure 4.17(a-e): Different steps of grid generation

Initially, sub grids are created from upstream to downstream at different locations and then merged by clicking the Merge Grid button in the GUI. A total of 199x399 grid points have been generated in the study area. Step by step, the grid generation process is presented in figure-4.17(a-e).

4.3.2 Grid generation in the Brahmaputra River near the Majuli, Assam

The grids are generated for a 55km stretch of the Brahmaputra river near Majuli, Assam in the second case. A similar procedure is adopted, as mentioned in section 4.3. The flow domain is discretized into 746x225 grid points. The sequence of grid generation is presented in figure 4.18.

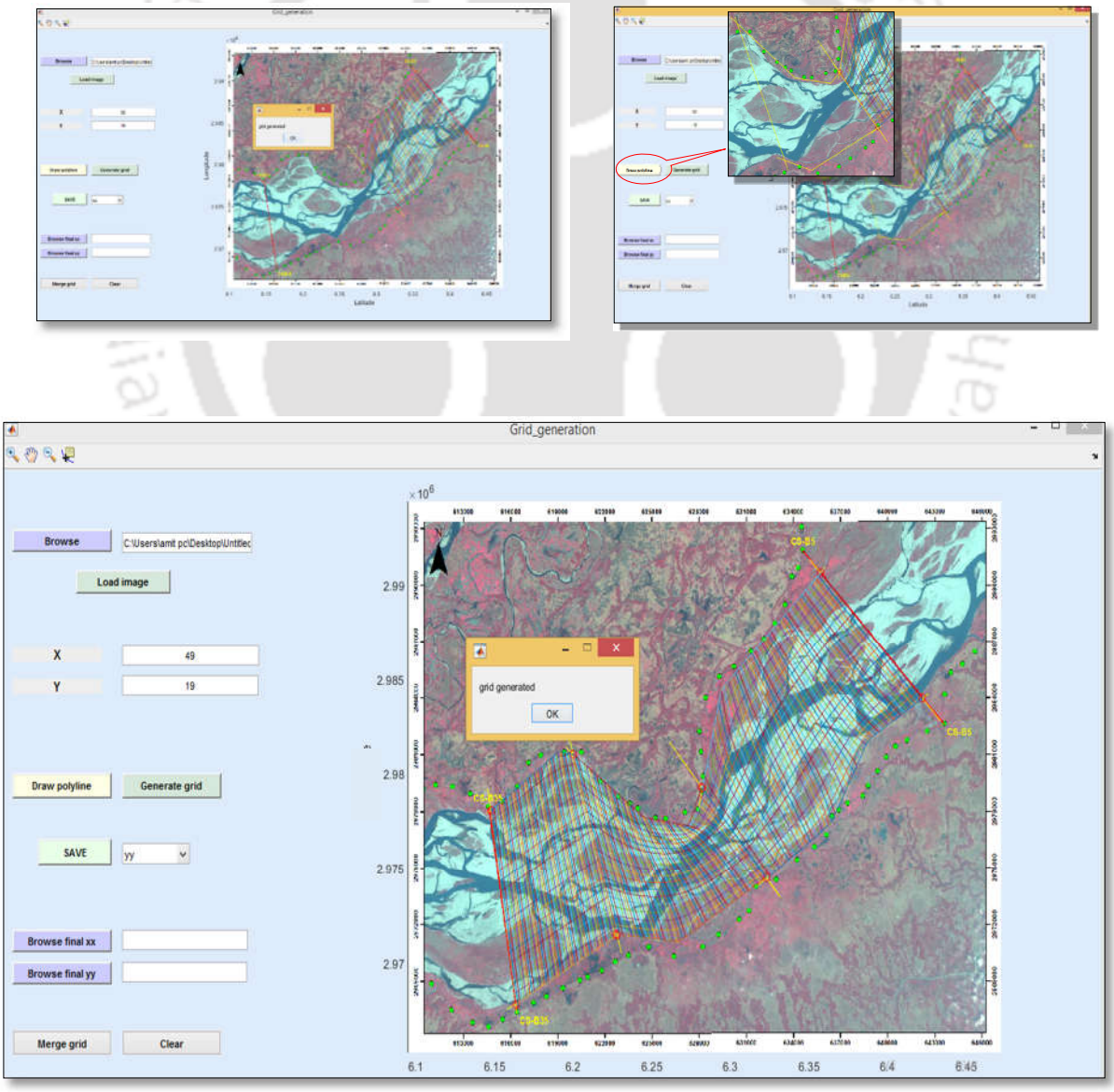

Figure 4.18: Grid generations in the Brahmaputra River near Majuli, Assam

4.4 Field Survey for model calibration and validation

The hydrodynamic model is applied in three different reaches, and computed outputs are compared with the field measured data. For model calibration and validation, extensive field surveys are carried out to obtain the bed level information, velocity data, and flow discharge. In some cases, field data such as Stage-discharge information, bed level elevations, and velocity at different points are collected from the competent authority. The details of the field survey conducted at different locations are presented below.

4.4.1 Field survey near the Umananda Island, Guwahati, Assam

The model is applied on an 11km braided reach of the Brahmaputra River, near the Umananda river island. The area lies between 91°44'28.51" E, 26°12'05.91" N and 91°42'04.45" E, 26°10'15.64" N in the Guwahati region. The bed slope in this region is around 0.1m/km. At upstream, a small side channel is separated from the main channel by a sandbar (Figure 4.19(a)). The velocities are sampled by the boat-mounted current meter, and the sampling started from the left bank and continued till the right bank (figure-4.19(b)). The survey data consists of the bed level elevations, the velocity at the water surface, 0.2h from the water surface, and 0.8h from the water surface, where h is the flow depth. The stage-discharge curve is obtained from the active gauge site, Pandu, downstream of the Umananda river island. The bed elevations in the study area are surveyed using the echo sounder and presented in figure 4.21(b).

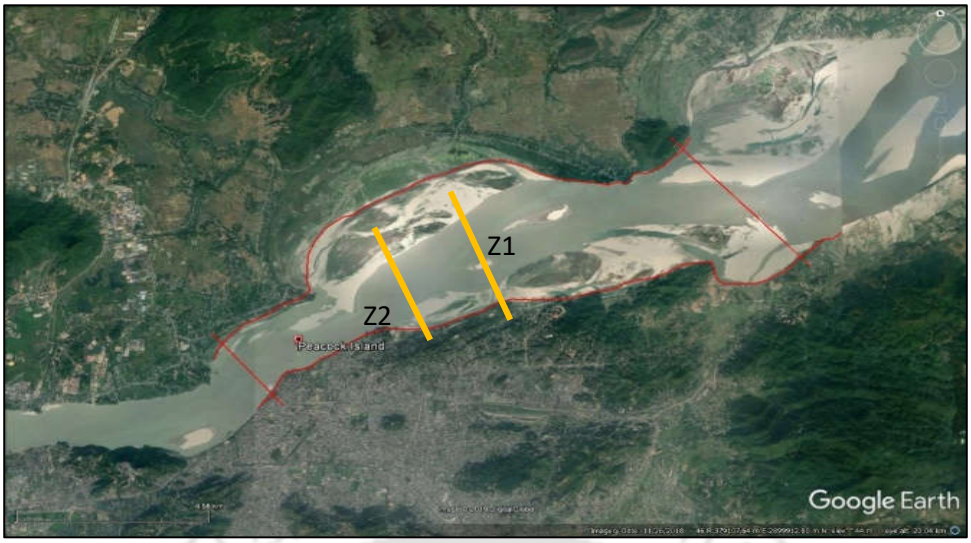

(a)

(b)

Figure 4.19: (a) Surveyed portion near the Umananda Island (b) Velocity sampling cross-section

4.4.2 Field survey near Majuli Island, Guwahati, Assam

A 3.45 km reach length (aspect ratio (b/h) >15) of Brahmaputra River, India, located within 26º45' N - 27º12' N latitude and 93º39' E - 94º35' E longitude is considered for model application. A bathymetric survey is conducted on May 25, 2019, at the study site. Details of the study area are shown in figure 4.20 (a). The flow velocity is measured using the cup-type

current meter. The photographs taken during the river survey are presented in figure-4.20(b). Discharge and water level at upstream and downstream is 9847cumec and 84.14m. The width of the cross-sections varies from 1.35 km to 1.08 km downstream. The grain size distribution curve for the sediment samples collected from the field is presented in figure-4.20(c).

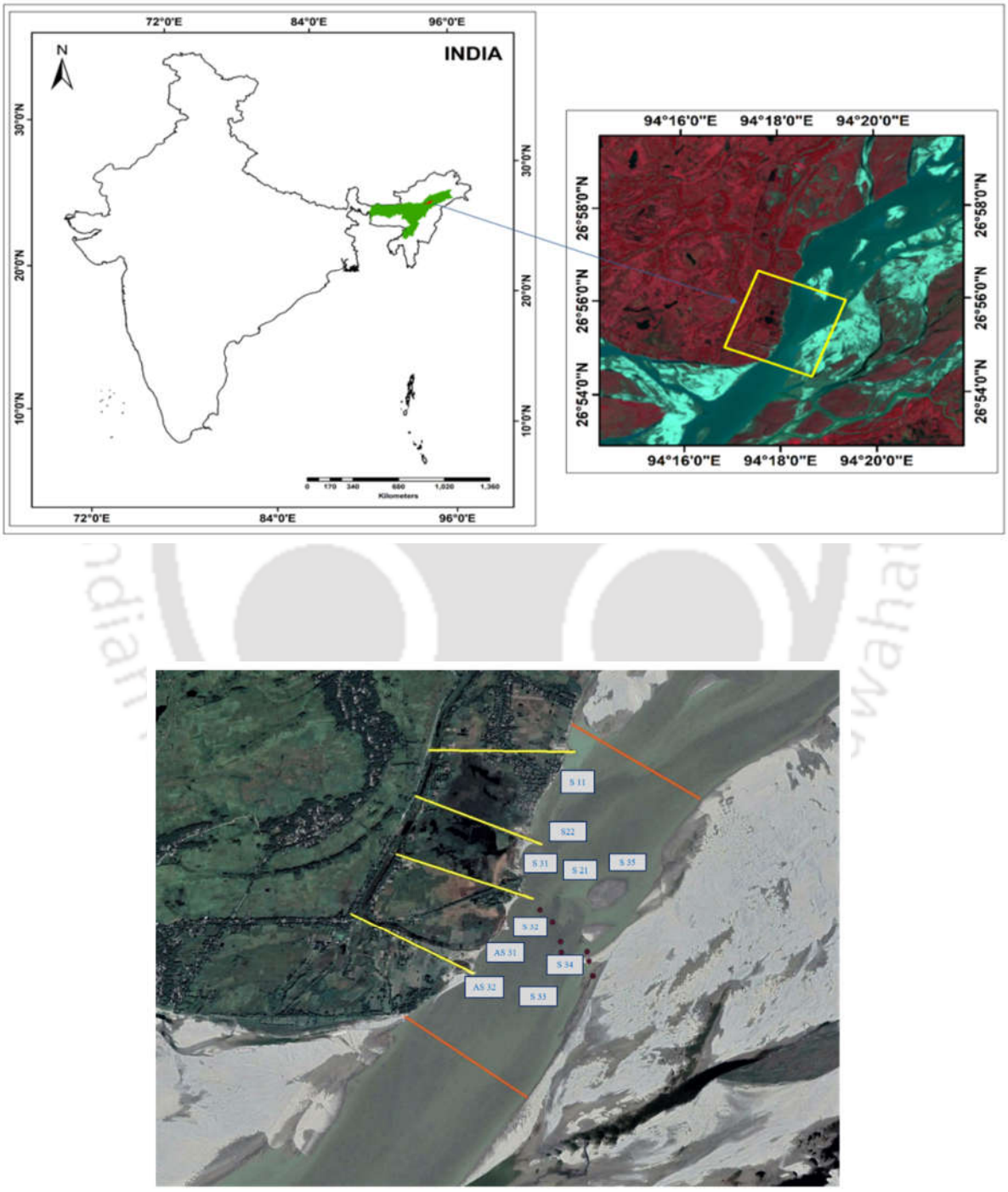

(a)

(b)

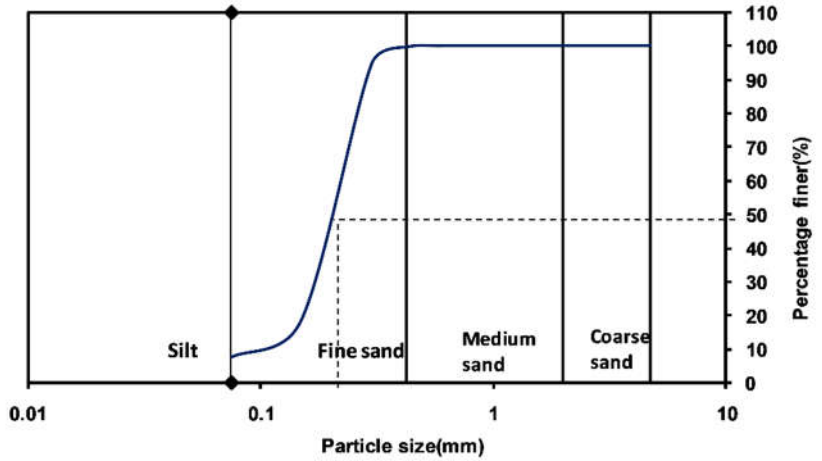

(c)

Figure -4.20-(a) Study area and velocity measuring points (b) Photographs taken during the survey (c) Particle size distribution curve

4.5 Field application of the model

4.5.1 Application of the model near the Umananda Island, Guwahati

The hydrodynamic model is applied in a braided reach of the Brahmaputra River near the Umananda Island. The study area map is downloaded from Google earth and georeferenced in GIS. The grids are generated in the flow domain using the grid generator. The computational time step for each simulation is set as 0.1 sec, and the model is run for steady-state conditions. With this time step, the Courant number is found to be 0.68. A total number of 200x400 grid points are generated, as shown in figure 4.21(a). In braided sections, the bed level undulations prominently affect the discharge distributions. At the upstream, discharge in the main channel is 3000 m^3/sec and in the sub-channel is 20 m^3/sec is distributed over the discretized domain. The sand bars in the braided portions produce negative depth, and thus a threshold depth of 0.1m is considered for the dry areas. The grid points with the threshold depth are excluded during the computational run. The CFL criteria are checked at each time step.

The computed depth contour is presented in figure-4.22(a). For the given streamflow condition, the maximum flow depth in the main channel is 15-18.75m, and the maximum current speed lies within 2.5-3 m/sec. In the sub-channel, the maximum flow depth is 12.66m with a current speed of 0.07-0.1 m/sec. At the confluence of the sub and main channel, the flow depth is 0.8-7 m, and the current speed is 0.45-1.2 m/sec. Model simulated flow depth and velocity are compared with the field measured data, as shown in figures 4.22(b) and 4.22 (c). The model predicted outputs are also compared with the MIKE21C outputs at different sections, as shown in figure-4.22.1. Results indicate a satisfactory agreement between the computed and observed results.

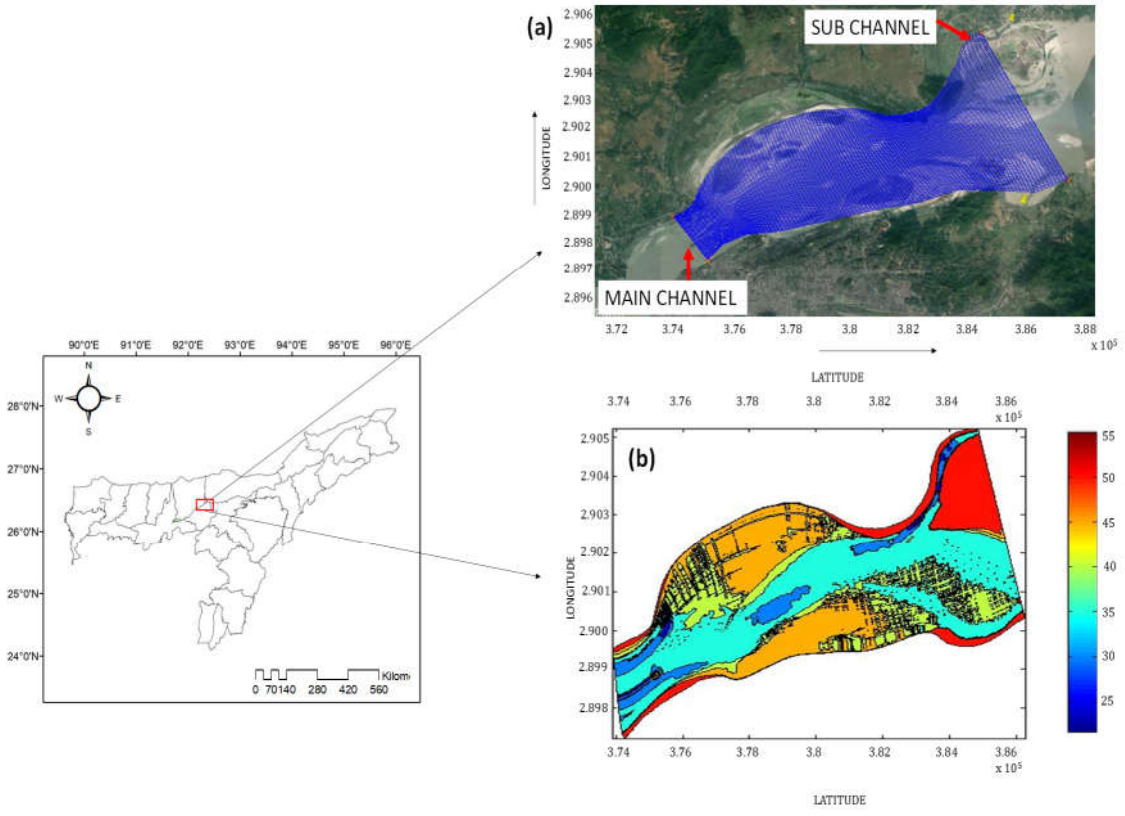

Figure 4.21: Map of the study area (a) Generated grid in the computational domain (b) Bed level elevations (m) in the domain

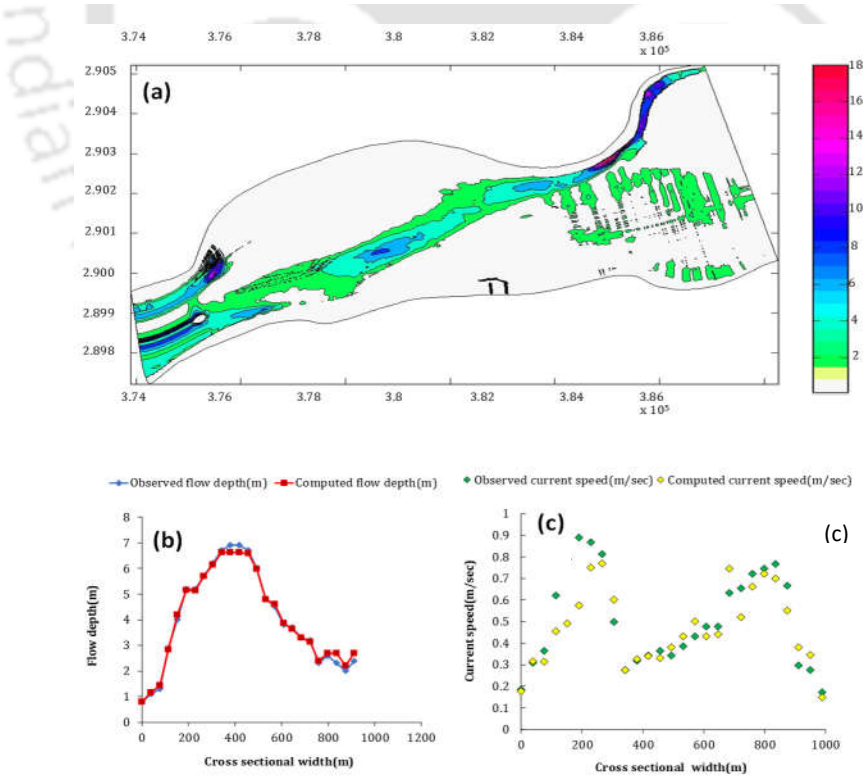

Figure 4.22 : (a) Computed flow depth contour in the domain (b,c) Comparison of computed and measured flow depth and velocity

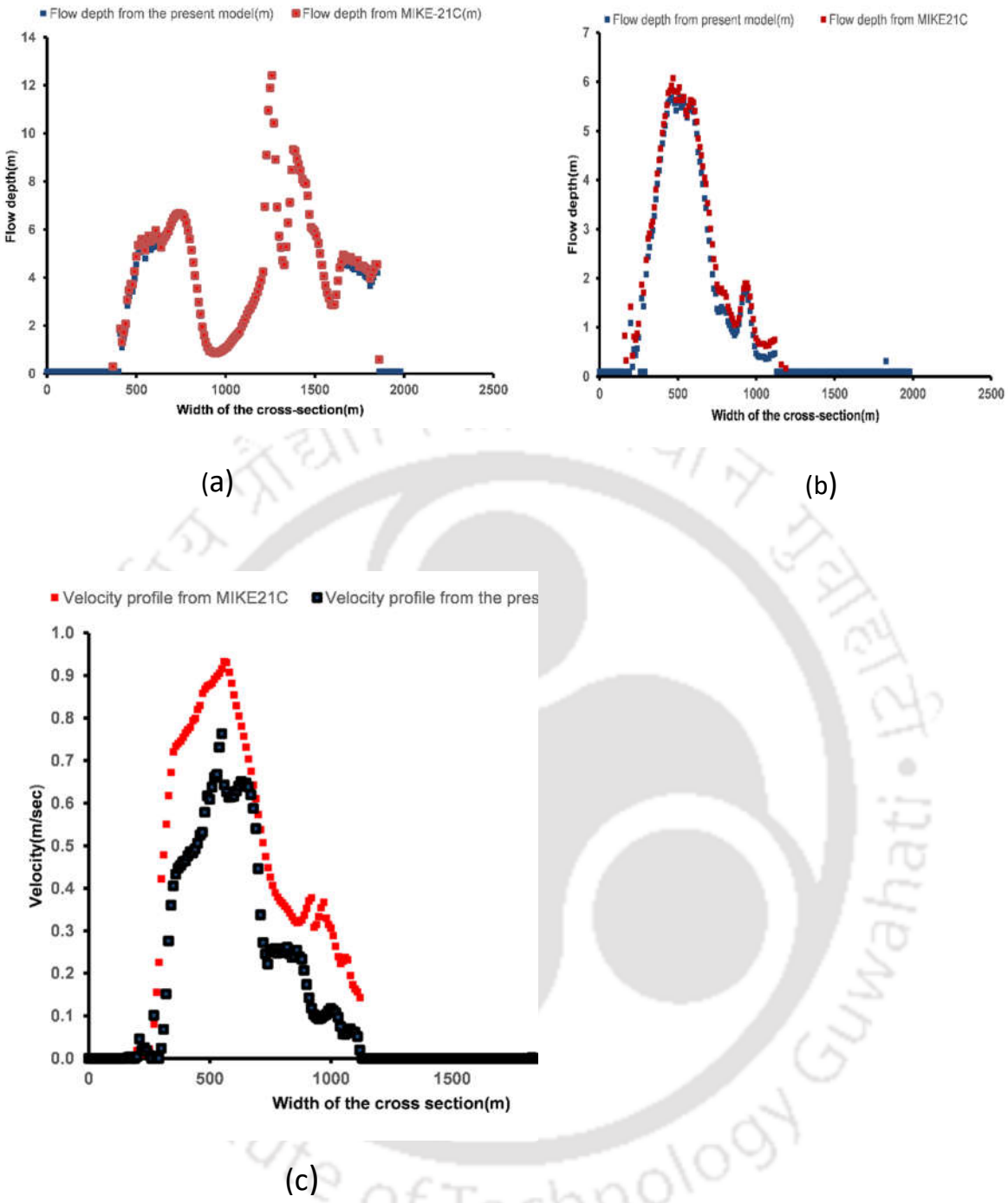

Figure 4.22.1**:** Comparison of the present model output with MIKE21C (a, b) Flow depth at Z1 and Z2 (c) Velocity profile at Z2.

4.5.2 Application of the model near the Majuli Island, Assam

In the second case, the modeled reach has a series of deflecting spurs (S1, S2, S3, and S4) from u/s to d/s located in the Brahmaputra River near the Majuli Island. The entire computational domain is discretized into 60x225 grid points. The time interval for simulation is 0.1 seconds.

All cell points with flow depths below the threshold depth value (0.1m) are excluded from the computation. CFL condition is used to check the model stability. Flow depth and the two-dimensional velocity components (u, v) are evaluated from the model. The grids are generated over the flow area, as shown in figure 4.23(a). Manning's roughness coefficient is calculated from Stickler's equation. Stickler's equation relates Manning's n value with the median particle diameter (d_{50}) taken from the particle size distribution curve shown in figure 4.20(c). Based on the d_{50}value, Manning's n is found out to be 0.033. Figure 4.23(b) shows the computed flow depth contours. The maximum flow depth is around 30-36m in the region for the given flow event. The velocity vectors between the spurs S2 and S3 are shown in figure 4.23(c). The numerical model is validated at different flow measurement points in the domain. The computed and observed results are shown in figure -4.24(a, b). There is a good agreement between the calculated and measured results (R^2 =0.71).

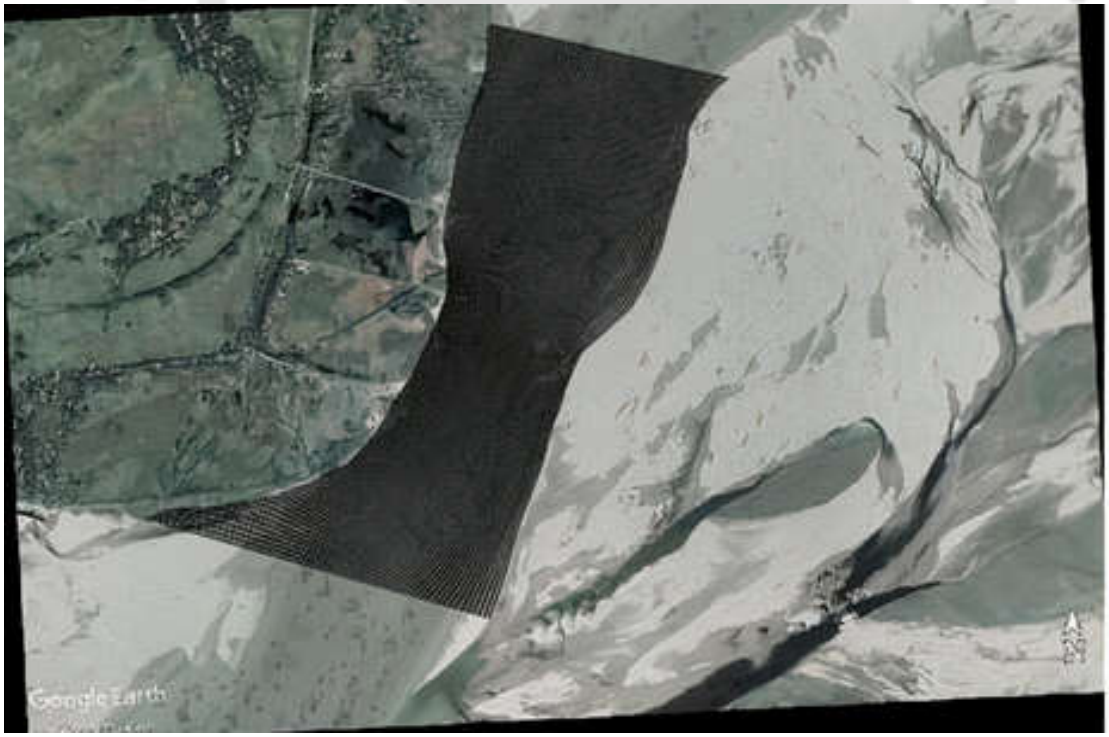

(a)

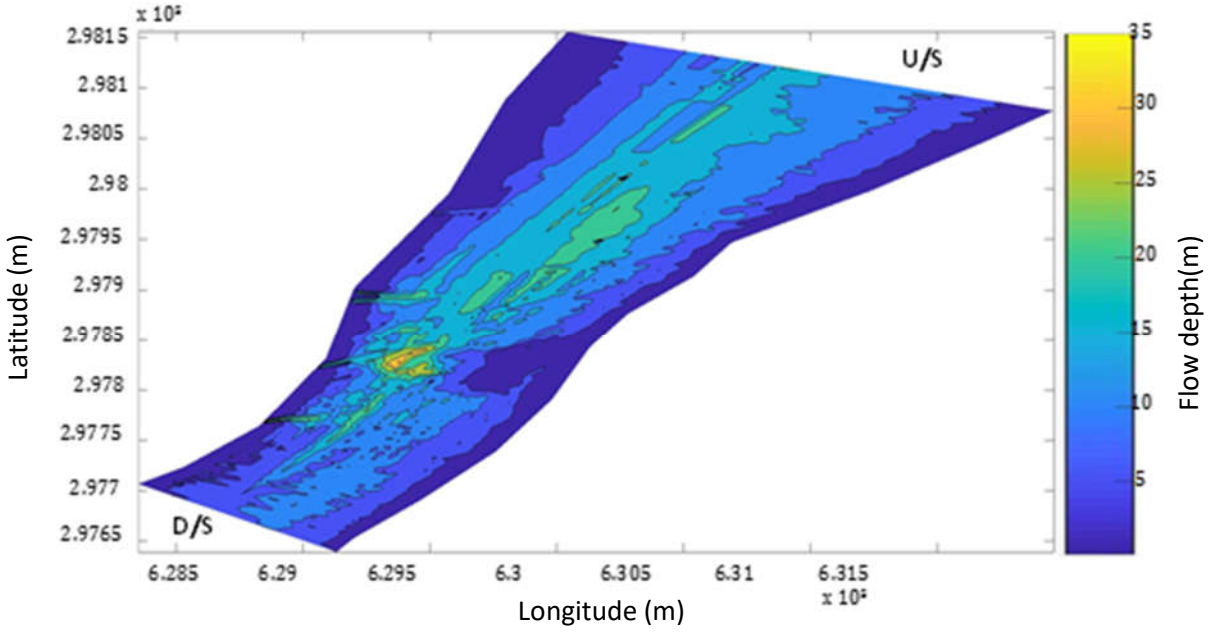

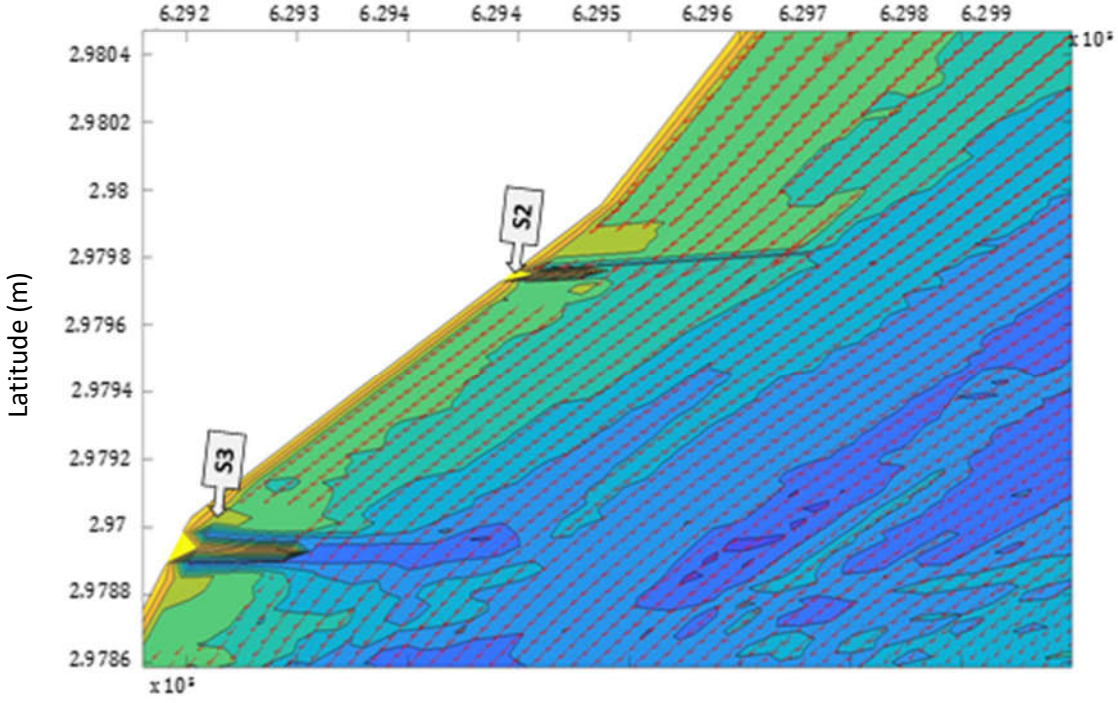

(b,c)

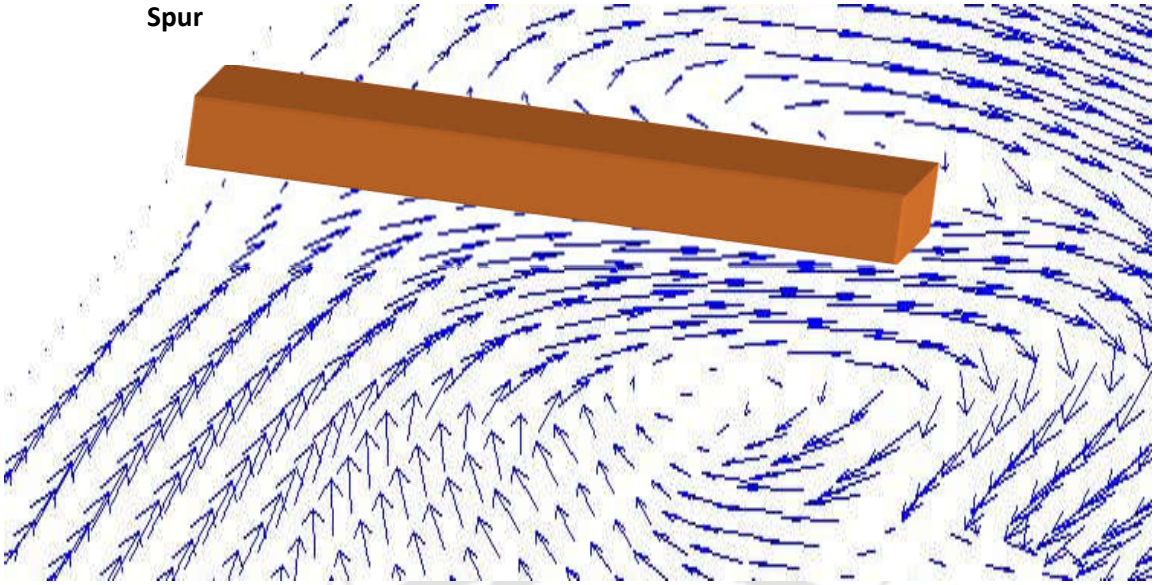

(d)

Figure 4.23 (a) Grids in the flow area (b) Computed flow depth in the flow area (m) (c) Computed velocity in the flow area (d) Formation of recirculation zone downstream of spur

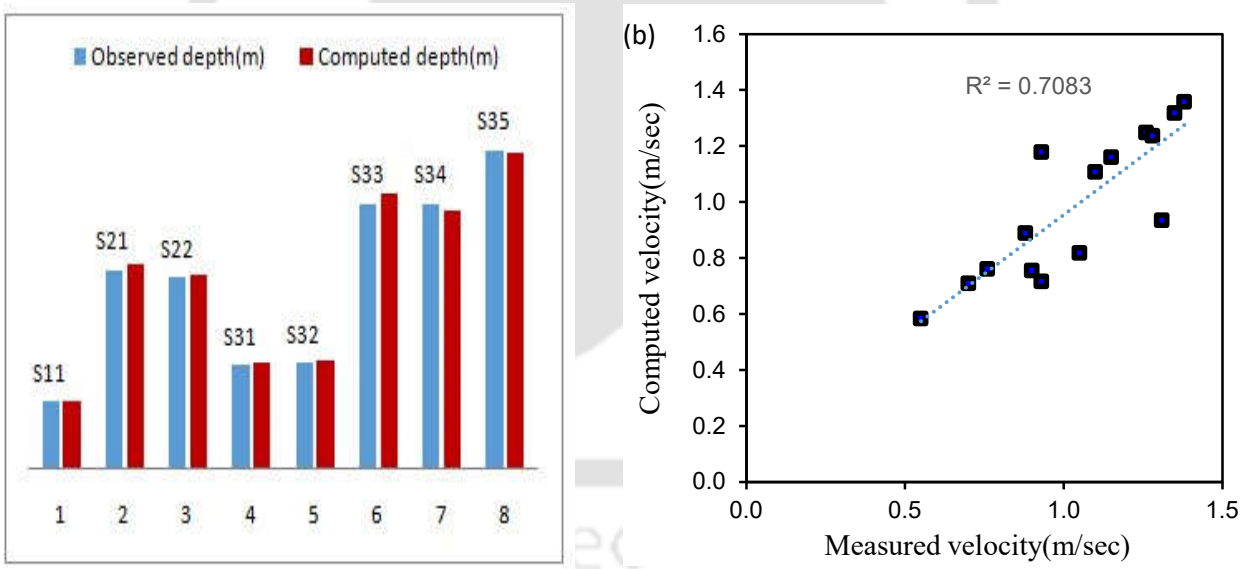

Figure 4.24 Comparison of the computed and measured (a) Flow depth (b) velocity

4.5.2.1 Influence of boundary condition near flow-structure interaction zone

The model performance is evaluated at two different boundary conditions near the solid groin walls. The groin walls are considered entirely rigid in the first case, and the no-slip condition is used. For instance, in figure 4.25 (i), the streamwise and transverse velocity at the grid points

(i, j) are considered zero during the computation. This indicates that no momentum flux exchange occurs, and the water depth is frozen with the initial value.

$$\in(i,j)=\in(i,j),\ u(i,j)=0,\ v(i,j)=0$$

However, in the second case, the water waves that impinge on the spurs' rigid surface are modeled considering the reflecting boundary conditions (figure 4.25-(ii)). The normal component of the vectors along the streamflow direction are assigned at cell points (i, j)

$$\in(i,j)=\in(i,j),\ \text{and } u(i+1,j)=-u(i-1,j)$$

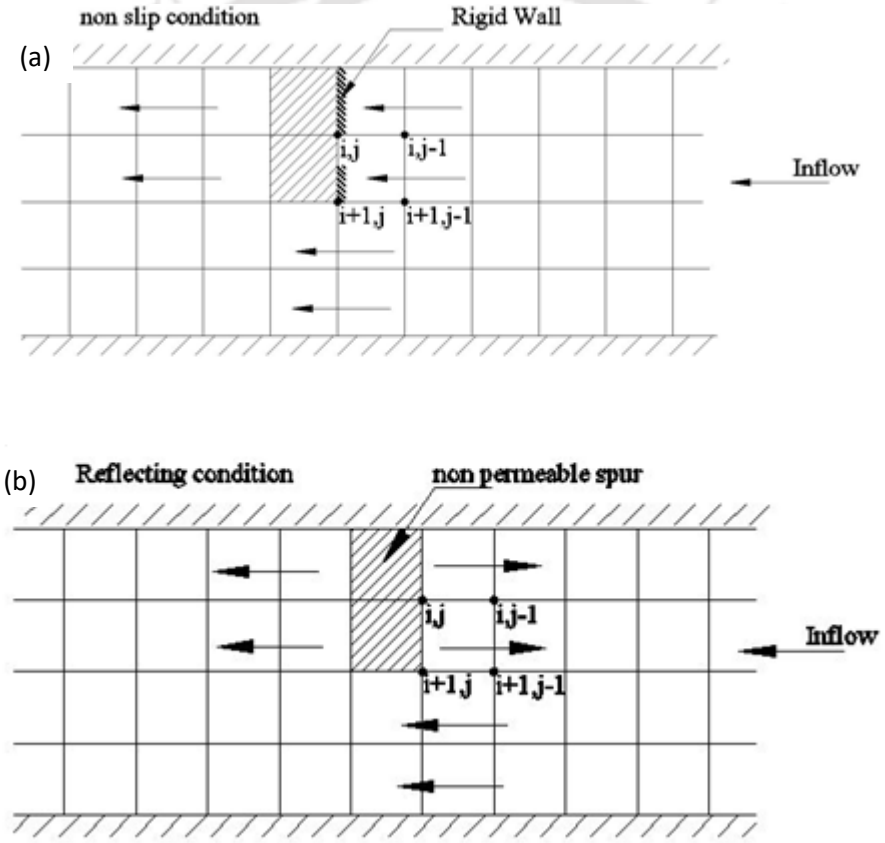

Figure 4.25(a) Reflection boundary condition and (b) no slip boundary condition

The influence of wall boundary conditions near the groins affected regions is investigated using two statistical measurements, Viz. Nash-Sutcliffe efficiency (NSE) and Root mean square error (RMSE) (Table 4.1).

$$\text{RMSE}=\sqrt{\frac{1}{n}\sum_{i=1}^{n}(f_i - y_i)^2} \tag{4.9}$$

$$\text{NSE}=1-\frac{\frac{1}{n}\sum_{i=1}^{n}(f_i-y_i)^2}{\frac{1}{n}\sum_{i=1}^{n}(y_i-\bar{y})^2} \tag{4.10}$$

where, y_i is the observed data and f_i is the model predicted data and $\bar{y}$ is the average value in the observed dataset.

Table 4.1: Statistical index for model evaluation

Statistical index	Flow depth		Current speed	
	Reflection boundary condition	No-slip boundary	Reflection boundary condition	No-slip boundary
NSE	0.996	0.991	0.605	0.221
RMSE	0.533	0.825	0.119	0.285

Excellent performance is observed from the model computed flow depth profile (NSE range 0.75-1) with both boundary conditions. The closer the NSE values to 1, the better is the model performance. On the contrary, a lower RMSE value is found for the computed flow depth profile with the refection boundary condition (RMSE=0.533) compared to the no-slip condition (RMSE=0.825). Both findings indicate that the variation of the boundary conditions near the fluid-structure interaction zone has less influence on the flow depth profile. However, the current speed in the vicinity of the spur dykes is affected. As shown in Table 1, the reflection

boundary condition shows superior in simulating the velocity profile (RMSE=0.11, NSE=0.60) compared to the no-slip state (RMSE=0.28, NSE=0.22). In a natural flow, the waves got deflected after attacking the spur walls, and neighboring regions experience forming a mixing layer and a recirculation zone downstream (Figure-4.23(iv)). Incorporating the reflection boundary condition with the numerical models ensures the deflecting wave effects and captures the mixing layer phenomenon near the dyke wall. It is observed that the present model adequately captures the formation of the recirculation zone at the d/s of the spur wall due to the wave effect. However, the 2D-SWD models with the no sip condition assume the zero velocity at those points, which is not entirely correct as it contradicts the natural flow. These findings suggested the importance of considering the reflecting boundary condition rather than the no-slip condition while applying the model near the fluid-structure interaction region.

4.5.2.2 Exploring the dredging possibility near the Nimatighat, Majuli from the model application

High silt carrying capacity and gradient variations of the Brahmaputra River causes aggradations and degradations at different locations. The four spurs are constructed to prevent bank erosion in the Majuli, deflect the bank's flow, and promote silting in the neighboring areas. However, near the Nimatighat, the main channel is contracted in the presence of a large sandbar. During monsoon, 30000 to 50000 cumec of flow deflected from the series of spurs passes through the contracted portion and directly hit the Nimatighat and causes heavy erosion near the bank. It is the interest of the stakeholders to carry out river training work in that stretch to reduce soil and property loss. A numerical model study is essential for the decision-making process before implementing any possible river training measures in the field. Proper representation of the braided stretch and bed level variations is challenging to model in field scale, and therefore, a 2D hydrodynamic model is a good alternative for flow prediction. The primary objective of this simulation is to apply the 2D hydrodynamic model in a highly braided stream to quantify the velocity distributions near the eroded bank and adopt the best alternative

out of a single measure or from a couple of measures. Three possible dredging widths and a series of the permeable spur are considered in the simulation (figure-4.26).

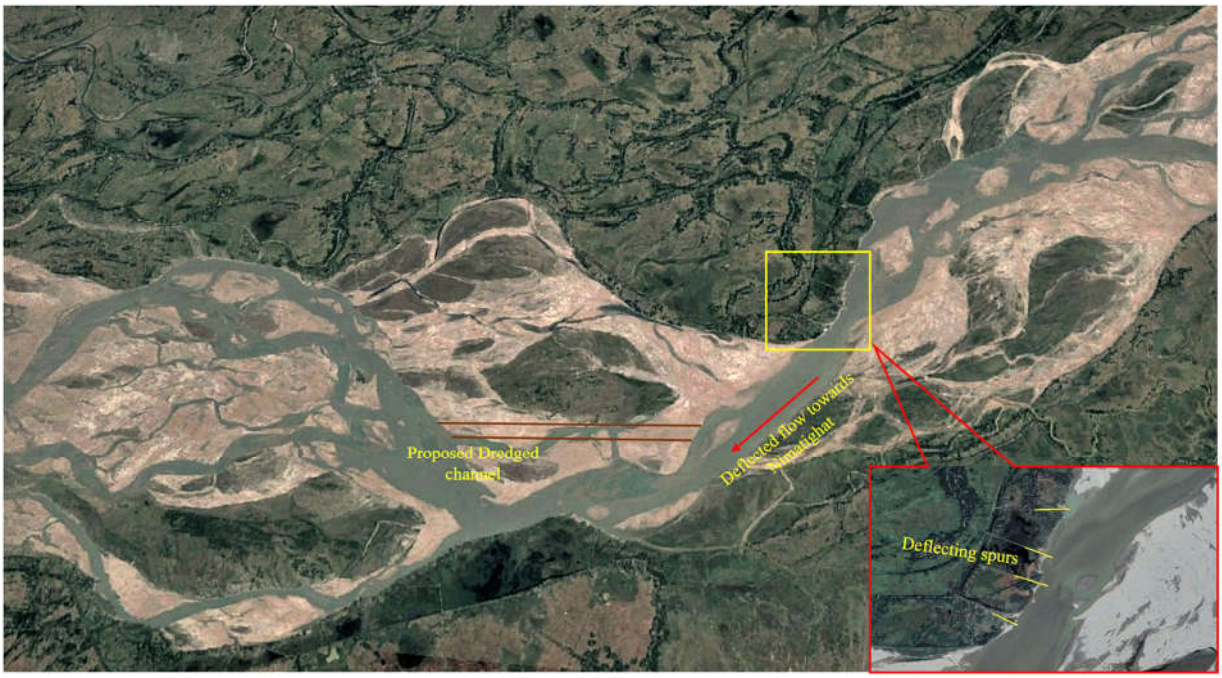

Figure 4.26: Study area with proposed dredging

4.5.2.1 First case: Dredging of the sandbar with three different width

In the first case, the model is simulated by considering the three dredging widths in the channel. Width in probable dredged locations is considered as 150m, 300m, and 450m. The bed profile before and after the dredging is presented in figure -4.27(a-b). The total grid points considered in the simulation are 746x225. Boundary conditions are provided from the stage-discharge curve, and the model is run with a discharge of 30000 m^3/sec.

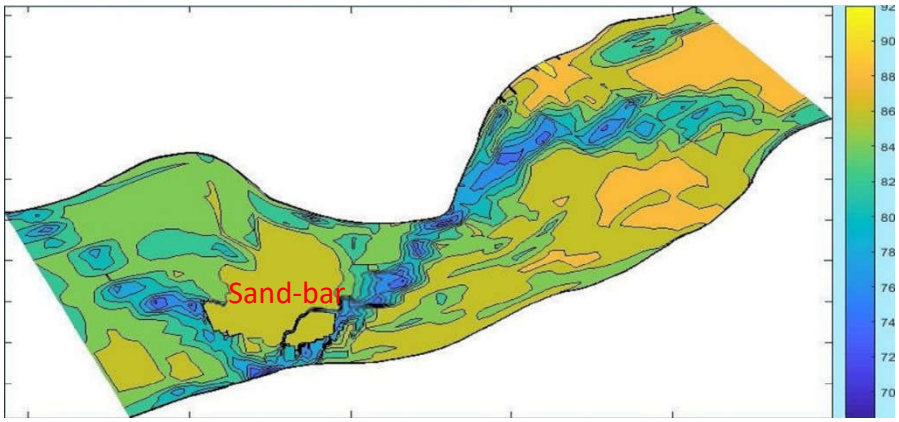

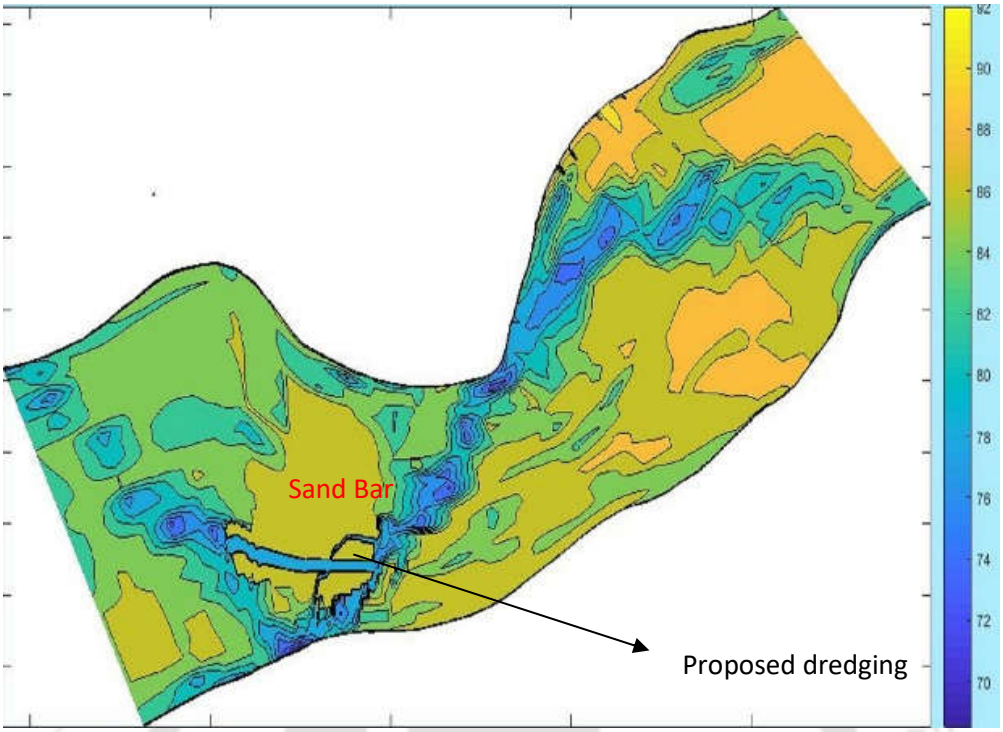

Figure 4.27: Bed profile before and after sandbar dredging

Figure 4.28: Flow parameter observation points near the south bank

The locations at which computed results are checked are shown in figure-4.28. The maximum current speed near the bank is within the range of 1.2-1.35m/sec for the given flow event. However, under different dredged conditions, the near bank velocity progressively reduces and is found within the 0.6-0.75m/sec. It is observed that the velocity of the main channel near the

bank does not show appreciable change after dredging was done. The maximum velocity in the main channel gets reduced by order of 6% to 7%. The velocity profiles at different dredging conditions are presented in figure -4.29. Compared to the width of the main channel, the 150-250m width of the dredged channel also appears insufficient to draw enough water. In the dredged channel, through the entry velocity is slightly higher (in the order of 0.85-1), the outlet velocity drops near the outlet. If high sediment-laden water enters the channel, the sediment might get deposited in the dredged channel. So, the maintenance of the channel is an essential factor to be considered. The channel initially created can be expanded gradually to have an effective result.

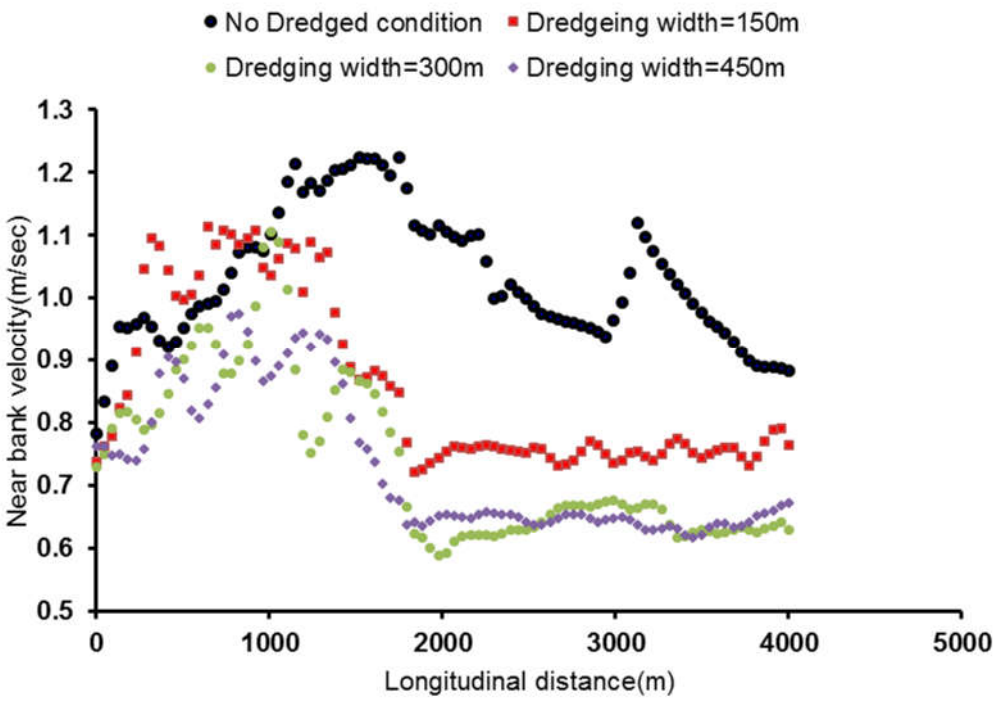

Figure 4.29: Near bank velocity profile

4.5.2.2 Second case: Dredging of the sandbar with a porcupine screen at the upstream

In this case, a series of porcupines is incorporated upstream of the 450m dredged channel and extended up to the affected portion of the bank. Figure 4.30 shows the proposed locations for the installation of the porcupine screens.

Figure 4.30: Location of the porcupine screen

The porcupine screens mainly serve as permeable groins. These screens are installed up to several kilometres from the bank to the river body. It reduces the velocity near the affected regions and facilitates the deposition by obstructing the sediment-laden water. The effect of porcupine screens is incorporated in the model by increasing the roughness values at the installed locations. The computed velocity profiles with and without the porcupine screens are presented in figure -4.31.

The results from the previous simulations indicate that without the porcupine screens, the velocity at the upstream of the 450m dredged channel is 0.75-0.92 m/sec. In this case, the screens are installed entirely in the affected area, and the current speed reduces to 0.6-0.85m/sec. Although the velocity difference is not significantly changing with the porcupine screens, it is essential to consider the morphological alterations in the affected area. However, the sediment transport or deposition calculations are not considered in this work, which is crucial for bank protection works, especially in the Brahmaputra River. A detailed cost-benefit analysis is required before the implementation of the project.

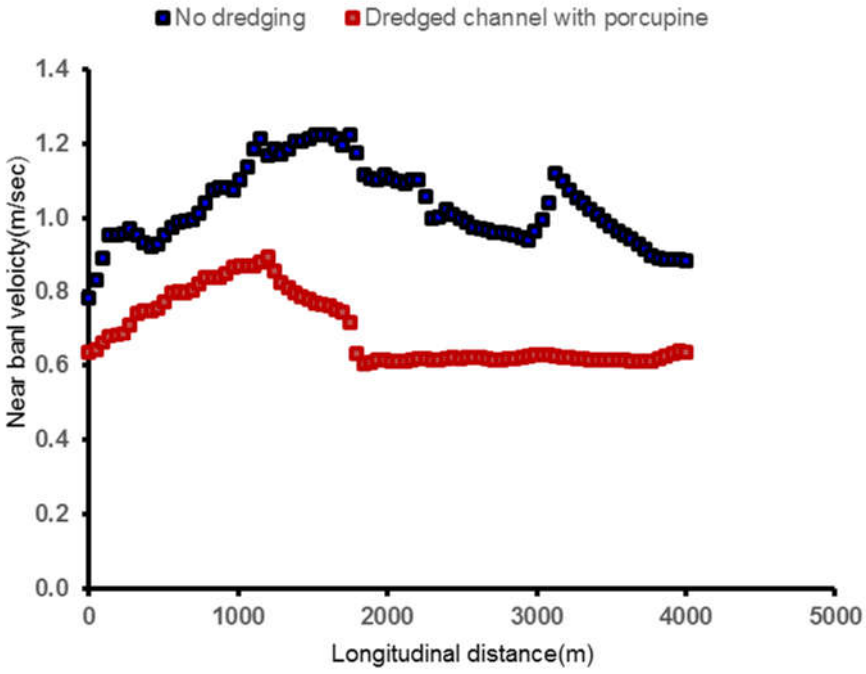

Figure-4.31Computed velocity profile before and after the installation of the porcupines

4.5.3 Application of the model in Tiding River, Arunachal Pradesh

Rivers in hilly terrain may carry unprecedented high monsoonal discharge because of the adverse combination of the storm in its upper catchments. Discharge variation often causes changes in the morphology of such a river, particularly near the river bank formed by loosely-packed materials. The Tiding is a river of this nature and is located in a remote area of Arunachal Pradesh. The Bridge on the Tiding River faces a problem due to the high monsoonal current of the river. Extensive erosion of the right bank hillside has also threatened the approach road on the right flank as it passes through that portion. As the road leads to the Indo-China border, disruption of communication is of serious concern, and it was desired to have a permanent solution. The location of the river is shown below. From the following figure-4.32, it is observed that the river meets with a main contributing tributary of the Lohit River just downstream of the Tiding Bridge.

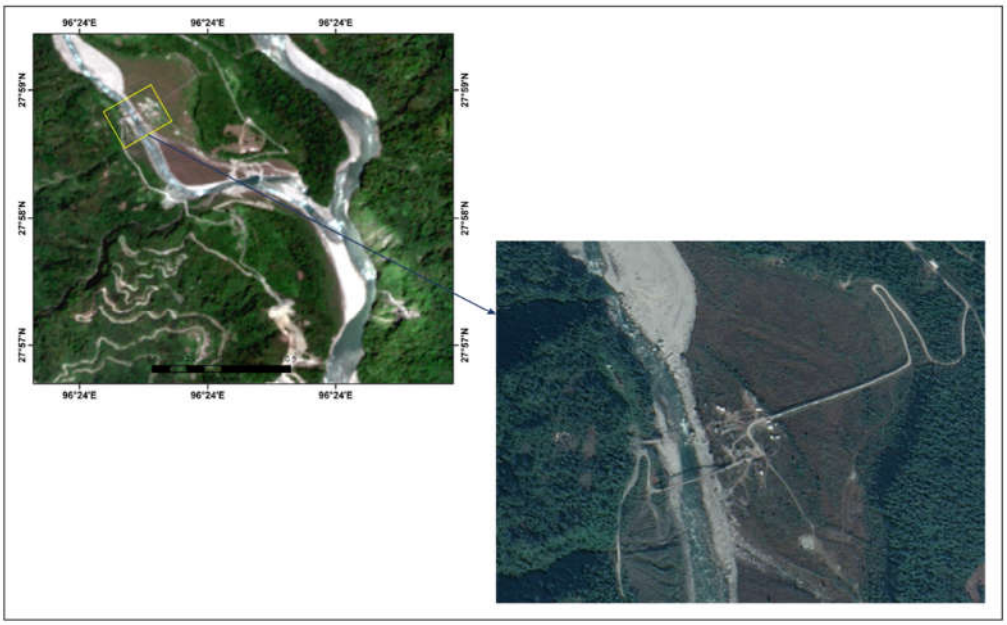

Figure-4.32. Map of the study area

The extent of the modeling area is selected, and the computational grid is designed for the river (figure-4.33(a)). The bathymetry data is entered into the computational grid, i.e., bed levels are specified in each computational grid point (figure 4.33-(b)). Necessary model parameters are provided based on the available standard value. For Manning's roughness coefficient, an n value of 0.06 is used in the simulations. The highest observed discharge was 3755.00cumec. Also, with the impact of climate change and land-use change, discharge may increase in the future. Therefore, 4000cumec is considered in the hydrodynamic simulation, i.e., with an increase of 10%. The output from the hydrodynamic model comprises flow velocity in two directions, water depth, and water surface elevation, at all computational points at all-time steps. The flow domain is discretized into 145x11 grid points. Bathymetry of the river was generated using the longitudinal and cross-sectional data provided by the BRTF.

(a)

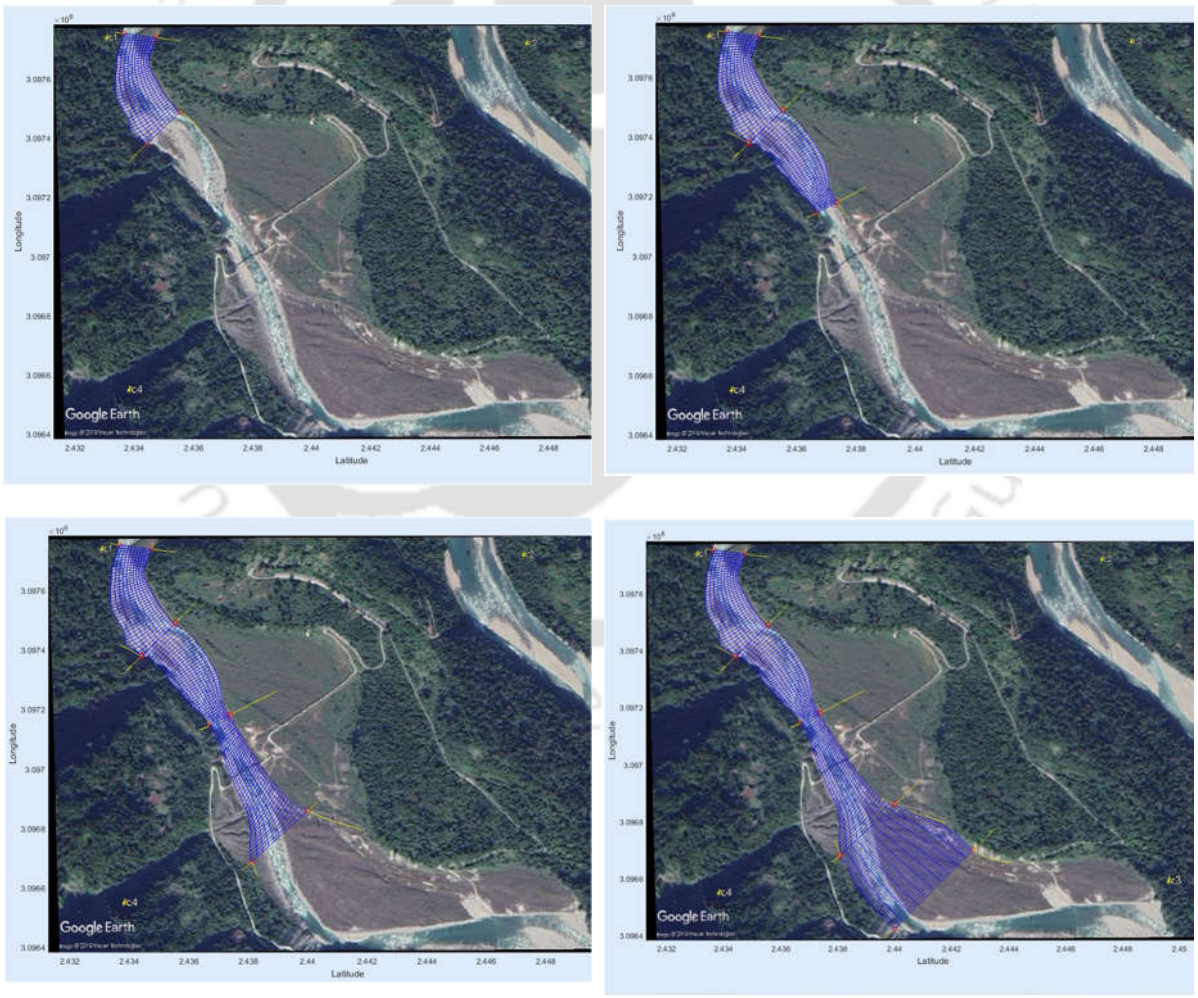

(b)

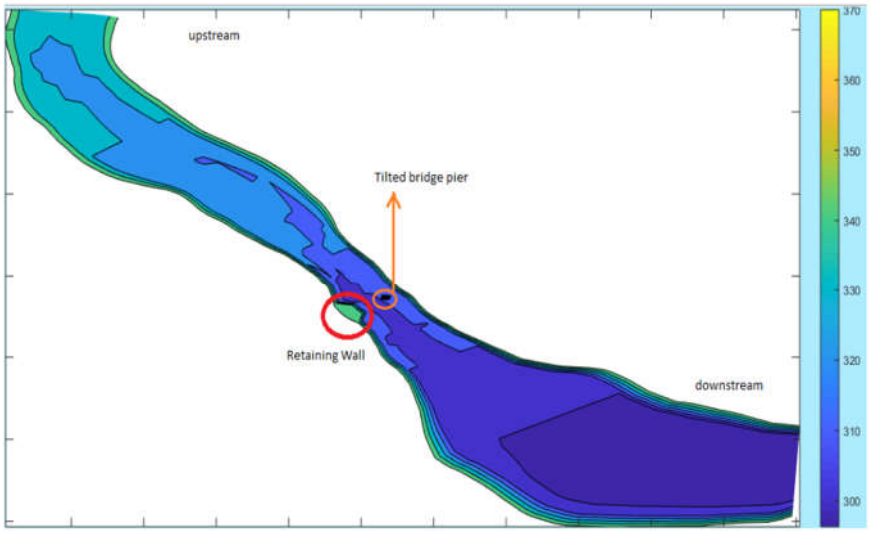

(c)

Figure-4.33-(a) Modeled portion of the study area (b) Grid generation in the study area (c) Bed profile in the domain

Scenario 1: Removing the tilted pier at the middle of the river

The flow velocity at some specific points was very high in the order of 7m/s to 10m/s.The model computed flow depth, and velocity profiles are presented in figure-4.34(a-b). The computed depth from the model developed are compared with the MIKE21C results at a cross-section downstream of the bridge and found to be in good agreement. The high velocities may affect the right bank near the bridge pier and hence must be protected. The direction of velocity vectors is towards the right bank downstream of the right pier and may affect the bank. As the near bank bridge pier behaves like a deflecting spar, a circulating flow at its immediate downstream is observed, causing deep scouring of this portion. Thus, a retaining wall and an apron are suggested at the bridge pier portion, as shown in figure-4.33(iii).

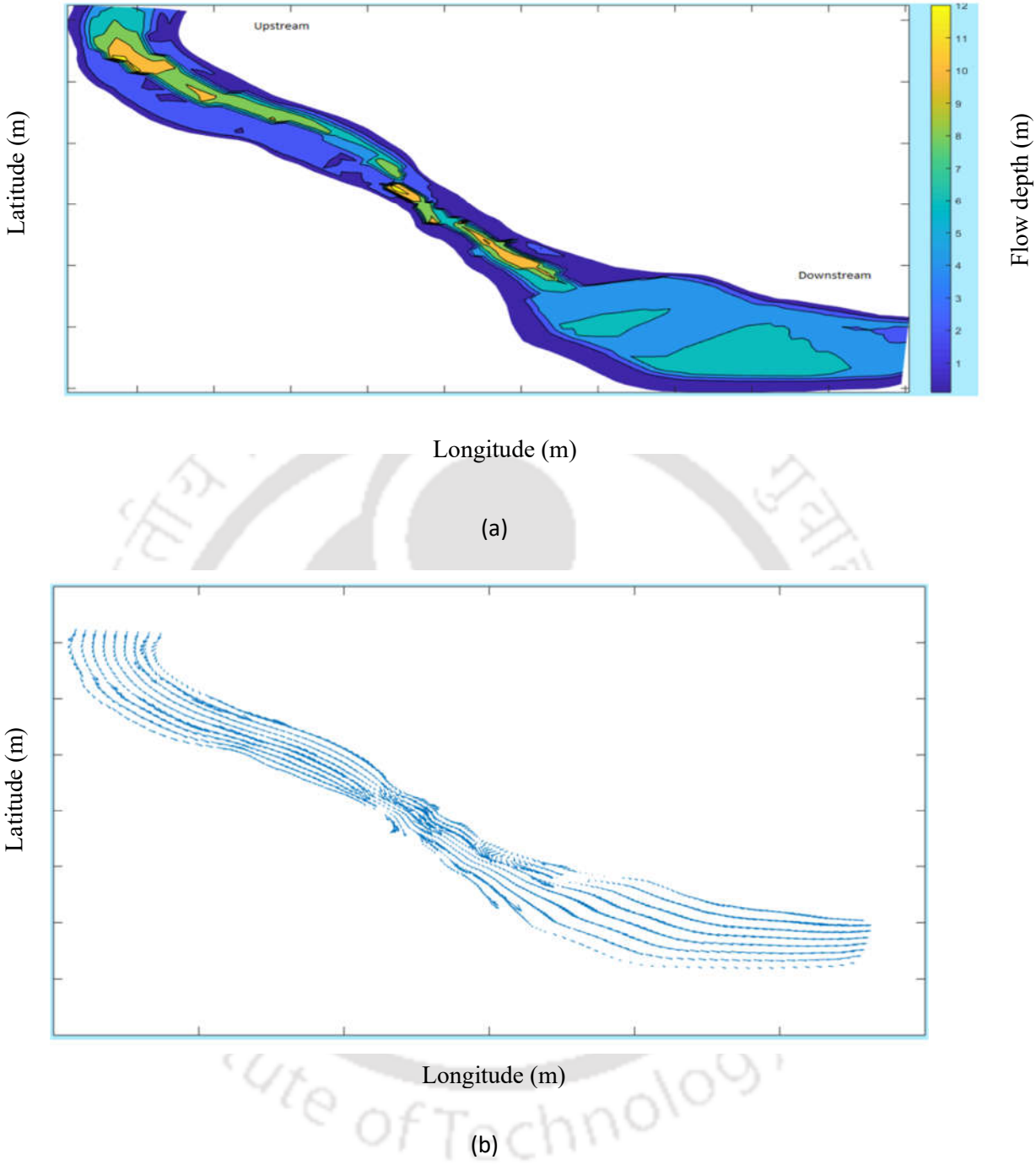

Figure 4.34: (a) Computed flow depth (b) Computed velocity vector

Scenario 2: Presence of the tilted pier at the middle of the river

In this simulation, the tilted pier with the retaining wall is considered in the middle of the river. The comparison of the computed flow depths from the present model and MIKE21C is presented in figure-4.35. Due to the pier, the velocity in the high flow period has not undergone

much change. However, there is a possibility that the high flow velocity observed in the model may further dislocate the pier to some other place, and this might cause an adverse flow scenario. Also, there will be some secondary flow in the bottom layer of flow towards the bank because of the obstruction. Thus, considering these possibilities, it is advisable to remove the tilted pier to have a free flow through the main channel to reduce flow concentration near the bank.

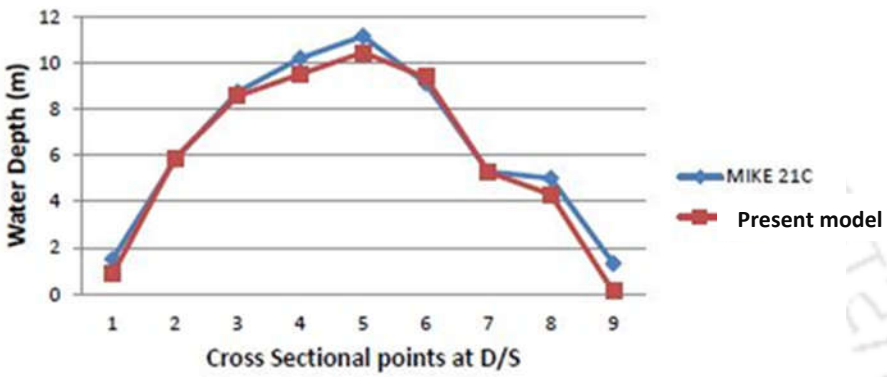

Figure 4.35: Comparison of flow depth from the present model and MIKE21C

From the simulation, it is clear that during high monsoonal flow, the flow velocity for a discharge in the order of 4000cumec becomes as high as 7.5m/s in most portions. Except for some portions at the nose of the near right bank pier, the velocity can reach up to 11m/s. The objective of the proposed river training work was to reduce flow velocity near the bank to prevent toe scouring. As the velocity near the bridge section, which is the narrowest, can be very high, the design of the apron needs to be done accordingly.

4.6 Conclusion

From this chapter following conclusions can be drawn

1. The performance of the numerical model is assessed by applying it to some classical hydraulic problems such as dam break flow, transcritical flow with and without shock, steady flow over a hump, and flood wave propagation downstream due to dam breach.

Evaluation of the model performance ensures that the present model behavior is robust and convenient to apply under diverse flow conditions with wavy topography. Model outputs are validated with the published results and found satisfactory.

2. Grids for the hydrodynamic simulations are generated by solving a set of elliptic partial differential equations(PDE). The grid generator is applied in two different curvilinear stretches of the Brahmaputra River.

3. Field surveys are carried out at different stretches of the Brahmaputra river to calibrate and validate the model. The model is applied in different stretches of the Brahmaputra River under different flow scenarios. The stability and the robustness is checked under the varying bed profiles, flow discharge, and different channel geometry

   (i) In the first case, the hydrodynamic model is applied in a braided stretch of the Brahmaputra River near the Umananda island.The model is run to steady-state, and the computed outputs are compared with the field measured data and the simulated results from MIKE21C. The model is applied in a 3.45 km stretch of the Brahmaputra River near the Majuli Island in the second case. The modeled reach consists of a series of spurs. The computed and measured flow depth and velocities are compared and found satisfactory (R^2). The NSE and RMSE are found as 0.605 and 0.119.

   (ii) In the third case, the influence of sidewall boundary conditions on the flow computations near the flow-structure interaction zone is carried out. Two different boundary conditions are used in the simulation. It is observed that the results obtained from the reflection boundary conditions are quite satisfactory than the no-slip condition.

(iii) In the fourth application, the dredging possibility near the Majuli island is explored from the model simulation. The Nimatighat region is highly susceptible to erosion, and the possible counteracting measures are investigated from the numerical model. In the first case, a pilot channel is excavated in the bathymetry data with three possible dredging widths (150m, 250m, 450m), and in the second case, a porcupine screen is installed upstream of the dredged channel. Results from simulations indicate that without the porcupine screens, the velocity at the upstream of the 450m dredged channel is 0.75-0.92 m/sec. However, with screens, the current speed reduces to 0.6-0.85m/sec.

(iv) Finally, the model is applied in the Tiding River to investigate the flow parameters near the bridge. A total of 145x11 grid points are used for numerical simulation. The computed outputs are also compared with the MIKE21C. It is observed that, during high monsoonal flow, the velocity is 7.5m/s, and at the nose of the right bank pier, the velocity can reach the order of 11m/s.

CHAPTER-5

A FULLY COUPLED TWO DIMENSIONAL FLOW ROUTING MODEL IN VEGETATED OPEN CHANNEL

5.1 Introduction

Aquatic vegetation influences the in-stream roughness, floodplain management and alters the magnitude and distribution of flow parameters. The vegetation attributed to roughness changes the hydrodynamic characteristics of the flow. In the stream, the vegetation may be widely scattered or remain close to each other. The random distribution of the vegetation contributes to different degrees of flow resistance and modifies the momentum fluxes within the vegetation area. The computational accuracy in the hydrodynamic simulations increases with the proper configuration of the vegetation within the models leading to the precise estimation of the modified roughness values. In this work, a new technique is developed to configure the vegetation within a hydrodynamic model. The modified n values from the vegetation are integrated into the hydrodynamic computations. The coupled model is calibrated and validated with the published experimental results. The calibrated model with hypothetical vegetation is applied into different flow scenarios to understand the vegetation influence on (i) specific energy in a converging mixed-flow channel, (ii) the secondary current strength near the outer bank in a U-type channel, and (iii) Riparian vegetation impact on the near bank velocity field downstream of a spur.

5.2 Determination of the roughness coefficient in the vegetation area

The methods developed by Arcment and Scheinder (Arcement and Schneider 1989) can be used to compute the total resistance for the flow-through rigid emergent vegetation. The

expression put forwarded by them to calculate the modified Manning's n_v is expressed in Equation (5.1)

$$n_v = n_0 * \text{sqrt}[(1+\frac{\gamma * C1)}{2*g*L}) * \frac{1}{{n_0}^2} * (R^{\frac{4}{3}})] \quad (5.1)$$

Where n_0=resistance in non-vegetated portion, γ= Vegetation density, L=reach length, R=hydraulic radius, and C1=effective drag coefficient.Effective drag coefficient proposed by Schneider

$$C1 = -10*R+22.5 \quad (5.2)$$

The vegetation density in the above expression is calculated from (Shields et al. 2017)

$$m = \frac{\sum Av_i}{A} \quad (5.2.1)$$

A is the cross-sectional area (m^2), and Av_i is the frontal area of the i^{th} vegetation element blocking the flow (m^2). From figure-5.1(a), if $h_v$is the height of the rigid emergent stem, D_i is the stem diameter, and h is the water depth, then Av_i is calculated as, Av_i =h*D_i

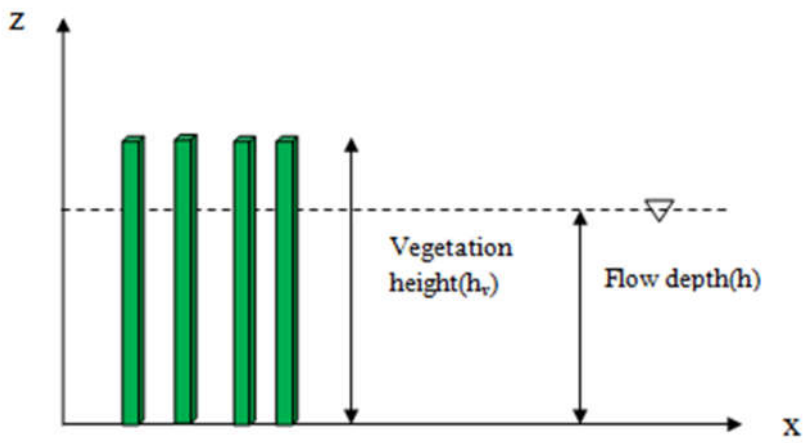

(a)

5.3 Coupling of rigid vegetation within the hydrodynamic model

The present study uses a fully coupled approach to integrate the vegetation parameters with the shallow water model. Before running the model, the flow domain is discretized into finite-

difference grid points both in the lateral and longitudinal directions. The simulation starts with these grid points by setting an initial value of the primitive variable (water depth,h) and a default Manning's n value. The ghost cells are defined laterally and longitudinally within the grid spacing, and the rigid stems are assigned at those cell points. The vegetation density is then calculated from the number of stems per unit of grid area and substituted in equation 5.1.

Let, X and Y are the coordinates of the grid points generated in the x and y direction, then the distance between them is calculated as

$$\Delta x = \text{squareroot}\{((X,Y+1)-(X,Y-1))^2+(X,Y+1)-(X,Y-1))^2)\} \quad (5.3)$$

$$\Delta y = \text{squareroot}\ \{((X+1,Y)-(X-1,Y))^2 +((X+1,Y)-(X-1,Y))^2)\} \quad (5.4)$$

The discretization procedure is illustrated in figure 5.1(b). In the figure, the computational points are represented by (i,j),(i-1,j), (i,j-1) and (i,j+1). The distance between the grid points (Δx, Δy) are calculated from equations 5.3 and 5.4. In the non-vegetated regions, the mass and momentum fluxes are calculated at these points. However, in the vegetated portions, ghost cells are created, and rigid vegetation are assigned. For instance, between grid point (i,j) and (i,j+1),some ghost cells (p,q), (p_1,q_1),….., (p_n,q_n)are created along the x-direction. A similar procedure is adopted along the y-direction. The vegetation density is expressed as the ratio between the areas covered by the vegetation to the total cross-sectional area. Different characteristics in the vegetated portions, such as the number of stems in x and y direction (V_x and V_y) and the area covered by the vegetation (A_v), are calculated as follows

$$V_x = \Delta x /x1,\ V_y = \Delta y/y1,\quad n_{tv}=V_x * V_y,\ \text{Vegetation density,}\ \ m= A_{vl}/A \quad (5.5)$$

The present coupling procedure is advantageous because it incorporates significantly finely distributed stems within the hydrodynamic calculations without affecting the model stability and computational efficiency.

The model solves the governing equations and computes the flow depth and velocity within the computational domain. The vegetation density obtained from equation (5.5) is substituted in equation (5.1) to calculate Manning's roughness values from the vegetation. The attributed 2D roughness from the distributed vegetation in the longitudinal and lateral directions are averaged and assigned at the vegetated regions. With these values, the hydrodynamic

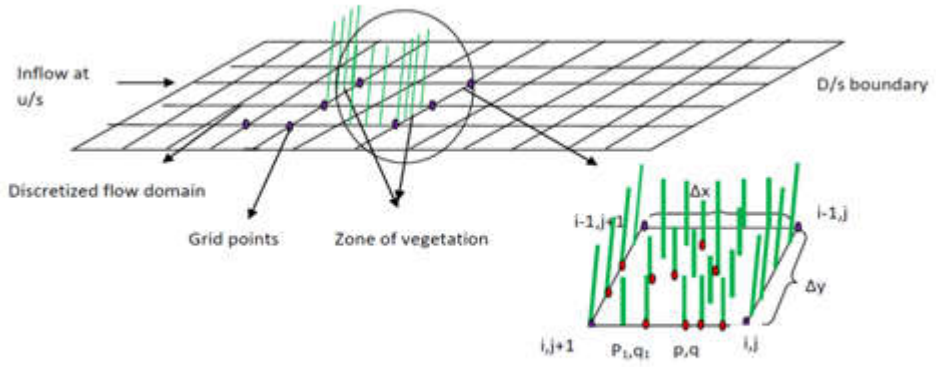

(b)

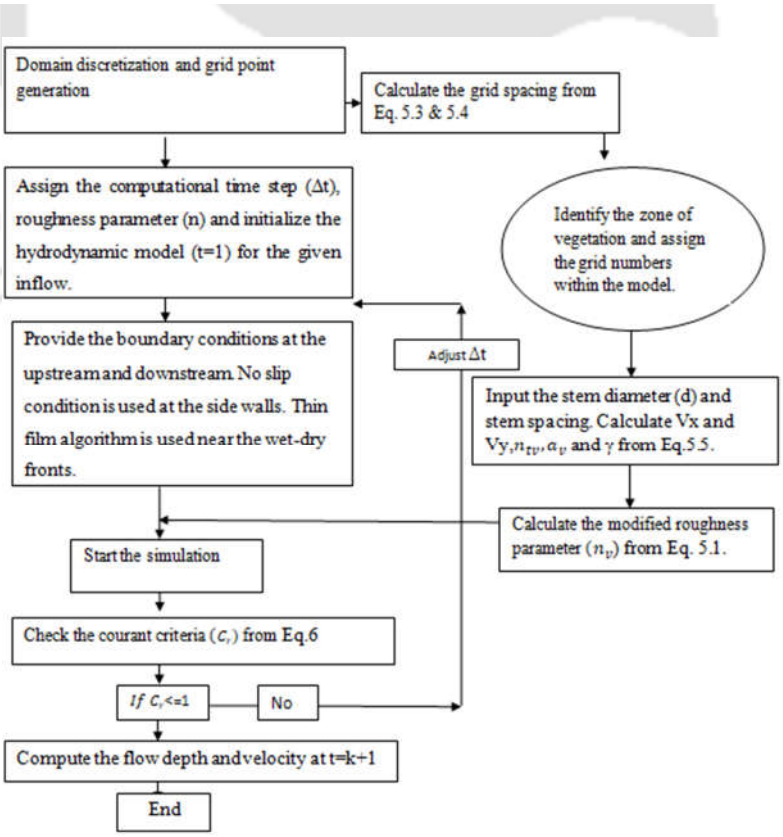

(c)

Figure 5.1 (a):Emergent vegetation height and flow depth (b) Schematic representation of the discretized domain with vegetation (c) Flow chart of the model

simulation starts and runs till the steady state. The model stability is checked from the Courant criteria. During each time step, the roughness value at the vegetation region is updated from the computed flow depth obtained at the next time level. Figure5.1 (c) shows the flow chart of the model.

5.4. Application of the model

5.4.1 Flow simulation in a rectangular channel with varying vegetation density

The performance of the present model is assessed by setting up the model with series of experimental test cases carried out by (Wang et al. 2018). They have performed the experiments in a closed-loop open surface recirculating rectangular channel at the Mechanism and process of gully erosion laboratory, Beijing Forest University, China. The channel dimension is 12.5x .3x.3 (m), and the bed slope is set to .001. The experimental section was 3 m downstream from the entrance to establish a fully developed flow regime. The length of the observation section was 7 m. Artificial plants made of polyvinyl chloride (PVC) pipes with an outer diameter d = 1 cm and height h_v = 10 cm were used to imitate rigid emergent vegetation. The Acoustic Doppler Velocimeter (ADV) and micrometer were adopted to observe the velocity and water depth in the longitudinal direction. The vegetation patches are arranged in staggered patterns within the numerical model to form regular triangles to match with the experimental setup.The experiments are performed with three different vegetation densities Sparse (1%), Middle (2%), and Dense (4%). The vegetated and non-vegetated testing areas were alternatively mounted in 1 m intervals, and with 1 m vegetated sections, the arrangements were oriented along the summit, backslope, and footslope as shown in Figure 5.2: Sparse-Middle-Dense (SMD); Sparse-Dense-Middle (SDM); Dense-Sparse-Middle (DSM) and Middle-Dense-Sparse (MDS).

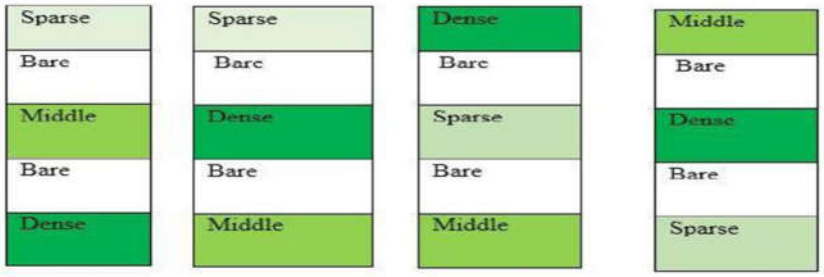

Figure 5.2: Vegetation arrangement in the experimental channel

The entire computational domain is discretized into 30x57 finite-difference grid points. In the vegetated regions, the rigid stems are assigned at the ghost cells at a spacing of .05m,.1m, and .11m in the longitudinal direction and .06m in the lateral direction. With these points, the simulation starts by assigning the flow rates at the upstream boundary. Table-5.1 shows the flow rates at different vegetation arrangements.

Table-5.1: Discharge data at different vegetation pattern for the rectangular channel

Type of vegetation	Stem diameter	Vegetation Pattern	Discharge(L/sec)						
Rigid, emergent	10mm	Non-vegetated	1.12	1.75	2.07	2.60	3.12	3.52	3.98
		SMD	1.05	1.65	2.00	2.43	2.95	3.4	3.82
		SDM	.73	1.42	1.78	2.30	2.78	3.22	3.65
		MDS	.90	1.56	1.80	2.30	2.85	3.30	3.70
		DSM	.55	1.3	1.85	2.15	2.65	3.15	3.80

The time step for each simulation is considered as 0.1 seconds which gives a courant number of 0.90. The updated n values from different vegetation arrangements are calculated and substituted in the hydrodynamic model. The computed and experimental velocity profiles are presented in figure-5.3 (a-f). Results indicate a good correlation between the measured and the predicted values. Without the vegetation, the maximum velocity in the channel is found as 0.55

m/sec, and with different arrangements of vegetation, it reduces to 0.1-0.27m/sec. Figure-5.3(g) shows Manning's n values and found that in non-vegetated regions, it ranges from .05—0.1. However, with the vegetation, it increases maximum up to 0.35.

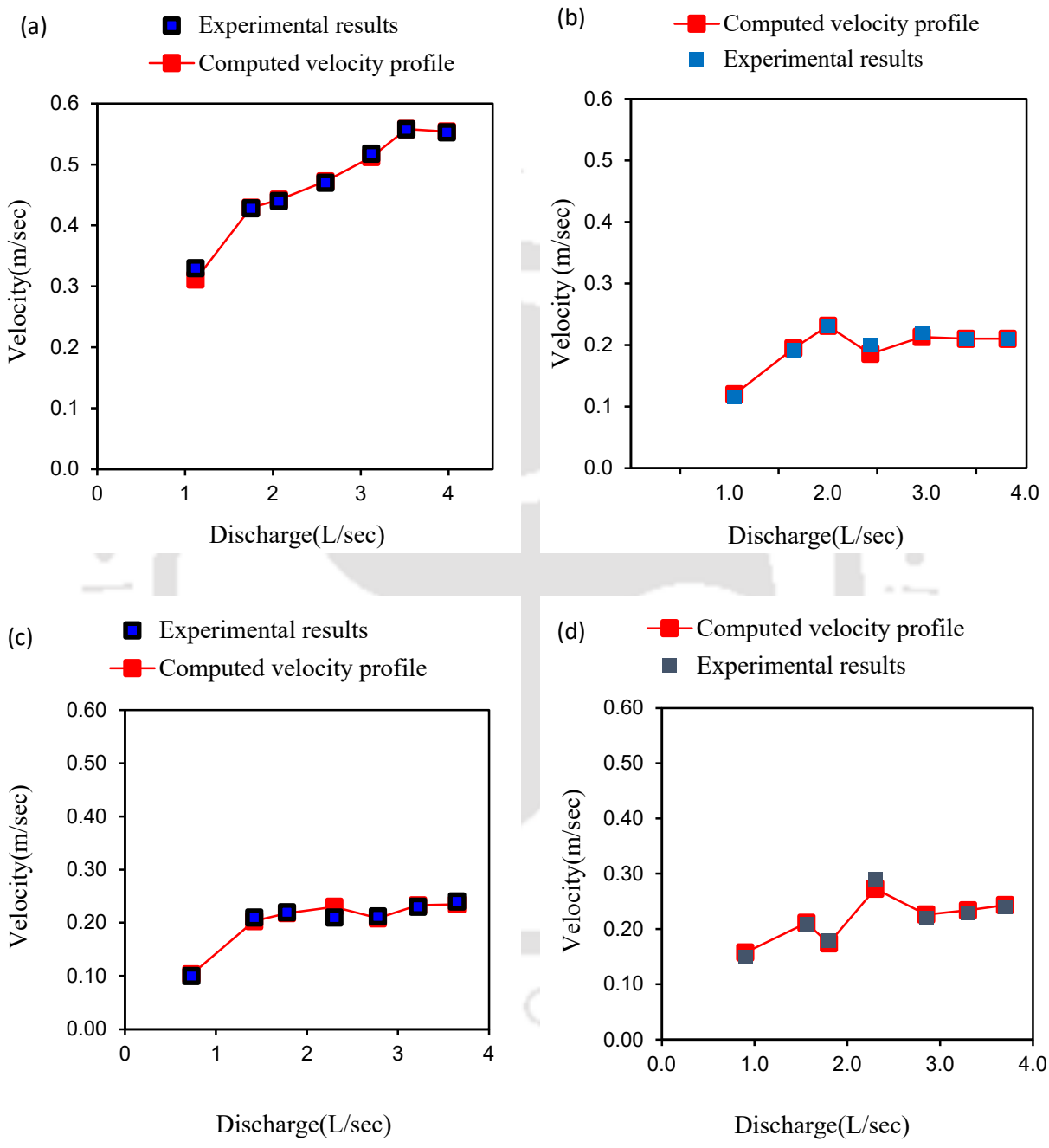

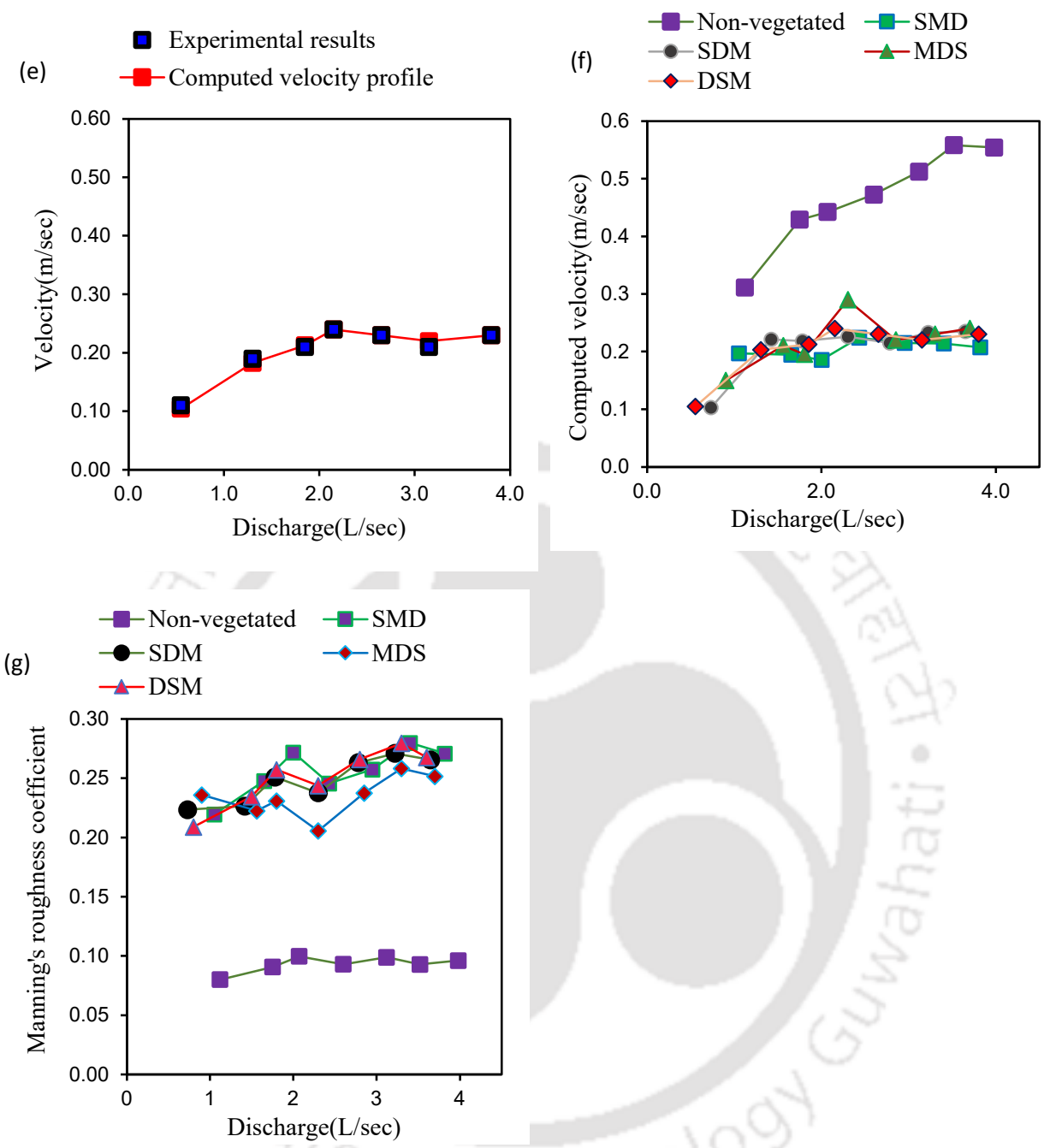

Figure 5.3: Comparison of computed and experimental velocity under different vegetation density (a) Bare (b) SMD (c) SDM (d) MDS (v)DSM (e) Computed velocity profiles with all combinations f) Manning's n Values at different vegetation arrangement

5.4.2 Impact of vegetation on the flow state in the transcritical condition

The mixed flow regimes indicate the presence of both subcritical and supercritical states in a natural channel. The supercritical flow is highly unstable and observed in mountainous terrains having a steep slope with high velocity. In the supercritical state, the waves move with very high velocity and cause erosion in the bed and sides of the channel. However, in the valley portion, the slope becomes gentle, the flow behaves as subcritical, and reaches a stable state. By adopting the vegetation cover at different locations, the flow state can be altered, and near the vulnerable reaches, the flow may convert to a much stable condition. This simulation is performed with two hypothetical vegetation densities to investigate its impact on the mixed flow.

A natural flow passing through a contracted section develops a supercritical state, and for the above reasons, it is highly undesirable in the channel. The mixed flow condition in contracting natural channels is idealized by adopting the experimental study reported by (Klonidis and Soulis 2001). The test channel was composed of two straight sections connected by a 1.49 m long straight-walled contraction with a width of 0.629 m and 0.314 m at the inlet and outlet. The upstream discharge and the downstream water level are presented in table-5.2.

Table-5.2: Channel dimension and flow rate for converging channel

Channel width (m)	Discharge (m^3/sec)	Downstream water level(m)	Type of vegetation	Stem diameter	Vegetation density (stems/m^2)
At u/s = 0.629 At d/s = 0.314	0.046	0.1132	Rigid Emergent	10mm	1) 27 2) 324

The computational domain is discretized into 21×37 grid points (figure-5.4(a)). The model is run with the vegetated and non-vegetated conditions. With vegetation, two different stem

densities are included in the model. In the first case, density is maintained as 27 stems/m^2, and in the second case, it is increased to 324 stems/m^2. Figure-5.4(b) shows the location of the vegetation in the channel. The flow is subcritical upstream of the contraction and slightly supercritical (F_r~ 1.02) near the downstream boundary. Manning's n value is taken as 0.012. The time step is chosen as 0.015 seconds, which gives a courant number of 0.78. The velocity contour map is shown in figure 5.4(c). It indicates the maximum velocity in the channel lies between 0.09-1 m/sec.

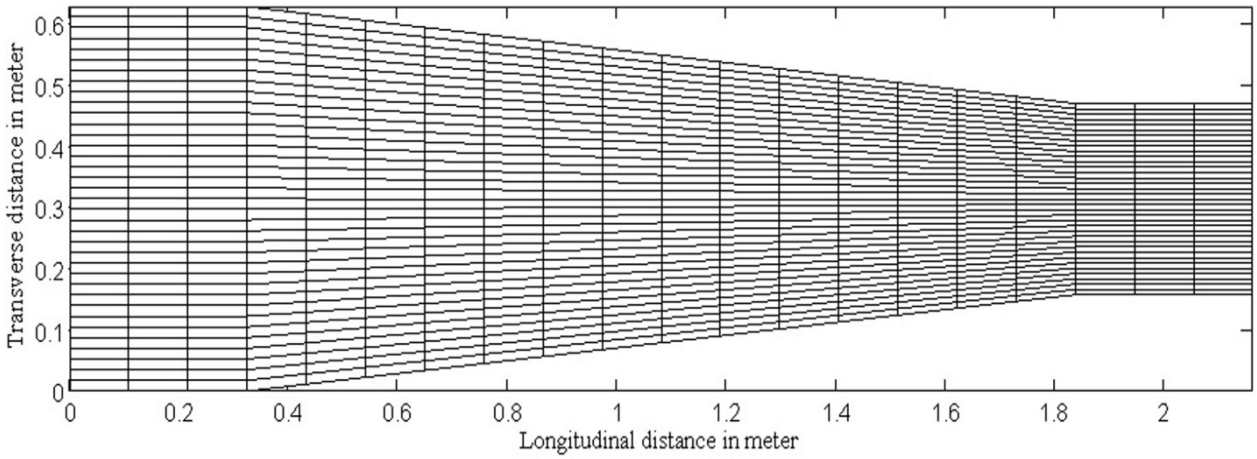

(a)

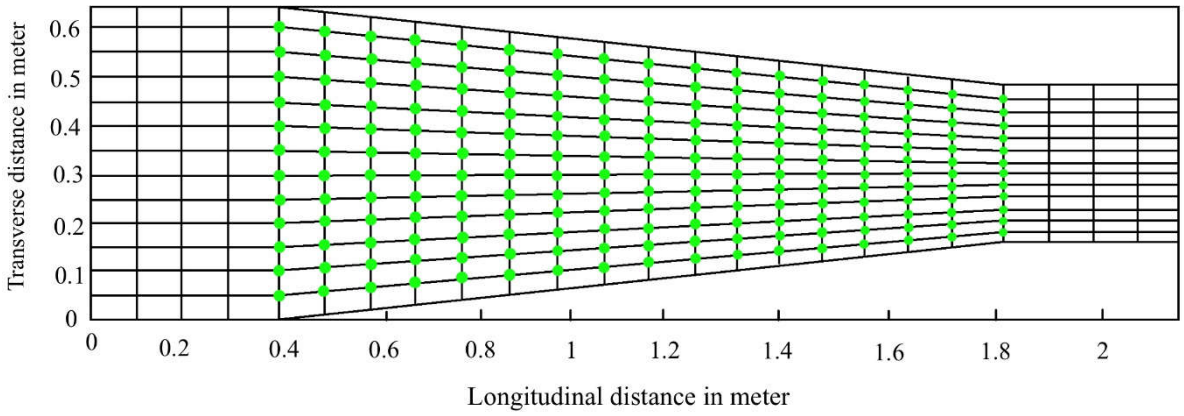

(b)

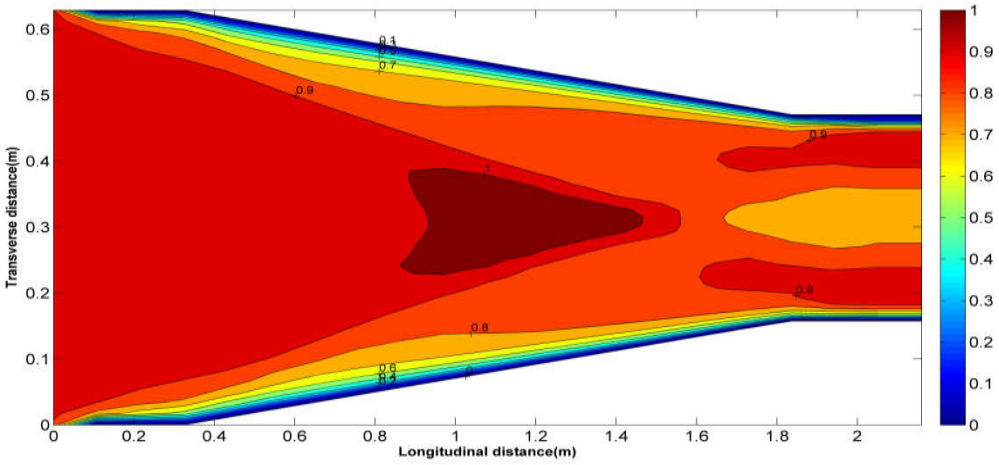

(c)

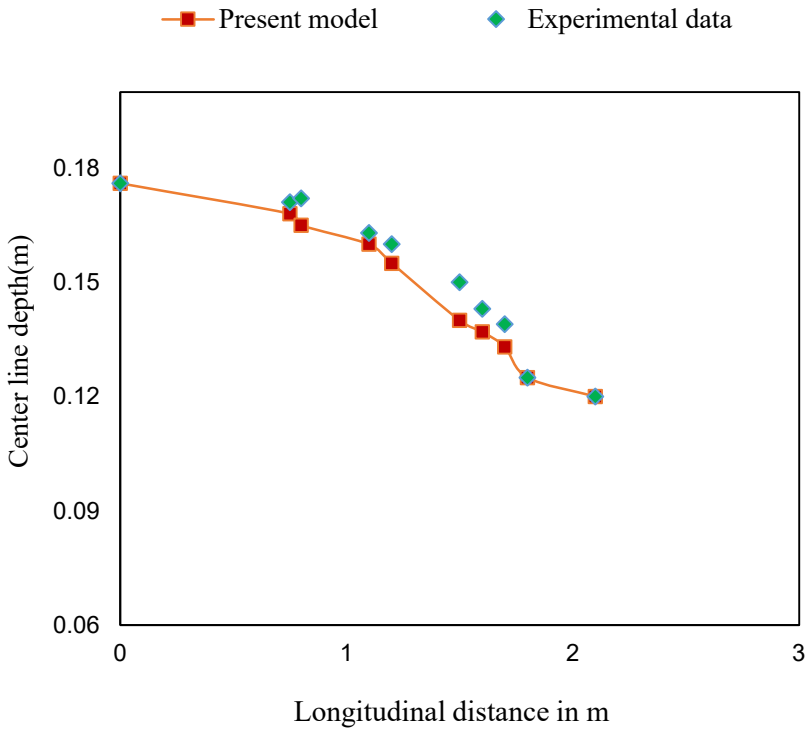

(d)

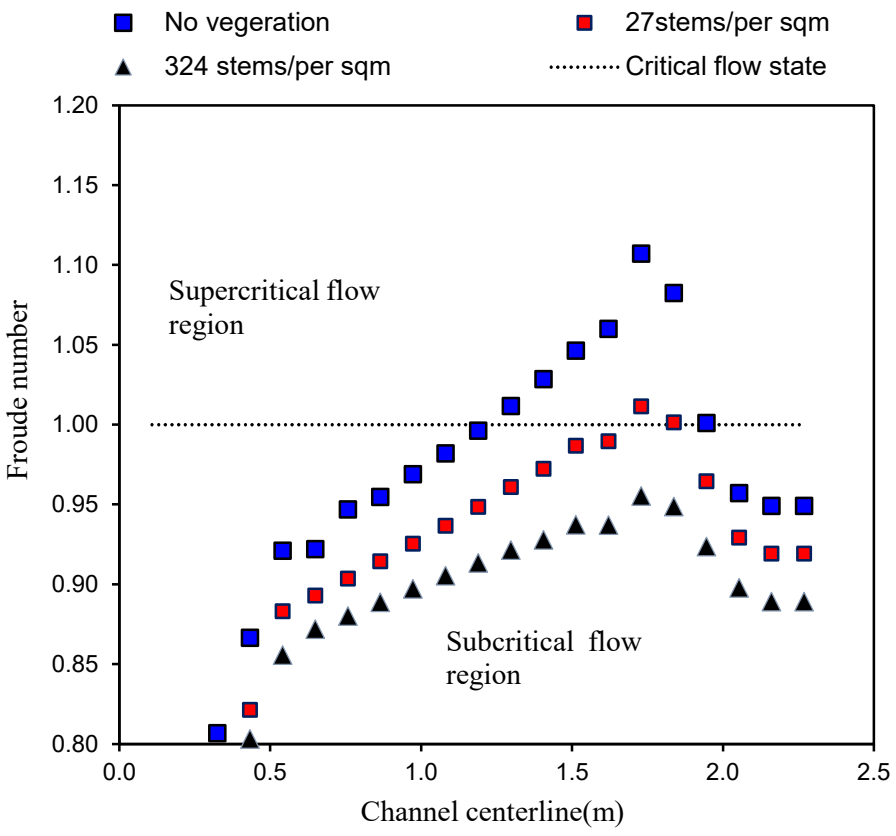

(e)

Figure 5.4: (a) Grids in the converging channel b) Distribution of vegetation in the channel (c) Velocity contour map (d) Comparison of the computed and experimental result(e) Flow state at different vegetation density

The computed and measured flow depths are presented in Figure 5.4(d). Results indicate a good agreement between the computed and the experimental result. Figure 5.4(e) shows the variation of the Froude number along the channel centerline. Both the subcritical and supercritical flow are found in the channel without vegetation. The vegetation densities are substituted in equation 5.1 to calculate Manning's n values. The n value substantially increases at high vegetation density due to which velocity profile is modified, and the entire flow behaves as a subcritical flow. These alterations within the domain result in almost a stable condition compared to the mixed flow scenario.

5.4.3 Impact of vegetation on the centrifugally induced secondary current near the outer bank of a U-type channel

In this case, the coupled model is applied to investigate the vegetation influence on the secondary current strength near the outer bank in a bent channel. The secondary current is a characteristic feature of flow in open channel bends. The centrifugal acceleration forces the higher velocity current towards the outer curve and comparatively low-velocity current towards the inner bank. This anomaly in the flow structure is responsible for the high rate of erosion near the bends. The secondary current strength near the outer bank is estimated from (Vaghefi et al. 2015). The secondary current strength as the ratio between the lateral and streamwise kinetic energy and derived the following expression for a bent channel,

$$S_{xy}=\frac{K_{lateral}}{K_{main}}, K_{lateral}=\frac{{V_y}^2}{2g}, K_{main}=\frac{V^2}{2g}, V=\sqrt{{v_x}^2+{v_y}^2} \qquad (5.6\text{-a,b,c,d})$$

where, S_{xy}=secondary current strength, $K_{lateral}$ = lateral flow kinetic energy and K_{main}= Main flow kinetic energy, V= main flow velocity, V_y= Lateral flow velocity, V_x=Streamflow velocity

The experimental study conducted by (Rozovski 1957) is considered here for model application. The test channel is a 180^0curve connected by two straight channels of length 0.5 m each. The channel width is 0.8 m with an internal radius of 0.4 m. The Manning's n value is taken as 0.01 in the simulation as the channel is smooth. The flow rates and the channel dimensions are provided in table-5.3.

Table-5.3: -Channel dimension and flow rate for the U-type channel

Channel dimensions(m)	Discharge (m^3/sec)	Downstream water level(m)	Type of vegetation	Stem diameter	Vegetation density (stems/m^2)
Channel width=0.8 Internal radius=0.4	Q=0.0123	0.0561	Rigid emergent	10mm	1. 61 2. 92

For numerical simulation, the entire flow domain is discretized into a 21x57 number of grid points (figure 5.5(a)). With these grid points, the simulation starts with an upstream discharge of 0.0123m^3/sec. The time step is considered as 0.01 seconds, and the courant number is found 0.82. The model runs with three different conditions. Initially, no vegetation are incorporated in the channel. The location of the vegetation is presented in figure-5.5(b). Under no vegetated conditions, the velocity near the outer banks is observed within the range of 0.35-0.4 m/sec. The model outputs are validated with the experimental results reported by (Molls and Chaudhry 1995). The outer and inner bank computed and measured flow depth is compared against the experimental results. Figure 5.5(c-d) presented the flow depth and velocity profile in the test section. The computed velocity vectors are shown in figure 5.5(e). Results indicate a good agreement between the predicted and the measured result.

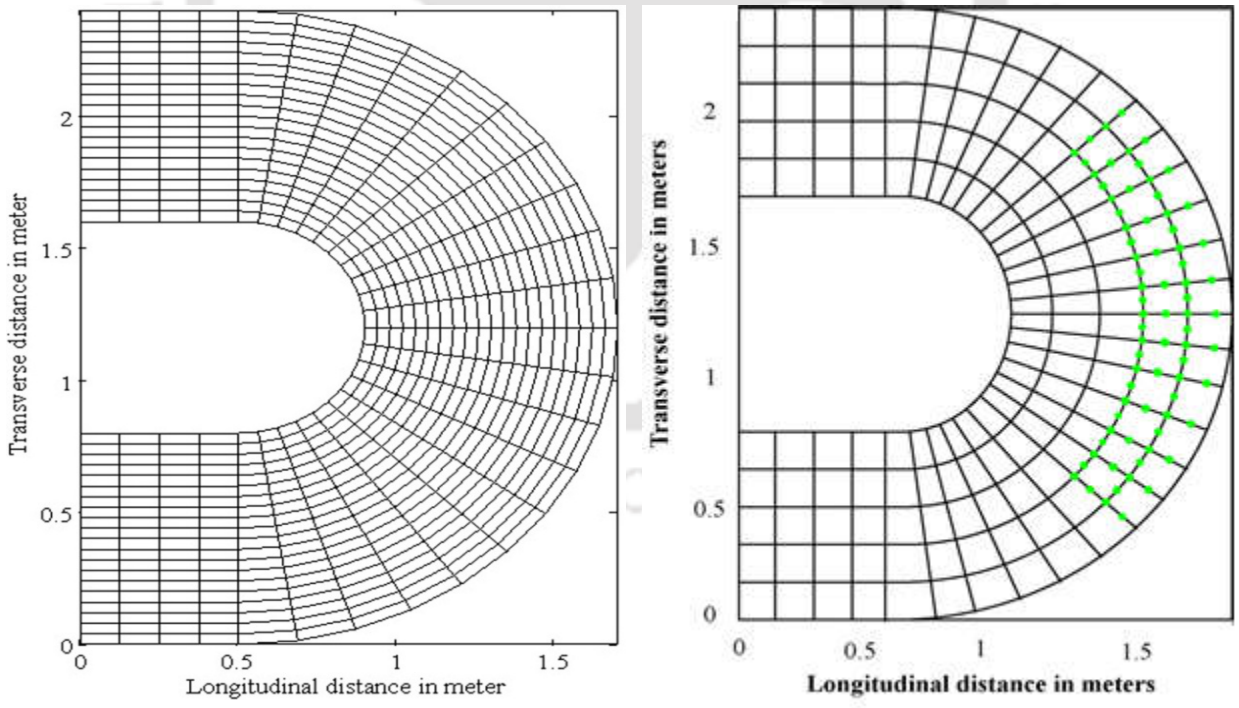

(a) (b)

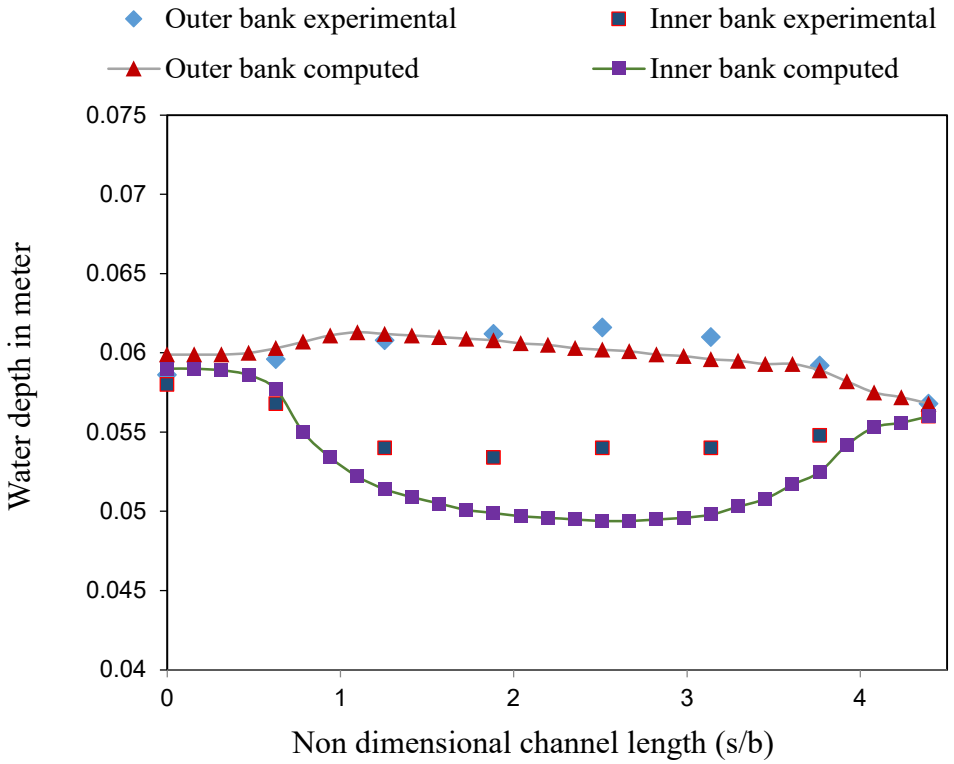

(c)

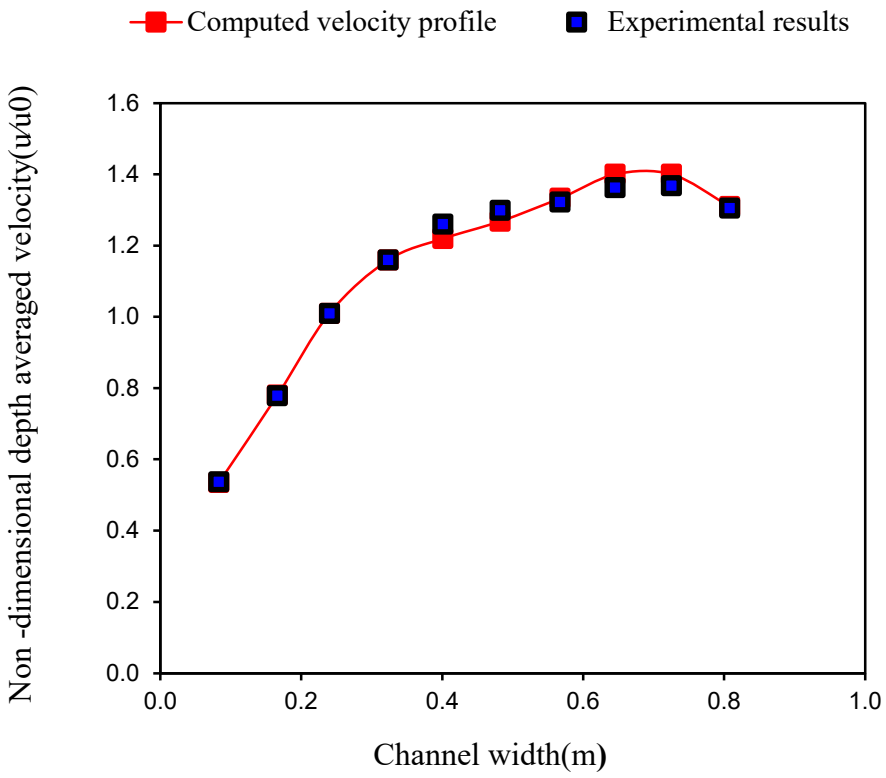

(d)

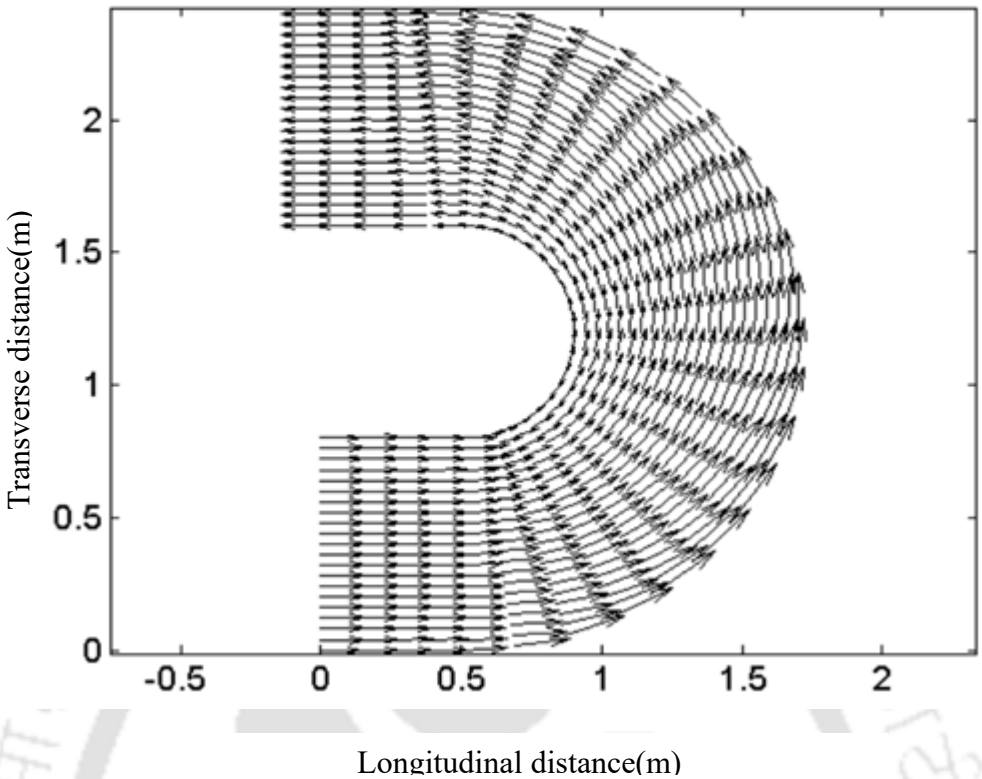

(e)

In the second and third simulations, rigid stems are assigned to the model. The vegetation density is maintained at 61stems/m^2 and 92 stems/m^2, respectively. The velocity contour maps with and without the vegetation are presented in figure 5.5(f-h). The results indicate that with higher vegetation density, velocity near the outer bank drops to 0.27-0.32 m/sec. From equation 5.6 (a-d), the centrifugally induced non-dimensional secondary current strength is expressed as the ratio between the main flow kinetic energy to the lateral flow kinetic energy. The hydrodynamic model employed during the study solves the momentum equations in the longitudinal and lateral directions, and the velocity components are calculated at each computational cell. The main channel flow velocity is obtained by taking the resultant of streamwise (u) and lateral (v) components. Under the non-vegetated condition, the simulated outputs indicate that the maximum velocity occurs at the bend apex and thus the secondary current strength. However, incorporating the vegetation with different densities in the numerical model, the roughness value increases. With this modified roughness, the momentum

fluxes in the longitudinal and lateral directions are reduced. This reduction in momentum flux lowers the velocity near the bend, and finally, the magnitude of secondary current strength decreases, as shown in figure-5(i).

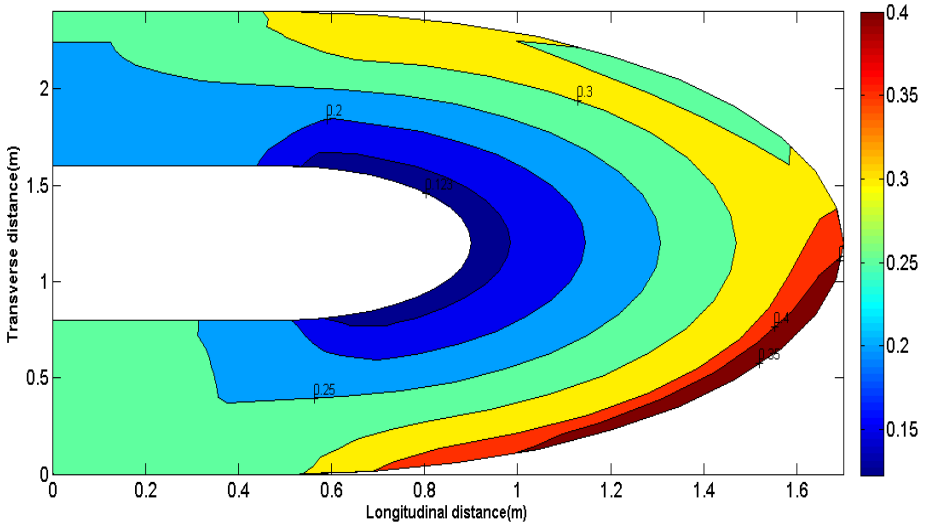

(f)

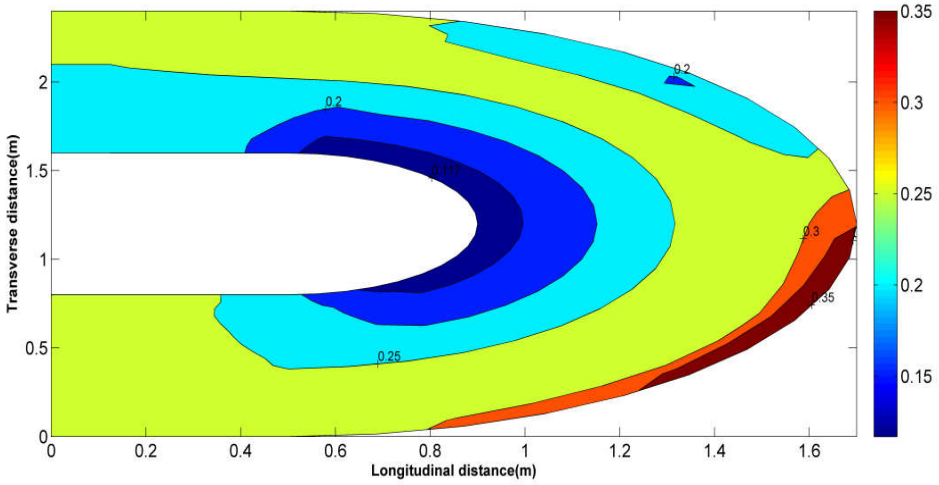

(g)

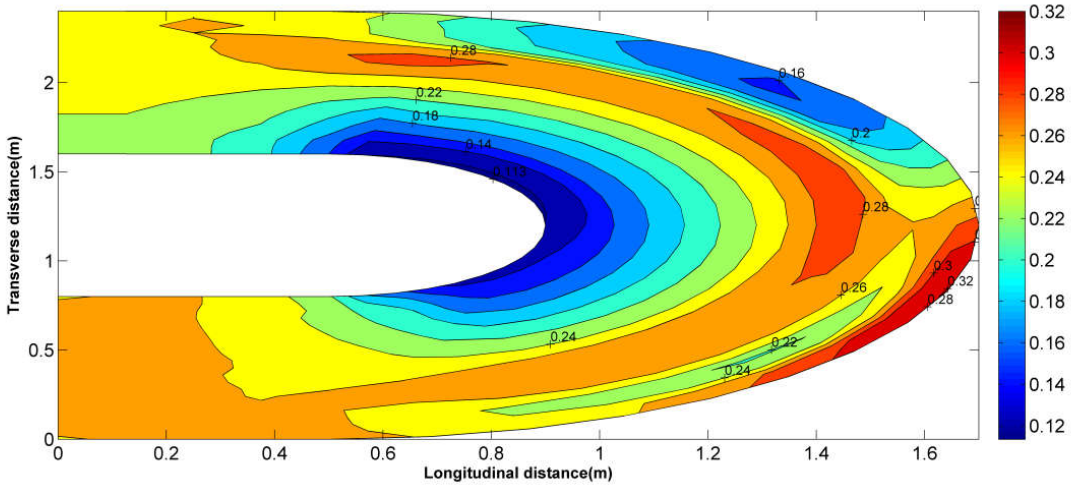

(h)

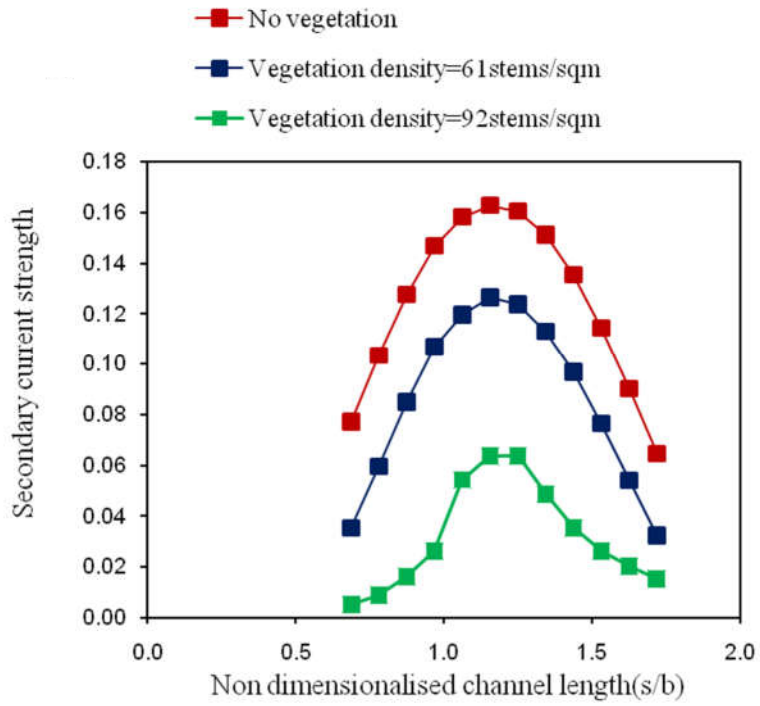

(i)

Figure 5.5: (a) Generated grids in the computational domain(b)Location of vegetation near the outer bank (c)Comparison of computed and measured water depth(d) Comparison of computed and measured velocity at the outlet (e) Computed velocity vectors in the flow domain (f) Velocity contour map with no vegetation near the outer bank (g) Velocity contour map with vegetation density 61stems/m^2 near the outer bank (h) Velocity contour maps with vegetation density 92 stems/m^2near the outer bank (i) Comparison of Secondary circulation strength at different scenarios

5.5.4 Riparian vegetation influence on the velocity profile near recirculation zone

Riparian vegetation improves the riverbank stability by increasing the soil shear strength and armoring the bank. Vegetation along the toe of a streambank deflect the flow away from banks, reduce the velocity, and altering the forces applied to the bank surface.

In this case, the coupled model is applied to investigate the vegetation influence on the near bank velocity profiles. The details of the study area and field survey are elaborated in section 4.4.2. The modeled area consists of a series of deflecting spurs. Spur dikes or groynes are often used as hydraulic structures for bank protection and river training works. These walls aligned with the flow direction constrict the river width causing the flow separation and the recirculation of downstream streamlines. The details of the channel geometry, flow characteristic, and stem properties are given in Table-5.4. The discretized domain is already presented in figure 4r (b). The time step for each simulation is taken as 0.1 seconds, which gives a courant number of 0.73.

Table-5.4: Geometric, vegetation, and flow characteristics of the study reach in the Brahmaputra River near the Majuli Island

Reach Dimensions (km)	Discharge (m^3/sec)	Downstream Water Level(m)	Type of Vegetation	Stem Diameter	Vegetation Density (stems/m^2)
Length=3.25 Channel width at u/s= 1.35 Channel width at downstream=1.08	9847	84.14m	Rigid emergent	20mm	231

The dry areas within the flow domain are excluded from the computation by assigning a threshold depth value (≈0.01m). The solid non-submerged groins are simulated by using the reflection boundary condition. Manning's roughness coefficient is calculated from Stickler's

equation. Based on the d_{50} value, Manning's n is found out to be 0.033. Flow depth and the two-dimensional velocity components (u, v) are evaluated from the model. The computed flow depth contours are presented in figure 4u(i). The maximum depth in the region is found within the range of 30-35m. The model validation is already explained in the previous chapter.

The arrangement of the rigid stems at cross section-57, located downstream of the spur S3, is shown in figure5.6 (a). The vegetation are assigned at the toe of the bank. The model captures the recirculation vortex downstream of the spur S3 and in the vicinity of the banks. The formation of the return flow region is presented in figure 4.23(d). The inclusion of near bank vegetation in the model increases Manning's n values and modifies the velocity profiles. The computed velocity profiles with and without the vegetation are shown in figure 5.6(b). It is found that without the vegetation, the maximum velocity is within the range of .22-.35m/sec. However, with the near bank vegetation, it reduces up to 0.15-0.27m/sec.

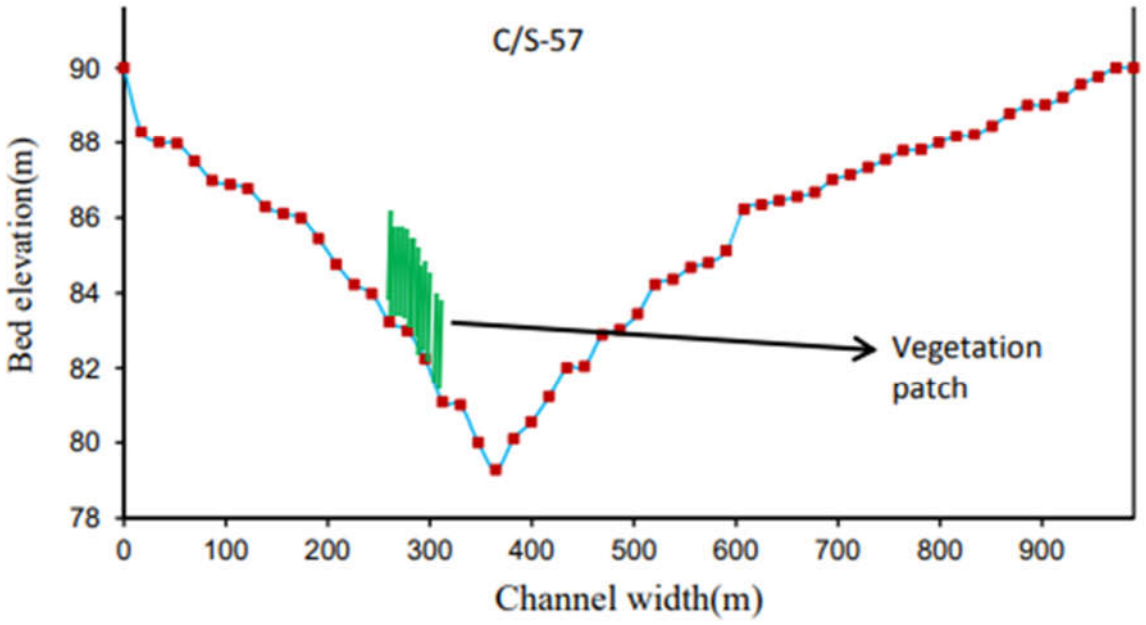

(a)

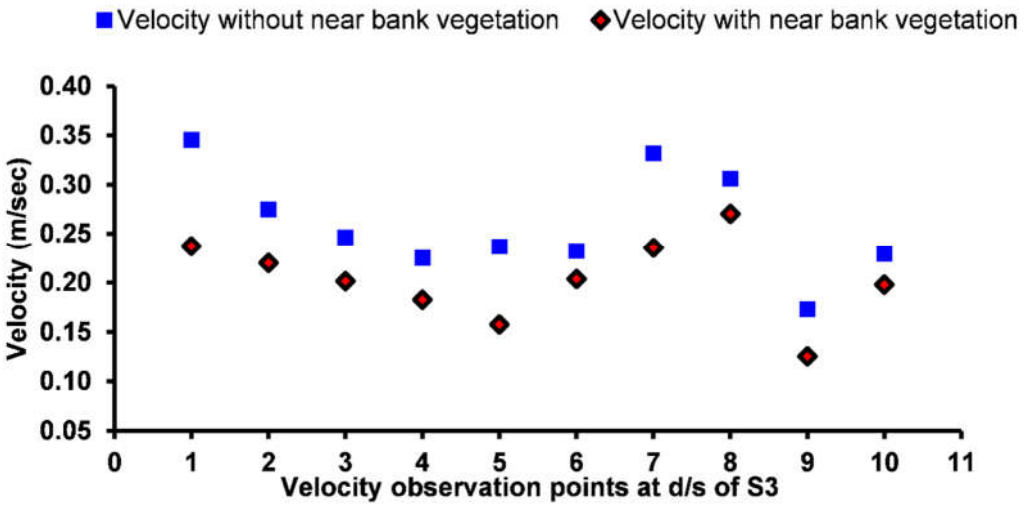

(b)

Figure 5.6(a): Vegetation configuration at the toe of the bank (b) Velocity profile near the recirculation zone with and without vegetation

The model performance is evaluated using two statistical measurements, Root mean square error (RMSE) and Nash-Sutcliffe efficiency (NSE)

$$\text{RMSE}=\sqrt{\frac{1}{n}\sum_{i=1}^{n}(f_i - y_i)^2} \tag{5.7}$$

$$\text{NSE}=1-\frac{\frac{1}{n}\sum_{i=1}^{n}(f_i-y_i)^2}{\frac{1}{n}\sum_{i=1}^{n}(y_i-\bar{y})^2} \tag{5.8}$$

Where, y_i is the observed data and f_i is the model predicted data and $\bar{y}$is the average value in the observed dataset.Table-5.5 shows the RMSE(≈0.13) and NSE(≈0.82) values of the model. NSE ranges 0 and 1 indicates an acceptable level of performance. However, lower RMSE suggests a good fit of the predicted values with the observed data.

5.6 Conclusion

This work proposes a fully coupled two-dimensional shallow water model with rigid emergent vegetation. The rigid stems are assigned at the subgrids, and the modified n values are integrated into the hydrodynamic equations. The model predicted outputs are calibrated and validated with the published experimental results and found satisfactory. The model application is further extended to three different cases. In the first case, it is observed that the entire mixed flow regimes in a converging channel are changed to subcritical flow at high vegetation density. In the second case, the vegetation influence on the centrifugally induces secondary current strength is estimated from the model. The computed streamwise and lateral velocities from the model are used in the secondary current strength calculation. Results indicate that dense vegetation effectively reduces the secondary current near the outer bend. The different combinations of vegetation arrangements are applied in the model to select the best possible combination to counteract the secondary current and address the erosion possibilities near the outer bank in a bent channel. Finally, the model is applied in the Brahmaputra river reach with a series of spurs. The impact of riparian vegetation on the near bank velocity profile is assessed from the model. The rigid stems are incorporated near the foot slope, downstream of the spur S3. The results show that with the vegetation, the velocity profile near the recirculation zone is reduced. The present model can be further improved by incorporating the turbulence terms in the hydrodynamic model for estimating the secondary current and vortex strength.

CHAPTER-6

A quasi three dimensional hydrodynamic model for vertical velocity distribution in open channel flow with and without vegetation

6.1 Introduction

Velocity distribution at river cross-sections is very much fundamental to hydraulic engineering. Magnitude and distribution of the velocity components in open channels are extremely affected by the degree of complexity in bed topography, bed roughness parameters, flow obstructions and diversion structures, channel geometry, and turbulence in the flow. The one (1D), two-dimensional (2D) are widely accepted numerical techniques to predict the velocity components by depth averaging the momentum fluxes from the governing shallow water equations. With the fast developments in two-dimensional modeling, 1D models have become obsolete in velocity computations. The 2D models predict the streamwise and transverse velocity components in the longitudinal and lateral direction in an open channel. However, the 2D models do not provide any velocity information in the vertical direction because of their depth-averaged forms. The three-dimensional models have the advantage of computing the streamwise, transverse, and vertical velocity profiles in open channels. Still, the degree of accuracy, computational cost, model stability, complexity in solution, and mesh flexibility during its application in wide and complex topographic rivers is under investigation (Vincenzo and S. 1998). However, for instance, the vertical velocity profiles in open channels are substantially modified under the influence of aquatic vegetation at different degrees of stem density and vegetation characteristics, especially with submerged types. In that regard, the integration of vegetation dynamics into the 3D models and the solution of the equations becomes more complicated while applied in the natural terrain.

Acoustic doppler techniques such as Acoustic Doppler current profiler (ADCP), Acoustic Doppler velocimeter (ADV), and current meter methods are often employed in the field estimation of the vertical profiles. Difficulties in sampling during high floods considerably reduce their application in the discharge measurements. Similarly, analytical methods estimate the depthwise distribution of velocity from the river bed up to the free surface by dividing the flow region into layers. Near the river bed at the viscous sub-layer, the linear velocity distribution, above the sub-layer in the mid-portion of the vertical, the Prandtl-von Karman logarithmic law and near the water surface a power-law profile is used to express the vertical velocity profile in a cross-section. Song and Yang(1979) revealed that implementing the boundary conditions between the flow layers and the requirement of several parameters for a single water column are significant drawbacks for applying analytical models in a natural stream.

This chapter proposes a quasi-three-dimensional framework to compute the vertical velocity profile by integrating the developed two-dimensional hydrodynamic model with Shanon's entropy. The main advantages of quasi 3D approaches are the simplicity in applications, less computational cost, and the ability to capture the vegetation dynamics in open channels. The entropy theory is a probabilistic approach of vertical velocity distribution model relating the maximum and depth-averaged velocity in a channel cross-section through a dimensionless entropy parameter M. The computed 2D hydrodynamic outputs (h, u, v) are integrated with the entropy equation to distribute the velocity profiles from the bed to the free surface. The entropy models are quite superior to the mixing length models because of the leverage of getting a non-infinite value of near-bed energy gradients. Primarily, the attractive features of the entropy theory while coupling with two-dimensional shallow water models are the requirement of fewer input

parameters in velocity distribution and the potential of capturing the vertical profile anomaly such as the dip phenomenon in the natural channel.

The developed framework is applied in two different cases. In the first case, the model is applied in the Brahmaputra River near Majuli Island. In the second case, the proposed approach is used to compute the vertical velocity profile in a vegetated channel with submerged flexible vegetation. The 2D hydrodynamic model is integrated with the vegetation drag force and applied in a series of experimental case studies having different vegetation parameters such as stem density, plant diameter, degree of submergence, etc. The configuration of the flexible stems under different streamflow is evaluated from the large deflection cantilever beam theory. The main advantage of applying the beam theory is that it can effectively capture higher degrees of stem flexibility under different flow events. The computed hydraulic parameters from the shallow water model are used in Shannon's entropy theory and Reynolds's stress equation to calculate the vertical velocity in the free water layer and the vegetation region. The computed outputs are compared with the published experimental results.

6.2 Vegetation Model

6.2.1 Deflection of the flexible vegetation

The variation in the upstream water levels at different flow events influences the curve length of the flexible stems. Under high flow events, the load on the stem increases leading to a higher degree of reconfiguration and vice versa. The projected deflection height of the flexible stem is estimated from the larger deflection cantilever beam approach by assuming that vegetation gravity and buoyant force due to water is negligible (Whittaker et al. 2015). In figure 6.1,z coordinates represent the distance from the bed to the top of the vegetation; L is flexible vegetation height

before bending and h_v is the projected deflection height. The representative vertical velocity profile in an open channel with submerged flexible vegetation is shown in figure-6.2.

Imposed average load P, on flexible stems due to the upstream water head is expressed as (Huai et al. 2013)

$$P = \frac{\rho g s_f h}{m} \tag{6.1}$$

Where m is the vegetation density per unit area, s_f is the energy slope, ρ is the density of water (KN/m^3) , h is the total flow depth (m), θ is the angle of rotation after bending, EI is the flexural rigidity ($N.m^2$)and g is the acceleration due to gravity. The curve length(S) of the element after bending can be calculated by implementing the large deflection beam theory proposed by (Chen 2010)

$$S = \int_0^{h_v} \frac{dz}{\sqrt{1 - \left[\left(\frac{P}{2EI}\right) * \left(\frac{z^3}{3h_v} - z^2 + zh_v\right)\right]^2}} \tag{6.2}$$

Where h_v= height of the vegetation (m) and z=any depth along the vertical (m)

6.2.2 Velocity distribution in the vegetated layer

In the vegetation layer, the velocity profile is estimated from the momentum equation by applying the force balancing between the Reynolds shear stress, vegetation roughness, and vegetation roughness

$$\frac{d\tau}{dz} + \rho g S_f - \frac{dF_x}{dz} = 0 \tag{6.3}$$

Net Resultant force (F_x)on the bending vegetation is evaluated from the drag force and the friction force component, and finally, the velocity profile in the vegetation layer is expressed as (Huai et al. 2013a)

$$\alpha = \sqrt{\frac{C_d m D}{0.3(H - h_v)}} \tag{6.4}$$

$$U = \frac{2gS_f\{\alpha * h * exp(\alpha * (z - h_v)) + 1\}}{\sqrt{mD\left\{C_d\left[1 - \left(\frac{P}{2EI}\right)^2\left(\frac{z^3}{3h_v} - z^2 + zh_v\right)^2\right] + C_f * C_p\left(\left(\frac{P}{2EI}\right)\left(\frac{z^3}{3h_v} - z^2 + zh_v\right)^3\right)\Big/\sqrt{1 - \left[\left(\frac{P}{2EI}\right)\left(\frac{z^3}{3h_v} - z^2 + zh_v\right)^2\right]}\right\}}} \tag{6.5}$$

At $z = h_v$

$$u_v = \frac{2gS_f(\alpha h + 1)}{\sqrt{mD\left\{C_d\left[1 - \left(\frac{Ph_v}{6EI}\right)^2\right] + C_f C_p\left(\left(\frac{Ph_v^2}{6EI}\right)^3\right)\Big/\sqrt{1 - \left[\left(\frac{Ph_v^2}{6EI}\right)^2\right]}\right\}}} \tag{6.6}$$

where,

C_d = Drag coefficient, C_p=perimeter of the stem cross-section and C_f = friction coefficient, α = Constant relating the hydraulic and vegetation characteristic.

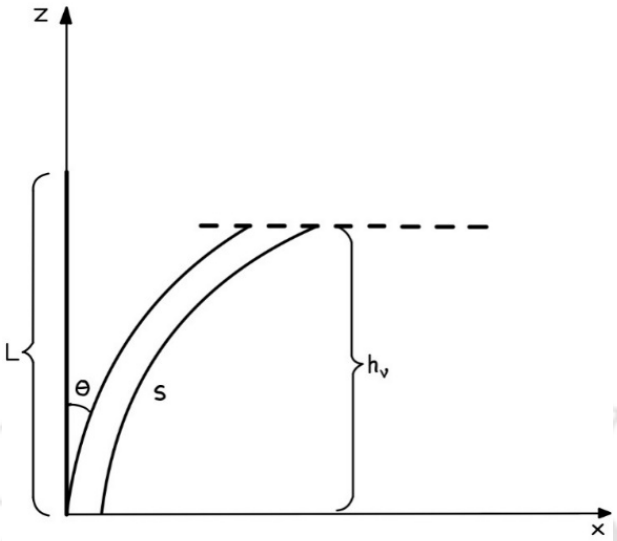

Figure 6.1: Deflection of Flexible Vegetation (Huai et al. 2013)

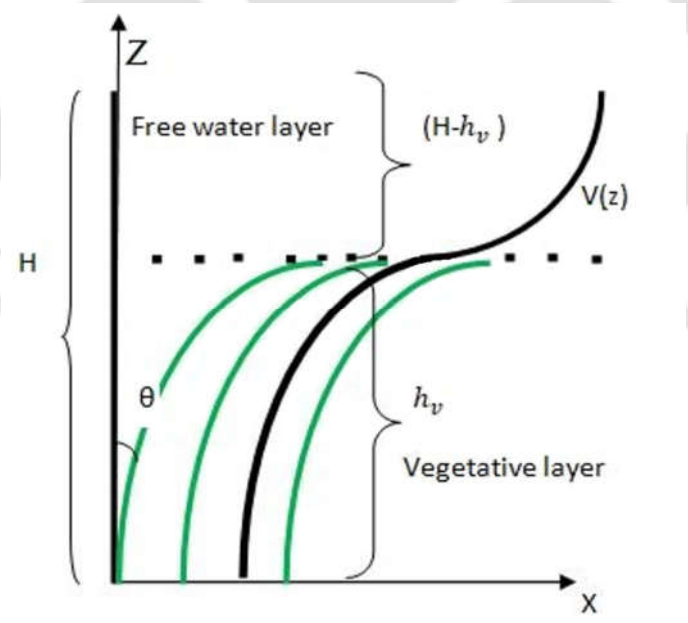

Figure 6.2: Velocity profile in an open channel with submerged flexible vegetation

6.2.3 Shannon's entropy theory for velocity distribution in the free water layer

The expression of vertical velocity distribution from the entropy concept was derived by Chao-Lin Chiu (1989) using the maximum entropy principle (POME) to the Shannon entropy (Shannon 1948). A unique coordinate system was defined for representing the flow such that the velocities are a function of ξ. The velocity is assumed to increase from zero (at $\xi = \xi_o$) to a maximum value u_{max} (at $\xi = \xi_{max}$).

$$\frac{u}{u_{max}} = \frac{1}{M}\ln\left[1 + (e^M - 1)\frac{\xi - \xi_o}{\xi_{max} - \xi_o}\right] \tag{6.7}$$

where, M = Dimensionless entropy parameter and u_{max} =maximum velocity in the velocity profile

The term $\frac{\xi - \xi_o}{\xi_{max} - \xi_o}$ is analogous to the cumulative distribution function, which can be represented as

$$\frac{\xi - \xi_o}{\xi_{max} - \xi_o} = \int_0^u k(u)du \tag{6.8}$$

where $k(u)$, $0 \le u \le u_{max}$ Represents the probability density function, which can be obtained by maximizing Shannon's entropy(Chiu 1989; Shannon 1948).

$$k(u) = e^{a_1 + a_2 u} \tag{6.9}$$

where the parameters a_1 and a_2 are related to M and u_{max} by the following equations

$$a_2 = \frac{M}{u_{max}} \tag{6.10}$$

$$e^{a_1} = \frac{M}{u_{max}(e^M - 1)} \tag{6.11}$$

If the velocity u increases with respect to the vertical distance y from zero at the channel bed (y = 0) to the u_{max} at the surface ($y = D$). The ξ can be formulated as

$$\xi = \frac{y}{D}, \qquad 0 \leq \xi \leq 1$$

The entropy parameter, M which is a characteristic of a channel domain that remains constant, and can be related with the average and maximum velocity in a channel cross-section as (Chiu and Tung 2002),

$$\phi(M) = \left(\frac{e^M}{e^M - 1} - \frac{1}{M}\right) = \frac{u_{avg}}{u_{max}} \tag{6.12}$$

where, u_{avg} =Mean c/s velocity in the vegetated region

The vertical velocity profile is then distributed in the free water layer from the following equation (Moramarco and Singh 2010b)

$$\frac{u_v}{u_{max}} = \frac{1}{M} ln\left[1 + (e^M - 1)\left(\frac{z - y_o}{h_{max} - h_o}\right)\right] \tag{6.13}$$

Where, h_{max} =Location of maximum velocity in the vertical,h_0=Location of zero velocity in the vertical, g =acceleration due to gravity and $\phi(M)$ is a function of entropy parameter**.**

6.3 Study area and field measurements

The details of the study area and the field measurements are already explained in section 4.4.2.

6.4 Initial and Boundary condition

The initial and boundary conditions used during the simulation are explained in section 5.3.

6.5 Application of the model

6.5.1 Application of the model in the Brahmaputra River near Majuli, India

The entire computational domain is discretized into 60x225 grid points. The computational time for each simulation is 0.1 seconds. The model solves the 2D equations and computes the flow depth(h), streamwise(u), and transverse velocity(v) at each grid point. The details of the computations and validations of the model near Majuli Island are presented in section 4.5.2.

The computed outputs are substituted in the entropy model to estimate the vertical velocity profile (w). The depth average velocity from the model and the observed maximum velocity in the channel cross-section is substituted in equation 6.13 to calculate the $\phi(M)$ and the entropy parameter M. These values are substituted in equation 6.9 to compute the vertical velocity profile. The model is primarily used to distribute the vertical velocity at two points near spur 1(S11) and spur-2 (S21) and spur-4(S41). The observed free surface velocity computed depth-averaged velocity, and the flow depth substituted in the entropy model to obtain the depthwise distributed velocity profile. From the field observations, the maximum velocity at S11, S22, and S41 are found as 1.28 m/sec, 0.76 m/sec, and 1.05 m/sec.

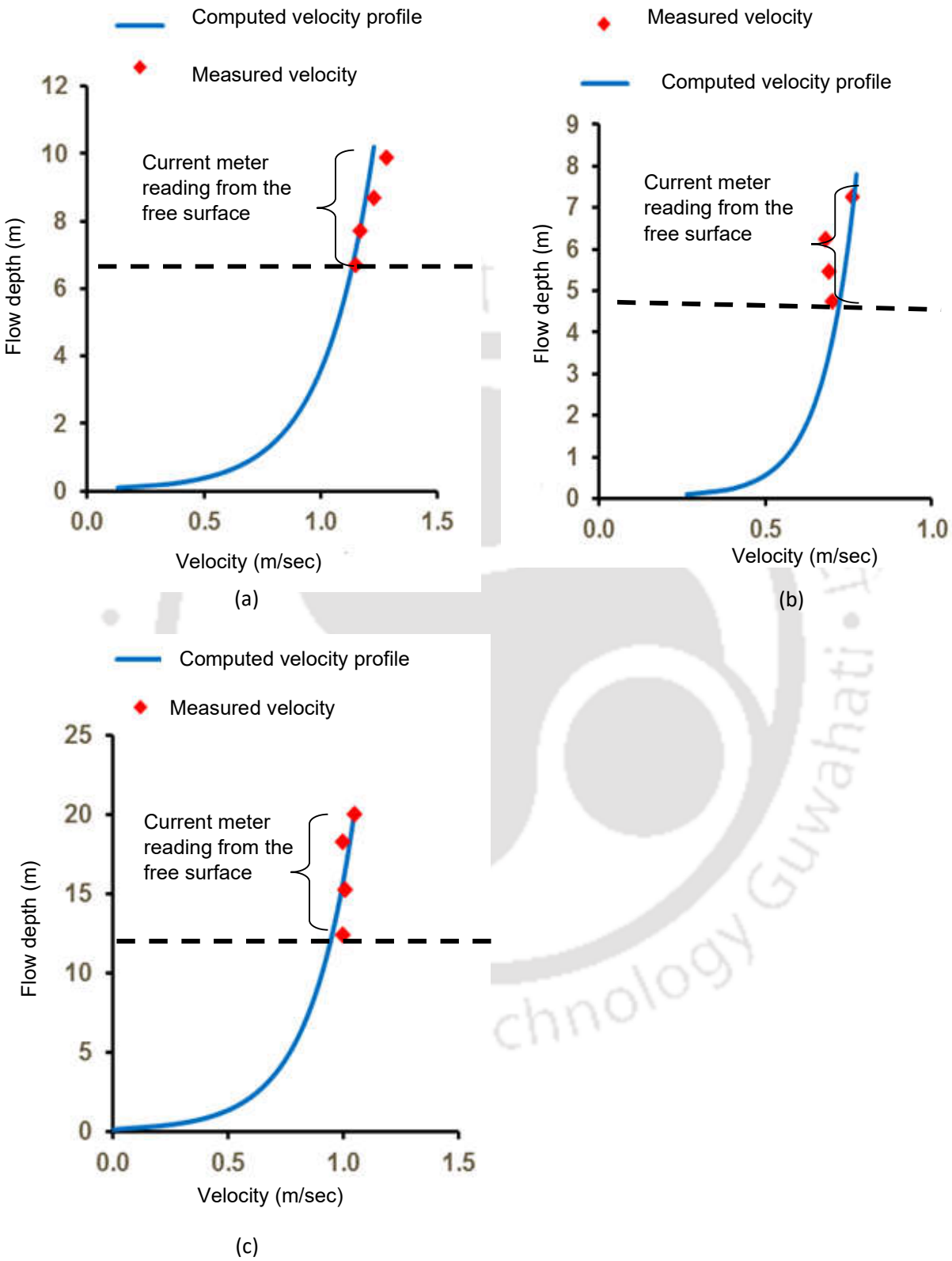

Figure 6.3 Vertical velocity profiles at S11, S22 and S41

Figure 6.3(a-c) shows the computed and observed velocity profile along the vertical. The current meter readings are available up to 3-4m depth from the water surface. Thus the velocity in the top flow layers is presented in the figures. The coefficient of correlation between the model predicted and the observed data is found as 0.73. The results indicate a satisfactory agreement between the field measured results and the computed outputs.

The groin walls and the channel aspect ratio influence the vertical velocity distribution. The points AS31 and AS32 are located near the solid spur S2 (within a range of 36m and 54m). The current meter profile shows the maximum velocity below the free surface, indicating the dip in the vertical profiles at these points. The current meter readings are taken at three points: one at the surface and at 1m and 2m from the free surface. The flow separation at the nose of the spur S2 integrates the cross-stream circulation into the flow and transfers the low momentum water column (near the sidewall) to the center. For the continuity requirement, high momentum fluids diverted from the free surface to the bed. The points AS31 and AS32 nearer to the wall experience the dip in the velocity profile. The secondary circulation effect keeps reducing towards S11 and S21, located away from the sidewall. No dip phenomenon was observed in these profiles. In general, narrower channels have a small aspect ratio (width/depth) and experience a strong secondary current compared to the wider channels. However, one interesting finding from this study is that irrespective of the channel aspect ratio (b/h) and flow characteristics, the secondary circulation is most effective near the sidewalls affecting the vertical velocity profiles. The strength of the secondary current is not prominent away from the spurs. The measured surface velocities are found maximum at almost all other surveyed points located away from the spurs. This finding is quite helpful for the field practitioners to consider some necessary modifications in the spur design.Figure-6.4 shows the measured vertical profiles at AS31 and AS32.

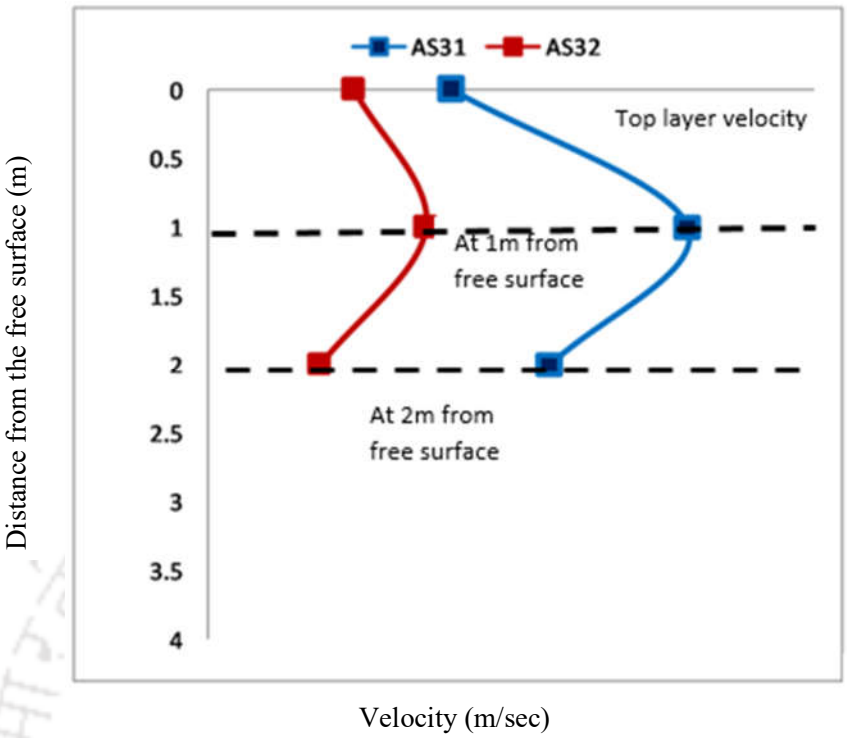

Figure 6.4 Dip phenomenon in velocity profile near the hydraulic structures

6.5.2 Estimation of vertical velocity profile with submerged flexible vegetation

A semi-coupled approach is developed to compute the three-dimensional flow structure in a vegetated channel having flexible stems at different degrees of submergence and vegetation density. The configuration of the flexible stems under different streamflow is evaluated from the large deflection cantilever beam theory. The main advantage of applying the beam theory is that it can effectively capture higher degrees of stem flexibility under different flow events. The computed hydraulic parameters from the shallow water model are used in Shannon's entropy theory and Reynolds's stress equation to calculate the vertical velocity in the free water layer and the vegetation region. Two sets of published experimental datasets are used in the validation of the model.

6.5.2.1 Semi coupled approach for velocity distribution

A complete quasi three-dimensional framework is developed by coupling the velocity distribution model (6.5-6.9) with the 2-D hydrodynamic model (equation 3.38 and 3.38.2). Figure 6.3 shows the flowchart of the proposed model.

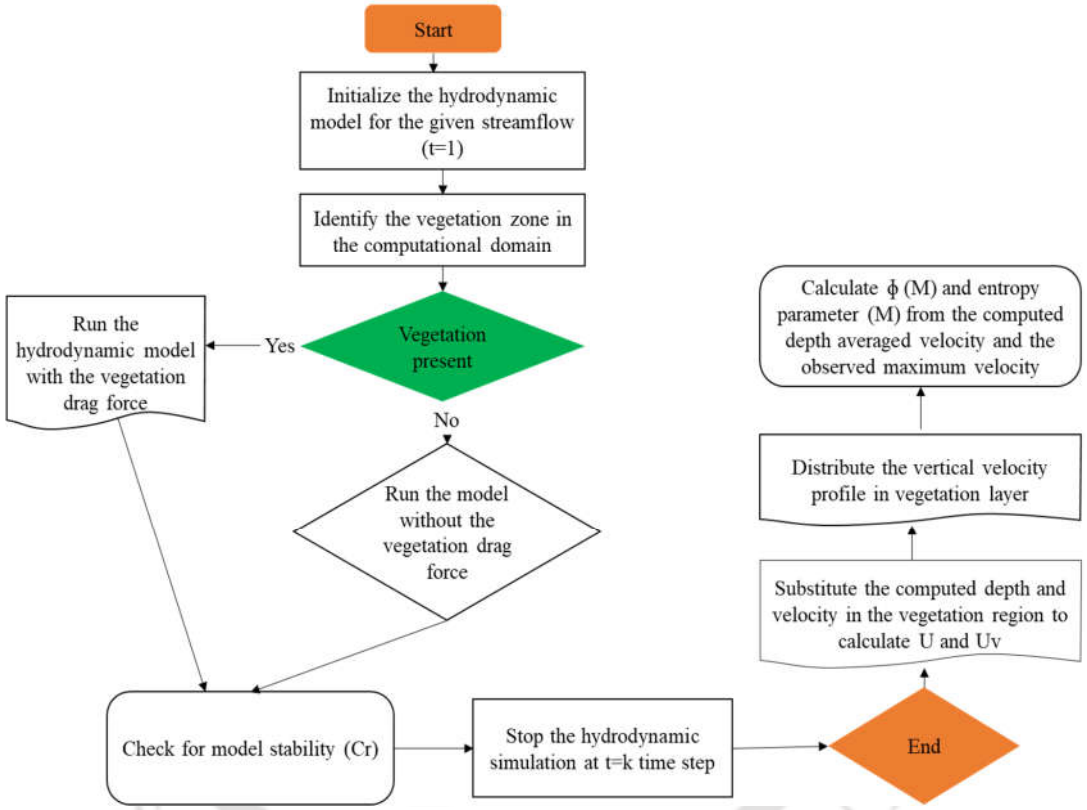

Figure 6.5: Flowchart of the model

Before running the model, the flow domain is discretized into finite-difference grid points both in the lateral and longitudinal direction by solving a set of elliptic partial differential equations. With these grid points, the model begins by setting an initial value of the primitive variable to the generated grids. The flow resistance offered from the flexible stems is incorporated explicitly by integrating the hydrodynamic drag into the source term of the shallow water model. The apparent velocity approach proposed by Stone and Shen(2002) is used to compute flow resistance within

the stem layer. Primarily, the bending phenomenon is governed by the rigidity of the flexible stems. At a high velocity with less dense vegetation, the projected bending height (h_v) will be more than the high dense vegetation. The large deflection cantilever beam theory is used in the model to capture the reconfiguration of the flexible stems from high flow to low flow events. The projected bending height calculation accuracy is evaluated by comparing the model computed results with the measured data. A small amount of error (φ=0.00001) is assigned during the calculation, and the iteration continues till it satisfies the criteria.

The computed flow depth from the hydrodynamic model is substituted in equation-6.1 for imposed load (P) calculation over the flexible stem. From equation 6.1, it is observed that the imposed load over the flexible stem is an inverse function of vegetation density. It indicates that for a given flow event, the load on the stem will be less at high vegetation density and vice versa. Once the load (P) is obtained, h_v is calculated iteratively from equation-6.2. The momentum fluxes along the longitudinal and transverse directions are computed at the next step. The vegetation drag force calculation is exempted from the momentum equation in the non-vegetation regions. The hydrodynamic model runs till steady-state. The model stability criteria are checked from the CFL criteria. According to this criterion, if the Courant number is less or equal to one, the model is considered stable. If this criterion is not satisfied, the time step is readjusted, and the preceding iterations are repeated.

The computed outputs from the hydrodynamic simulations are used in the velocity distribution equations to estimate the vertical velocity profile in the second phase. The entire flow region is divided into two flow layers: the vegetation and free water layers. The vegetation characteristics such as drag-influenced flow depth (h), patch density (m), stem diameter(D), drag coefficient (C_d), bend vegetation height (h_v), and flexural rigidity (EI) are substituted in equations 6.5 and 6.6 for

velocity computation within the vegetation zone and at the crown.The computed depth averaged velocities from the shallow water model is used in the calculation of the entropy parameter (M). The cross-sectional observed maximum velocity is used in equation 6.12 to calculate Ø (M) and the entropy parameter (M) in the channel cross-section. The calculated M is used to compute velocity profile (u) at different depths (z) above the vegetation region to the free water surface from equation-6.13.

6.5.2.2 Application of the model in vegetated channel

The performance of the present model is assessed by setting up the model with two different experimental test runs.

Case-1 Calibration and validation of the model with the experimental study of Kurbak et al. (2012)

In the first case, the experiments carried out by (Kubrak et al. 2012) are used in the simulation. The model computed output is then compared with the experimental outputs reported in their laboratory flume experiment. They have conducted the experiments in the hydraulic laboratory in a vegetated flume in the department of Hydraulic structure, Warsaw Agricultural University. The experiment was performed in a glass-walled flume of 16m length, 0.58m wide, and 0.6m depth. In their investigation, the cylindrical stems of elliptical cross-sections having diameter d1=0.00095m and d2=0.0007m were placed in a removal plate of 3m length, .58 m wide made of PVC. The longitudinal and transverse velocity profiles were measured using a programmable electromagnetic liquid velocity meter. The schematic diagram of the experimental channel is available in Kubrak et al. (2012). The details of the different test runs of the experimental flume are listed in Table-1.

In the numerical simulation, the entire domain is discretized into 191finite-difference grid points. The grid spacing in the channel is taken as Δx=0.5m and Δy=0.1m. However, in the vegetated

region, the stems are placed at a more refined grid spacing. The Mannings or Chezy's roughness coefficient is an essential parameter for shallow water simulations. These coefficients are generally estimated from the mean diameter of the bed material. They have expressed the bed roughness in terms of equivalent sand grain roughness in their experimental work. Thus, following (Marriott and Jayaratne 2010), the given equivalent sand grain roughness (k_s=0.0001, .0018, .0150)are converted to manning's roughness parameter (n), and it ranges between .008-.018. The discharge in the channel varies from 0.0333-0.0751$m^3/\sec$. These flow rates are provided as the upstream boundary condition. The flexural rigidity used in the experimental and the numerical studies are the same throughout. The time step is considered as 0.35 seconds, which gives a courant number of 0.93. The volume fraction of vegetation (Nepf 2011) is incorporated in the drag force calculation, and its value ranges between 0.32-1.558. The no vegetation regions are exempted from the drag force computation. The imposed load is computed for different flow events. The hydrodynamic simulation provides the flow depth and velocity information at different discharges and locations in the channel. The computed velocity profiles from the shallow water model for experiment numbers 1.2.1 and 4.1.1is are shown in Figure 4. In experiment no 1.2.1, a very high vegetation density (m=10000) is used with a moderate flow rate of 0.0422 m^3/sec. However, in experiment 4.1.1, vegetation density is significantly lower. The x-axis and y-axis represent the length and width of the channel. The representation of the flexible stems within the hydrodynamic model is presented in figure-4(c). The resistance offered by the vegetation retard the flow momentum and reducing the velocity in the channel. The vegetation covers a region of 3x.58m in the channel.

Table 6.1: Flow and vegetation parameters for simulation (Kubrak et al. 2012)

Flow Parameters	**Experiment Number**						
	1.2.1	1.1.3	2.1.1	2.2.1	3.1.1	3.2.1	4.2.1
Flow rate, Q (m^3/sec) (m^3/sec)	0.0422	0.0333	0.0525	0.0751	0.0605	0.0693	0.0693
Water depth, H (m)	0.2236	0.2475	0.2386	0.2131	0.2386	0.1962	0.2077
Vegetation height,h_v (m)	0.161	0.164	0.153	0.132	0.151	0.132	0.138
Bottom slope (S) (%)	8.7	8.7	8.7	17.4	8.7	17.4	17.4
Drag coefficient (C_d)	1.4	1.4	1.4	1.4	1.4	1.4	1.4
Equivalent sand grain roughness (k_s) (m)	0.0001	0.0001	0.0001	0.0001	0.0018	0.0018	0.0150
Friction coefficient (C_f)	0.4	0.4	0.4	0.4	0.4	0.4	0.4
Vegetation density (m^{-2})	10000	10000	2500	2500	2500	2500	2500
Flexural rigidity (EI) (Nm^{-2})	5.81 x10^{-5}	5.81 x10^{-5}	5.81 x10^{-5}	5.81 x10^{-5}	5.81 x10^{-5}	5.81 x10^{-5}	5.81 x10^{-5}

From the computed velocity contour maps, it is found that, within that region, the velocity profile is significantly decreased, as shown in figure-4(a, b). The velocity profile from the above figures indicates that in the non-vegetated regions, the maximum velocity lies between .09-0.14 m/sec for the given discharges. However, from the velocity contour maps, it is observed that with vegetation,

the computed depth-averaged velocity is 0.01m/sec to 0.03 m/sec. It is observed that the velocity progressively reduces at a higher vegetation density (m=10000) region compared to the lower vegetation density (m=2500). The bending profile of the flexible stem under the influence of different loads is calculated and compared with the measured results. Figure-6.6 shows the correlation coefficient between the computed and measured bending profiles of the flexible stems and found satisfactory.

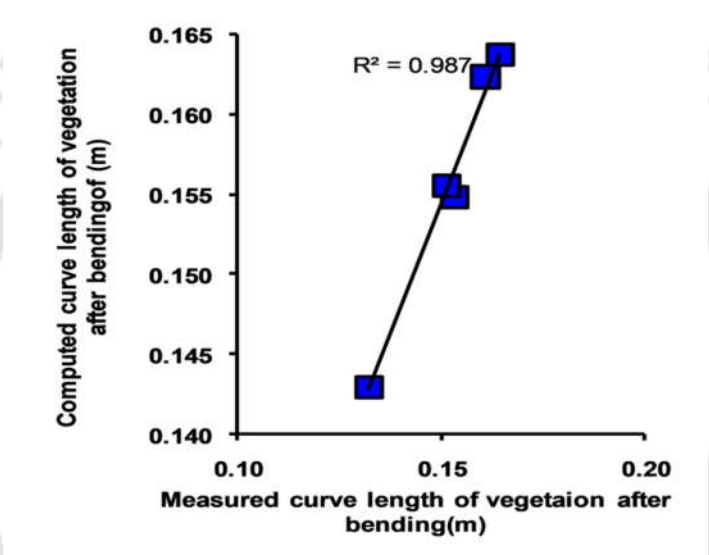

Figure 6.6: Correlation coefficient between the measured and predicted curve length of the flexible stem

For illustrating the vertical velocity distribution model, the present study considered experiment no 4.1.1. After reaching the steady-state, the computed water level is substituted in Reynold's stress model to calculate the vertical velocity profile within the vegetation zone and at the crown of the stem. The maximum velocity at the crown is found as 0.67m/sec. The entropy model is used in the free water layer by subtracting the vegetation depth from the total water depth. The depth-averaged

velocities from the hydrodynamic simulation are between 0.01-0.015 m/sec, and the maximum velocity is 0.92m/ sec.

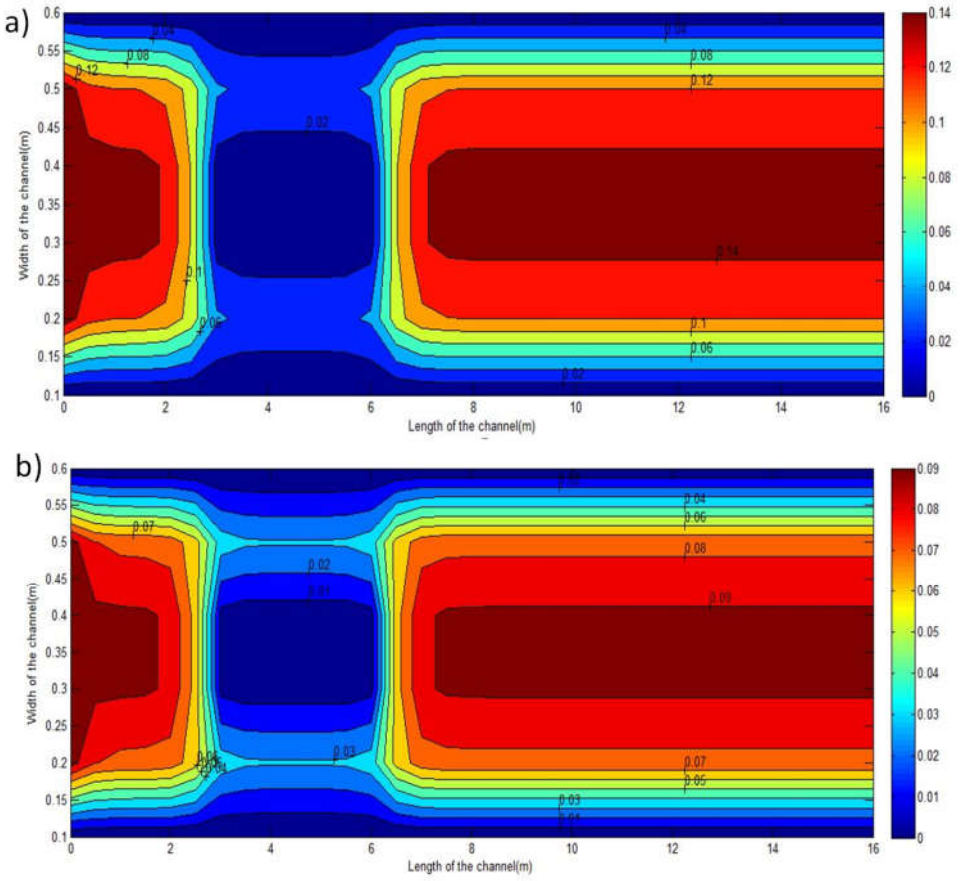

Figure 6.7: Computed depth-averaged velocity profile for the experiment (a) 1.2.1 (b) 4.2.1

The configuration of the vegetation within the hydrodynamic model is presented in figure-6.8

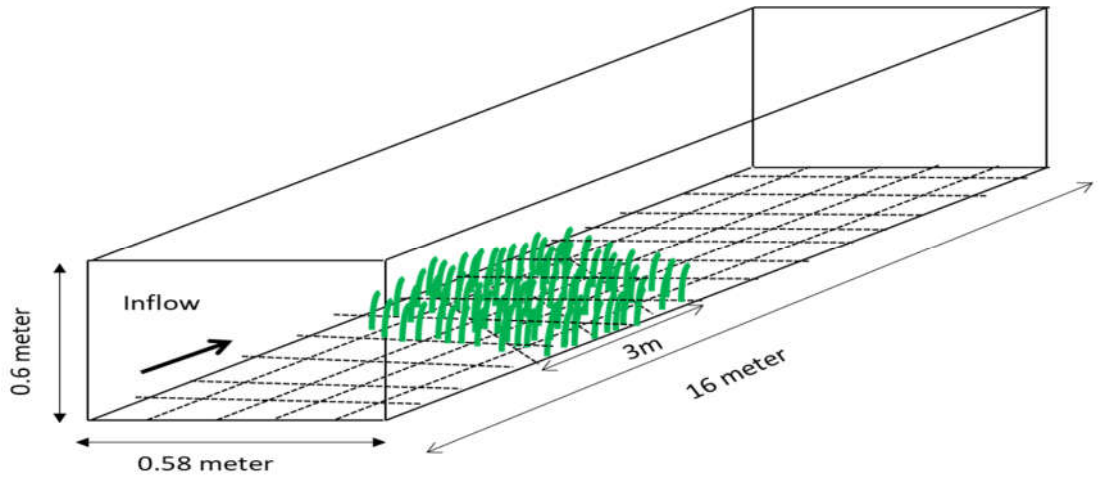

Figure 6.8: Configuration of vegetation within the hydrodynamic model

From these two values, Ø (M) and the entropy parameter (M) are calculated and substituted in equation 28 to calculate the velocity profile. The computed vertical velocity profiles for different experiments are presented in figure-6.9. The figure indicates that the present model predicts the velocity profiles under different flow events with high accuracy.

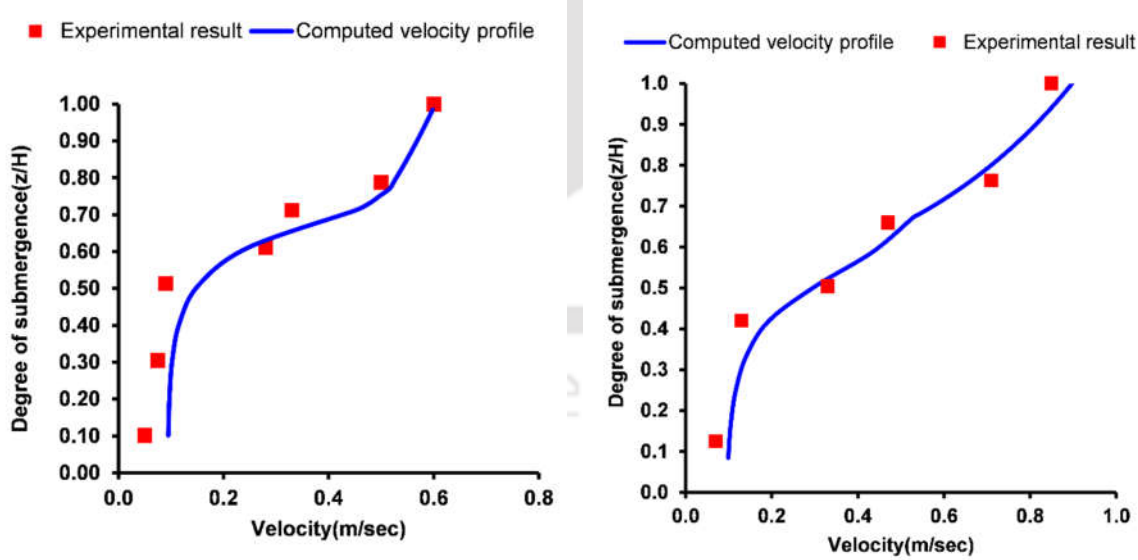

(a) (b)

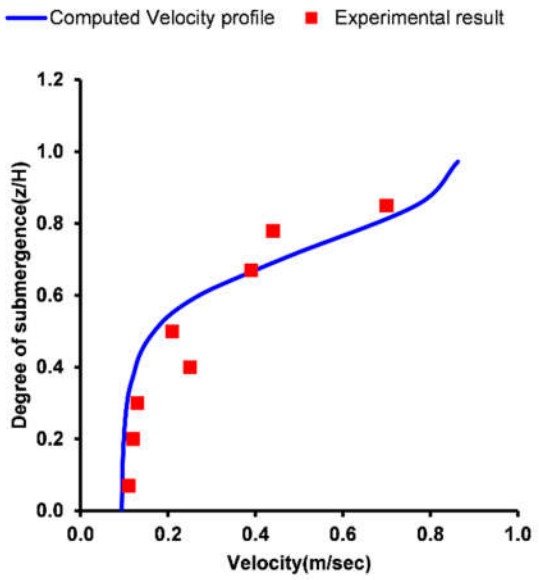

(c)

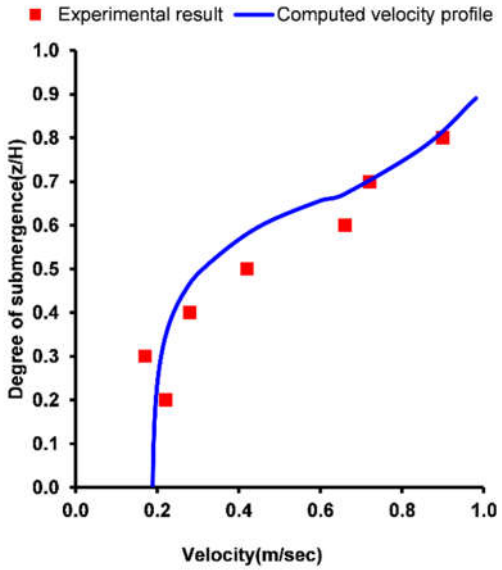

(d)

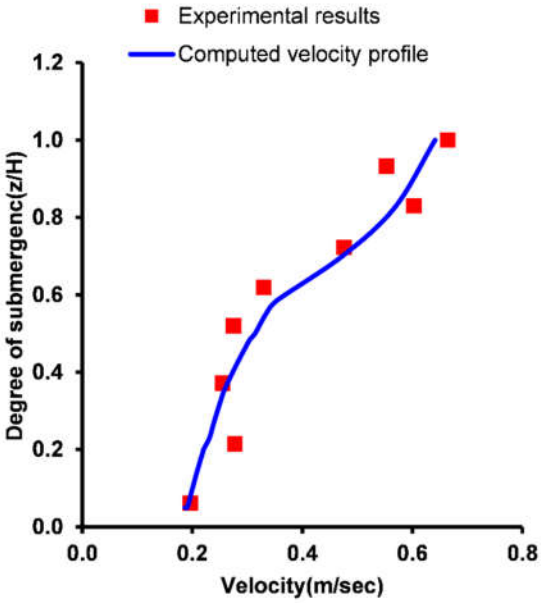

(e)

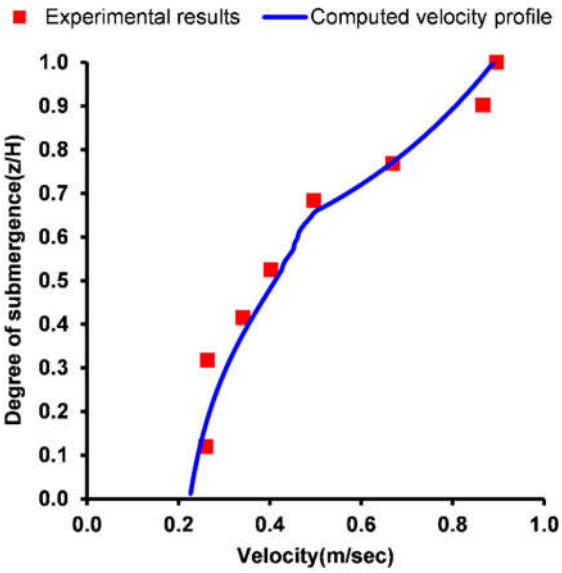

(f)

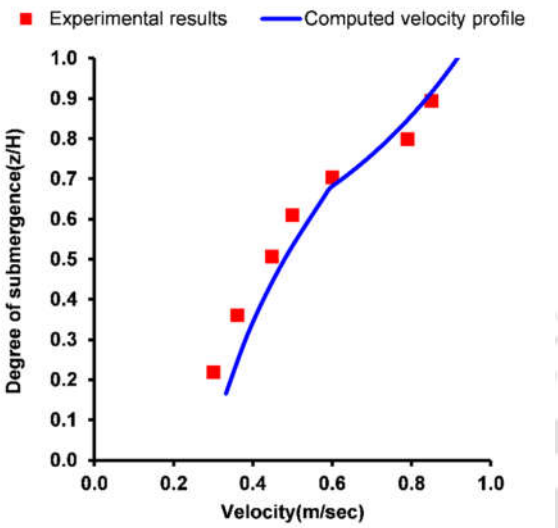

(g)

Figure 6.9: Comparison of computed and measured velocity profiles at experiment number (a) 1.2.1 (b) 1.1.3 (c)2.1.1 (d) 2.2.1 (e) 3.1.1 (f) 3.2.1 (g) 4.1.1

Case-2 Calibration and validation of the model with the experimental study of Jarvela (2005)

In the second case, the experimental study conducted by Järvelä (2005) is used in the simulation. The experiments were conducted in a 50m long and 1.1m wide recirculating glass-walled flume. The vegetation was rooted in a thin-walled metal box. The average length and width of the stems are 280mm and 2.8mm, respectively. The vegetation covered the test area with an average density of 12000 stems/m^2. Discharge was released from a header tank to the flume through a silting basin and a flow straightener. Flow velocities were measured using a 3D acoustic Doppler velocimeter manufactured by Nortek. Water surface along the test section was measured using a differential pressure transducer in 3-7 longitudinal sections averaging over a period of 30-60 seconds. The Deflected vegetation heights are determined visually using a ruler or a measuring tape fixed to the flume wall. The experimental datasets used in the simulation are presented in table-6.3. The way of estimation for vertical velocity profiles is similar, as mentioned in the previous case. The entire

flow domain is discretized into finite-difference grid points over which the drag-induced hydrodynamic computations are taking place. Figure 6.10 shows the computed and measured vertical velocity profiles. The capacity of the entropy model to mimic the near-bed finite velocity gradients helps in converging the solution with the experimental results.

The discrepancy in the observed and computed results is checked using two statistical performance measures Viz. Root mean square error (RMSE) and mean absolute error (MAE).

$$MAE = \sum_{i=1}^{n} \frac{(Predicted\ velocity_i - Measured\ velocity_i)^2}{N} \tag{6.10}$$

$$RMSE = \sqrt{\sum_{i=1}^{n} \frac{(Predictedvelocity_i - Measuredvelocity_i)^2}{N}} \tag{6.11}$$

Table 6.3: Flow and vegetation parameters for simulation (Järvelä 2005)

Experiment number	Flow depth(h) (m)	Discharge(Q) (m^3/sec)	Vegetation deflected height(m) (h_v)	Friction slope (s_f)	Shear velocity (u_*)	Friction factor	C_f
R4-1	0.306	0.04	0.205	0.0015	0.0388	2.35	0.00638
R4-2	0.3084	0.1	0.155	0.0036	0.0735	0.95	0.00559
R4-3	0.4065	0.04	0.23	0.0005	0.0287	1.84	0.00638
R4-4	0.4041	0.1	0.19	0.0013	0.0521	0.76	0.00559
R4-5	0.407	0.143	0.16	0.002	0.0696	0.57	0.00532
R4-6	0.5044	0.04	0.245	0.0002	0.0211	1.27	0.00638

R4-7	0.495	0.1	0.22	0.0006	0.0416	0.68	0.00559
R4-8	0.7065	0.1	0.26	0.0002	0.027	0.50	0.00559
R4-9	0.7037	0.143	0.215	0.0003	0.0384	0.44	0.00532

The RMSE and MAE values indicate a satisfactory agreement between the measured and the computed results. The MAE and RMSE are found as 0.079 and 0.1148. The values indicate that the proposed model can estimate the vertical velocity profile in an open channel with submerged flexible vegetation. The R^2 values between the measured and predicted outputs are found to be 0.767 and presented in figure-6.11.

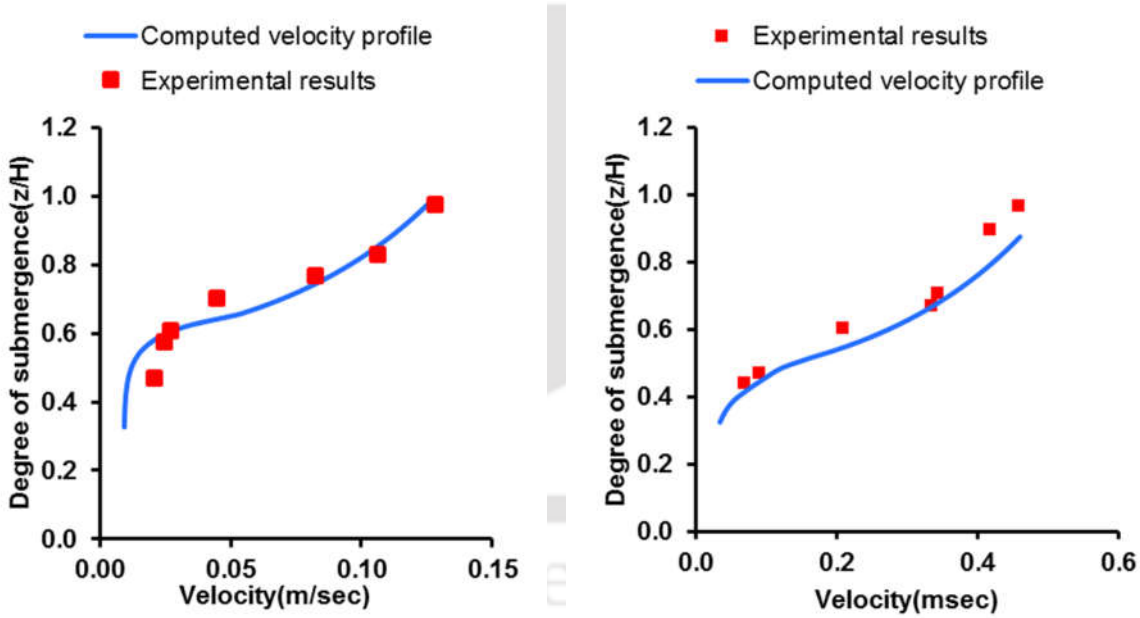

(a) (b)

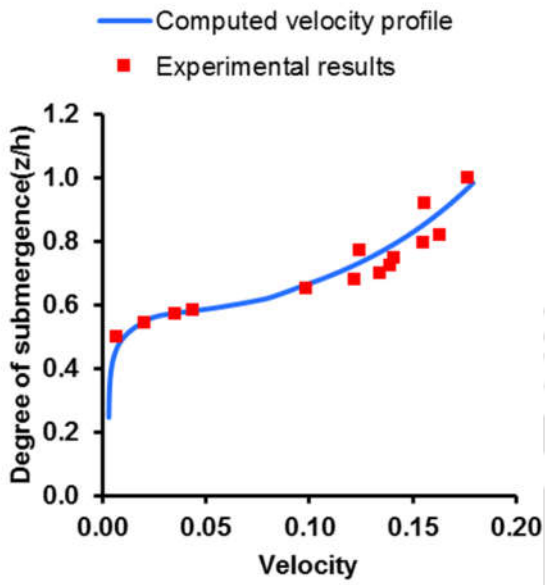

(c)

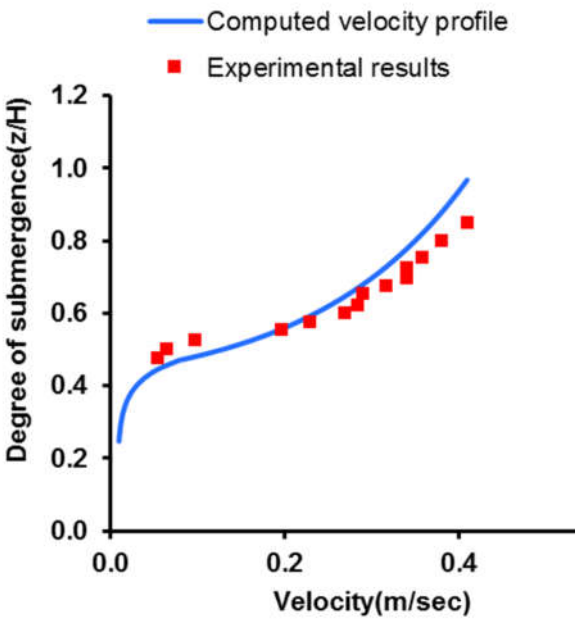

(d)

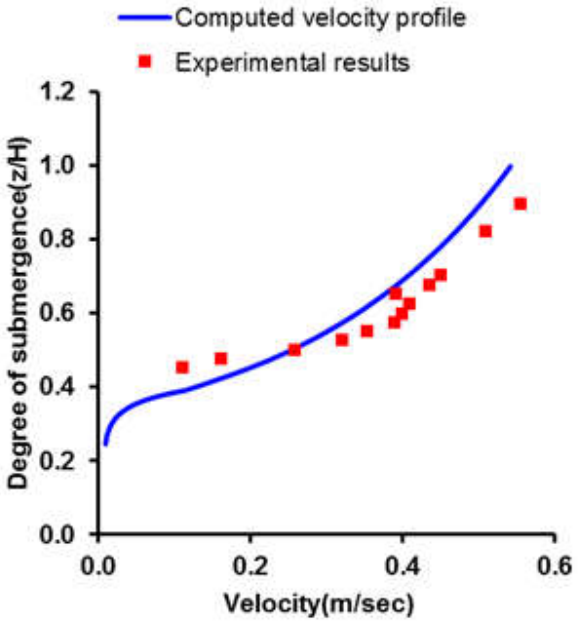

(e)

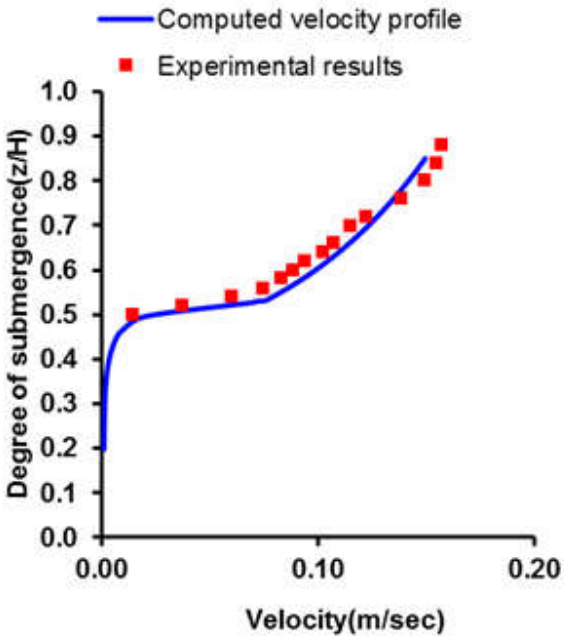

(f)

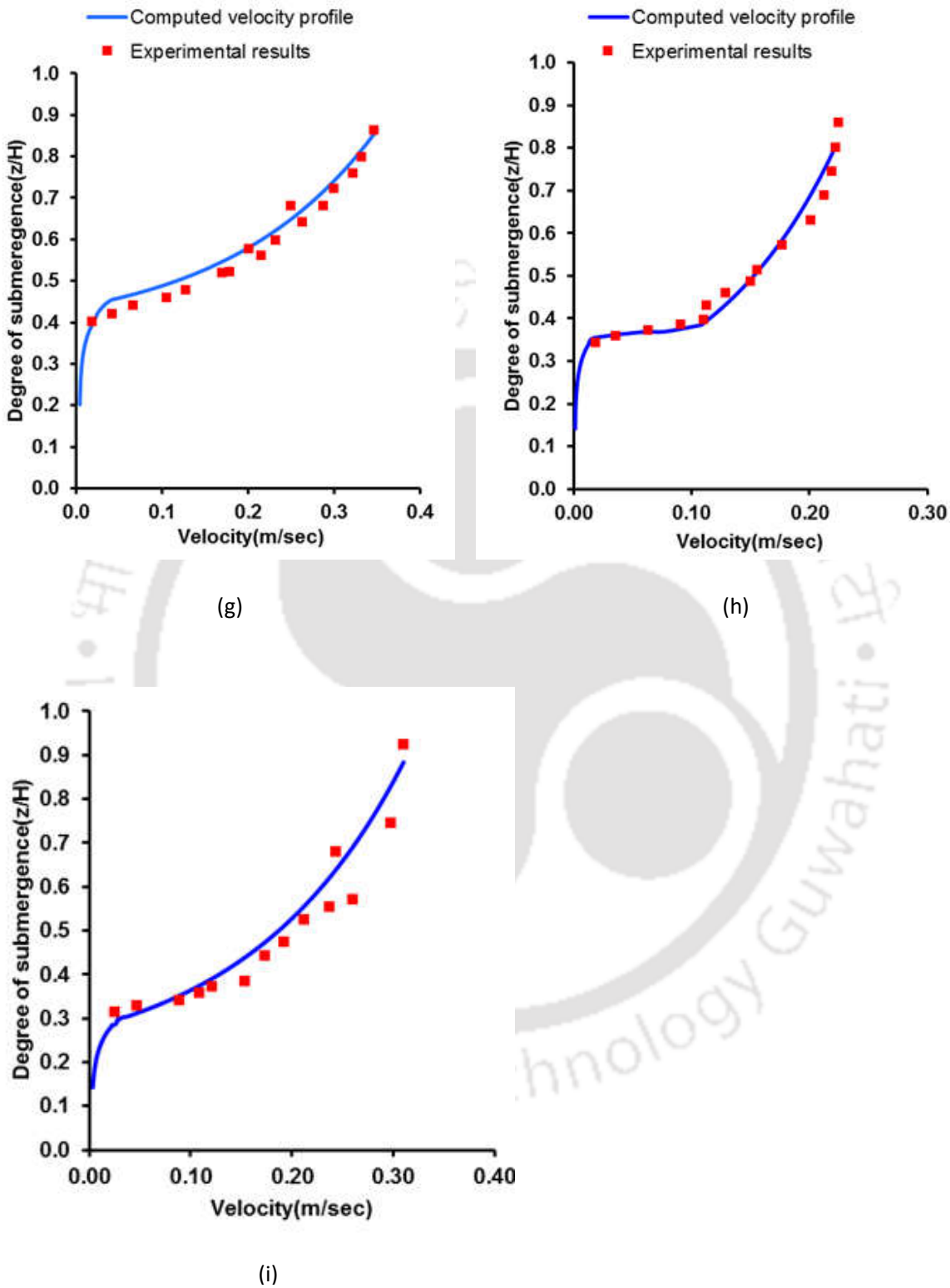

Figure 6.10: Comparison of computed and measured velocity profiles at experiment number (a) R4-1 (b) R4-2 (c)R4-3 (d) R4-4 (e) R4-5 (f) R4-6 (g) R4-7(h) R4-8 (i) R4-9

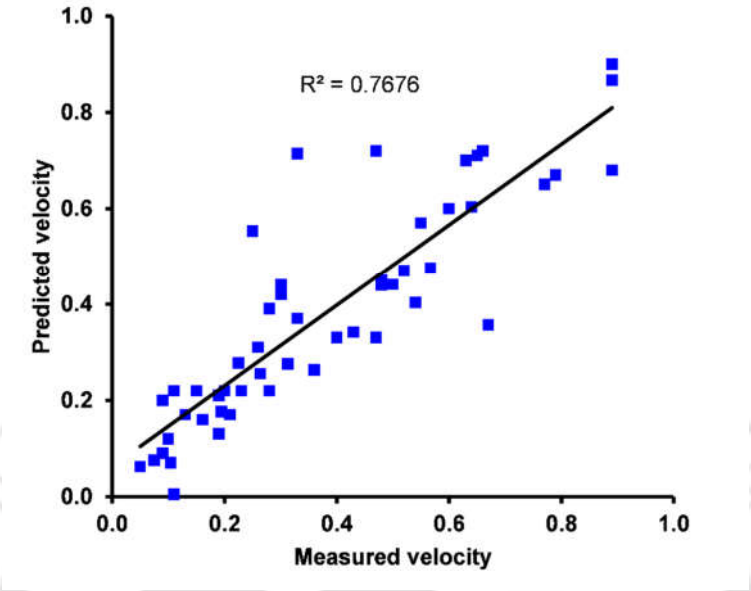

Figure 6.11: Coefficient of correlation between the measured and computed results

6.6 Dynamics of entropy parameter in a vegetated channel

The mean velocity in channel cross-sections changes as the vegetation density varies from sparse to dense. The roughness parameter and the flow blockage offered by densely distributed submerged flexible canopies are higher than the sparsely distributed vegetation for a given discharge. These velocity variations at different degrees of vegetation density also influence the channel entropy parameter (M), a function of $\frac{U_{avg}}{u_{max}}$. This anomaly in the flow structure influences the velocity distribution process in the channel section. A relationship between the vegetation characteristics (H/h_v) and entropy parameter M at different vegetation densities (m) is investigated from a series of simulations. Five different flow scenarios are taken and $^{H}/_{h_v}$ varies from 1.27-1.93. Eight different vegetation density is incorporated (2000-10000 /m^2) in the entropy model. The interrelation between the entropy parameter and the vegetation density is presented in

figure-6.12. It is observed that a power-law relation ($y = ax^b$) is best suited between the entropy parameter and the vegetation density at differentH/h_v. From figure -6.12, it is observed that the entropy parameter progressively decreases as the vegetation density changes from sparse to dense.

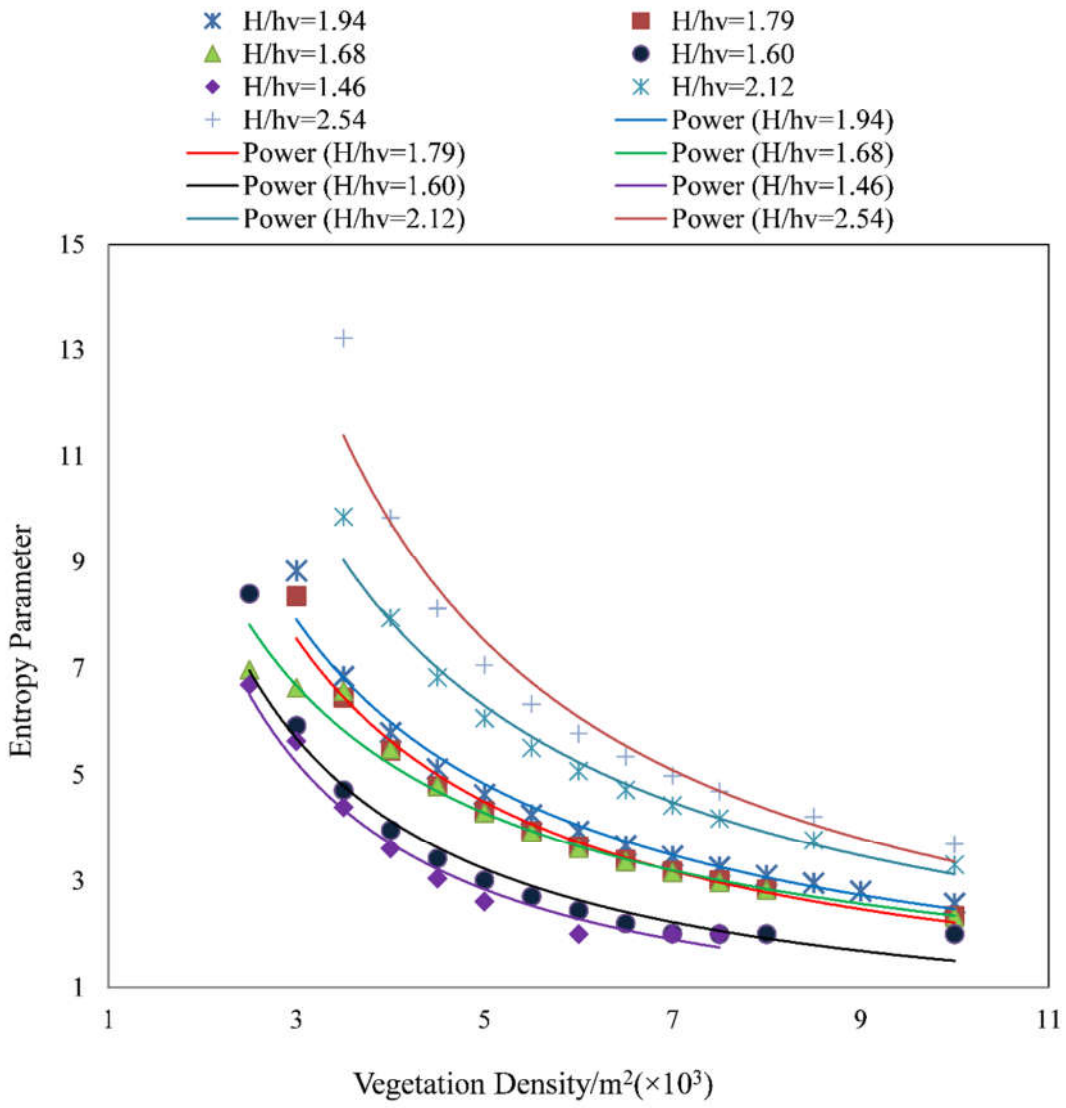

Figure 6.12: Relation between the vegetation density and entropy parameter

Table 6.3: Coefficient of Correlation at different $\frac{Flow\ depth}{Vegetation\ height}$

H/h_v	$Correlation, R^2$
1.94	0.9865
1.79	0.9871
1.68	0.9796
1.60	0.9376
1.46	0.967

6.7 Conclusion

From this chapter following concluding points can be drawn

1) A quasi 3D modeling framework is developed to estimate the flow depth (h) and three-dimensional velocity components (u, v, w) in an open channel. The vertical velocity profiles are calculated by substituting the computed flow (h) and the depth-averaged velocity in the entropy model. Model findings are validated with the field observed results and found satisfactory. The sidewall influence on the secondary circulation generation and its impact on the vertical velocity profile are seen clearly from this study. Near the spur, the dip phenomenon is dominantly present in the velocity profiles. However, no such phenomenon was observed at the points located away from the structures. This finding could be helpful for field engineers to design sustainable hydraulic structures in the study area. However, the model in the present state is not capable of capturing the non-systematic anomaly in the vertical profile that may exist due to various other factors. There is a scope

of model improvement by considering the complex flow-sediment interactions and the turbulence regimes in the simulations.

2) The integration of entropy theory with the shallow water model provides a simplified yet effective approach for vertical velocity distribution in the vegetated open channel. The drag force with the shallow water model computes the hydrodynamics in the vegetated regions. The computed outputs are substituted in the entropy theory and Reynold's stress equation to estimate the vertical flow structure. The applicability of the model is checked in two different test channels with submerged flexible vegetation. The results indicate that a good agreement between the measured and the computed data. This present approach can effectively integrate into river restoration projects, habitat modeling, and river ecology studies to provide helpful insight into determining the velocity profile under vegetated channel flow.

3) The entropy parameter at a river section is primarily an indicator of channel geometry and morphological characteristics. However, the vegetation density alters the flow patterns leading to the modification of the entropy parameter. The relationship between the entropy parameter and vegetation density is calculated from the model, and a power-law relation is observed between these two parameters.

CHAPTER-7

Hydrological-hydrodynamic nexus for evaluation of fish habitat suitability: A Case Study in the Bhogdoi River, India

7.1 Introduction

The preservation of the freshwater ecosystem primarily implies maintaining and protecting the diverse aquatic habitats under the lotic environments. From the eco-hydrological point, the fundamental definition of the habitat is the part of the river that fish or other benthic invertebrates at their different life stages prefer for survival and reproduction. The aquatic habitat modeling contributes to the precise understanding of the hydrological regimes over the freshwater species and presents a management approach for their conservation. For instance, through habitat modeling, one can estimate the ecological flow rate needed to maintain the ecosystem integrity and good environmental status. Some of the factors that need to be considered while establishing the environmental flow regimes are the quantity, frequency, duration, and quality of the water flow in the domain. The physically-based hydraulic habitat algorithms that linked the hydrological descriptions of the different flow regimes, including the environmental flows to the fish life stages, are efficient ways to predict the suitable habitat in the marine environment. It provides a coupled approach that integrates the temporarily varying hydrological matrices to the hydraulic models that compute the spatial variations of the flow parameters in complex environments. The hydrological alteration, seasonal drying-wetting in intermittent streams are factors that influence the ecosystem diversity. The computational efficiency in complex terrains and the capacity of representing the vegetation in hydrodynamic simulations increases the potential application of hydrodynamic-habitat models in aquatic ecological studies. The presence of shrubs and macrophytes influences

the aquatic ecology and habitat diversity in vegetated channels by modifying the flow pattern. Aquatic vegetations often act as a cover for the fish species and provide the spawning and breeding area. The species diversity is adversely impacted by hydraulic structures such as weirs and barrages in the stream. In a recently published report, it is found that the irrigation barrage construction in the Ganga River at Haridwar results in large-scale destruction of fish near the downstream pool. As such, before constructing any hydraulic structures, it is essential to carry out a downstream impact study on the aquatic species using a physical-based hydraulic-habitat model.

The capability of the developed model for flow simulation in complex terrains and vegetated channels expands its application in the habitat modeling study. As mentioned in the previous chapter, the model can compute the flow parameters (flow depth and velocity) under both rigid and highly flexible stems. The velocity and flow depth profiles obtained from the simulations are used in constructing the habitat curves for the targeted species. Depending upon the habitat preference of the targeted species, the present model can apply in both vegetated and non-vegetated conditions. For example, some fish species at their full-grown stage reside in a bare substrate (sandy-silty soil, clay or loamy soil, gravel) rather than the vegetated region. In those cases, the model without the vegetation is used in the computation. The present model can also be applied to estimate the downstream flow at different weir/barrage release conditions required for the species sustainability. The flow rates under the different operational conditions of the weir /barrages are fed at the inflow boundary of the hydrodynamic model and computed the flow depth and velocity downstream. The habitat curves are then constructed using these computed outputs and calculate the optimal flow rates required for the targeted species.

With a case study in Bhogdoi River, Assam, India, this chapter evaluates the impact of streamflow variations on the adult Bhangun fish (Labeo Bata) found in that river. The targeted

species is adult, non-migratory, and prefers to reside in sandy clay soil. The Assam state government has proposed a lift irrigation scheme in the Bhogdoi River, India, to increase the irrigation potential in the region. The approximate cost of the proposed project is 480 lakhs, and it will irrigate 300 Ha of agricultural area (District Irrigation Plan 2016-2021). The execution of the scheme will provide sufficient irrigation water for the agricultural lands. However, the proposed site for the scheme is a fishing hub for the local communities with more than 30 aquatic species. Thus, the proposed project may also modify the hydraulic characteristics of the reach, which may lead to the decline or extinction of particular fish species living in it. Findings from the study will feed into the action plan on maintaining the adequate flow rate before implementing the project. The ecological flow rates are obtained from flow duration curve analysis (FDCA) and flow duration curve shifting (FDCS) methods to indicate the hydrological changes under different environmental management scenarios.

7.2 Material and Method

7.2.1 Study area

River Bhogdoi, a southern sub tributary of the Brahmaputra River, is chosen as the present study area. River Bhogdoi is an interstate river occupying the geographical territories of Nagaland and Assam, India. It originates from Long Samtang of Mukokchung (Naga Hills in Nagaland) and flows into the Kakodonga river (North-west of Jorhat city, Assam) (Figure7.1). Its geographical location is $26^0 28'$N to$26^0 49'$N and $94^0 03'$E to$94^0 28' E$. The climate of the basin is subtropical monsoon climate. The average annual rainfall is about 215cm. Its drainage density in the Assam region (plain area) is around 87km /sq km, and the average gradient is 114 cm/km. The river covers approximately 162.5 km measured from its source up to its mouth and a total basin area of 916 km^2.

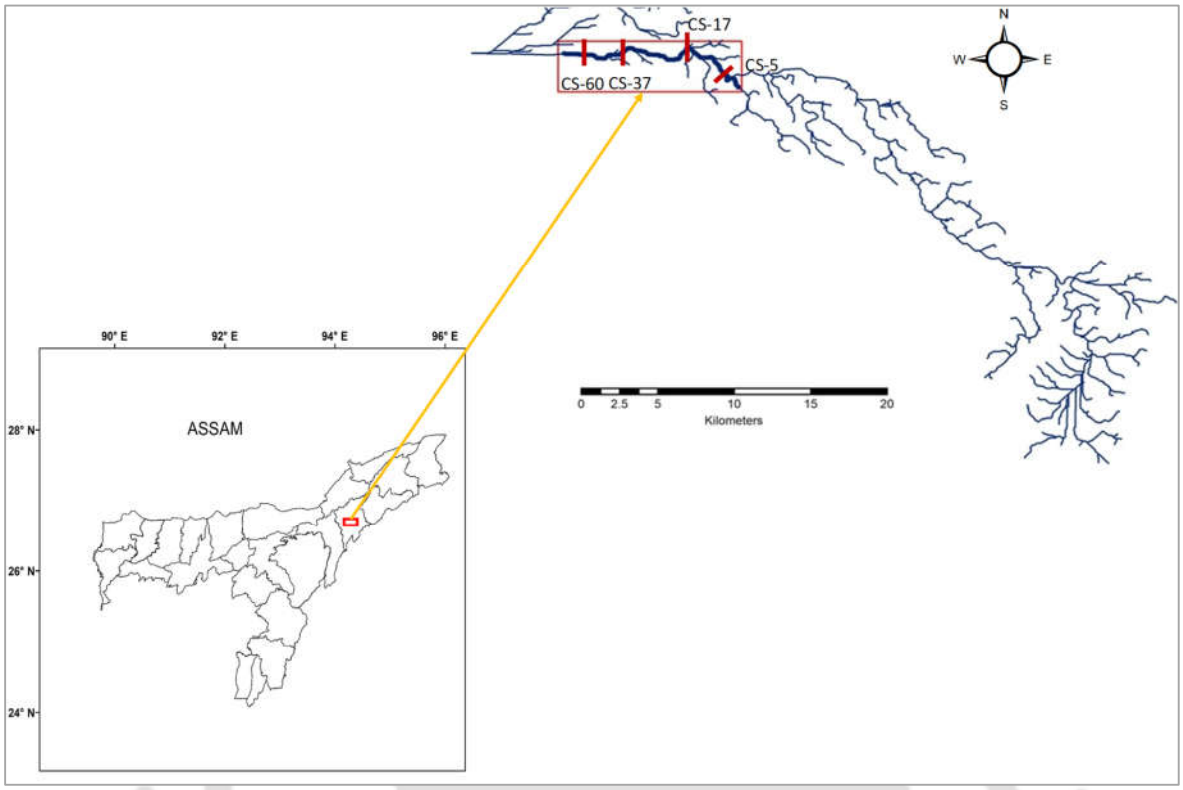

Figure 7.2: Study Area

7.2.2 Hydrological methods for ecological /environmental flow (EF) estimation

The ecological sustainability of the aquatic biota present in the Bhogdoi River system is primarily dependent on the rainfall amount. The basin receives maximum rainfall during summer and less in winter because of the southwest monsoon. With the lack of ecological information, the critical flow rate in the channel is calculated from two hydrological methods. The features of these methods are described below:

7.2.2.1 Flow duration curve analysis (FDCA) method

Flow duration curve analysis (FDCA) is a commonly used hydrologic method for conducting environmental flow assessment in a channel Vogel and Fennessey (1995). FDC is a cumulative frequency curve that indicates the streamflow availability as a percentage of time during the year. To prepare FDC, mean monthly flow data available at the gauged site are ranked according to the

magnitude, and their exceedance probability matrices are evaluated. Smakhtin (2001) stated that in a flow duration curve, the design low flow lies somewhere between 70 %(Q_{70}) and 90 %(Q_{90}). Q_{90} and Q_{95} are the most used low flow indicators in a channel (Pyrce 2004). Figure-7.2 shows the flow duration curve (FDC) of the study area.

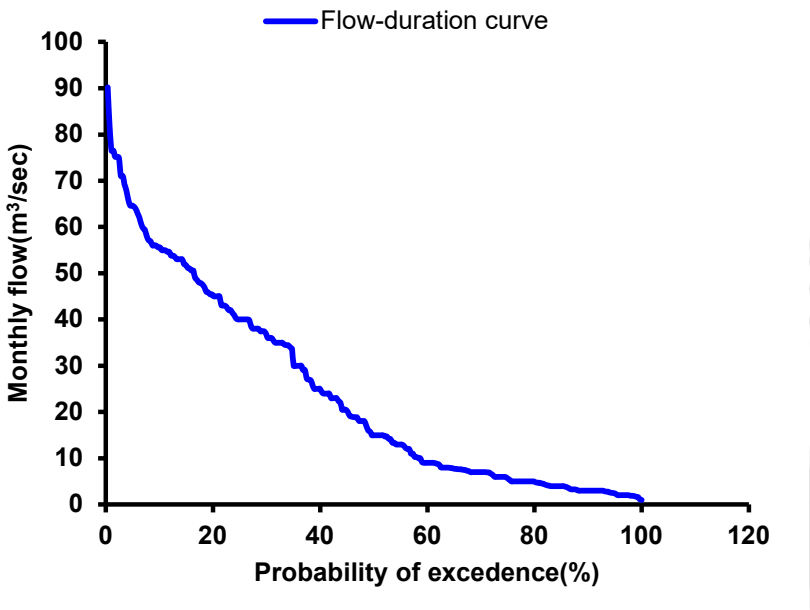

Figure 7.2: Flow duration curve

7.2.2.2 Flow duration curve shifting (FDCS) method

FDCS is a new method developed by Smakhtin and Anputhas (2008) to quantify the environmental flow. This method is proposed to determine the default flow duration curve characterizing a summary of EF for each environmental management class (EMC). Here, six EMC viz. EMCs A, B, C, D, E & F were defined. These classes represent river health as indicated by its significance in the flow system and sustainability. Details about these six EMCs classes are described in Table 7.1. The curves that provide a summary of EF are obtained by shifting the original FDC to the left along a defined probability axis. The probability axis consists of a set of 17 fixed percentage points

viz. 0.01, 0.1, 1,5, 10, 20, 30, 40, 50, 60, 70, 80, 90, 95, 99, 99.9 and 99.99% respectively, which are used as step in the shifting procedure. These 17 percentages were selected to ensure the entire flow range is covered. A lateral shift of one step means moving from one number to the next number in the list of 17 percentile. For instance, the lateral shifting of the original FDC to EMC-A (minor modification in-stream) indicates that the FDC is shifted by one step towards the left along the probability axis. This means that flow that was exceeded 99.99 percent of the time in the original FDC will now be exceeded 99.9 percent of the time, 99.9 percent becomes the flow at 99 percent, and so on.

Table 7.1: Discharges at different environmental management scenarios

Station	A.T road gauge station
Record period	1991-2015
Mean annual Runoff (MAR) (m^3/sec)	24.05
FDCA method (m^3/sec)	Q_{90} 2.077 Q_{95} 2.477
FDCS method	
Default management classes	EF (% MAR) at different EMC
EMC-A (Natural): Pristine condition or minor modification In-stream and riparian habitat	75.3
EMC-B (Slightly modified): Largely intact biodiversity and habitat despite water resource development and basin modification.	54.8
EMC-C (Moderately modified): The habitats and the biota have been disturbed, but basic ecosystem functions are still intact. Some sensitive species are lost and reduced in extent. Alien species present.	38.5

EMC-D (Largely modified): Large changes in natural habitat, biota, and basic ecosystem functions have arrived. A lower than expected species richness. Much lowered presences of intolerant species. Allien species prevail.	26.3
EMC-E (Seriously modified): Habitat availability and diversity have declined. A strikingly lower than expected species richness. Only tolerant species remain. Indigenous species can no longer breed. Allien species have invaded the ecosystem.	17.8
EMC-F (Critically modified): Modifications have reached a critical level, and the ecosystem has been completely modified with almost total loss of natural habitat and biota. In the worst case, the basic ecosystem function has been destroyed, and the changes are irreversible	12.3

Similarly, the lateral shifting of the original FDC to EMC-B (slightly modified) type river indicates that the original FDC will shift two steps to the left along the probability axis, which means a 90% flow would reduce to 99% flow and so on. This is graphically demonstrated in Figure 7.3. Again, the percentage between the specified 17 values is determined by linear interpolation.

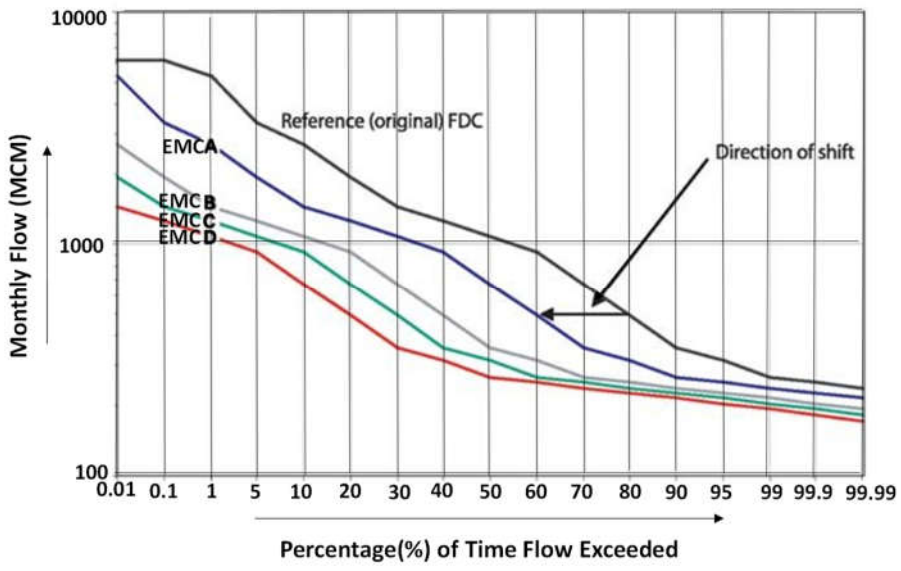

Figure 7.3: Estimation of Environmental Flow duration curves for different EMC

The curve obtained from the above calculation does not represent the actual flow sequence. Instead, it represents the summary of environmental flow acceptable for a particular EMC. Using the interpolation techniques proposed by Hughes and Smakhtin (1996), the calculated environmental FDCs can be converted to actual environmental flow time series in terms of percentage of mean annual runoff (MAR). The procedure is graphically presented in Figure 7.4. Here for demonstration, monthly data of the initial two years periods are shown. The interpolation method to construct the environmental flow time series curve for a particular flow event consists of four steps. Initially, for each month, identify the percentage point position or the streamflow hydrograph on the original FDC. In the second step, read off the monthly flow values of the equivalent percentage point from the Environmental FDC (EMC-A) at different ecological management classes. In the third step, construct the environmental flow-time series curve. Finally, obtain the environmental flow rates from the flow-time series curve at different months. The same procedure is carried out for all the monthly flow data. Further details about the interpolation method can be found in Hughes and Smakhtin (1996).

7.3 Hydrodynamic model

7.3.1 Governing equation and numerical scheme

The governing equations and the numerical scheme are elaborated in sections 3.4 (Equation 3.35-3.37) and 3.5.2.

7.3.2 Initial and boundary condition

The water surface at a falling gradient from upstream to downstream is applied as an initial condition. The observed and calculated environmental flow rates are assigned at the upstream and water levels at the downstream boundary.

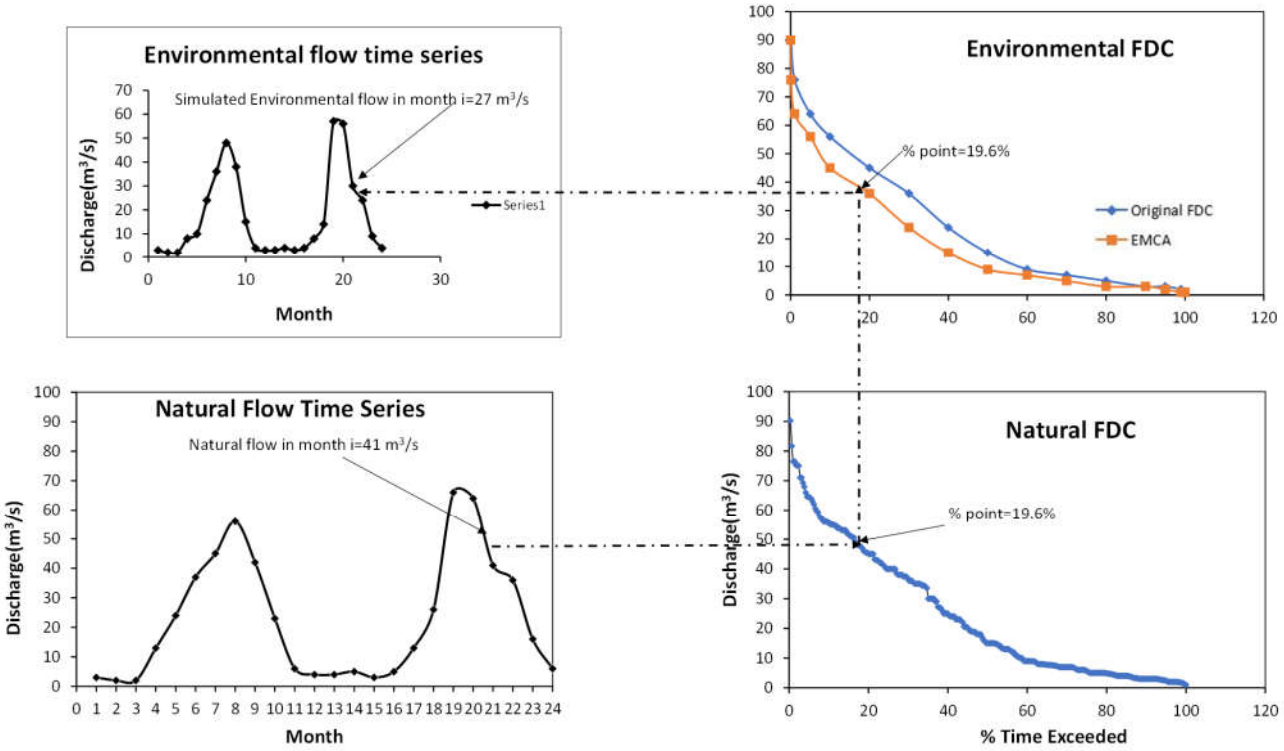

Figure 7.4: Generation of Environmental flow time series from the Environmental FDC

7.3.3 Stability of the model

The model stability is checked from the CFL condition. The method used for Courant number calculations is provided in section 3.5.3.

7.4 Habitat suitability curves and the WUA calculation for the Bhangun fish

Habitat suitability indices (HSI) are the weighting factor for a particular species that relates the hydraulic parameters with the ecological indicators. The indices are decided based on the available water depth, flow velocity, and substrate covers for the aquatic habitats in the flow domain. Substrate cover refers to the bed surface materials (Sand, gravel, clay, etc.) on which the marine organisms reside (Brown et al. 2000). Habitat preferences of some of the indigenous fish species available in the region are tabulated below

Table-7.2 Habitat preference of some indigenous fish species in Assam, India

Species Name	Scientific Name	Suitable Habitat		
		Flow depth	Velocity	Substrate cover
Bhangun	Labeo Bata	Medium	Moderate	Sandy-Clay soil
Rohu	Labeo Rohita	High	Medium-high	Sandy bed
Kholihona	Colisa Fasciata	Small	low	Clayey soil
Kurhi	Labeo Gonius	Medium	low	Clay soil

The target species considered in this study is the adult Bhangun fish, who are non-migratory and prefer to stay in one habitat throughout their lives (Mathur 1973; Mathur and Robbins 1971). It is available mainly in medium flow depth with moderate velocity regions and sandy-clayey soil with small gravel substrate. In-depth communication with the local fishing community was also carried out to gather expert opinions about the suitable aquatic environment of the targeted fish. The flow-habitat relationship is expressed in WUA by incorporating the habitat suitability curves (HSC) in the hydrodynamic model for different flow events. These curves represent the favorable hydraulic and ecological conditions of the target species in the river. These curves are constructed by relating the hydrodynamic variables to the behavior of the target species in the aquatic environment (Bovee 1982). The suitability indices range from 0 (unsuitable for the aquatic species) to 1 (excellent condition). Computed hydrodynamic parameters from the model are used to construct the habitat suitability curves**.** In this study, the curves for the target species are developed by considering the three parameters viz. flow depth, current speed, and the substrate cover.

The weighted usable area for the target fish is estimated from the composite suitability index (CSI) and the total flow area in the domain. The HSI at the cell points are combined to develop the composite suitability matrix for the study reach. WUA is then obtained by multiplying the composite suitability index with the cross-sectional area.

If h,v,h1,v1,h2,v2 and h3,v3 are the computed flow depth and velocity at grid point (i,j) ,(i+1,j),(i+1,j+1)and (i,j+1) then the weighted average flow depth and velocity at cell 1 (as shown in figure 7.5) is obtained by using a four-point averaging method(equation-5).The corresponding suitability indices for flow depth H and velocity V at cell-1 is obtained from the habitat suitability curves(HSC), and CSI is calculated from equation-6

$$H = 1/4(h + h1 + h2 + h3),\ \ V = 1/4(v + v1 + v2 + v3) \tag{7.1}$$

$$CSI_{i,j}=HSI_{h(i,j)}*HSI_{v(i,j)}*HSI_{(substrate\ cover)} \tag{7.2}$$

The weighted usable area (WUA) in the channel is calculated from equation-7.3

$$WUA = \sum_{i,j=1}^{N} 1\, CSI_{i,j} * A_{i,j} \tag{7.3}$$

Where $CSI_{i,j}$= composite suitability index and $A_{i,j}$ = cross-sectional area

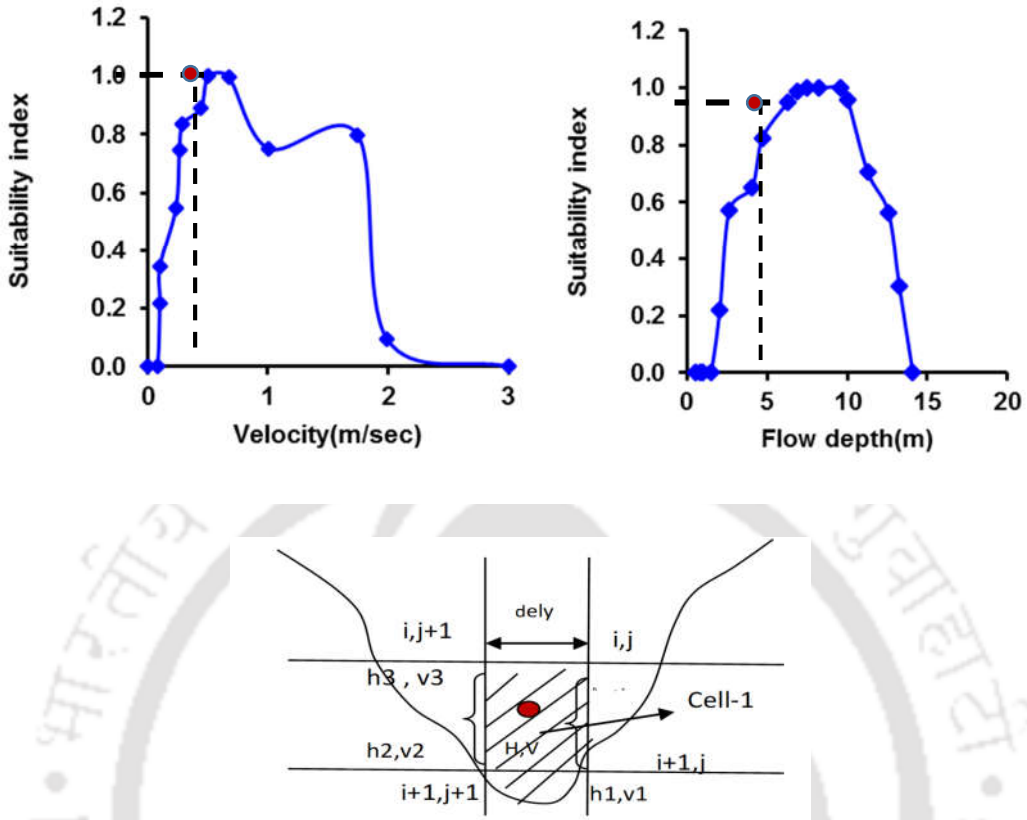

Figure 7. 5: Composite suitability index at cell -1 in a channel section

7.5 Result and discussion

7.5.1 Environmental flow rates from FDCA method

The flow duration curve is prepared from the 24 years average monthly data obtained from the state water resource department. The maximum and average recorded discharges from this flow series data are found to be 90 m^3/sec and 24m^3 /sec. Q_{90} and Q_{95} (low flow indicators) in the channel are found as 2.077 and 2.477m^3/sec.

7.5.2 Environmental flow rate from (EFR) FDCS method

This method evaluates the environmental flow by laterally shifting the flow duration curve towards the left direction and express the flow rate as a percentage of mean annual runoff (MAR). GEFC (Global environmental flow calculator) model employed here works on the FDCS principle to assess the EFR.Table-1 shows the EFR corresponding to the different management classes. It is found that the ecosystem function progressively degraded if the flow reaches 12% of MAR (Class-F) in the stretch. However, the stream maintains biodiversity and ecological resilience at 54.3-75.3 % (Class-A & B) MAR. At present, the E-flow rates corresponding to EMC-A and EMC-B are the best possible flow condition in the stream since there is not much basin level modification. The minimum flow required under the two EMC is found as 18 and 13.25m^3 /sec. Discharge at Q_{90} and Q_{95}(≈ Class F EMC) are not feasible with the existing stream condition; hence it is not considered for further simulation. Figure -7.6 shows the environmental flow rates calculated from the above two methods.

7.5.3 Hydrodynamic -habitat simulation in the domain

The flow rates from the hydrological analysis are used in the shallow water model to compute the hydraulic parameters, viz. water depth and current speed at different cross-sections. Six different flow scenarios are simulated with the hydrodynamic model to estimate these parameters. The flow depth contours obtained from the simulation under the different flow scenarios are shown in figure -7.7. The computational time step is considered as 0.1sec, and the model is run till a stable condition is met. Manning's roughness coefficient is calculated from Stickler's equation. Stickler's equation relates the manning's roughness coefficient with the mean particle diameter (d_{50}). The mean particle diameter (d_{50}) of the domain is taken from the sieve analysis study carried out by Buragohain and Khaund (Buragohain and Khaund 2019). Based on the $d_{50,}$ the manning's n value

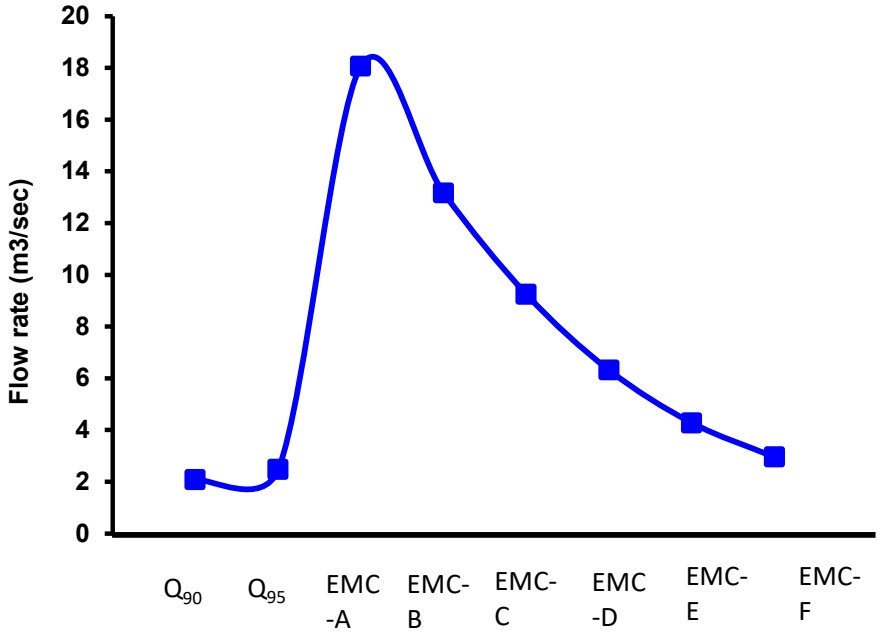

Figure 7.6: Flow rates $(m^3/s)$for different EMC, Q_{90} and Q_{95}

is found out to be 0.03. The same n value is applied in the simulation as the bed material within the modeled reach was similar (mostly sandy soil). During each calculation, the model stability is checked using the CFL status and found satisfactory. The model outputs are validated with the observed water level data available at c/s -5 and c/s-17, as shown in Figure -7.8 (a, b). The observed velocity data in the modeled area is taken from the study conducted by Bharali and Goswami (Bharali and Goswami 2016). The computed velocities are compared with these data presented in Figure 7.8(c). Results show a satisfactory agreement between the computed outputs and the measured data.

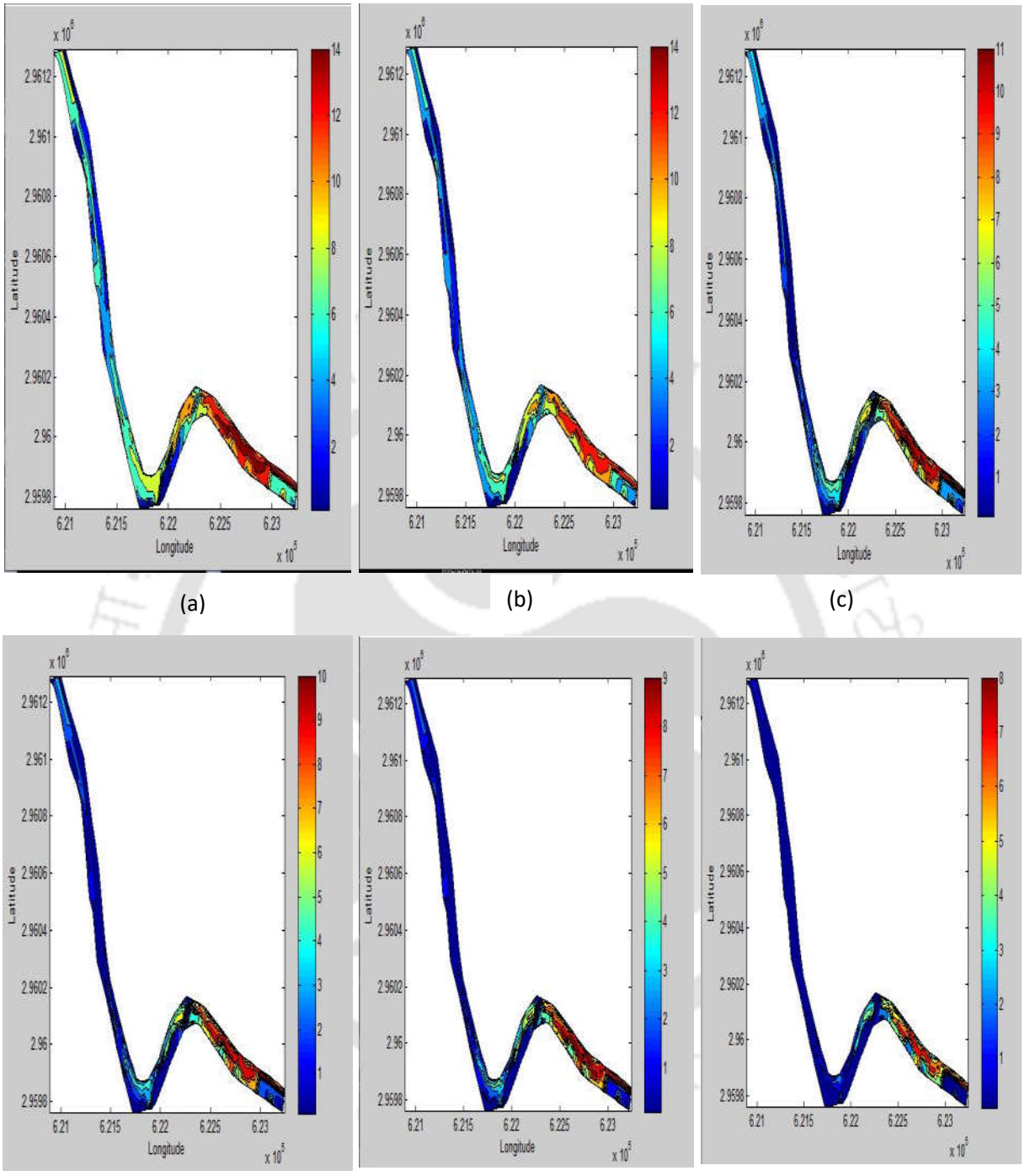

Figure 7.7: Flow depth contours form the hydrodynamic computations (a) Q=90 m^3/sec (b) Q=75 m^3/sec (c) Q=60 m^3/sec (d) Q=45 m^3/sec(e) Q=30 m^3/sec (f) Q=18.13 m^3/sec

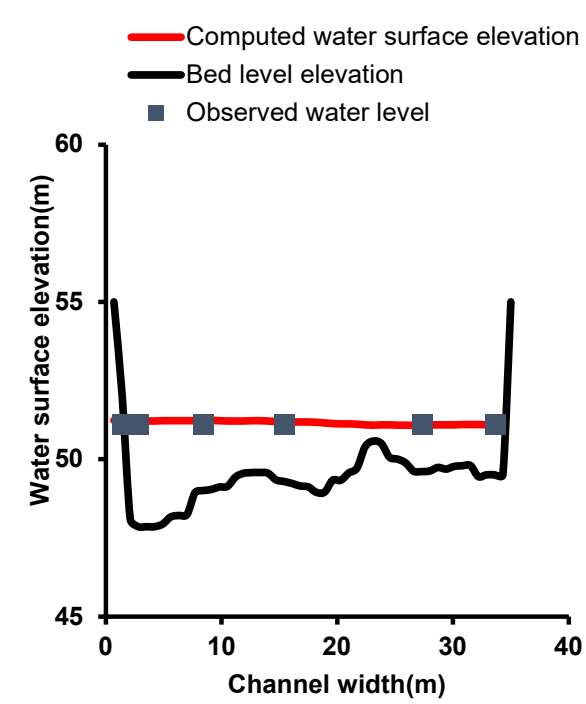

(a)

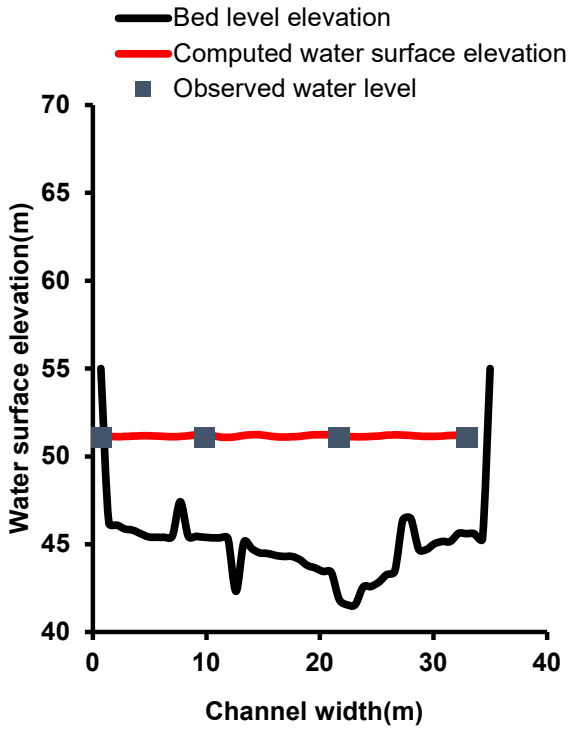

(b)

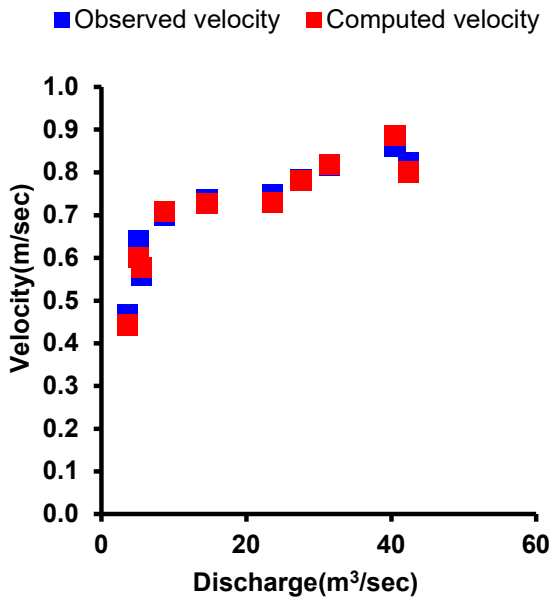

(c)

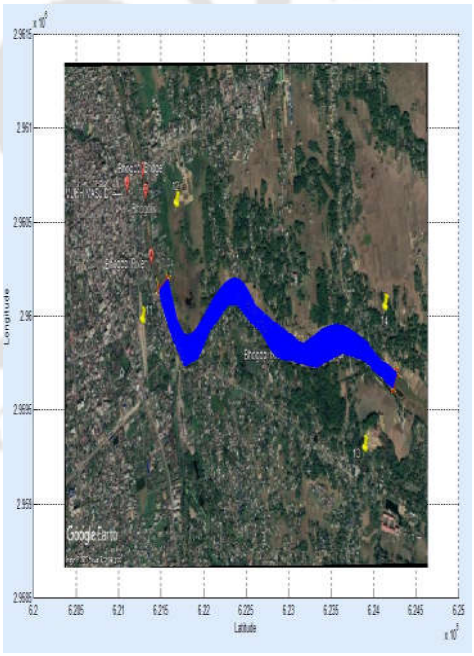

(d)

Figure 7.8: (a), (b) Computed and observed water level (c) Comparison of the computed and measured velocity (d) Generated grids in the flow domain

The model performance is evaluated using two statistical indices: Root mean square error (RMSE) and Nash-Sutcliffe efficiency (NSE).

Root mean square error (RMSE)

$$RMSE = \sqrt{\frac{1}{n}\sum_{i=1}^{n}(f_i - y_i)^2} \tag{7.4}$$

Nash-Sutcliffe efficiency (NSE)

$$NSE = 1 - \frac{\frac{1}{n}\Sigma_{i=1}^{n}(f_i - y_i)^2}{\frac{1}{n}\Sigma_{i=1}^{n}(y_i - \underline{y})^2} \tag{7.5}$$

Where y_i is the observed data and f_i is the model predicted data and $\underline{y}$ is the average value of the observed data

The range of NSE and RMSE values is presented in table-7.2. The entire flow domain is discretized into 40000(200x200) mesh points, as shown in Figure 7.8(d). The hydrodynamic outputs indicate that the flow depth changes between 30-60% at the maximum and the calculated E-flow rate. The water depth and the current speed in the domain are found as14.75m and 3.5 m/sec, respectively, for the maximum discharge in the flow area. The flow depth and current speed information gathered from the hydrodynamic computations are used as critical parameters in developing the habitat suitability curves (HSC) for the target species.

Table-7.3: Statistical index for model evaluation

Statistical index	NSE	RMSE
	0.975	0.208

The HSC presented in figure 7.9(a) indicates that the suitability index for the target species progressively increases when the flow depth changes from the lower to the medium flow depth (7.5-8m) and gradually decreases near the high depth regions. Similarly, the suitability index is maximum at the locations where the velocity vectors ranged between 0.8-1.1 m/sec in the domain, as shown in figure7.9 (b). Near the maximum and minimum current speed regions, the suitability index is reduced to 0. The reason being the targeted fish prefers to stay in a moderate water depth and velocity region. Figure 7.9(c) shows that the maximum suitability index value for the substrate cover is the sandy clay soil. It indicates that the sandy clay soil is the suitable substrate cover for the target species.

7.5.4 Evaluation of WUA and CSI estimation

The composite suitability index and the WUA are calculated from Equations 7.2 and 7.3. The total flow area and the WUA for the six different streamflow events are shown in figure -7.10. The optimal flow rate for the target species is decided from the calculated WUA. At high discharge, the flow depth and velocity in the domain significantly increase, and the total flow area is maximum. However, this is not a preferable habitat condition for the adult Bhangun fish, as indicated by the lowest WUA.

Similarly, the flow depth and current speed corresponding to EMC A and EMC-B are found within the range of 4.2-7m and 0.25-0.7 m/s. The calculated WUA is also significantly less and insufficient for the adult species to sustain at this flow rate. Figure 7.10 indicates that the favorable habitat condition for the target fish is when the flow in the channel ranges between 30-60 m^3/s. An increasing trend is observed within these flow rates, and a gradually decreasing WUA profile is noted beyond this range.

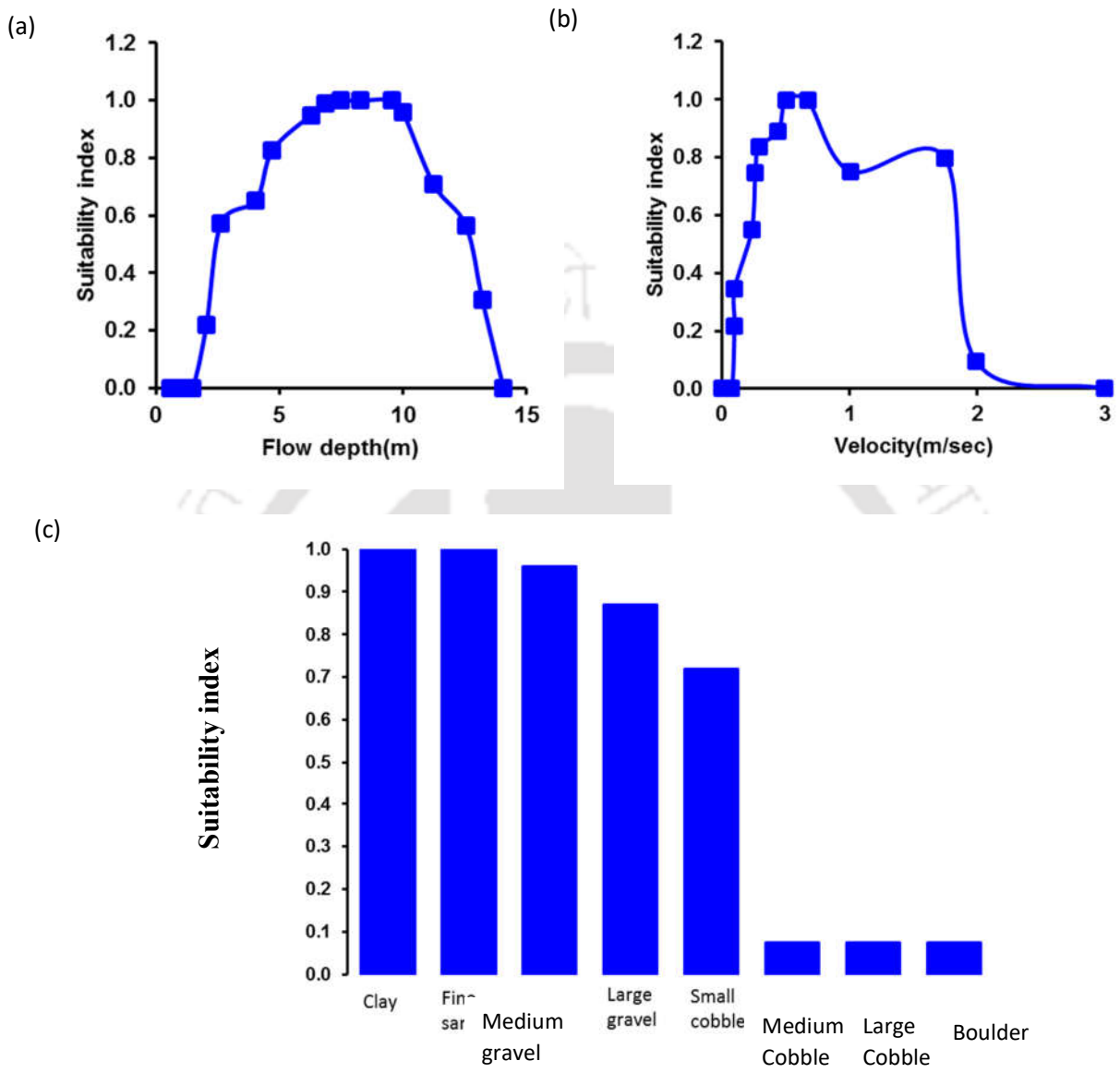

Figure 7.9: Habitat suitability curves for the adult Bhangun Fish in the Bhogdoi River, Assam

Thus, the channel flow should be maintained to this extent to sustain the target aquatic species. The flow depth and velocity at this flow range are found between 7.2-9.1 m, and 0.85-1.3 m/sec, respectively.

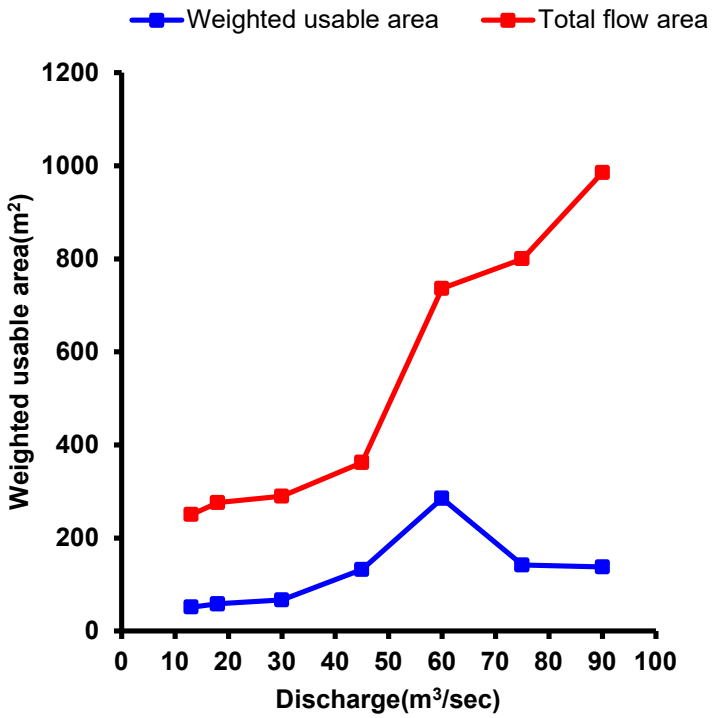

Figure 7.10: Weighted usable area for the Bhangun fish in the Bhogdoi River, India

7.6 Conclusion

In this chapter, an Eco-hydrological assessment is carried out to estimate the optimal flow requirement for the Bhangun fish in the Bhogdoi River. Two hydrological methods based on flow duration curves are used to study the environmental flow rate calculation. Hydrodynamic simulation is carried at different discharges by employing a two-dimensional shallow water model and validated with the observed data. The RMSE and NSE values indicate a good model performance. The suitability indices for the targeted fish species are generated from the computed flow parameters in the domain. It is observed that the maximum flow and the ecological flowrate do not provide a suitable habitat condition for the target species to reside in the channel. It is

necessary to undertake proper restoration strategies to conserve the targeted fish population in the reach. The inclusion of the hydrodynamic habitat modeling study on decision-making strategies before executing the proposed irrigation scheme will help stakeholders understand the required flow rate in the stream to maintain ecological sustainability. This modeling approach can be further extended in different tributaries to decide the optimal water allocation and favorable habitat condition for the targeted species at different life stages.

CHAPTER-8

CONCLUSION

8.1 Introduction

A brief summary for each of the objectives carried out during the study has been presented at the end of each chapter. A comprehensive summary and general discussion followed by the future scope of the entire research work is presented here.

8.2 General discussion and conclusion

8.2.1 Development of two –dimensional unsteady flow simulation mnodel in natural terrain

Reviewing the different studies on the mathematical form of shallow water model, two different formulations are observed. The water depth appears as a temporal derivative in the mass conservation equation and at the source term in one formulation. However, water surface elevation replaces the flow depth in the mass and momentum equations in the second approach. The bed elevations in natural domains, especially in braided streams, are highly undulating, and the presence of bed gradient in the source term probably affects the model performance. Due to the inconsistent bed slope discretizations, there is a possibility of model failure near the wet-dry interface. Thus, a non-conservative formulation of the shallow water model is derived by balancing the flux gradient and the source terms in the momentum equation and used during the study. The advantage of the formulation is that it uses the water surface elevation in the mass conservation equation and water surface gradient in the source term, giving sufficient flexibility to apply the shallow water model in wavy terrains.

Mathematically the governing flow equations are non-linear and hyperbolic. In that case, numerical methods such as finite difference, finite volume, and finite element are used to solve

these equations. Different studies indicate that the finite difference method is a simple and effective technique to solve these equations. The explicit MacCormack predictor-corrector finite difference scheme is a marching finite difference scheme that predicts the flow variables by solving the mass and momentum equations. However, the numerical scheme is second-order accurate and generates spurious oscillations in the solution domain. These numerical oscillations are suppressed by employing the TVD scheme along with the Mac-Cormack predictor-corrector method. The governing equations are transformed into boundary-fitted coordinates to facilitate the application of the present model in the curvilinear domains. The developed model is then calibrated and validated with the available experimental and analytical studies, and the performance of the model is found excellent. The model application is further extended to field problems, mainly a braided reach of the Brahmaputra River in Guwahati and near Nimatighat, Jorhat, India, A mountainous terrain of Tiding River, Arunachal Pradesh, India, and a braided terrain with four non-submerged groins near Majuli Island, India. The upstream and downstream boundary conditions are feed into the model from the observed data, and the computed outputs are compared with the field-measured results. The results from the simulation agree well with the measured data.

8.2.2 Coupling of vegetations within the developed model

The aquatic plants are an integral part of the natural domains and influence the hydrodynamics of vegetated sections. The presence of vegetation modifies the flow sediment behavior, habitat cover for aquatic species, and turbulence regimes. The aquatic vegetation is broadly classified into rigid and flexural depending upon the stem rigidity. In this study, a fully coupled flow and rigid vegetation model is proposed and applied to laboratory flume problems and a natural channel. The roughness from the vegetation is computed from the Arcment and Scheinder (1989) and integrated into the momentum equation. Initially, the coupled model is validated with the experimental study

conducted by Wang et al. (2018) and found satisfactory. Later the model is employed to evaluate the influence of different vegetation densities over the transcritical flow state, secondary current strength, and near bank velocity profiles. The computed results indicate that using the different densities of vegetation, the magnitude of the centrifugally induced secondary current progressively decreases near the outer bend of the curved channel.

8.2.3 Developememt of a quasi three dimensional framework for vertical velocity profile estimation in vegetated and non-vegetated channel

The governing shallow water equations are in depth-averaged form. Hence, the considerable information of the velocity profile along the vertical direction cannot be achieved, which is essential for estimating the scour depth and designing a stable hydraulic structure. In this work, a quasi-three dimensional approach is proposed for distributing the vertical velocity profile by linking Shanon's entropy theory with the developed 2D model. The computed profiles are compared with the current meter readings gathered from the field and found satisfactory. Also, the influence of submerged flexible vegetation over the vertical velocity structure is computed from the quasi 3D model. The vegetation drag from the flexible stem is integrated into the hydrodynamic model. The bending of flexible vegetation under different flow events is calculated from the large deflection cantilever beam theory. The velocity profile in the vegetation layer is estimated from Reynold's stress equation, while in the free water layer, the entropy model is applied. The performance of the proposed model is evaluated with two experimental datasets performed by Jarvela (2005) and Kurbak et al.(2008). The results are found satisfactory.

8.2.4 Ecohydraulic approach for adequate flow rate prediction for the Bhangun fish in Bhogdoi River, India

With this understanding, the applicability of the proposed model is extended in the field of aquatic ecology. An Eco-hydrological assessment is carried out to estimate the optimal flow requirement for the Bhangun fish in the Bhogdoi River, Assam, India. The environmental flow rates in the domain are estimated from FDCS and FDCA methods. From FDCA method, Q_{90} and Q_{95} are used as low flow indicators whereas in FDCS method, environmental flow duration curves are established and flow rates corresponding to different environmental management classes are estimated.The results from the hydrodynamic simulations indicate that maximum depth and velocity lies within the range of 12.75-14m and 2.7-3.5m/sec. Based on the discussion with the fishing community and the computed hydrodynamic parameters habitat suitability curves are constructed for the targeted species. Results indicate that for the sustainability of the target species, the minimum flow in the Bhogdoi River must be maintained between $30m^3$/sec-$60m^3$/sec.

8.4 **Scope for future work**

Some of the possible works that can be carried out in the future are mentioned below

1) The present shallow water model neglects the turbulence terms during the hydrodynamic computations. The inclusion of a strong turbulence closure model such as k-epsi and k-omega model with the governing equations may increase the model efficiency while simulating the vegetation effect on the open channel flow.
2) The sediment transport in a natural channel is an essential aspect while designing a suitable ecosystem for the aquatic species. The erosion and deposition at different locations will give a proper insight into habitat suitability for different species. Moreover, the morphological changes in the domain due to channel dredging can be reasonably predicted by incorporating the sediment transport formulations with the shallow water model. As such, sediment transport studies can be carried out in the future.

3) The model can be applied to compute the required flow rate for different endangered aquatic species at different life stages such as the breeding stage, growth stage, and adult stage. Similarly, the flow rate can be decided for different aquatic species to survive under the influence of different vegetation characteristics such as stem diameter, canopy density, etc.
4) A reservoir optimization model can be coupled with the developed hydrodynamic routing model to optimize release from an upstream reservoir to have optimal flow rates considering the need for different fish species.
5) The model can be coupled with the heterogeneous vegetations (flexible and rigid) in a stream to investigate the combined effect over the flow pattern

REFERENCE

1. Absi, R. (2011). "An ordinary differential equation for velocity distribution and dip-phenomenon in open channel flows." *Journal of Hydraulic Research*, 49(1), 82–89.
2. Afzalimehr, H., Maddahi, M. R., Sui, J., and Rahimpour, M. (2019). "Impacts of vegetation over bedforms on flow characteristics in gravel-bed rivers." *Journal of Hydrodynamics*, 31(5), 986–998.
3. Alessandro, V., and Lorenzo, B. (2006). "Divergence Form for Bed Slope Source Term in Shallow Water Equations." *Journal of Hydraulic Engineering*, American Society of Civil Engineers, 132(7), 652–665.
4. Ammari, A., Moramarco, T., and Meddi, M. (2017). "A simple entropy-based method for discharges measurements in gauged and ungauged river sites: The case study of coastal Algerian rivers." *Bulletin de l'Institut Scientifique*.
5. Amreeva, G., and Kurbak, A. (2007). "Experimental studies on the dimensional properties of half Milano and Milano rib fabrics." *Textile Research Journal*, Sage Publications Sage UK: London, England, 77(3), 151–160.
6. Arcement, G. J., and Schneider, V. R. (1989). "Guide for selecting Manning's roughness coefficients for natural channels and flood plains." US Government Printing Office Washington, DC.
7. Arthington, Á. H., Naiman, R. J., Mcclain, M. E., and Nilsson, C. (2010). "Preserving the biodiversity and ecological services of rivers: new challenges and research opportunities." *Freshwater Biology*, Wiley Online Library, 55(1), 1–16.
8. Baptist, M. J. (2003). "A flume experiment on sediment transport with flexible, submerged vegetation." *International workshop on riparian forest vegetated channels: hydraulic,*

morphological and ecological aspects, RIPFOR, Trento, Italy.

9. Baptist, M. J., Babovic, V., Rodríguez Uthurburu, J., Keijzer, M., Uittenbogaard, R. E., Mynett, A., and Verwey, A. (2007). "On inducing equations for vegetation resistance." *Journal of Hydraulic Research*, Taylor & Francis, 45(4), 435–450.
10. Bellos, C. V, Soulis, J. V, and Sakkas, J. G. (1991). "Computation of two-dimensional dam-break-induced flows." *Advances in Water Resources*, 14(1), 31–41.
11. Bellos, V., and Hrissanthou, V. (2011). "Numerical simulation of a dam-break flood wave." *European Water*, 33, 45–53.
12. Bharali, R. J., and Goswami, R. (n.d.). "A Study on the Relationship between Siltation and Flow Parameter of a Typical Alluvial River-Studied Open Channel Flow Bhogdoi River." *International Journal of Advanced Engineering Research and Science*, AI Publications, 3(5), 236730.
13. Bockelmann, B. N., Fenrich, E. K., Lin, B., and Falconer, R. A. (2004). "Development of an ecohydraulics model for stream and river restoration." *Ecological Engineering*, 22(4), 227–235.
14. Bomers, A., Schielen, R. M. J., and Hulscher, S. J. M. H. (2019). "The influence of grid shape and grid size on hydraulic river modelling performance." *Environmental Fluid Mechanics*, 19(5), 1273–1294.
15. Bovee, K. D. (1982). "A guide to stream habitat analysis using the instream incremental flow methodology." *Instream Flow Information Paper. United States Fish and Wildlife Service. FWS/OBS-82/26*, 12(82), 1–248.
16. Brown, S. K., Buja, K. R., Jury, S. H., Monaco, M. E., and Banner, A. (2000). "Habitat suitability index models for eight fish and invertebrate species in Casco and Sheepscot

Bays, Maine." *North American Journal of Fisheries Management*, Taylor \& Francis, 20(2), 408–435.

17. Buckman, L. J. (2013). "Hydrodynamics of partially vegetated channels: stem drag forces and application to an in-stream wetland concept for tropical, urban drainage systems."
18. Burkhardt-Holm, P., Giger, W., GUttinger, H., Ochsenbein, U., Peter, A., Scheurer, K., Segner, H., Staub, E., and Suter, M. J.-F. (2005). "Where have all the fish gone?" ACS Publications.
19. Carollo, F. G., Ferro, V., and Termini, D. (2002). "Flow velocity measurements in vegetated channels." *Journal of Hydraulic Engineering*, American Society of Civil Engineers, 128(7), 664–673.
20. Chao-lin, B. (1991). "Application of entropy concept in o p e n - c h a n n e l f l o w study." 117(5), 615–628.
21. Chao-Lin, C., and Abidin, S. C. A. (1995). "Maximum and Mean Velocities and Entropy in Open-Channel Flow." *Journal of Hydraulic Engineering*, American Society of Civil Engineers, 121(1), 26–35.
22. Chen, L. (2010). "An integral approach for large deflection cantilever beams." *International Journal of Non-Linear Mechanics*, 45(3), 301–305.
23. Chen, Y.-C., and Chiu, C.-L. (2004). "A fast method of flood discharge estimation." *Hydrological Processes*, John Wiley & Sons, Ltd, 18(9), 1671–1684.
24. Chiu, C.-L. (1989). "Velocity distribution in open channel flow." *Journal of Hydraulic Engineering*, American Society of Civil Engineers, 115(5), 576–594.
25. Chiu, C.-L., and Tung, N.-C. (2002). "Maximum velocity and regularities in open-channel flow." *Journal of hydraulic engineering*, American Society of Civil Engineers, 128(4),

390–398.

26. Dauwalter, D. C., and Fisher, W. L. (2008). “Spatial and temporal patterns in stream habitat and smallmouth bass populations in eastern Oklahoma.” *Transactions of the American Fisheries Society*, Taylor \& Francis, 137(4), 1072–1088.
27. David, L. (2008). “Flow through Rigid Vegetation Hydrodynamics.” Thesis of Master of Science, Virginia Polytechnic Institute and State University.
28. Defina, A., and Bixio, A. C. (2005). “Mean flow and turbulence in vegetated open channel flow.” *Water Resources Research*, John Wiley & Sons, Ltd, 41(7).
29. Fennema, R. J., and Chaudhry, M. H. (1986). “Explicit numerical schemes for unsteady free-surface flows with shocks.” *Water Resources Research*, John Wiley & Sons, Ltd, 22(13), 1923–1930.
30. Fennema, R. J., and Hanif Chaudhry, M. (1989). “Implicit methods for two-dimensional unsteady free-surface flows.” *Journal of Hydraulic Research*, Taylor & Francis, 27(3), 321–332.
31. Fiedler, F. R., and Ramirez, J. A. (2000). “A numerical method for simulating discontinuous shallow flow over an infiltrating surface.” *International Journal for Numerical Methods in Fluids*, John Wiley & Sons, Ltd, 32(2), 219–239.
32. Fischer-Antze, T., Stoesser, T., and Olsen, N. R. B. (2001). “Modélisation numérique 3D d’un écoulement en canal avec végétation submergée.” *Journal of Hydraulic Research*, 39(3), 303–310.
33. Garcia-Navarro, P., and Saviron, J. M. (1992). “McCormack’s method for the numerical simulation of one-dimensional discontinuous unsteady open channel flow.” *Journal of Hydraulic Research*, Taylor & Francis, 30(1), 95–105.

34. Gholami, V., and Khaleghi, M. R. (2013). “The impact of vegetation on the bank erosion (case study: The haraz river).” *Soil and Water Research*, 8(4), 158–164.
35. Gillihan, T. (2013). “Dynamic vegetation Roughness in the riparian zone.”
36. Ginting, B. M. (2017). “A two-dimensional artificial viscosity technique for modelling discontinuity in shallow water flows.” *Applied Mathematical Modelling*, 45, 653–683.
37. Glenz, C., Iorgulescu, I., Kienast, F., and Schlaepfer, R. (2008). “Modelling the impact of flooding stress on the growth performance of woody species using fuzzy logic.” *Ecological Modelling*, 218(1), 18–28.
38. Goutal, N. (1997). *Proceedings of the 2nd workshop on dam-break wave simulation*. Department Laboratoire National d’Hydraulique, Groupe Hydraulique Fluviale.
39. Greco, M. (2015). “Effect of bed roughness on 1-D entropy velocity distribution in open channel flow.” *Hydrology Research*, 46(1), 1–10.
40. Green, J. C. (2005). “Modelling flow resistance in vegetated streams: Review and development of new theory.” *Hydrological Processes*, 19(6), 1245–1259.
41. Hannah, L., Midgley, G., Andelman, S., Araújo, M., Hughes, G., Martinez-Meyer, E., Pearson, R., and Williams, P. (2007). “Protected area needs in a changing climate.” *Frontiers in Ecology and the Environment*, Wiley Online Library, 5(3), 131–138.
42. Hernandez-Duenas, G., and Beljadid, A. (2016). “A central-upwind scheme with artificial viscosity for shallow-water flows in channels.” *Advances in Water Resources*, 96, 323–338.
43. Houghton, D. D., and Kasahara, A. (1968). “Nonlinear shallow fluid flow over an isolated ridge.” *Communications on Pure and Applied Mathematics*, Wiley Subscription Services, Inc., A Wiley Company New York, 21(1), 1–23.

44. Huai, W., Wang, W., and Zeng, Y. (2013a). “Two-layer model for open channel flow with submerged flexible vegetation.” *Journal of Hydraulic Research*, 51(6), 708–718.
45. Huai, W., Wang, W., and Zeng, Y. (2013b). “Two-layer model for open channel flow with submerged flexible vegetation.” *Journal of Hydraulic Research*, Taylor & Francis, 51(6), 708–718.
46. Huai, W., Zhang, J., Katul, G. G., Cheng, Y., Tang, X., and Wang, W. (2019). “The structure of turbulent flow through submerged flexible vegetation.” *Journal of Hydrodynamics*, 31(2), 274–292.
47. Huang, Z., Yao, Y., Sim, S. Y., and Yao, Y. (2011). “Interaction of solitary waves with emergent, rigid vegetation.” *Ocean Engineering*, Elsevier, 38(10), 1080–1088.
48. Hughes, D. A., and Smakhtin, V. (1996). “Daily flow time series patching or extension: a spatial interpolation approach based on flow duration curves.” *Hydrological Sciences Journal*, Taylor \& Francis, 41(6), 851–871.
49. Isaacson, E., Stoker, J. J., and Troesch, A. (1958). “Numerical solution of flow problems in rivers.” *Journal of the Hydraulics Division*, American Society of Civil Engineers, 84(5), 1–18.
50. J., F. R., and Hanif, C. M. (1990). “Explicit Methods for 2-D Transient Free Surface Flows.” *Journal of Hydraulic Engineering*, American Society of Civil Engineers, 116(8), 1013–1034.
51. Järvelä, J. (2005). “Effect of submerged flexible vegetation on flow structure and resistance.” *Journal of hydrology*, Elsevier, 307(1–4), 233–241.
52. John, D., and Anderson, J. (1995). “CFD john d anderson.pdf.”
53. Junna, W., and Zhonglong, Z. (2019). “Evaluating Riparian Vegetation Roughness

Computation Methods Integrated within HEC-RAS." *Journal of Hydraulic Engineering*, American Society of Civil Engineers, 145(6), 4019020.

54. Kalita, H. (2016). "A New Total Variation Diminishing Predictor Corrector Approach for Two-Dimensional Shallow Water Flow." *Water Resources Management*, 30.
55. Kalkwijk, J. P. T., and De Vriend, H. J. (1980). "COMPUTATION OF THE FLOW IN SHALLOW RIVER BENDS." *Journal of Hydraulic Research*, Taylor & Francis, 18(4), 327–342.
56. Kashaigili, J. J., Kadigi, R. M. J., Lankford, B. A., Mahoo, H. F., and Mashauri, D. A. (2005). "Environmental flows allocation in river basins: Exploring allocation challenges and options in the Great Ruaha River catchment in Tanzania." *Physics and Chemistry of the Earth, Parts A/B/C*, Elsevier, 30(11–16), 689–697.
57. Keramaris, E., Pechlivanidis, G. I., and Pechlivanidis, I. G. (2015). "The Different Impact of a Half-Separated Gravel and Vegetated Bed in Open Channels." *Environmental Processes*, 2(1), 123–132.
58. Khwairakpam, E., Khosa, R., Gosain, A., and Nema, A. (2020). "Habitat suitability analysis of Pengba fish in Loktak Lake and its river basin." *Ecohydrology*, 13(1).
59. Kim, S. K., and Choi, S. U. (2019). "Comparison of environmental flows from a habitat suitability perspective: A case study in the Naeseong-cheon Stream in Korea." *Ecohydrology*, 12(6).
60. Klonidis, A. J., and Soulis, J. V. (2001). "An implicit scheme for steady two-dimensional free-surface flow calculation." *Journal of Hydraulic Research*, Taylor & Francis, 39(4), 393–402.
61. Klopstra, D., Barneveld, H. J., Noortwijk, J. M., and van Velzen, E. H. (2002). "Analytical

model for hydraulic roughness of submerged vegetation presented at : submerged vegetation." *The 27th congress of the internaltional association for hydraulic research, San Francisco, 1997; Proceedings of Theme A, Managing Water: coping with scarcity and abundance*, (3).

62. Kubrak, E., Kubrak, J., and Rowiński, P. M. (2012). "Influence of a method of evaluation of the curvature of flexible vegetation elements on vertical distributions of flow velocities." *Acta Geophysica*, 60(4), 1098–1119.
63. Kundu, S. (2017). "Prediction of velocity-dip-position over entire cross section of open channel flows using entropy theory." *Environmental Earth Sciences*, Springer Berlin Heidelberg, 76(10), 1–16.
64. L., A. M., Q., C. Z., and L., K. M. (2004). "Modeling Low Flows on the Cosumnes River." *Journal of Hydrologic Engineering*, American Society of Civil Engineers, 9(2), 126–134.
65. Li, P.-W., and Fan, C.-M. (2017). "Generalized finite difference method for two-dimensional shallow water equations." *Engineering Analysis with Boundary Elements*, 80, 58–71.
66. Li, Q., Cai, T., Wang, H., Xue, Y., Bai, L., Li, P., You, B., and others. (2009). "Computation methods of minimum and optimal instream ecological flow for the upper Huaihe River, China." *IAHS publication*, 20, 122.
67. Liang, D., Falconer, R. A., and Lin, B. (2006). "Comparison between TVD-MacCormack and ADI-type solvers of the shallow water equations." *Advances in Water Resources*, 29(12), 1833–1845.
68. Liang, D., Lin, B., and Falconer, R. A. (2007). "A boundary-fitted numerical model for flood routing with shock-capturing capability." *Journal of Hydrology*, 332(3), 477–486.

69. Liang, D., Wang, X., Falconer, R. A., and Bockelmann-Evans, B. N. (2010). "Solving the depth-integrated solute transport equation with a TVD-MacCormack scheme." *Environmental Modelling & Software*, 25(12), 1619–1629.

70. Liang, Q., and Borthwick, A. G. L. (2009). "Adaptive quadtree simulation of shallow flows with wet-dry fronts over complex topography." *Computers and Fluids*, 38(2), 221–234.

71. Ling, Z., and Qin, C. (2015). "Numerical Modeling of Surface Waves over Submerged Flexible Vegetation." *Journal of Engineering Mechanics*, American Society of Civil Engineers, 141(8), A4015001.

72. Louaked, M., and Hanich, L. (1998). "TVD scheme for the shallow water equations." *Journal of Hydraulic Research*, Taylor & Francis, 36(3), 363–378.

73. Luhar, M., and Nepf, H. M. (2011). "Flow-induced reconfiguration of buoyant and flexible aquatic vegetation." *Limnology and Oceanography*, John Wiley & Sons, Ltd, 56(6), 2003–2017.

74. Luhar, M., and Nepf, H. M. (2013). "From the blade scale to the reach scale: A characterization of aquatic vegetative drag." *Advances in Water Resources*, Elsevier, 51, 305–316.

75. Lundgren, L., and Mattsson, K. (2020). "An efficient finite difference method for the shallow water equations." *Journal of Computational Physics*, 422, 109784.

76. Manners, R., Schmidt, J., and Wheaton, J. M. (2013). "Multiscalar model for the determination of spatially explicit riparian vegetation roughness." *Journal of Geophysical Research: Earth Surface*, John Wiley & Sons, Ltd, 118(1), 65–83.

77. Marini, G., Fontana, N., and Singh, V. P. (2017). "Derivation of 2D Velocity Distribution in Watercourses Using Entropy." *Journal of Hydrologic Engineering*, 22(6), 04017003.

78. Marriott, M., and Jayaratne, R. (2010). “Hydraulic roughness--links between Manning’s coefficient, Nikuradse’s equivalent sand roughness and bed grain size.” *Advances in Computing and Technology 2010*, University of East London, School of Architecture Computing and Engineering, 27–32.

79. Mathur, D. (1973). “Food Habits and Feeding Chronology of the Blackbanded Darter, Percina nigrofasciata (Agassiz), in Halawakee Creek, Alabama.” *Transactions of the American Fisheries Society*, Taylor & Francis, 102(1), 48–55.

80. Mathur Ichthyological Associates, D., and Robbins, T. W. (1971). “Food Habits and Feeding Chronology of Young White Crappie, Pomoxis annularis Rafinesque, in Conowingo Reservoir.” *Transactions of the American Fisheries Society*, John Wiley & Sons, Ltd, 100(2), 307–311.

81. McNaughton, J. (2009). “Laboratory modeling of open channel flow past emergent vegetation.” *University of Manchester, Manchester, UK*, Citeseer.

82. Melek, K.-A. C., and A., M. M. (2007). “Kinematic and Diffusion Waves: Analytical and Numerical Solutions to Overland and Channel Flow.” *Journal of Hydraulic Engineering*, American Society of Civil Engineers, 133(2), 217–228.

83. Merritt, D. M., Scott, M. L., LeROY Poff, N., Auble, G. T., and Lytle, D. A. (2010). “Theory, methods and tools for determining environmental flows for riparian vegetation: riparian vegetation-flow response guilds.” *Freshwater Biology*, John Wiley & Sons, Ltd, 55(1), 206–225.

84. Ming, H. T., and Chu, C. R. (2000). “Two-dimensional shallow water flows simulation using TVD-MacCormack Scheme.” *Journal of Hydraulic Research*, Taylor & Francis, 38(2), 123–131.

85. Mirauda, D., and Russo, M. G. (2019). “Information entropy theory applied to the dip-phenomenon analysis in open channel flows.” *Entropy*, 21(6), 1–13.

86. Mitchell, D. S. (1974). “The effects of excessive aquatic plant populations.” *Aquatic Vegetation and its use and control. UNESCO, Paris*, 50–56.

87. Molls, T., and Chaudhry, M. H. (1995). “Depth-averaged open-channel flow model.” *Journal of Hydraulic Engineering*, American Society of Civil Engineers, 121(6), 453–465.

88. Molls, T., and Zhao, G. (2000). “Depth-averaged simulation of supercritical flow in channel with wavy sidewall.” *Journal of Hydraulic Engineering*, American Society of Civil Engineers, 126(6), 437–445.

89. Moramarco, T., Saltalippi, C., Singh, V. P., and Asce, F. (2004). “Estimation of Mean Velocity in Natural Channels Based on Chiu ’ s Velocity Distribution Equation.” 9(1), 42–50.

90. Moramarco, T., and Singh, V. P. (2010a). “Formulation of the entropy parameter based on hydraulic and geometric characteristics of river cross sections.” *Journal of Hydrologic Engineering*, American Society of Civil Engineers, 15(10), 852–858.

91. Moramarco, T., and Singh, V. P. (2010b). “Formulation of the Entropy Parameter Based on Hydraulic and Geometric Characteristics of River Cross Sections.” *Journal of Hydrologic Engineering*, 15(10), 852–858.

92. Murphy, E. C. (1904). *Accuracy of stream measurements*.

93. Murty Bhallamudi, S., and Hanif Chaudhry, M. (1992). “Computation of flows in open-channel transitions.” *Journal of Hydraulic Research*, Taylor \& Francis, 30(1), 77–93.

94. Naot, D., Nezu, I., and Nakagawa, H. (1996). “Hydrodynamic behavior of partly vegetated open channels.” *Journal of Hydraulic Engineering*, American Society of Civil Engineers,

122(11), 625–633.

95. Nepf, H. M. (1999). “Drag, turbulence, and diffusion in flow through emergent vegetation.” *Water resources research*, Wiley Online Library, 35(2), 479–489.

96. Nepf, H. M. (2011a). “Flow and transport in regions with aquatic vegetation.” *Annual Review of Fluid Mechanics*, 44, 123–142.

97. Nepf, H. M. (2011b). “Flow and Transport in Regions with Aquatic Vegetation.” *Annual Review of Fluid Mechanics*, Annual Reviews, 44(1), 123–142.

98. Niayifar, A., Oldroyd, H. J., Lane, S. N., and Perona, P. (2018). “Modeling Macroroughness Contribution to Fish Habitat Suitability Curves.” *Water Resources Research*, John Wiley & Sons, Ltd, 54(11), 9306–9320.

99. Nikora, V. (2010). “Hydrodynamics of aquatic ecosystems: An interface between ecology, biomechanics and environmental fluid mechanics.” *River Research and Applications*, John Wiley & Sons, Ltd, 26(4), 367–384.

100. Nikora, V., McLean, S., Coleman, S., Pokrajac, D., McEwan, I., Campbell, L., Aberle, J., Clunie, D., and Koll, K. (2007). “Double-Averaging Concept for Rough-Bed Open-Channel and Overland Flows: Applications.” *Journal of Hydraulic Engineering*, 133(8), 884–895.

101. Osborne, A. R. (1989). “Barren mountains, raging rivers: The ecological and social effects of changing land use on the Lower Yangzi periphery in late imperial China.” Columbia University.

102. Ouyang, C., He, S., Xu, Q., Luo, Y., and Zhang, W. (2013). “A MacCormack-TVD finite difference method to simulate the mass flow in mountainous terrain with variable computational domain.” *Computers & Geosciences*, 52, 1–10.

103. Papadaki, C., Soulis, K., Muñoz-Mas, R., Martinez-Capel, F., Zogaris, S., Ntoanidis, L., and Dimitriou, E. (2016). "Potential impacts of climate change on flow regime and fish habitat in mountain rivers of the south-western Balkans." *Science of The Total Environment*, 540, 418–428.

104. Peres, D. J., and Cancelliere, A. (2016). "Environmental Flow Assessment Based on Different Metrics of Hydrological Alteration." *Water Resources Management*, 30(15), 5799–5817.

105. Petryk, S., and Bosmajian III, G. (1975). "Analysis of flow through vegetation." *Journal of the Hydraulics Division*, American Society of Civil Engineers, 101(7), 871–884.

106. Pfeiffer, M., and Ionita, M. (2017). "Assessment of Hydrologic Alterations in Elbe and Rhine Rivers, Germany." *Water* .

107. Poff, N. L., Allan, J. D., Palmer, M. A., Hart, D. D., Richter, B. D., Arthington, A. H., Rogers, K. H., Meyer, J. L., and Stanford, J. A. (2003). "River flows and water wars: emerging science for environmental decision making." *Frontiers in Ecology and the Environment*, John Wiley & Sons, Ltd, 1(6), 298–306.

108. Pu, J. H., Hussain, A., Guo, Y. kun, Vardakastanis, N., Hanmaiahgari, P. R., and Lam, D. (2019). "Submerged flexible vegetation impact on open channel flow velocity distribution: An analytical modelling study on drag and friction." *Water Science and Engineering*, Elsevier Ltd, 12(2), 121–128.

109. Pyrce, R. (2004). "Hydrological low flow indices and their uses." *Watershed Science Centre,(WSC) Report*, (04–2004).

110. Rahman, M., and Chaudhry, M. H. (1998). "Simulation of dam-break flow with

grid adaptation." *Advances in Water Resources*, 21(1), 1–9.

111. Rozovski\u\i. (n.d.). *Flow of water in bends of open channels*.

112. S., S. C. C., and Ted, Y. C. (1979). "Velocity Profiles and Minimum Stream Power." *Journal of the Hydraulics Division*, American Society of Civil Engineers, 105(8), 981–998.

113. Seo, I. W., Kim, Y. Do, and Song, C. G. (2014). "Validation of Depth-Averaged Flow Model Using Flat-Bottomed Benchmark Problems." *The Scientific World Journal*, (D. Liang, ed.), Hindawi Publishing Corporation, 2014, 197539.

114. Shan, Y., Liu, X., Yang, K., and Liu, C. (2017). "Analytical model for stage-discharge estimation in meandering compound channels with submerged flexible vegetation." *Advances in Water Resources*, 108, 170–183.

115. Shannon, C. E. (1948). "A mathematical theory of communication." *The Bell system technical journal*, Nokia Bell Labs, 27(3), 379–423.

116. Shields, F. D., Coulton, K. G., and Nepf, H. (2017). "Representation of Vegetation in Two-Dimensional Hydrodynamic Models." *Journal of Hydraulic Engineering*, 143(8), 02517002.

117. Singh, V. P. (2013). *Entropy theory and its application in environmental and water engineering*. John Wiley \& Sons.

118. Siviglia, A., Nobile, G., and Colombini, M. (2008). "Quasi-conservative formulation of the one-dimensional saint-venant--exner model." *Journal of Hydraulic Engineering*, American Society of Civil Engineers, 134(10), 1521–1526.

119. Smakhtin, V., Revenga, C., and Döll, P. (2004). "A Pilot Global Assessment of Environmental Water Requirements and Scarcity." *Water International*, Routledge, 29(3),

307–317.

120. Smakhtin, V. U. (2001). “Low flow hydrology: a review.” *Journal of hydrology*, Elsevier, 240(3–4), 147–186.

121. Spurgeon, J., Pegg, M., Parasiewicz, P., and Rogers, J. (2019). “River-Wide Habitat Availability for Fish Habitat Guilds: Implications for In-Stream Flow Protection.” *Water* .

122. Stearns, F. P. (1883). “On the current-meter, together with a reason why the maximum velocity of water flowing in open channels is below the surface.” *Transactions of the American Society of Civil Engineers*, American Society of Civil Engineers, 12(1), 301–338.

123. Stoesser, T., Wilson, C. A. M. E., Bates, P. D., and Dittrich, A. (2003a). “Application of a 3D numerical model to a river with vegetated floodplains.” *Journal of Hydroinformatics*, 5(2), 99–112.

124. Stoesser, T., Wilson, C., Bates, P. D., and Dittrich, A. (2003b). “Application of a 3D numerical model to a river with vegetated floodplains.” *Journal of Hydroinformatics*, IWA Publishing, 5(2), 99–112.

125. Stone, B. M., and Shen, H. T. (2002). “Hydraulic Resistance of Flow in Channels with Cylindrical Roughness.” *Journal of Hydraulic Engineering*, 128(5), 500–506.

126. Strang, G. (1968). “On the Construction and Comparison of Difference Schemes.” *SIAM Journal on Numerical Analysis*, Society for Industrial and Applied Mathematics, 5(3), 506–517.

127. Tanaka, T., Yoshioka, H., Siev, S., Fujii, H., Ly, S., and Yoshimura, C. (2019). “A consistent finite difference local inertial model for shallow water simulation.” *Hydrological Research Letters*, 13(2), 28–33.

128. Tsakiris, G., and Bellos, V. (2014). “A Numerical Model for Two-Dimensional Flood Routing in Complex Terrains.” *Water Resources Management*, 28(5), 1277–1291.

129. Tseng, M.-H. (2004). “Improved treatment of source terms in TVD scheme for shallow water equations.” *Advances in Water Resources*, 27(6), 617–629.

130. Tsujimoto, T. (1999). “Fluvial processes in streams with vegetation.” *Journal of hydraulic research*, Taylor \& Francis, 37(6), 789–803.

131. “V E L O C I T Y DISTRIBUTION IN O P E N CHANNEL F L O W By Chao-Lin Chiu, 1 Member, ASCE.” (1989). *Manager*, 115(23463), 576–594.

132. Vaghefi, M., Akbari, M., and Fiouz, A. (2015). “An experimental study of mean and turbulent flow in a 180 degree sharp open channel bend: Secondary flow and bed shear stress.” *KSCE Journal of Civil Engineering*, 20.

133. van Veelen, T. J., Fairchild, T. P., Reeve, D. E., and Karunarathna, H. (2020). “Experimental study on vegetation flexibility as control parameter for wave damping and velocity structure.” *Coastal Engineering*, 157, 103648.

134. Velasco, D., Bateman, A., and Medina, V. (2008). “A new integrated hyro-mechanical model applied to flexible vegetation in riverbeds.” *Journal of Hydraulic Research*, 46(5), 579–597.

135. Verschoren, V., Meire, D., Schoelynck, J., Buis, K., Bal, K. D., Troch, P., Meire, P., and Temmerman, S. (2016). “Resistance and reconfiguration of natural flexible submerged vegetation in hydrodynamic river modelling.” *Environmental Fluid Mechanics*, 16(1), 245–265.

136. Vezza, P., Parasiewicz, P., Spairani, M., and Comoglio, C. (2014). “Habitat modeling in high-gradient streams: the mesoscale approach and application.” *Ecological*

Applications, John Wiley & Sons, Ltd, 24(4), 844–861.

137. Vincenzo, C., and S., S. G. (1998). "Numerical Simulation of 3D Quasi-Hydrostatic, Free-Surface Flows." *Journal of Hydraulic Engineering*, American Society of Civil Engineers, 124(7), 678–686.

138. Vismara, R., Azzellino, A., Bosi, R., Crosa, G., and Gentili, G. (2001). "Habitat suitability curves for brown trout (Salmo trutta fario L.) in the River Adda, Northern Italy: Comparing univariate and multivariate approaches." *River Research and Applications*, 17(1), 37–50.

139. Vogel, R. M., and Fennessey, N. M. (1995). "FLOW DURATION CURVES II: A REVIEW OF APPLICATIONS IN WATER RESOURCES PLANNING1." *JAWRA Journal of the American Water Resources Association*, John Wiley & Sons, Ltd, 31(6), 1029–1039.

140. Vyas, J. K., Perumal, M., and Moramarco, T. (2020). "Discharge Estimation Using Tsallis and Shannon Entropy Theory in Natural Channels." *Water* .

141. Wang, G.-T., Yao, C., Okoren, C., and Chen, S. (2006). "4-Point FDF of Muskingum method based on the complete St Venant equations." *Journal of Hydrology*, 324(1), 339–349.

142. Wang, X., Li, G., Qian, S., Li, J., and Wang, Z. (2019). "High order well-balanced finite difference WENO schemes for shallow water flows along channels with irregular geometry." *Applied Mathematics and Computation*, 363, 124587.

143. Wang, Y., Zhang, H., Yang, P., and Wang, Y. (2018). "Experimental Study of Overland Flow through Rigid Emergent Vegetation with Different Densities and Location Arrangements." *Water*, 10, 1638.

144. Welahettige, P., Vaagsaether, K., and Lie, B. (2018). "A solution method for one-dimensional shallow water equations using flux limiter centered scheme for open Venturi channels." *The Journal of Computational Multiphase Flows*, SAGE Publications Sage UK: London, England, 10(4), 228–238.

145. Whittaker, P., Wilson, C. A. M. E., and Aberle, J. (2015). "An improved Cauchy number approach for predicting the drag and reconfiguration of flexible vegetation." *Advances in Water Resources*, Elsevier Ltd., 83, 28–35.

146. Wilson, C., Stoesser, T., and Bates, P. D. (2005). "Modelling of Open Channel Flow through Vegetation." *Computational Fluid Dynamics: Applications in Environmental Hydraulics*, 395–428.

147. Wu, F. (2008). "Characteristics of flow resistance in open channels with non-submerged rigid vegetation." *Journal of Hydrodynamics, Ser. B*, Elsevier, 20(2), 239–245.

148. Wu, W., and Marsooli, R. (2012). "A depth-averaged 2D shallow water model for breaking and non-breaking long waves affected by rigid vegetation." *Journal of Hydraulic Research*, 50(6), 558–575.

149. Wu, Y., Falconer, R. A., and Struve, J. (2001). "Mathematical modelling of tidal currents in mangrove forests." *Environmental Modelling & Software*, 16(1), 19–29.

150. Xia, R. (1997). "Relation between Mean and Maximum Velocities in a Natural River." *Journal of Hydraulic Engineering*, 123(8), 720–723.

151. Yang, S.-Q., Tan, S.-K., and Lim, S.-Y. (2004). "Velocity Distribution and Dip-Phenomenon in Smooth Uniform Open Channel Flows." *Journal of Hydraulic Engineering*, 130(12), 1179–1186.

152. Yang, W., and Choi, S.-U. (2010). "A two-layer approach for depth-limited open-

channel flows with submerged vegetation." *Journal of Hydraulic Research*, Taylor & Francis, 48(4), 466–475.

153. Yang, Z., Bai, F., Huai, W., An, R., and Wang, H. (2017). "Modelling open-channel flow with rigid vegetation based on two-dimensional shallow water equations using the lattice Boltzmann method." *Ecological Engineering*, 106, 75–81.

154. Yi, S., and Panayiotis, D. (2010). "Modeling Unsteady Flow Characteristics of Hydropeaking Operations and Their Implications on Fish Habitat." *Journal of Hydraulic Engineering*, American Society of Civil Engineers, 136(12), 1053–1066.

155. Yin, X. A., Yang, Z., Zhang, E., Xu, Z., Cai, Y., and Yang, W. (2018). "A New Method of Assessing Environmental Flows in Channelized Urban Rivers." *Engineering*, Chinese Academy of Engineering, 4(5), 590–596.

156. Yu, H., and Huang, G. (2014). "A coupled 1D and 2D hydrodynamic model for free-surface flows." *Proceedings of the Institution of Civil Engineers: Water Management*, 167(9), 523–531.

157. Zhang, M., Qiao, H., and Xu, Y. (2017). "Numerical simulation of solitary wave propagation in a vegetated channel using an extended boussinesq model." *Journal of Marine Science and Technology (Taiwan)*, 25(1), 119–128.

158. Zhang, X., and Nepf, H. (2011). "Exchange flow between open water and floating vegetation." *Environmental Fluid Mechanics*, 11, 531–546.

159. Zhou, J. G., Causon, D. M., Mingham, C. G., and Ingram, D. M. (2001). "The Surface Gradient Method for the Treatment of Source Terms in the Shallow-Water Equations." *Journal of Computational Physics*, 168(1), 1–25.

PAPERS PRESENTED/PUBLISHED

1) **Baruah A,** Sarma, A. K. (2021), "A fully coupled two-dimensional flow – vegetation routing model in open channel flow" Enviromental Fluid Mechanics, Springer, http://link.springer.com/article/10.1007/s10652-021-09810-9

2) **Baruah A,** Sarma A K, & Hinge G. (2021),"Hydrological-hydrodynamic nexus for evaluation of fish habitat suitability in the Bhogdoi River, India" Journal of Hydrologic Engineering, 26(11), ASCE, 4021032. https://doi.org/10.1061/(ASCE)HE.1943-5584.0002127

3) **Baruah A,** Sarma A. K. (2020), **"**A quasi three dimensional hydrodynamic model for velocity distribution in open channel" ISH Journal of Hydraulic Engineering, Taylor and Francis, https://doi.org/10.1080/09715010.2020.1857665

4) **Baruah A,** Sarma A. K. (2020), " A simple and efficient two-dimensional hydrodynamic model for unsteady flow simulation in undulating bathymetryProgress in Computational Fluid Dynamics, an International Journal, 21(6), 369-377.

5) **Baruah A,** Sarma A. K. (2020), " Ecological flow assessment using hydrological and hydrodynamic routing model in Bhogdoi river, India" Modeling Earth Systems and Environment, Springer, DOI:10.1007/s40808-020-00982-9

6) Sarma A. K, **Baruah A(2018),** "A robust numerical scheme for simulation of transcritical flow in a braided river'; International conference in recent advancement in fluid and thermal science(I-CRAFT), BITS PILANI, DUBAI, (5-7 Dec) 2018, DOI: 10.1088/1742-6596/1276/1/012035,ISSN:1742-6596

7) **Baruah A,** Sarma D. J, & Sarma A K (2020), "A Geo-spatial and hydrodynamic analysis on the influence of flow diverting structures in a natural channel: A case study on Brahmaputra River near Majuli; Geo-spatial application for Natural resources management, (July 9-10,2020) NIRDPR-NERC, Guwahati.ISBN-978-81-8730-584-4

8) **Baruah Anupal,** Deka Priyam, Deka Ranjit, Sarma A K. "A 2D hydrodynamic model study in Brahmaputra River for implementation of bank protection work at Nimatighat", SWARM-2020.[Accepted]

9) Talukdar Gaurav, **Baruah Anupal** and Sarma A K "2D hydrodynamic model for evaluating impact of possible river front activities in an urbanized bank of Brahmaputra River" SWARM-2020[Accepted]